

**A study of the imprints of thermalisation on charged
particle emission using light front variables in
ultrarelativistic heavy-ion collisions**

National Centre for Nuclear Research

Warsaw, Poland



Doctoral Thesis

by

Rahul Ramachandran Nair

December 2019

Supervisor: Prof. dr hab. Teodor Siemiarczuk

This page is intentionally left blank

Acknowledgements

I would first like to thank my parents and sister for the relentless support they gave me for pursuing my PhD. I sincerely extend my gratitude to Prof. Teodor Siemiarczuk for accepting me as a PhD student at NCBJ Warsaw, advising me systematically and regularly, while allowing me to work with the natural pace I have. I would like to thank Prof. Ashok Kapoor (Chennai Mathematical Institute) and Prof. E. Harikumar (University Of Hyderabad) for the constant support they gave me to pursue in physics with their wise and timely interventions. I thank Prof. S. Chaturvedi (IISER, Bhopal) and Prof. Rukmani Mohanta (University Of Hyderabad) for the nice gestures extended to me. I thank Prof. K E Abraham, Prof. K.V Saban and Prof. Jacob Mathew (St. Berchmans College, Changanacherry) for the motivation and support they gave me to pursue my studies. I sincerely thank my Mridangam teacher T. S Satish Kumar (Changanacherry) for his teachings which helped me to keep up my nerve at difficult times. I would particularly like to thank Prof. C. B Ajayakumar for the crucial support he gave me during the initial phases of my adventures with the subject. I would like to thank Prof. Klaus Werner (Subatech, Nantes), Tanguy Pierog (Karlsruhe Institute of Technology, Germany), Maria Stefanek (Subatech, Nantes) for the advice and support on working with EPOS model. I thank Prof. Marcus Bleicher (Goethe University, Germany) for the consent to use the UrQMD model for my calculations. I thank Prof. Wladyslaw Trzaska (University of Jyväskylä) for allowing me to complete my service task with his team from Finland. I would like to thank Alexander Kalweit (CERN) for his support and very useful remarks about ALICE TPC. I thank Michael Floris (CERN), Marco Toppi (INFN, Frascati) and Alice Ohlson (Lund University, Sweden) for the useful discussions they offered. I would like to thank my good friends Robins Kurian, Govind. G. Nampoothiri (ISRO, Thiruvananthapuram), Antony Jose (Wojskowa Akademia Techniczna, Warsaw) and Preeti Dhankher (IIT, Bombay) for their true full and consistent support to me. I sincerely thank my friend Sanal Vadakkillam for the help he extended to me. I thank my friend Sapna Ravindran (Massey University, New Zealand) for collecting some rare reference materials for me from Australia. I extend my sincere gratitude to my friend Bharati Naik (IIT, Bombay) and Prof. Kajari Mazumdar (TIFR, Mumbai) for the help with the computational resources at a very crucial time of my studies. I thank Souvik Priyam Adhya (Charles University, Prague) for helping me with his experience in the

initial phase of my encounters with Monte Carlo models. I thank Deepa Thomas (University of Texas, Austin) and Rohin Narayan (Southern Methodist University, Dallas) for the support they gave me at various phases of my studies. I thank Prof. Piotr Goldstein (NCBJ, Warsaw) for the teachings on statistical mechanics and Prof. Jacub Wagner (NCBJ, Warsaw) for his teachings on QCD. I am grateful to Prof. Michal Spalinski, the head of the Doctoral study (NCBJ) for the help he extended to me. I would like to thank the secretaries Mrs Anna Piwek and Mrs Martyna Polny for the administrative assistance they offered me multiple times during my doctoral study. I sincerely thank Oleksandr Kovalenko (NCBJ, Warsaw) and Podist Kurashvilli (NCBJ, Warsaw) for the continuous support and help they both gave me throughout my stay in Warsaw and Geneva. I thank Paritosh Verma (NCBJ, Warsaw) for the warm hospitality he extended to me. Finally, I would like to thank all my teachers, friends and well-wishers whom I did not mention by name. Without all your support and help, I couldn't have pursued my studies. Thank you all.

Warsaw, Poland
December 2019

Rahul Ramachandran Nair

Streszczenie

W niniejszej pracy przedstawiono badanie możliwej termalizacji układu powstałego w zderzeniach relatywistycznych ciężkich jonów metodą wykorzystującą zmienną stożka świetlnego. Do analizy użyto wygenerowane zdarzenia przy energiach RHIC i dane z eksperymentu ALICE przy energiach LHC uzyskane na Dużym Zderzaczu Hadronów. Opisano koncepcję występowania materii składającej się z uwolnionych kwarków i gluonów oraz eksperymentalne próby wytworzenia takiej materii w laboratorium w zderzeniach ciężkich jonów. Omówiono pojęcie temperatury i sygnatury istnienia układu, który osiągnął równowagę termiczną w takich zderzeniach. Przedstawiono szczegółowy opis analizy z wykorzystaniem zmiennych stożka świetlnego oraz metod i koncepcji geometrycznych wykorzystanych w naszych badaniach. Modele UrQMD, EPOS i HIJING zostały zastosowane do symulacji zderzeń ciężkich jonów przy różnych energiach, a użycie zmiennych stożka świetlnego na poziomie fenomenologicznym do ich badania było wstępnym krokiem w kierunku analizy danych LHC. Schemat analizy pozwala podzielić cząstkiw przestrzeni fazowej na dwie grupy. Pokazano, że rozkłady kwadratu pędu poprzecznego, kąta biegunowego i zmiennej stożka światła cząstek należących do jednej z tych dwóch grup można opisać przy pomocy boltzmannowskiego rozkładu sparametryzowanego przez tę samą, w granicach błędów, wartość temperatury zależną od masy cząstki. Udaje się to zrobić dla cząstek o różnych masach i energiach zderzenia. Analizę przeprowadzono dla π^\pm , K^\pm , $p(\bar{p})$, η^0 , hiperony Λ , Σ , and Ξ dla zderzeń Au-Au w modelu UrQMD przy $\sqrt{s} = 200$ GeV, dla π^\pm , K^\pm i $p(\bar{p})$ dla zderzeń Au-Au w modelu EPOS przy $\sqrt{s} = 200$ GeV oraz π^\pm , K^\pm i $p(\bar{p})$ dla zderzeń Pb-Pb w modelu HIJING przy $\sqrt{s} = 2.76$ TeV. To pozwala nam myśleć, że osiągnięto termalizację w układzie, z którego emitowane są te cząstki. Model HIJING został również wykorzystany do wykazania, że wydzielenie grupy cząstek termalizowanych z użyciem zmiennych stożka światła jest wykonalne, nawet jeśli mamy kinematyczne cięcia na pośpieszności i pędu poprzecznym, związanych ze cechami detektorów w eksperymentach. Podano opis detektorów eksperymentu ALICE w punkcie 2 Dużego Zderzacza Hadronów, a następnie przedstawiono analizę przy pomocy zmiennych stożka świetlnego zderzeń Pb-Pb przy $\sqrt{s} = 2.76$ TeV z eksperymentu ALICE dla zidentyfikowanych π^\pm , K^\pm , $p(\bar{p})$ i deuteronów w zderzeniach o różnych centralnościach. Zawsze mogliśmy znaleźć grupę cząstek zachowujących się zgodnie ze statystyką Boltzmann. To skłania nas do domyslenia, że dla tak wybranej grupy cząstek powstałych w zderzeniach ciężkich jonów w eksperymencie ALICE na LHC, termalizacja została osiągnięta.

This page is intentionally left blank

Abstract

In this thesis, a study is presented of the possible thermalisation of the medium created in relativistic heavy-ion collisions using the scheme involving light front variables. Simulated events at RHIC energies and ALICE experimental data at the LHC energies from the Large Hadron Collider are used for this analysis. An introduction to the concepts regarding a quark-gluon deconfined medium is given and the experimental attempts to create such a system in the laboratory in heavy-ion collisions are described. The concept of temperature and the signatures of the existence of a system which has reached thermal equilibrium in such collisions are discussed. A detailed description of the light front analysis, the methods and geometrical aspects involved in our study are presented. UrQMD, EPOS and HIJING models were used to simulate the heavy-ion collisions at various energies and the light front scheme was applied on a phenomenological level as a preliminary step towards the analysis of the LHC data. The analysis scheme could separate the particles in the phase space into two groups. It is shown that the distributions of square of the transverse momentum, the polar angle and the light front variable of particles belonging to one among these two groups can be described with the Boltzmannian form for their energy distribution parameterised by the same, within the errors, value of the mass-dependent temperature irrespective of the particle species studied and the available centre of mass-energy of the collisions. The analysis has been carried out for π^\pm , K^\pm , $p(\bar{p})$, η^0 , the hyperons Λ , Σ , and Ξ from Au-Au UrQMD collisions at $\sqrt{s} = 200$ GeV, for π^\pm , K^\pm and $p(\bar{p})$ from Au-Au EPOS collisions at $\sqrt{s} = 200$ GeV, and for π^\pm , K^\pm and $p(\bar{p})$ from Pb-Pb HIJING collisions at $\sqrt{s} = 2.76$ TeV. This enables us to think that a possible thermalisation has been reached in the medium from which these particles are emitted. The HIJING model was also used to demonstrate that the light front analysis is feasible even when we have kinematic cuts on pseudorapidity and transverse momentum owing to the specifications of the experimental setups. The details of the ALICE apparatus at point 2 of the Large Hadron Collider are given followed by the presentation of the light front analysis of Pb-Pb collisions at $\sqrt{s} = 2.76$ TeV from the ALICE experiment. The identified particle species namely π^\pm , K^\pm , $p(\bar{p})$ and deuterons from Pb-Pb collisions at various centralities were used to perform the light front analysis and we could always find a group of particles which follows the Boltzmann statistics. This impels us to think that for the so selected group of particles a thermalisation has been reached in the heavy-ion collisions in ALICE experiment at LHC.

This page is intentionally left blank

Contents

| | | |
|----------|---|-----------|
| 1 | Introduction | 1 |
| 2 | Quark Gluon Plasma and Heavy Ion Collisions | 3 |
| 2.1 | Naive picture of a deconfined state of matter | 3 |
| 2.2 | Pre-QCD studies of the hadronic matter | 5 |
| 2.3 | The QCD empowered era and 'Quark-Gluon Plasma' | 5 |
| 2.4 | Heavy Ion Collisions | 8 |
| 2.5 | Our attempt with Boltzmann distribution and light front variables | 19 |
| 3 | Light front variables at hadron colliders | 21 |
| 3.1 | Forms Of Relativistic Dynamics | 21 |
| 3.2 | The Lobachevsky geometry in nuclear collisions | 22 |
| 3.3 | Scale invariant Light Front variables | 26 |
| 3.4 | Definition and properties | 27 |
| 3.5 | Kinematically Forbidden Regions | 30 |
| 3.6 | Properties of Light Front distribution | 30 |
| 3.7 | Our scheme of study with Light Front Variables | 30 |
| 3.8 | Some counter-arguments from the past | 34 |
| 4 | Light Front Analysis with UrQMD, EPOS and HIJING models | 37 |
| 4.1 | Description of the UrQMD Model | 37 |
| 4.2 | Light Front Analysis of UrQMD Collisions at $\sqrt{s} = 200$ GeV | 40 |
| 4.3 | Description of EPOS event Generator | 48 |
| 4.4 | Light Front Analysis of EPOS Collisions at $\sqrt{s} = 200$ GeV | 49 |
| 4.5 | Description of HIJING event Generator | 53 |

| | | |
|----------|--|------------|
| 4.6 | Light Front Analysis of HIJING Collisions at $\sqrt{s} = 2.76$ TeV | 53 |
| 4.7 | Summary of the Monte-Carlo studies and conclusions | 58 |
| 5 | ALICE Experiment at The Large Hadron Collider | 60 |
| 5.1 | The Large Hadron Collider (LHC) | 60 |
| 5.2 | The ALICE Experiment | 62 |
| 5.3 | Detectors in ALICE | 62 |
| 6 | Analysis of the Pb-Pb collisions at $\sqrt{s} = 2.76$ TeV in ALICE | 78 |
| 6.1 | Light Front Analysis of the ALICE Data | 78 |
| 6.1.1 | ALICE Data set and Analysis Framework | 79 |
| 6.1.2 | Trigger and Event Selections | 79 |
| 6.1.3 | Track Selection and cuts | 79 |
| 6.1.4 | Particle Identification Scheme using TPC - Raw data distributions | 80 |
| 6.1.5 | Estimation of Correction factor using Monte Carlo | 81 |
| 6.1.6 | Systematic errors | 82 |
| 6.1.7 | Basic Analysis Strategy & Resulting Plots | 84 |
| 6.2 | A Comprehensive view of the analysis and Conclusions | 108 |
| 6.3 | Levchenko's paper revisited | 115 |
| 7 | Summary & Conclusions | 117 |
| A | UrQMD input file for minimumm bias data simulation | 120 |
| B | Real Data & Monte Carlo Anchored Run Numbers | 121 |

List of Figures

| | | |
|-----|---|----|
| 2.1 | Space-time history of the universe. The figure is taken from [4] | 4 |
| 2.2 | Running Coupling Constant of QCD. It is customary to quote α_s at 91 GeV which is the mass of the Z boson. The figure is taken from [2]. | 7 |
| 2.3 | Dependence of the energy density as a function of the temperature of the hadronic matter at $\mu_B = 0$ given by lattice QCD calculations at finite temperature for zero quark masses. The figure is taken from [18] | 9 |
| 2.4 | Phase diagram of hadronic matter (left, From [19]) and water (right, From [20]) | 9 |
| 2.5 | Schematic view of the Spacetime picture of a heavy-ion Collision (From [21]) | 10 |
| 2.6 | Geometry of a heavy-ion collision (From [23]). \mathbf{p} denotes momentum of a particle emerging from the collision. The reaction plane is marked, and the orthogonal mid-rapidity plane $\theta = \pi/2$, is labeled as $\eta = 0$ | 12 |
| 2.7 | Bjorken scenario of a heavy-ion collision. The drawing is inspired by the Figure:10 in [25] | 15 |
| 2.8 | Elliptic flow in a heavy-ion Collision. Figure is taken from [37] | 18 |
| 2.9 | The Weibel instability (The Figure is taken from [37]) | 19 |
| 3.1 | A simplex in the Lobachevsky space | 26 |
| 3.2 | Schematic view of the surfaces of constants | 27 |
| 3.3 | The schematic view of the surfaces of constant ζ^\pm | 31 |
| 3.4 | ζ , $\cos(\theta)$ and p_T^2 distributions of π^\pm in the reaction $p\bar{p} \rightarrow \pi^\pm X$ at a centre of mass energy of around 6 GeV. The temperatures obtained from this analysis are 119 ± 3 , 86 ± 3 and 105 ± 1 MeV respectively from the distributions with $\tilde{\zeta}$ taken as 2.0. Figures are taken from [47] | 35 |
| 3.5 | The predictions of angular distributions in the c.m.s at 40 GeV/c for $\zeta > \tilde{\zeta}$ from the calculations in [55] (Figure:3 in [55]). | 35 |

| | | |
|------|---|----|
| 4.1 | List of Baryons in UrQMD (Taken from [62]). | 38 |
| 4.2 | List of Mesons in UrQMD (Taken from [62]). | 39 |
| 4.3 | ζ , p_T^2 and $\cos(\theta)$ distributions fitted with equations 3.40, 3.44 and 3.43 respectively for UrQMD π^\pm . The green curve in the ζ distributon is the extrapolation of the fit. | 41 |
| 4.4 | Peyrou p_T - p_Z plot of π^\pm . The red region corresponds to $\zeta > 6.35$ | 41 |
| 4.5 | ζ , p_T^2 and $\cos(\theta)$ distributions fitted with equations 3.40, 3.44 and 3.43 respectively for UrQMD kaons. The green curve in the ζ distributon is the extrapolation of the fit. | 42 |
| 4.6 | Peyrou p_T - p_Z plot of K^\pm . The red region corresponds to $\zeta > 5.65$ | 42 |
| 4.7 | ζ , p_T^2 and $\cos(\theta)$ distributions fitted with equations 3.40, 3.44 and 3.43 respectively for UrQMD protons. The green curve in the ζ distributon is the extrapolation of the fit. | 43 |
| 4.8 | Peyrou p_T - p_Z plot of UrQMD protons . The red region corresponds to $\zeta > 5.0$ | 43 |
| 4.9 | ζ , p_T^2 and $\cos(\theta)$ distributions fitted with equations 3.40, 3.44 and 3.43 respectively for UrQMD $\Sigma(1192)$. The green curve in the ζ distributon is the extrapolation of the fit. | 44 |
| 4.10 | Peyrou p_T - p_Z plot of $\Sigma(1192)$. The red region corresponds to $\zeta > 4.85$ | 44 |
| 4.11 | ζ , p_T^2 and $\cos(\theta)$ distributions fitted with equations 3.40, 3.44 and 3.43 respectively for UrQMD $\Xi(1317)$. The green curve in the ζ distributon is the extrapolation of the fit. | 45 |
| 4.12 | Peyrou p_T - p_Z plot of $\Xi(1317)$. The cyan region corresponds to $\zeta > 4.90$ | 45 |
| 4.13 | ζ , p_T^2 and $\cos(\theta)$ distributions fitted with equations 3.40, 3.44 and 3.43 respectively for UrQMD η^0 . The green curve in the ζ distributon is the extrapolation of the fit. | 46 |
| 4.14 | Peyrou p_T - p_Z plot of η^0 . The red region corresponds to $\zeta > 5.60$ | 46 |
| 4.15 | ζ , p_T^2 and $\cos(\theta)$ distributions fitted with equations 3.40, 3.44 and 3.43 respectively for UrQMD Λ^0 . The green curve in the ζ distributon is the extrapolation of the fit. | 47 |
| 4.16 | Elementary Interaction in EPOS (left) and Multiple Interaction (right) via the exchange of energy-conserving ladders in parallel. Figure is taken from [69] | 49 |
| 4.17 | ζ , p_T^2 and $\cos(\theta)$ distributions for EPOS Pions fitted with equations 3.40, 3.44 and 3.43 respectively. The green curve in the ζ distributon is the extrapolation of the fit. | 50 |
| 4.18 | Peyrou p_T - p_Z plot of π^\pm . The red region corresponds to $\zeta > 6.35$ | 50 |
| 4.19 | ζ , p_T^2 and $\cos(\theta)$ distributions for EPOS kaons fitted with equations 3.40, 3.44 and 3.43 respectively. The green curve in the ζ distributon is the extrapolation of the fit. | 51 |
| 4.20 | Peyrou p_T - p_Z plot of K^\pm . The red region corresponds to $\zeta > 5.50$ | 51 |

| | | |
|------|---|----|
| 4.21 | ζ , p_T^2 and $\cos(\theta)$ distributions for EPOS protons fitted with equations 3.40, 3.44 and 3.43 respectively. The green curve in the ζ distributon is the extrapolation of the fit. | 52 |
| 4.22 | Peyrou p_T - p_Z plot of p . The red region corresponds to $\zeta > 5.0$ | 52 |
| 4.23 | HIJING π^\pm distributions. The green curve in the ζ distributon is the extrapolation of the fit. | 55 |
| 4.24 | HIJING K^\pm distributions. The green curve in the ζ distributon is the extrapolation of the fit. | 56 |
| 4.25 | HIJING $p(\bar{p})$ distributions. The green curve in the ζ distributon is the extrapolation of the fit. | 57 |
| 4.26 | Estimated Temperature v/s Mass from the Monte Carlo models using light front analysis. | 59 |
| 5.1 | Schematics of the CERN accelerator complex. Figure is taken from [98] | 61 |
| 5.2 | ALICE - A Large Ion Collider Experimental setup. The figure is taken from [105] | 62 |
| 5.3 | Layout of the Inner tracking system. The figure is taken from [107] | 63 |
| 5.4 | Specific energy-loss signal Vs momentum in Pb-Pb collisions for ITS standalone tracks measured with the ITS. The figure is taken from [106] | 65 |
| 5.5 | Layout of ALICE TPC. The Figure is taken from figure([108]) | 66 |
| 5.6 | Schematic illustration of TPC and readout chambers. The figure is taken from [111] | 67 |
| 5.7 | Specific energy-loss signal Vs rigidity in Pb-Pb collisions as measured by ALICE TPC. The figure is taken from [112] | 69 |
| 5.8 | Schematic layout of one of the 18 TOF super modules inside the ALICE space frame. The figure is taken from [114] | 71 |
| 5.9 | β Vs Momentum of particle tracks as measured by TOF. Figure is taken from [115] | 72 |
| 5.10 | Distribution of the summed amplitudes in V0 fitted with Glauber model (red curve).[126] | 77 |
| 6.1 | dE/dx vs TPC Momentum | 81 |
| 6.2 | Flow chart of the light front analysis Scheme | 85 |
| 6.3 | ALICE $ \zeta $, p_T^2 and $ \cos(\theta) $ distributions fitted with (3.40), (3.44), and (3.43) respectively for π^\pm , 0 – 5% centrality. The green curve in the ζ distributon is the extrapolation of the fit. | 86 |
| 6.4 | ALICE $ \zeta $, p_T^2 and $ \cos(\theta) $ distributions fitted with (3.40), (3.44), and (3.43) respectively for π^\pm , 5 – 10% centrality. The green curve in the ζ distributon is the extrapolation of the fit. | 87 |
| 6.5 | ALICE $ \zeta $, p_T^2 and $ \cos(\theta) $ distributions fitted with (3.40), (3.44), and (3.43) respectively for π^\pm , 10 – 20% centrality. The green curve in the ζ distributon is the extrapolation of the fit. | 88 |
| 6.6 | ALICE $ \zeta $, p_T^2 and $ \cos(\theta) $ distributions fitted with (3.40), (3.44), and (3.43) respectively for π^\pm , 20 – 40% centrality. The green curve in the ζ distributon is the extrapolation of the fit. | 89 |

| | | |
|------|--|-----|
| 6.7 | ALICE $ \zeta $, p_T^2 and $ \cos(\theta) $ distributions fitted with (3.40), (3.44), and (3.43) respectively for π^\pm , 40 – 60% centrality. The green curve in the ζ distributon is the extrapolation of the fit. . . | 90 |
| 6.8 | ALICE $ \zeta $, p_T^2 and $ \cos(\theta) $ distributions fitted with (3.40), (3.44), and (3.43) respectively for π^\pm , 60 – 80% centrality. The green curve in the ζ distributon is the extrapolation of the fit. . . | 91 |
| 6.9 | ALICE $ \zeta $, p_T^2 and $ \cos(\theta) $ distributions fitted with (3.40), (3.44), and (3.43) respectively for π^\pm , 0 – 80% centrality. The green curve in the ζ distributon is the extrapolation of the fit. . . | 92 |
| 6.10 | ALICE $ \zeta $, p_T^2 and $ \cos(\theta) $ distributions fitted with (3.40), (3.44), and (3.43) respectively for K^\pm , 0 – 5% centrality. The green curve in the ζ distributon is the extrapolation of the fit. . . | 93 |
| 6.11 | ALICE $ \zeta $, p_T^2 and $ \cos(\theta) $ distributions fitted with (3.40), (3.44), and (3.43) respectively for K^\pm , 5 – 10% centrality. The green curve in the ζ distributon is the extrapolation of the fit. . . | 94 |
| 6.12 | ALICE $ \zeta $, p_T^2 and $ \cos(\theta) $ distributions fitted with (3.40), (3.44), and (3.43) respectively for K^\pm , 10 – 20% centrality. The green curve in the ζ distributon is the extrapolation of the fit. . . | 95 |
| 6.13 | ALICE $ \zeta $, p_T^2 and $ \cos(\theta) $ distributions fitted with (3.40), (3.44), and (3.43) respectively for K^\pm , 20 – 40% centrality. The green curve in the ζ distributon is the extrapolation of the fit. . . | 96 |
| 6.14 | ALICE $ \zeta $, p_T^2 and $ \cos(\theta) $ distributions fitted with (3.40), (3.44), and (3.43) respectively for K^\pm , 40 – 60% centrality. The green curve in the ζ distributon is the extrapolation of the fit. . . | 97 |
| 6.15 | ALICE $ \zeta $, p_T^2 and $ \cos(\theta) $ distributions fitted with (3.40), (3.44), and (3.43) respectively for K^\pm , 60 – 80% centrality. The green curve in the ζ distributon is the extrapolation of the fit. . . | 98 |
| 6.16 | ALICE $ \zeta $, p_T^2 and $ \cos(\theta) $ distributions fitted with (3.40), (3.44), and (3.43) respectively for K^\pm , 0 – 80% centrality. The green curve in the ζ distributon is the extrapolation of the fit. . . | 99 |
| 6.17 | ALICE $ \zeta $, p_T^2 and $ \cos(\theta) $ distributions fitted with (3.40), (3.44), and (3.43) respectively for $p(\bar{p})$, 0 – 5% centrality. The green curve in the ζ distributon is the extrapolation of the fit. . . | 100 |
| 6.18 | ALICE $ \zeta $, p_T^2 and $ \cos(\theta) $ distributions fitted with (3.40), (3.44), and (3.43) respectively for $p(\bar{p})$, 5 – 10% centrality. The green curve in the ζ distributon is the extrapolation of the fit. . . | 101 |
| 6.19 | ALICE $ \zeta $, p_T^2 and $ \cos(\theta) $ distributions fitted with (3.40), (3.44), and (3.43) respectively for $p(\bar{p})$, 10 – 20% centrality. The green curve in the ζ distributon is the extrapolation of the fit. . . | 102 |
| 6.20 | ALICE $ \zeta $, p_T^2 and $ \cos(\theta) $ distributions fitted with (3.40), (3.44), and (3.43) respectively for $p(\bar{p})$, 20 – 40% centrality. The green curve in the ζ distributon is the extrapolation of the fit. . . | 103 |
| 6.21 | ALICE $ \zeta $, p_T^2 and $ \cos(\theta) $ distributions fitted with (3.40), (3.44), and (3.43) respectively for $p(\bar{p})$, 40 – 60% centrality. The green curve in the ζ distributon is the extrapolation of the fit. . . | 104 |

| | | |
|------|--|-----|
| 6.22 | ALICE $ \zeta $, p_T^2 and $ \cos(\theta) $ distributions fitted with (3.40), (3.44), and (3.43) respectively for $p(\bar{p})$, 60 – 80% centrality. The green curve in the ζ distributon is the extrapolation of the fit. | 105 |
| 6.23 | ALICE $ \zeta $, p_T^2 and $ \cos(\theta) $ distributions fitted with (3.40), (3.44), and (3.43) respectively for $p(\bar{p})$, 0 – 80% centrality. The green curve in the ζ distributon is the extrapolation of the fit. | 106 |
| 6.24 | Results of the light front analysis over ALICE raw deuterons assuming a flat correction factor in the region $0.40 < p_T < 0.90$ GeV/c and $ \eta < 0.8$ | 107 |
| 6.25 | p_T Ranges for the identified particle species | 110 |
| 6.26 | Paraboloids corresponding to the $\tilde{\zeta}$ values used in this analysis for various particle species. | 111 |
| 6.27 | Temperature obtained from the light front scheme in the minimum bias trigger as a function of the mass of the particle. (see equation 4.8) | 112 |
| 6.28 | Temperature versus centrality percentile. The regions of centrality percentile considered are 0 – 5%, 5 – 10%, 10 – 20%, 20 – 40%, 40 – 60% and 60 – 80%. The mean value is used to mark the points. (see equation 4.8) | 113 |

This page is intentionally left blank

Chapter 1

Introduction

The standard model of particle physics describes the fundamental forces governing the universe except the gravitational force. Quantum Chromodynamics(QCD) is the part of it which takes into account the strong nuclear force. With the advent of QCD and the discovery of asymptotic freedom, the theoretical existence of a deconfined state became clear. Today QCD provides the theoretical basis for our understanding of hot and dense matter and fuels up various tools for the studies related to this topic. It is a well-believed proposition that the matter in this whole universe existed at the time of big bang as a hot dense non-Abelian plasma. Ultrarelativistic nucleus-nucleus collisions aim to create such a state the in a laboratory. **Thus the reality about the existence of signatures of thermalisation in the heavy-ion collisions is of prime interest for the physicists to understand the early dynamics of this universe.** In this thesis, we study the existence of a thermalised medium in heavy-ion collisions using the Boltzmann distribution and light front variables- an approach which divides the particles in the phase space into two groups for further studies. The general structure of this thesis is as follows. In the next chapter, we will revisit the ideas related to the deconfined state of matter and that of heavy-ion collisions. A brief discussion on the history of the study of hadronic matter under extreme conditions is given, followed by the advent of QCD and its consequences in the approach towards such efforts. The Bjorken picture of a heavy-ion collision leads us to a point where we expect a quark-gluon deconfined state to exist. Once we assume the actual existence of such a state, the natural question which arises is that: **did it get thermalise at all?** We will see some of the theoretical and experimental attempts to answer this question. Statistical mechanics tells us that the system that can be described by the Boltzmann distribution has reached a maximum entropy state. **This is equivalent to saying that the system already forgot its past!** We will review the Boltzmann distribution which has been used later in our calculations. A glancing view over our approach using light

front variables towards thermalisation can also be seen. It was the idea by V. Garsevanishvili in the early 70s that the shape of the distributions of the light front variable has something to do with the dynamics of a possible existence of the thermalised medium in hadron-hadron or nucleus-nucleus collisions. In this thesis, we explore its possibilities at RHIC and LHC energies. We also do address some of the critical arguments against this approach such as mass dependence and dependence on the available centre of mass-energy in the collisions. In Chapter 3, we will see the historic introduction of light front form by Dirac in 1949. The basic analysis scheme and the techniques used in this thesis to separate the particles into two groups will be presented in a detailed manner. **The approach has some geometrical significance as well.** In particular with an underlying Lobachevsky space. We will review the beautiful Lobachevsky geometry and will see how it comes into the arena of nucleus-nucleus collisions. Some of the earlier attempts in this direction and some counter-arguments proposed against the idea will also be discussed. The next challenge is to implement the light front analysis scheme to the collider data. As a preliminary to the LHC data analysis, we study the simulated events to test the various steps involved in our plan of action. In Chapter 4, a discussion on UrQMD, EPOS and HIJING event generators used for this purpose will be presented together with the results we have obtained from the light front analysis using these models. In Chapter 5, we will see the presentation of the ALICE experimental setup. The implementation of light front analysis using ALICE data becomes the prime focus now. There are innumerable challenges in implementing the analysis at this level, starting from data selection, event selection, centrality determination, track selection, particle identification, estimation of proper correction factors etc while incorporating the detector acceptance and abilities. A journey through these steps will be presented rigorously with the outcomes of it in Chapter 6. We will see that the light front analysis of ALICE data is feasible in spite of all these challenges. It gives some very positive hints towards our understanding of the possible existence of a thermalised system in these collisions. It also poses some open questions regarding the interpretation of the estimated temperatures and possible reasons for the scheme to work at ultrarelativistic energies for masses varying from pions to deuterons. We will conclude the thesis in Chapter 7 with a comprehensive view of the results and the conclusions that we have reached from the whole of these studies, together with some suggestions regarding possible future analysis on this topic.

Chapter 2

Quark Gluon Plasma and Heavy Ion Collisions

In this chapter, we will see a very brief overview of the physics of the deconfined state of matter called quark-gluon plasma (QGP). The experimental system where there exists a possibility of the formation of such a state of matter is the relativistic heavy-ion collisions(HIC). We will see the basic geometry of such collisions and the possible reasons to expect a QGP formation in HICs stemming from J.D Bjorken. The property of asymptotic freedom causes the QCD theory to permit the deconfined state of quarks and gluons [1]. The preliminary aim of the study presented in this thesis is to search for the possible existence of a thermalisation in the medium formed in heavy-ion collisions at the LHC energies. The Boltzmann distribution is the natural way of describing a system which has reached *a maximum entropy state* where the system has *minimal information about its past*. We will see a discussion of these topics together with some of the main existing arguments and ideas in favour of the experimental existence of a thermalised and deconfined quark-gluon system.

Naive picture of a deconfined state of matter

The possibility of a deconfined state of quarks and gluons was predicted at high temperature (or pressure) and a first phase diagram of such a hadronic matter was attempted in 1975 [3]. At very high temperatures, the system will have flavour, colour, charge, and spin states as the degrees of freedom and there exist a possibility for the matter to behave as an ideal relativistic liquid. To pictureise, assume that we are heating a container of the vacuum. First, the black body radiation will start to fill the vacuum followed by the pairing of these photons to form electrons and positrons. If we continue to heat it, it will pair up to produce pions. Now assume that we heat it further up to the order of Λ_{QCD} [1], and assume that the pions can

overlap, the density of the quarks and gluons will be very large which will cause them to lose the memory of which hadron they are bound to. Consequently, they can move around the system freely. Note that the mechanism of the possible formation of this state of the matter might not be exactly similar as in the above thought experiment. Such a state of matter is believed to have existed at the time of big bang as the most primordial matter of the universe which would later hadronize to form the fundamental particles. The idea

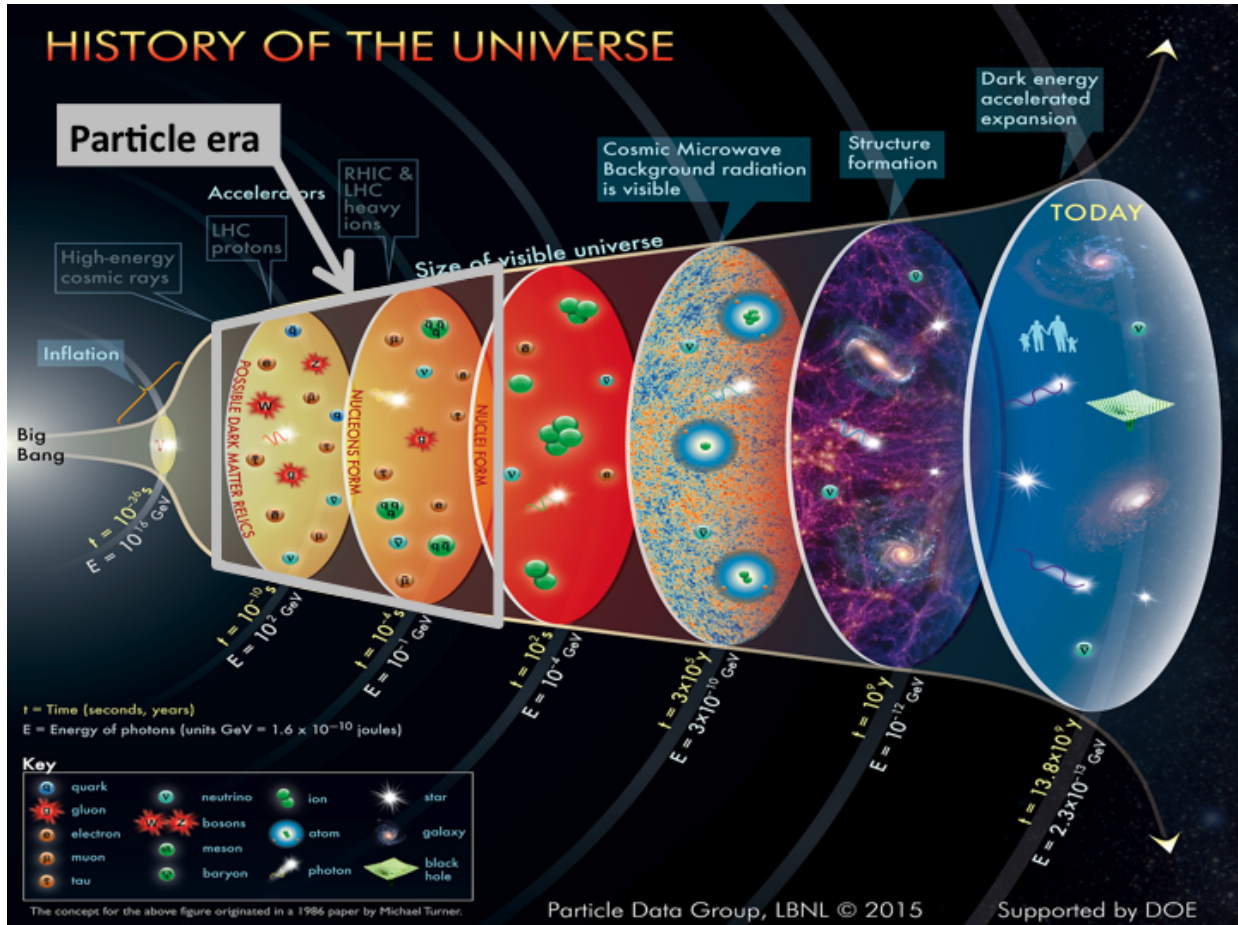


Figure 2.1: Space-time history of the universe. The figure is taken from [4]

is that as *time* goes by, these particles constitute to form more complex systems like atoms and molecules, finally resulting in structures like stars and galaxies that we see around today. Figure 2.1 shows a pictorial representation of this space-time history of the universe.

Pre-QCD studies of the hadronic matter

Even before the formulation of Quantum Chromodynamics, there were predictions about the critical temperature of the hadronic matter by Hagedorn ([5], [6]). The temperature he found from his calculation is called the Hagedorn temperature of T_H . In his paper, Hagedorn formulated an equation which describes the number of hadronic species as a function of their mass and it is given by

$$\rho(m) = \frac{A}{m^2 + 500MeV^2} \exp\left(\frac{m}{T_H}\right) \quad (2.1)$$

where $\rho(m)$ is the density of hadron species per mass unit. If one fits this equation to the experimental data, the value for T_H would be around the mass of pion if all known species of hadrons are taken into account for the calculation. If the temperature of the matter reaches above the Hagedorn temperature, then the partition function which describes the statistical behaviour of the gas will have divergences which are induced by $\rho(m)$ [7]. Due to this reason, T_H was considered as the maximum temperature the hadronic matter can reach. A temperature $T > T_H$ would mean that the density is above 1 hadron per $f m^3$!. Hence, in that case, the hadrons can overlap each other and considering them as point particles becomes invalid. Hence the conclusions of Hagedorn were mostly invalid for $T > T_H$. The quark content of the hadrons would play an important role here. We now know that the dynamics are then governed by QCD.

The QCD empowered era and 'Quark-Gluon Plasma'

In 1973, H.D. Politzer, D.J. Gross and F. Wilczek discovered the asymptotic freedom in the non-Abelian gauge theory of strong nuclear force ([8], [9]). If the Lagrangian of a gauge theory is invariant under the transformations which obey the rules of a non-Abelian group, we call it a non-Abelian gauge theory. The Lagrangian density of QCD can be written as

$$\mathcal{L} = -\frac{1}{4} G_{\mu\nu}^a G_a^{\mu\nu} - \sum_n \bar{\psi}_n \gamma^\mu [\partial_\mu - ig A_\mu^\alpha t_\alpha] \psi_n - \sum_n m_n \bar{\psi}_n \psi_n \quad (2.2)$$

where t_α are the 3x3 Gell-Mann matrices. They are the generators of the colour group fulfilling the SU(3) non-Abelian commutation relations given by

$$[t_\beta, t_\gamma] = if_{\beta\gamma}^\alpha t_\alpha \quad (2.3)$$

where $f_{\beta\gamma}^\alpha$ are the QCD structure constants, $G_a^{\mu\nu}$ are the colour field tensors which are the gluonic part of the Lagrangian density, ψ_n are the Dirac spinors constituting the quark part of the Lagrangian density, A_μ^α are the four-potential of the gluon fields with α running from 1 to 8 and $g = \sqrt{4\pi\alpha_s}$ which is the coupling constant. The quarks have three colour charge states forming the basis of a 3-dimensional vector space. Unlike photons in the case of quantum electrodynamics, gluons carry colour charge resulting in the strong interaction between them. QCD is a renormalizable gauge theory. This means that the divergences that are appearing in the calculation of the cross-sections in various processes in the theory can be nullified by the method of regularization and renormalization of the QCD Lagrangian. The QCD coupling constant α_s (appearing in 2.2 through g) depends on the transferred four-momentum Q^2 in an interaction. Since the gluons can interact with each other in this theory, the coupling constant depends strongly on Q^2 . A first-order perturbative QCD calculation will give us an approximate expression for the coupling constant as

$$\alpha_s = \frac{4\pi}{\beta_0 \ln\left(\frac{Q^2}{\Lambda^2}\right)} \quad (2.4)$$

where

$$\beta_0 = 11 - \frac{2}{3}n_f \quad (2.5)$$

with n_f being the number of quark flavours active at the scale of Q^2 . The Λ in QCD is an adjustable parameter which is fixed by the experiments ($\Lambda \approx 0.22\text{GeV}$). This will lead to the following situation that at very high energies the coupling strength becomes very small and one can say that it vanishes asymptotically (see Figure 2.2). This would mean that the quarks are no more bound and are deconfined. This property of the theory is known as asymptotic freedom. It leads to the possibility of the existence of a deconfined state of quarks and gluons ([3], [10]). Based on these ideas, a hadronic phase diagram was proposed in [10]. The transition of the hadronic matter to the deconfined state became then the main point of interest. Whether this transition is a smooth one as in the case of gas to ordinary electromagnetic plasma [12] or does it happen through a *phase transition*?, whether the deconfined state has reached to a thermal equilibrium via interactions (*thermalisation*)? Or did it hadronise without getting thermalised?. These questions started to emerge and various kinds and levels of attempts were made (and ongoing till date!) to find conclusive solutions to some of these fundamental questions. The deconfined state was later named as 'quark-gluon plasma' first time in a paper by Edward V. Shuryak in 1978 taking inspiration from the analogy of hadrons dissociating into colour flavoured quarks and gluons with atoms dissociating into ions and electrons in a normal plasma [11]. In the absence of the quark masses, the QCD Lagrangian exhibits chiral symmetry. It also has flavour

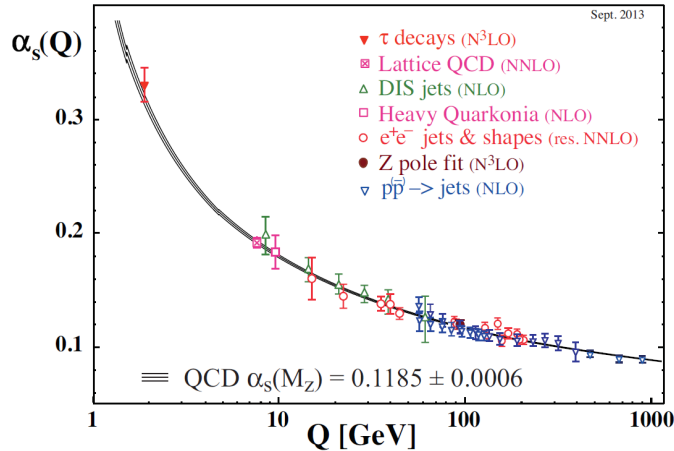


Figure 2.2: Running Coupling Constant of QCD. It is customary to quote α_s at 91 GeV which is the mass of the Z boson. The figure is taken from [2].

symmetry since the quark interactions do not depend on the quark flavour. This means that the massless QCD Lagrangian is invariant under helicity and flavour transformations. The quark condensate $\langle q\bar{q} \rangle$ must be zero if the Lagrangian has chiral symmetry. In reality, quarks have non-zero mass. This would mean that the chiral symmetry of the QCD lagrangian is broken and it is just an approximate symmetry of the theory. One can say that there is an explicit breaking of the chiral symmetry of QCD due to non zero quark masses. The vacuum state or the ground state of a theory may not be invariant under the symmetry group of transformations, even if the Lagrangian of the theory is. In that case, the vacuum state is not symmetric, the generators of the symmetry group do not annihilate it and we say that the symmetry is spontaneously broken. The chiral symmetry of QCD is that kind of symmetry which is spontaneously broken. Spontaneous symmetry breaking in a theory is manifested by the existence of pseudoscalar massless particles called Nambu-Goldstone bosons. In QCD, the chiral symmetry will undergo an additional explicit symmetry breaking due to the quark masses. Under this effect, the eight resulting Nambu-Goldstone bosons will acquire small masses compared to the other hadrons. The pions, kaons and eta mesons can be identified as the eight light pseudoscalar mesons, in this case, [13], [14]. Thus QCD could predict the existence of the Goldstone bosons and explain their small interaction cross-sections. The transition from chirally non-symmetric state to a chirally symmetric state of QCD has a close analogy with the ferromagnetic phase transition [15]. In a ferromagnetic phase transition, the isotropy symmetry is broken spontaneously. A ferromagnetic system suddenly becomes non-invariant to rotations at lower energies, or in the event of an external magnetic field. Likewise, at high energies, the QCD restores the chiral symmetry and the non zero quark masses take the role of the external magnetic

field whenever it is broken. The breaking of isotropy symmetry is a sufficient condition for the ferromagnetic phase transition. This lead to the idea of the existence of a phase transition in the process of transformation of the matter from hadronic to a colour deconfined state. So critical behaviours can be expected at such a transition. Also, the possibility of the existence of a separate chiral and deconfinement phase transition at two different critical temperatures emerges from these considerations. In the non-perturbative domain, lattice gauge theory calculations provide a tool to study and solve the equations of QCD. The space-time continuum is made into a finite number of discrete points called lattice where the solution of the theory can be obtained [16]. The Lattice QCD allows one to study the hadronic matter in the core of the neutron stars and it predicts the existence of a transition at the baryonic potential $\mu_B = 0$ with $T_c \approx 170 MeV$ with a critical energy density $\epsilon \approx 0.7$ which is consistent with the chiral symmetry breaking down of the QCD (see Figure: 2.3) [17]. The energy density versus temperature resembles that of an ideal ultra relativistic gas above this T_c . But the proportionality factor is about 20% less than the expected value for massless quarks and gluons. The lattice QCD calculations predict that, for non zero quark masses the transition can be just a cross over with no critical behaviour [18]. For physical quark masses, lQCD predicts a T_c between 150-200 MeV. The order parameter predictions of lQCD are that the chiral and deconfinement transitions occur at the same temperature. The lQCD calculations for $\mu_B \neq 0$ suggest the existence of a possible critical point at $\mu_B \approx 0.75M_N$ (where M_N being the nucleon mass) with a 2nd order phase transition. Beyond $\mu_B \approx 0.75M_N$, there can be a 1st order phase transition and at even higher values, there exist a possibility to have colour superconducting states. The hadronic matter phase diagram compared with that of water is shown in Figure 2.4.

Heavy Ion Collisions

The biggest challenge in the path towards understanding the possible existence and dynamics of the deconfined partonic state is to create it in a laboratory. Heavy-ion Collisions seem to provide a possibility of having such a non-Abelian medium in a laboratory. The study of deconfined state using heavy-ion collision touches a vast variety of fields like perturbative QCD, lattice QCD, relativistic hydrodynamics, gauge/gravity duality etc. Today, we have dedicated experimental setups at places like CERN, BNL, GSI which host experiments such as ALICE, ATLAS, CMS, STAR, PHENIX etc, to study heavy-ion collisions at the various centre of mass energies. During the collision process, a fraction of the available centre of mass-energy will dissipate into the internal degree of freedom of the system via strong interaction, and we expect that a tiny drop of

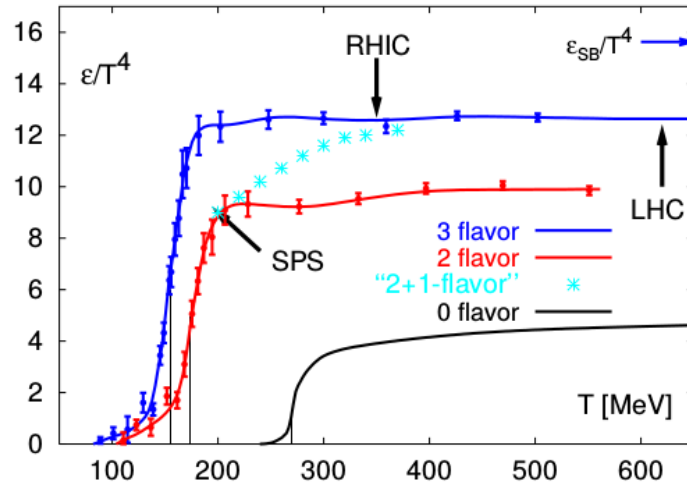


Figure 2.3: Dependence of the energy density as a function of the temperature of the hadronic matter at $\mu_B = 0$ given by lattice QCD calculations at finite temperature for zero quark masses. The figure is taken from [18]

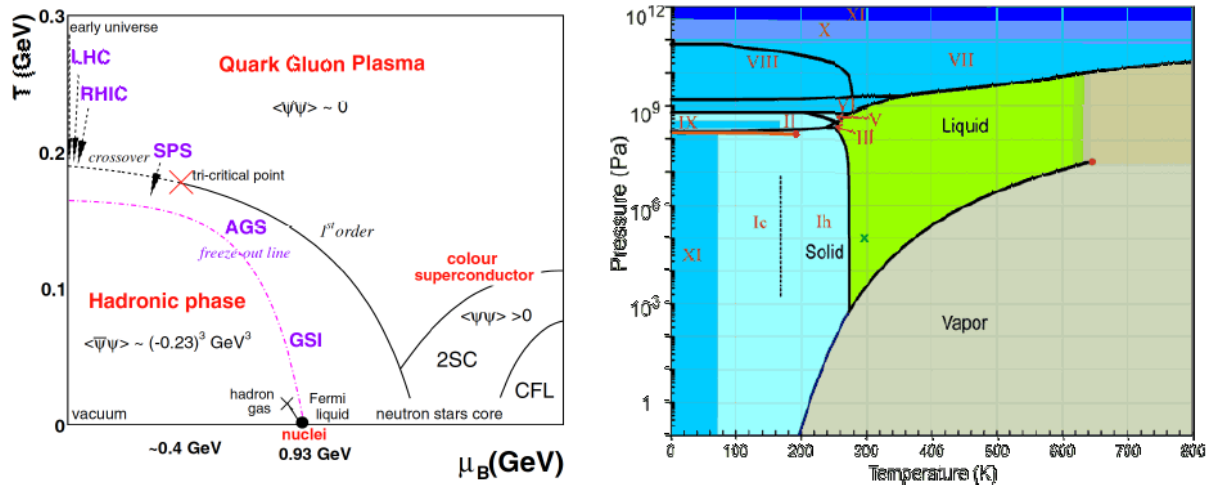


Figure 2.4: Phase diagram of hadronic matter (left, From [19]) and water (right, From [20])

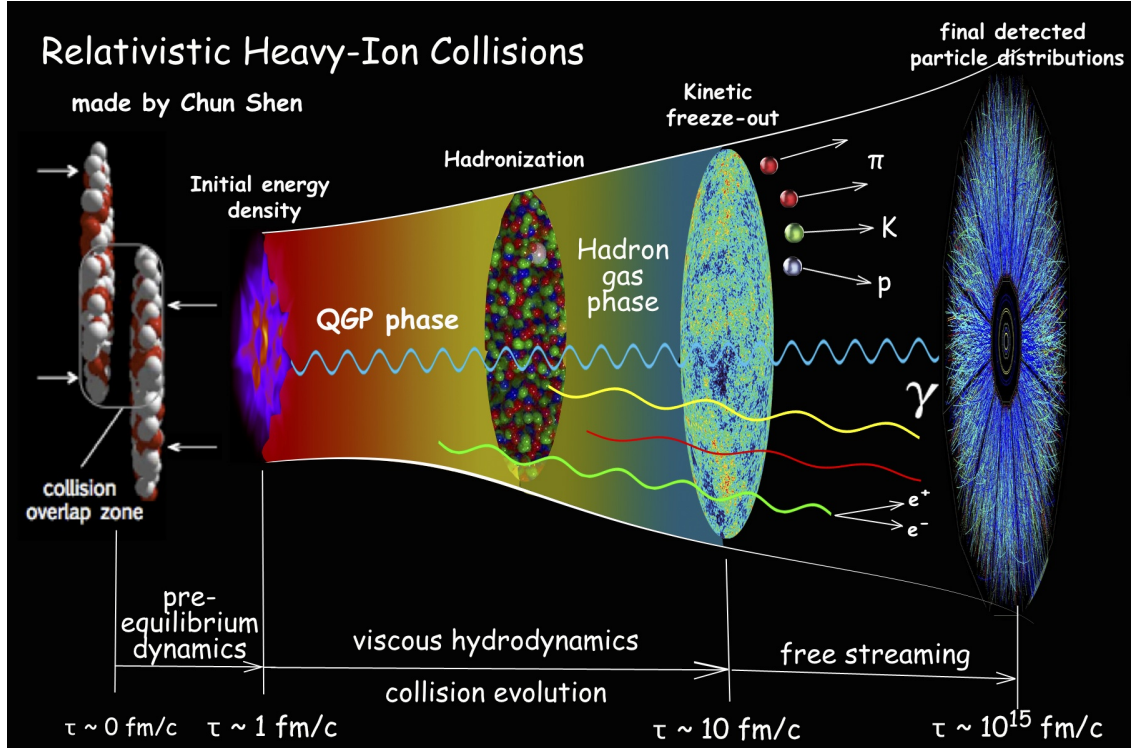


Figure 2.5: Schematic view of the Spacetime picture of a heavy-ion Collision (From [21])

the hadronic matter resembling the primordial matter at the time of big bang is formed in our laboratory. Due to the extreme pressure gradient existing between the drop and the surrounding, a rapid expansion of the system will take place. It will evolve through various processes like possible thermalisation, relativistic expansion, hadronization, kinetic and chemical freeze-outs, and free streaming. So we need dedicated works in setting up the collider, in studying the phenomenology of collision geometries, in studying the collisions with the various centre of mass energies, impact parameters etc. Dedicated detectors like STAR and ALICE are made to make vital measurements to extend our understanding of the hadronic matter under extreme conditions, mimicking the early moments of the universe. In addition to all this, a consistent and continuous interpretation of the whole collision process has to be made from the point of collision to the point of detection of particles by these detectors. In this respect, we can say that the heavy-ion colliders are telescopes having the farthest reach up to the point of the big bang (see Figure 2.5).

Basic geometry of heavy-ion collisions

Irrespective of the scales of interest in high energy physics, nuclei always remain extended objects [22]. In the case of a relativistic heavy-ion collision of two nuclei, the Lorentz contraction makes it to have a shape

of pancakes in the centre of mass frame of the collision. So the geometry of the collision has a significant role in the interpretation of the data and results from these collisions. While discussing the geometry of the collision, the following points are of prime focus.

- **Impact parameter (b):** The distance between the centres of two colliding nuclei projected to the azimuthal plane defines the impact parameter of the collision. A collision with $b = 0$ is a head-on collision. The centrality of the collision is a measure of this impact parameter and the experimental collisions are characterized based on their centrality.
- **Reaction plane:** The reaction plane in a heavy-ion collision is the plane defined by the impact parameter and the beam axis, along which the nuclei comes to collide (see Figure 2.6).
- **Number of Participating nucleons(N_{part}):** It is the total number of protons and neutrons which take part in the collision within the nuclei. Other non-participating nucleons are called spectator nucleons.
- **Number of collisions(N_{coll}):** It is the total number of incoherent nucleon-nucleon collisions
- **Multiplicity:** To collect the information about the centrality, and other properties of the medium created in heavy-ion collisions, scientists use the total number of particles produced and detected by the experimental setup. It can characterize the event and give important information about the geometry of the collisions. The soft QCD non-perturbative range of transverse momentum has a relatively huge number of particles compared to the hard part. So several models of the kind of colour glass condensate models are employed to describe the spectra in those regions. If one sticks to the idea of modelling a heavy-ion collision as a collection of several proton-proton collisions, a very basic estimation on the multiplicity can be made. But the experimental observations tell us that the number calculated in this fashion is larger than in reality and makes us conclude that collective behaviour is present in the medium formed during these collisions. Figure 2.6 shows the geometry of a heavy-ion Collision

The Glauber model

The geometrical quantities in heavy-ion collisions are computed using a probabilistic model called Glauber model [22]. The nuclear profile function or thickness in a nucleus \mathbf{A} with a density of $\rho(z, b)$ at a given longitudinal z and transverse b positions can be written as:

$$T_A = \int_{-\infty}^{+\infty} dz \rho(b, z) \tag{2.6}$$

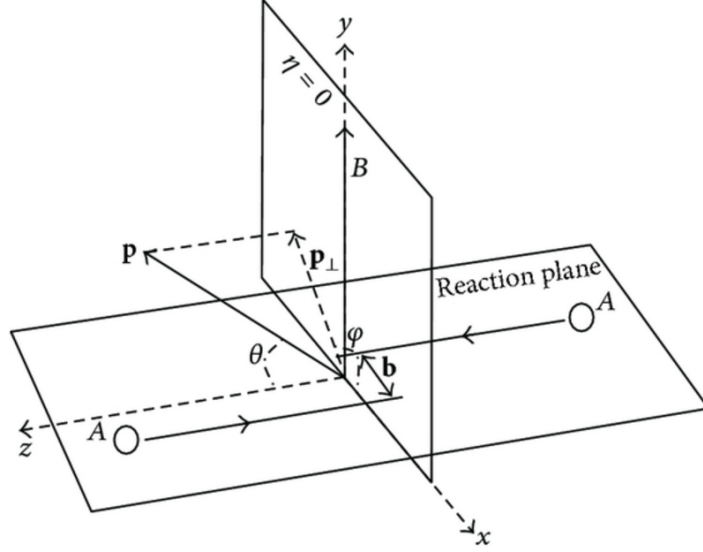


Figure 2.6: Geometry of a heavy-ion collision (From [23]). \mathbf{p} denotes momentum of a particle emerging from the collision. The reaction plane is marked, and the orthogonal mid-rapidity plane $\theta = \pi/2$, is labeled as $\eta = 0$.

A normalisation $\int T_A(b) = 1$ would result in the individual probability of a nucleon-nucleon interaction at a given impact parameter as $T_A(b)\sigma_{NN}^{inel}$. The probability of a proton to interact with n nucleons inside the nucleus can be written as:

$$P(n, b) = \binom{A}{n} [1 - T_A(b)\sigma_{NN}^{inel}]^{A-n} [T_A(b)\sigma_{NN}^{inel}]^n \quad (2.7)$$

From this one can calculate the number of collision at this impact parameter. The multiplicity distributions can be related to the number of participants or collisions. The individual probability of nucleon-nucleon interaction in a heavy-ion collision is within the *optical approximation*.

$$\int ds T_A(b) T_B(b-s) \sigma_{NN}^{inel} = T_{AB}(b) \sigma_{NN}^{inel} \quad (2.8)$$

Here, $T_{AB}(b)$ is known as the nuclear overlap function. For the case of nucleus-nucleus collisions, the above expressions give the number of collisions as:

$$N_{coll}^{AB}(b) = \sum_{n=0}^A n P(n, b) = AB T_{AB}(b) \sigma_{NN}^{inel} \quad (2.9)$$

Since we do not have the experimental access to the impact parameter, we rely on the multiplicity to get the information about the centrality of the collisions as mentioned earlier. In this thesis, the ALICE experimental data were analysed in six regions of centrality ranging from the most central to peripheral collisions. The centrality measurements at ALICE are mainly based on the registered multiplicity at the V0 detector (See 5.3).

Bjorken Scenario In Heavy Ion Collisions

If we assume that the entire available energy in the centre of the mass system is transferred as the internal degree of freedom during the collision, we can calculate an approximate value for the threshold beam energy for the QGP formation. The energy density of the resulting system can be written as:

$$\epsilon \approx \frac{\sqrt{2E_b \times m \times A}}{V} \quad (2.10)$$

where $V \approx \frac{4}{3}\pi \times (1.124)^3 \times A$. A is the atomic number and E_b is the beam energy. For the creation of QGP, we need an energy density of about $1\text{GeV}/\text{fm}^3$. It means that we need to have a minimum of $\sqrt{s}_{NN} = 6$ GeV per nucleon pair for the production of QGP in our labs. Since the entire available energy will not dissipate as the internal degrees of freedom of the system, in reality, we can further say that we need sufficiently large energies (than $\sqrt{s}_{NN} = 6$ GeV per nucleon pair) to have a deconfined hadronic matter in our collisions. In a very famous paper of Bjorken in 1983 [24], a possible scenario of a heavy-ion collision leading to the formation of the hot hadronic matter was imagined. A description of the initial energy density and its evolution in time was presented in this paper. In the ultrarelativistic heavy-ion collisions the nuclei have the shape of pancakes due to Lorentz contraction in the centre-of-mass system. If R is the radius of the nuclei and γ is the Lorentz factor, we can define the crossing time of the nuclei as:

$$\tau_{cross} = \frac{2R}{\gamma} \quad (2.11)$$

The time scale of the strong interaction can be estimated as

$$\tau_{strong} \sim \frac{1}{\Lambda_{QCD}} \sim 1\text{fm}/c \quad (2.12)$$

There were mainly two hypotheses in Bjorken's paper. It was assumed that in the ultrarelativistic heavy-ion collisions, the crossing time τ_{cross} of the nuclei is greater than the time scale of the strong interaction τ_{strong}

only if the available centre of mass-energy $\sqrt{s_{NN}}$ is above 25 GeV. This implies that the strongly interacting particles are formed after the nuclei have already crossed each other. The second assumption was that the produced particles have a uniform rapidity distribution resulting in the rapidity symmetry of the system. Consequently, an easier description of the hydrodynamical evolution of the system would follow from it. An expression for the energy density in the volume centred in the nucleus crossing plane measured at a time τ was calculated under these assumptions and it is given as:

$$\epsilon(y) = \left| \frac{dE_T}{dy} \right| \times \frac{1}{\pi R^2 \tau} \quad (2.13)$$

where y is the rapidity, E_T is the transverse energy, τ is the time of measuring of the energy density, $R \approx 1.124A^{1/3}$ and A is the atomic number. Bjorken estimated the energy density for heavy-ion collisions at an energy of $\sqrt{s_{NN}} = 500 \text{ GeV}$ to be around 2-20 GeV/fm^3 assuming a formation time of the order of the time scale of the strong interaction. The value was much above the critical energy density for the possible formation of QGP in the collision system. Assuming that the QGP is formed with such a high value of energy density, the partons will start to interact. If a mean energy $\langle E \rangle = 500 \text{ MeV}$ is assumed for the system, with an interaction cross-section of about 10 mb, the density of particles at the value of energy density estimated by Bjorken will be around 8-60 particles per fm^3 with a free path length of about 0.02 -0.12 fm, and one can hope that the system has been reached thermal equilibrium in time $\tau_{thermal}$. But the question whether the thermalisation has reached or not has to be tested with experimental results and interpreted by theoretical tools, especially when the assumptions that were made are really strong. After the thermalisation time ($\tau > \tau_{thermal}$), the system assumes to follow the hydrodynamical law given by

$$\frac{\partial \epsilon}{\partial \tau} = - \frac{\epsilon + p}{\tau} \quad (2.14)$$

where p is the pressure of the fluid. For the case of an ultrarelativistic ideal gas, $\epsilon = 3p$ and hence $\epsilon \approx \frac{1}{\tau^n}$ where $1 \leq n \leq 4/3$. Up to a time of $\tau \leq \tau_{long} \approx R$, the system will evolve longitudinally as the pressure gradient is larger along the beam direction than that in the transverse direction. After the time τ_{long} , the system is assumed to evolve in three dimensions until the freezeout phase. At the time of the freezeout, with the earlier assumption about the cross-section (10 mb), and considering that the path length is as large as the size of the system, with the density of particles of about 0.15 particles per fm^3 , the energy density would be around $0.075 \text{ GeV}/\text{fm}^3$. The process of hadronization of particles will follow and particles will finally reach the detectors. If one takes the freezeout temperature to be around 150 MeV, the value ϵ/T^4 will be around

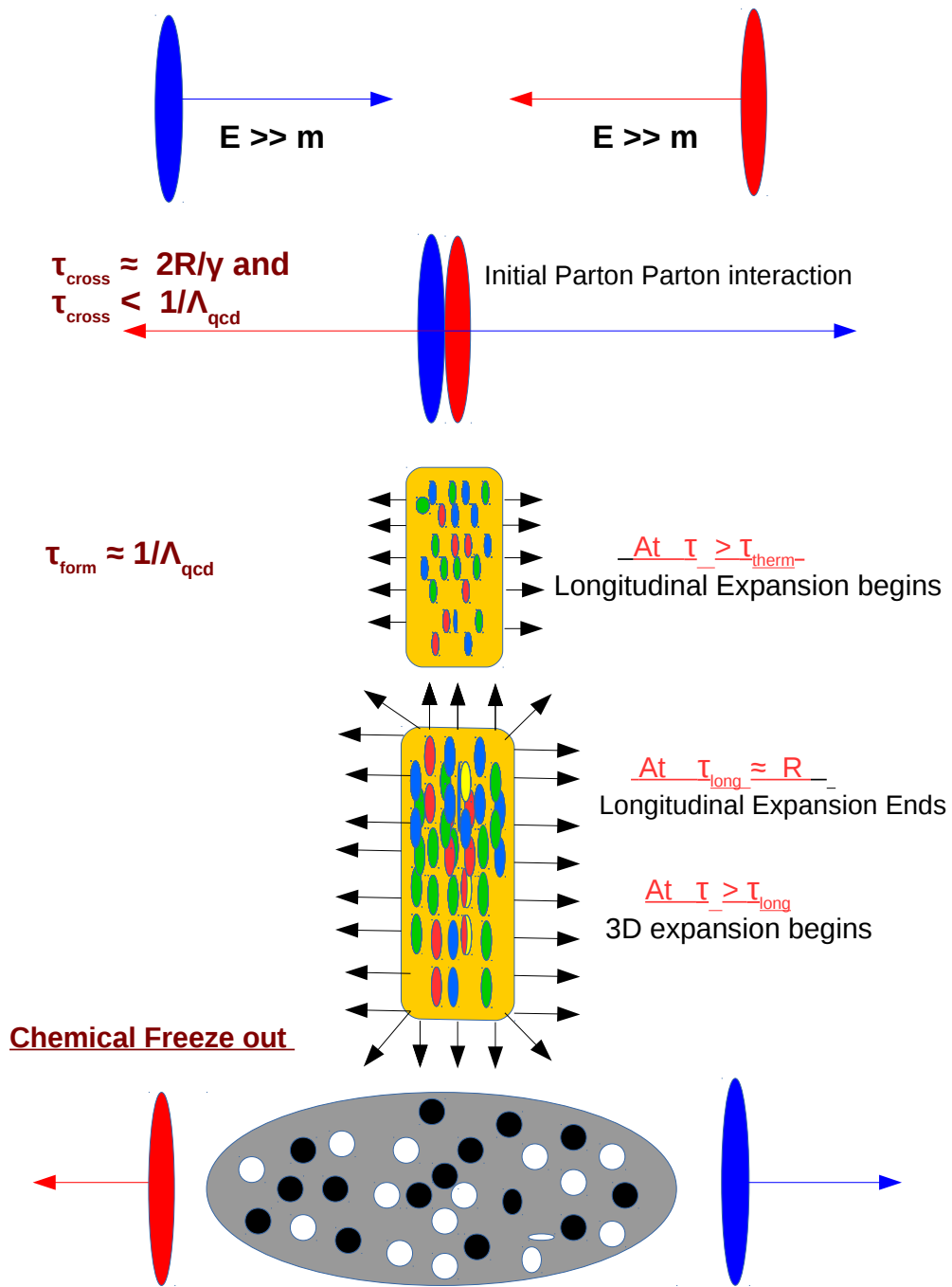


Figure 2.7: Bjorken scenario of a heavy-ion collision. The drawing is inspired by the Figure:10 in [25]

1.2 which is very close to the predictions of lattice QCD. A pictorial representation of the Bjorken scenario is shown in figure 2.7.

The temperature in heavy-ion collisions

Temperature is a term that we use in our everyday life very much frequently. The temperature for a gaseous or liquid medium is the measure of the average kinetic energy of the particles in the system. It is not very clear to us whether the partonic matter which is believed to exist in the heavy-ion collisions has reached a state where the constituent partons follow an isotropic momentum distribution, atleast locally, irrespective of their large average momentum. This is the root of the problem regarding thermalisation in heavy-ion collisions. Suppose we assume, that there exists such a deconfined state after all. Initially, the partons are distributed anisotropically in the momentum space. Now, what all possibilities can be considered to make the system thermalise? The most obvious answer to this question is that it is via interactions. Since the partonic system has both quarks and gluons in it, the possibility of interactions to consider was in plenty. The basic idea of the quark-gluon matter getting thermalised via elastic scattering of partons is as follows:

- In a two parton elastic scattering only two of the six momentum components of the two final partons are free because of the energy-momentum conservation and the angular distributions of the outgoing partons can be exactly defined.
- The probability of producing two partons in the incoming parton direction is larger than that in the direction perpendicular to it. The natural consequence is that in the most initial moments of a nucleus-nucleus collision, the produced partonic matter has more partons flying in the beam direction than in the direction perpendicular to it.
- Then the two parton scattering occurs which reduces the number of partons flying along beam direction and increases the same in the perpendicular direction.
- Simultaneously the scattering of two partons flying in the direction perpendicular to the beam reduces the number of partons flying perpendicular to the beam and increases the same moving along the beam.
- The beam direction already has more partons moving along. So the number of scattering will be larger along the beam which transfers more partons to the perpendicular direction as time goes by. Thus the partons gradually will get distributed more and more isotropically in momentum leading to a more uniform temperature for the system.

In the case of three parton scattering which happens not in a plane unlike the two parton case, we have a minimum of five free components of momentum. Hence, it is natural that the system will have more

easiness to reach isotropy via three parton scattering. In a 1992 paper [26], Edward Shuryak considered the $gg \rightarrow gg$ interaction for the gluon matter to thermalise. In this calculation, it was assumed that all the gluons present in the system suffer from scattering at the same time. With this assumption, one can obtain the thermalisation time of the order of 0.3 fm/c. However, for every gluons to undergo scattering at the same period of time, it requires cross-sections larger than 40 mb which is practically unachivable. Later, several attempts were made to explain the situation using the three-particle scattering ([27],[28]). In [27], it was assumed that the system can be described by a semi-classical Boltzmann transport equation, which then was solved by means of "the test particle Monte-Carlo method". The $gg \rightarrow ggg$ process was considered and a thermalisation was found to be reached at about $t = 1.6$ fm/c with a temperature of about 570 MeV. In [28], the kinetic on-shell Boltzmann equations for partons including the inelastic pQCD processes $gg \longleftrightarrow ggg$ was solved using a "3 + 1 dimensional Monte Carlo cascade". With an assumption about the initial conditions generated by minijets of $p_T > 2GeV$, it was demonstrated that the overall kinetic equilibration is driven mainly by the inelastic processes and is achieved on a scale of 1 fm/c. To summarise, the $gg \rightarrow gg$ and $gg \rightarrow ggg$ lead to a gluon-matter thermalisation time larger than 1 fm/c. The calculations on three parton scattering tells us that it can lead to a thermalised state of partons and the time required for the gluon matter to thermalise in this case is around 0.32 fm/c with a temperature of about 520 MeV. For the case of quark matter the elastic three parton scattering will lead to thermalisation at a time around 0.66 fm/c with a temperature of about 460 MeV. So the quark matter thermalises slower than the gluon matter via elastic three parton scattering.

Elliptic flow and thermalisation

A large majority of heavy-ion physicists believes that the elliptic flow observed from the experimental facilities at RHIC and LHC is stemming from the actual existence of a thermalised quark-gluon deconfined state ([29], [30]). The ability of ideal hydrodynamical models to explain the p_T dependence of elliptic flow was interpreted by many of them as an evidence of a QGP formation ([31], [32], [33], [34], [35], [36]). To understand these claims, let us consider the figure 2.8 which shows the picture of a heavy-ion collision, along the beam. The large circles are the nuclei which are two Lorentz-contracted pancakes. One nucleus is going into the page and the other one is heading towards the reader. If the situation is such that the nucleus-nucleus collision is a collection of independent nucleon-nucleon collisions, the distribution of particles will be isotropic in the transverse plane of the paper. So the transverse momentum distribution will be rotationally invariant around the beam axis. This will be the case if the particles from the collision are freely flying towards a detector.

Now, consider the case when the particles cannot fly freely towards the detector without colliding with those particles coming from other nucleon-nucleon collisions. Also, let us assume that there is a large number of such scattering, resulting in an approximate local thermal equilibration of these particles. After the crossing time, the almond-shaped collision region in the upper right figure in 2.8 will be filled with particles. Just outside its boundary, it will be a vacuum. So there will be a pressure gradient represented by the contours in the same figure. The pressure gradient must be larger along the short diameter of the almond. So the particles will be accelerated more to the right and left directions than to top and bottom. Due to this anisotropic acceleration, the particles when they reach the detector will have an anisotropy in transverse momentum in the lab frame as shown in the upper right figure in 2.8. In the local rest frame of the fluid, here a thermal medium, momentum distributions are isotropic as shown in the lower-left figure in 2.8. The two blue circles are for the fluid elements moving to the right and left directions, boosted to the lab frame. Thus, the superposition of these isotropic distributions in the in local fluid rest frames will create anisotropic momentum in the lab frame. The pressure (thermalisation pressure) gradient in the almond-shaped region is larger for the horizontal direction than the vertical one as depicted by the contour lines in figure 2.8. This introduces an anisotropic acceleration, leading to having an anisotropy in the momentum space in the lab frame (See the upper right figure in 2.8). This property is manifested in the measurement as 'flow', in

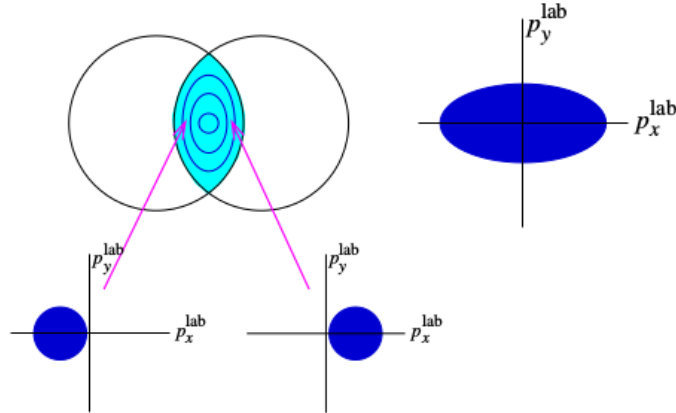


Figure 2.8: Elliptic flow in a heavy-ion Collision. Figure is taken from [37]

particular, the elliptic flow, which is claimed to be coming from the actual existence of a QGP-like a system. It is worth to mention that there exist weak-coupling and strong-coupling approaches to the QGP dynamics which are active fields of research [31].

Filamentation instability affecting the thermalisation of QGP

The filamentation or Weibel instability originally discovered in 1959 [38], can affect the possible thermalisation in the quark-gluon matter at the anisotropic phase ([39], [40]). To see this let us consider two homogeneous inter-penetrating currents of charged particles as in figure 2.9(a). Due to magnetic fields, the upgoing (downgoing) particles attract each other and prefer to get near each other as in 2.9(b). The magnetic fields associated with these 'filaments' are shown in 2.9(c). This introduces instability to the particle current and it is called the Weibel instability. Such an effect can alter the process of the deconfined state getting thermalised ([41], [42]).

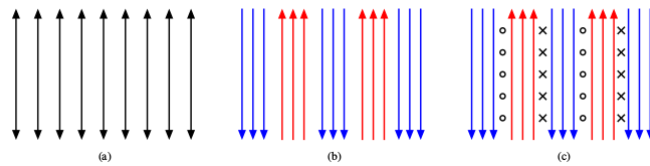


Figure 2.9: The Weibel instability (The Figure is taken from [37])

Our attempt with Boltzmann distribution and light front variables

In this thesis, we are closely following the analysis strategy introduced by V. Garsevanishvili using the light front variables to study the possible scenario of the existence of a medium which has reached thermal equilibrium in relativistic and ultrarelativistic heavy-ion collisions. The basic ingredient of the scheme is the Boltzmann distribution and light front variables. From elementary statistical mechanics, we know that the Boltzmann distribution emerges as a natural distribution of constituents of a system that has reached a maximum entropy state. It was proposed by a group lead by V. Garsevanishvili [47], that the light front distributions can be used to find a particular value for the relativistically invariant light front variable (ζ) such that the particles having the value greater than a critical value ($\tilde{\zeta}$) can be described by the Boltzmann distribution!

Boltzmann distribution as an equilibrium distribution

In this section, we see that the possibility of the description of a physical system using Boltzmann distribution tells us that we are looking at a system that has reached thermal equilibrium [43]. The Boltzmann distribution arises for discrete and continuous systems as a result of the system getting into a maximum entropy state.

Suppose that we have N identical particles. Each of these particles is in some state j where it is associated with an energy level ϵ_j . We would like to see how large is n_j , the number of particles observed at the j th state. The system configuration will tell us the number n_j . If we maximize the entropy of the system, we can immediately see that the probability of a particle to be at the j -state is

$$p_j = \frac{n_j}{N} = \frac{\exp(-\beta\epsilon_j)}{Z} \quad (2.15)$$

which is the Boltzmann distribution where $\beta = \frac{1}{k_B T}$ and $Z = \sum_j \exp(-\beta\epsilon_j)$ which is the partition function. Again, if we consider a system of N particles experiencing a potential V , in a volume Ω and suppose that the system is in thermal equilibrium at constant temperature T . If we look at the density ρ of particles at different places in the whole volume, it can be shown ([43]) that ρ can be expressed as

$$\rho = C \exp\left(-\frac{V}{k_B T}\right) \quad (2.16)$$

which is again the Boltzmann distribution. Now it becomes very clear that the description of a system using Boltzmann distribution means that the system has reached thermal equilibrium. We will use this fact in the following chapters to show that the group of particles selected from the full phase space using the light front scheme obeys Boltzmann distribution and hence it is natural to think that the thermal equilibrium has been reached in the medium which in our case is the medium formed during heavy-ion collisions.

Light Front variables for the study of thermal equilibrium

It was found that there exists a maximum in the distribution of the light front variable for the inclusive pions at low energy collisions [47]. In the context of the low energy experiments, it was also found that the characteristics of the particles contributing to the light front variable distribution on both sides of its maximum are very much distinct in nature. The constant value of the light front variable forms a paraboloid in the $p_Z - p_T$ space, which divides the particles in the phase space into two groups. The three distributions, namely the light front variable (ζ) distribution, the polar angle distribution and the p_T^2 distribution of one set of particles among the two groups can be described successfully by Boltzmann statistics. The logic from the earlier section about the Boltzmann distribution leads us to think that a thermal equilibrium was reached in the medium where the particles are coming from. There is an underlying geometrical significance to the kind of analysis that we just mentioned. More details on the definitions and properties of the variables, geometrical significance and the implementation of the analysis methods are explained in the following chapters.

Chapter 3

Light front variables at hadron colliders

In this chapter, an introduction of the light front form proposed by Dirac will be discussed. The role of Lobachevsky geometry in the context of nuclear collisions will be presented, followed by the introduction of Lorentz invariant light front variables as per the propositions of V. Garsevanishvilli which are used in the analysis presented in this thesis. The properties of light front variables will be discussed together with some of the earlier results obtained from the studies using those variables. A scheme of the analysis used in the succeeding chapters of this thesis will be presented in detail.

Forms Of Relativistic Dynamics

In his paper on the forms of relativistic dynamics [44], Dirac formulated the following two requirements on relativistically dynamic systems [45]:

- The General theory of relativity requires that the physical laws expressed in curvilinear space-time coordinates shall be invariant under coordinate transformations.
- The discovery of quantum mechanics leads to the point that the equation of motion shall be expressed in Hamiltonian form.

These are the conditions that limit the possible forms that a relativistically dynamical system can take although they do not define a relativistically dynamical system by themselves. In a nonrelativistic system, the evolution is governed by Hamiltonian with the evolution operator of the form $U(t) = \exp(-iHt)$, where $t = 0$ representing the initial condition. In the case of a relativistic system, any hypersurface Σ in the Minkowski space-time which does not contain time like components can be used to formulate the initial condition. If one tries to find the surfaces with maximum possible symmetries, one will end up with the concept of *stability*

group, G_Σ , the subgroup of Poincare group, which maps Σ to itself. The subset of generators of the full Poincare group, which generates G_Σ are called the *kinematic operators*. The rest of the generators which maps $\Sigma \rightarrow \Sigma'$ are called *dynamical operators*. If Σ has the following property

$$\forall x, y \in \Sigma : \exists g \in G_\Sigma \rightarrow x = gy \quad (3.1)$$

then Σ is said to be *transitive* and all points in this hypersurface are equivalent. If we consider only transitive hypersurfaces for initial conditions, then we have only five possible forms for the relativistically dynamical system which corresponds to five subgroups of the full Poincare group. Three such forms were discussed by Dirac himself and the next two were given by Leutwyler and Stern [46].

The forms given by Dirac are as follows

- **Instant Form** : $p^0 = 0$
- **Point Form** : $p^2 = a^2 > 0, x^0 > 0$
- **Front Form** : $p^0 \pm p^3 = 0$

The two forms given by by Leutwyler and Stern are

- $(p^0)^2 - (p^1)^2 - (p^2)^2 = a^2 > 0, x^0 > 0$, and
- $(p^0)^2 - (p^3)^2 = a^2 > 0, x^0 > 0$

Of these, the light front combination of variables were used to formulate a scheme to separate the particles coming out from nuclear collisions by V. Garsevanishvili([47], [51]). In this thesis, we are using the scheme at RHIC energies and LHC energies via phenomenological models and ALICE experimental data.

The Lobachevsky geometry in nuclear collisions

In the year of 1826, the Russian theoretical physicist N.I Lobachevsky established rules for a new geometry wherein it exists infinitely many lines passing through a point in a plane which does not intersect a given line L. In the family of such lines, a pair of limiting lines exist, which are called parallel lines to L ([48], [49]). If a perpendicular line L0 is drawn from a line L1 to another line L2, the angle formed by L1 and the perpendicular line L0, Π is $\pi/2$ in Euclidean planimetry. But in the Lobachevsky planimetry, it is less than $\pi/2$ and it depends on p which is the height from which L0 is drawn. This is the angle of parallelism $\Pi = \Pi(p/k)$, where k is called the Lobachevsky constant, which is a characteristic length in the Lobachevsky geometry. Using the intrinsic geometry of the surface which is orthogonal to the bundle of parallel lines(

Lobachevsky named this plane as orisphere), he showed the following relation

$$\tan\left[\frac{1}{2}\Pi(x)\right] = e^{-x} \quad (3.2)$$

Whenever one deals with the Lobachevsky geometry, the constant k appears in the part where it differs from the Euclidian geometry. In the Lobachevsky geometry, the sum of angles of a triangle is less than π and the area of the triangle is

$$\Delta = k^2(\pi - A - B - C) \quad (3.3)$$

where A, B, C are the angles and a, b, c being the opposite sides of the corresponding angles. He verified the formula using a triangle with the diameter of earth's orbit as the base and the third point is a distant star fixed to a point. For any arbitrary triangle in the Lobachevsky geometry, the following four formulae were derived

$$\cosh\left(\frac{c}{k}\right) = \cosh\left(\frac{a}{k}\right)\cosh\left(\frac{b}{k}\right) - \sinh\left(\frac{a}{k}\right)\sinh\left(\frac{b}{k}\right)\cos(C) \quad (3.4a)$$

$$\sinh\left(\frac{b}{k}\right)\sin A = \sinh\left(\frac{a}{k}\right)\sin B \quad (3.4b)$$

$$\cot(A)\sin(C) + \cosh\left(\frac{b}{k}\right)\cos(C) = \coth\left(\frac{a}{k}\right)\sinh\left(\frac{b}{k}\right) \quad (3.4c)$$

$$\cos(C) + \cos(A)\cos(B) = \sin(A)\sin(B)\cosh\left(\frac{c}{k}\right) \quad (3.4d)$$

For a right handed triangle in this new geometry, he derived following six equations

$$\cosh\left(\frac{c}{k}\right) = \cosh\left(\frac{a}{k}\right)\cosh\left(\frac{b}{k}\right) \quad (3.5a)$$

$$\cosh\left(\frac{c}{k}\right)\tan(A)\tan(B) = 1 \quad (3.5b)$$

$$\sinh\left(\frac{a}{k}\right) = \sinh\left(\frac{c}{k}\right)\sin(A) \quad (3.5c)$$

$$\cos(A) = \cosh\left(\frac{a}{k}\right)\sin(B) \quad (3.5d)$$

$$\tanh\left(\frac{a}{k}\right) = \sinh\left(\frac{b}{k}\right)\tan(A) \quad (3.5e)$$

$$\tanh\left(\frac{b}{k}\right) = \tanh\left(\frac{c}{k}\right)\cos(A) \quad (3.5f)$$

Using equations 3.4 and equations 3.5, any trigonometric problem in the Lobachevsky geometry can be solved. Based on the new hyperbolic geometry he discovered, Lobachevsky extended his calculations and developed the analytic and differential geometry of a new space called **Lobachevsky space**. Lobachevsky proved that the intrinsic geometry of the sphere with radius ρ does not depend on the Euclid's fifth axiom and due to Euclid's third axiom, both in the Lobachevsky and Euclid's geometry, the values allowed for ρ is between zero and infinity. Both the geometries can be used to describe the parallels and meridians on a sphere with polar coordinants θ and ϕ . If we set the following "distances",

Length of the equator = $2\pi r$

Distance from north pole to $(\theta, \phi) = \theta r$

Distance travelled along the parellel ($\theta = constant$) to $(\theta, \phi) = \phi r \sin(\theta)$

Then the metric form of the sphere is

$$r^2(d\theta^2 + \sin^2(\theta)d\phi^2) \quad (3.6)$$

with an elemental area of

$$r^2 \sin(\theta) d\theta d\phi \quad (3.7)$$

For the Euclidean geometry, $r = \rho$. But for Lobachevsky geometry,

$$r = k \sinh\left(\frac{\rho}{k}\right) \quad (3.8)$$

In the limit $k \rightarrow \infty$ Lobachevsky geometry is equivalent to the Euclidean one (with later being applicable only when $\frac{\rho}{k}$ is sufficiently small). Now it is clear that the difference between the two geometries are manifested in the relation between r and ρ . The metric form of in Lobachevsky space is given by

$$ds^2 = d\rho^2 + r^2(d\theta^2 + \sin^2(\theta)d\phi^2) \quad (3.9)$$

and elemental volume is

$$dV = r^2 \sin(\theta) d\rho d\theta d\phi \quad (3.10)$$

From equations 3.8 and 3.9, we can derive all the results concerning Lobachevsky space. The following four

functions of spherical coordinates

$$x = r \sin(\theta) \cos(\phi) \quad (3.11a)$$

$$y = r \sin(\theta) \sin(\phi) \quad (3.11b)$$

$$z = r \cos(\theta) \quad (3.11c)$$

$$u = \cosh\left(\frac{\rho}{k}\right) \quad (3.11d)$$

would define a three dimensional surface in the four dimensional centroaffine space with cartesian coordinates. This is a hyperboloidal sheet given by

$$k^2 u^2 - x^2 - y^2 - z^2 = k^2 \quad (3.12)$$

The reorientation of this relation for u

$$u = \sqrt{1 + (x^2 + y^2 + z^2)/k^2} \quad (3.13)$$

will give us a one to one mapping of Lobachevsky space into the hyperbolic surface. From equations 3.8 and 3.11, by differentiating one can obtain

$$ds^2 = dx^2 + dy^2 + dz^2 - k^2 du^2 \quad (3.14)$$

and hence, we see that

$$(k^2 + x^2 + y^2 + z^2)k^2 du^2 = (x dx + y dy + z dz)^2 \quad (3.15)$$

This shows that the surface described by 3.13 with metric as in equation 3.14 is identical to Lobachevsky geometry. If we assume that the Lobachevsky constant k is equal to the velocity of light in vacuum and the distance ρ is the rapidity s of the particle, then equations 3.11 are the components of the 4-velocity of a particle. Hence we see that the hyperboloidal surface defined in the velocity space has Lobachevsky geometry. A simplex in Lobachevsky space is shown in figure 3.1. The particles 1, 2 and 3 with rapidities ρ_1, ρ_2 , and ρ_3 forms the vertices of the triangle with sides forming the relative rapidities. Suppose that 2 is at rest in the laboratory frame, then α_2 corresponds to the angle of the registered particle. Hence Lobachevsky geometry is connected directly with the high energy collisions. Moreover the surface defined in the velocity

space is a realisation of the Lobachevsky space itself. We will use this fact and define the scale invariant light front variables for the further analysis of the simulated and experimental data in this thesis to study some dynamical characteristic of the collision.

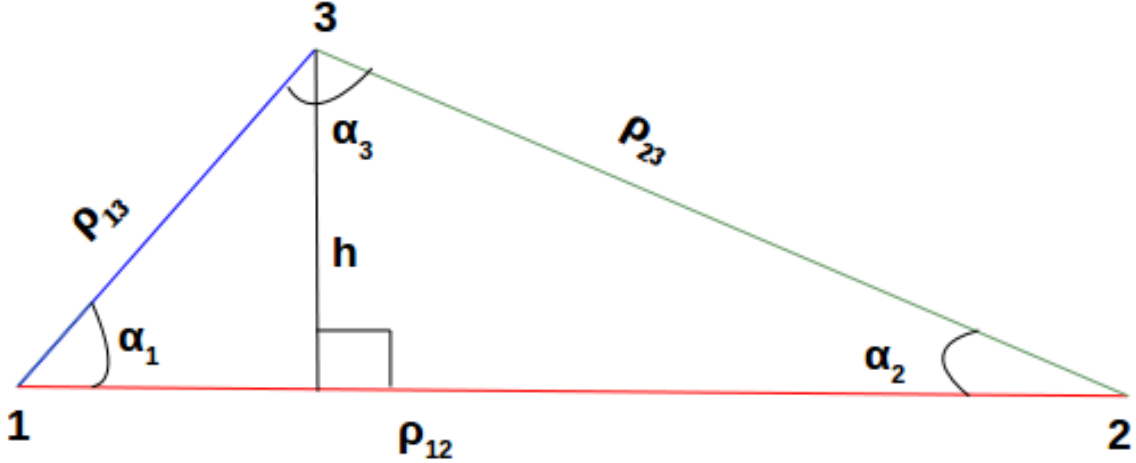


Figure 3.1: A simplex in the Lobachevsky space

Scale invariant Light Front variables

The light front scheme was introduced in [47] primarily to differentiate between pionisation and fragmentation components in a pion spectrum. The existence of low momentum, secondary pions with almost isotropic angular distribution in the centre of mass system of the colliding hadrons (or nuclei) is called *pionisation*. On the contrast, *fragmentation* components have a sharply anisotropic angular distribution in the centre of the mass system. The idea of studying single-particle distributions to understand the production dynamics is very old and well established. In this context, the choice of kinematic variables in terms of which observable quantities are represented bear a very significant role. The variables which we commonly use are the Feynman variable $x_F = \frac{2p_z}{\sqrt{s}}$ ([50]), rapidity $y = \frac{1}{2} \ln \left(\frac{E+p_z}{E-p_z} \right)$, the transverse scaling variable $x_T = \frac{2p_T}{\sqrt{s}}$ etc. When we have an azimuthal symmetry, $x_F = \text{constant}$ forms a planar surface $p_z = x_F \sqrt{s} / 2$ in the $p_z - p_T$ plane. The surfaces of constant y are hyperboloids in the $p_z - p_T$ plane having an analytic form $p_z^2 \left[\left(\frac{1+e^{2y}}{1-e^{2y}} \right) - 1 \right] - p_T^2 = m^2$. The surfaces of constant x_T are the planes $p_T = \frac{x_T \sqrt{s}}{2}$ in the momentum space as shown in Figure (3.2).

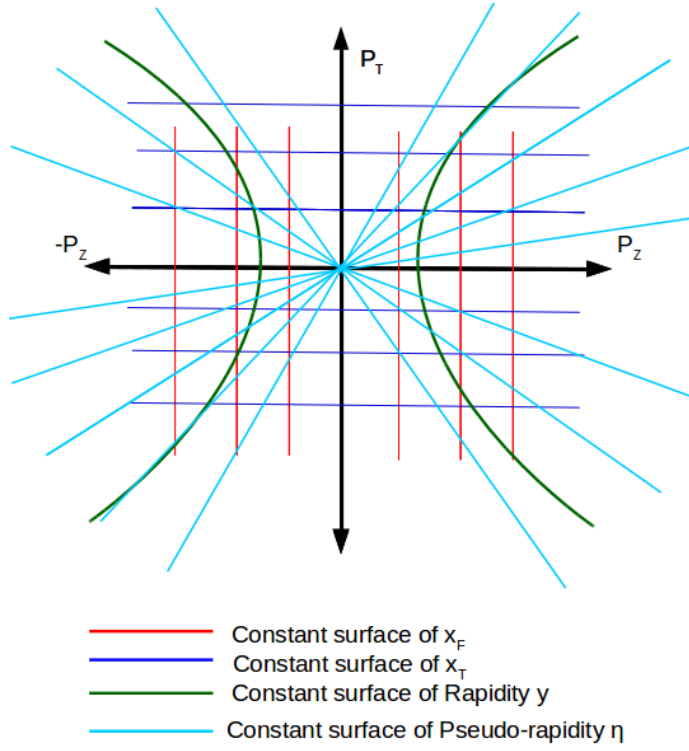


Figure 3.2: Schematic view of the surfaces of constants

Definition and properties

Consider an arbitrary four momentum $p_\mu(p_0, \vec{P})$, we can write the light front combinations as:

$$p_\pm = p_0 \pm p_3 \quad (3.16)$$

If p_μ is on the mass shell (ie, $p^2 = m^2$) we can define a horospherical coordinate system using the combinations $p_\pm, \vec{p}_T = (p_1, p_2)$ on the corresponding mass shell hyperboloid $p_0^2 - \vec{P}^2 = m^2$. As we saw in the previous section, the corresponding hyperboloid in the velocity space is the realization of the curved space with constant negative curvature or the Lobachevsky space (For more references, see [51], [52], [54]). The following relations define the horospherical coordinate system:

$$u_0 + u_3 = e^a \quad (3.17)$$

$$u_0 - u_3 = e^{-a} + e^a \gamma_\perp^2 \quad (3.18)$$

$$u_\perp = (u_1, u_2) = e^a \gamma_\perp \quad (3.19)$$

where $\gamma_\perp = (\gamma_1, \gamma_2)$

$$(u_1, u_2, u_3) \longrightarrow (e^a, \gamma_\perp) \quad (3.20)$$

$$\frac{dP}{E} = e^{2a} da d\gamma_\perp \quad (3.21)$$

$$E \frac{d\sigma}{dp} = \frac{1}{\pi m^2} \frac{d\sigma}{da d\gamma_\perp^2} \quad (3.22)$$

If $a = 0$, $u_0 + u_3 = 1$. This means that the horosphere in the Lobachevsky space, on the upper sheet of the hyperboloid $u_0^2 - \vec{u}^2 = 1$ is a two dimensional surface with Euclidian geometry. The coordinates (a, γ_\perp) are related to the quantities that we measure, that is (p_z, \vec{P}_\perp) as in the equations given below:

$$a = \ln \frac{E + p_z}{m} = \ln \frac{\sqrt{p_\perp^2 + p_z^2 + m^2} + p_z}{m} \quad (3.23)$$

$$\gamma_\perp = \frac{p_\perp}{E + p_z} = \frac{p_\perp}{\sqrt{p_\perp^2 + p_z^2 + m^2} + p_z} \quad (3.24)$$

Now, if we consider the scale invariant variables in terms of the 4-momenta of $p_\pm^a, p_\pm^b, p_\pm^c$ of particles in the inclusive reaction:

$$a + b \longrightarrow c + X \quad (3.25)$$

as given below:

$$\xi^\pm = \pm \frac{p_\pm^c}{p_\pm^a + p_\pm^b} \quad (3.26)$$

where z axis is taken to be the collision axis ($p_z = p_3$) and a, b, c can be leptons, hadrons or heavy-ions. If we write these variables in the centre of mass frame, we will get the following expressions:

$$\xi^\pm = \pm \frac{E \pm p_z}{\sqrt{s}} = \pm \frac{E + |p_z|}{\sqrt{s}} \quad (3.27)$$

Where, s is the Mandelstam variable and

$$E = \sqrt{p_Z^2 + p_T^2 + m^2} \quad (3.28)$$

is the energy, p_Z is the Z-component of the momentum. The positive sign in the above equation (3.27) is used for the positive hemisphere and negative sign is used for the negative hemisphere. It is convenient to define a new variable ζ for to enlarge the region of smaller ξ values as in the following equation:

$$\zeta^\pm = \mp \ln(|\xi^\pm|) \quad (3.29)$$

ζ and a are related to as in the expression given below:

$$\zeta^+ = -a - \ln\left(\frac{m}{\sqrt{s}}\right) \quad (3.30)$$

The invariant differential cross section in terms of these variables can be written as:

$$E \frac{d\sigma}{d\mathbf{p}} = \frac{|\xi^\pm|}{\pi} \frac{d\sigma}{d\xi^\pm dp_T^2} = \frac{1}{\pi} \frac{d\sigma}{d\zeta^\pm dp_T^2} \quad (3.31)$$

In the limiting case of high p_Z and high p_T these variables goes to the more familiar Feynman variables as follows:

$$\xi^\pm \longrightarrow \frac{2p_Z}{\sqrt{s}} = x_F \quad (3.32)$$

$$\xi^\pm \longrightarrow \frac{m_T}{\sqrt{s}} \longrightarrow \frac{p_T}{\sqrt{s}} = \frac{x_T}{2} \quad (3.33)$$

where

$$m_T = \sqrt{p_T^2 + m^2} \quad (3.34)$$

respectively for the corresponding limits. We can also see that these variables can be written in terms of the Feynman variable and rapidity as in the following expression:

$$\xi^\pm = \frac{1}{2} \left(x_F + \sqrt{x_F^2 + x_T^2} \right) \quad (3.35)$$

where

$$x_T = \frac{2m_T}{\sqrt{s}} \quad (3.36)$$

and

$$y = \pm \frac{1}{2} \ln \frac{(\xi^\pm \sqrt{s})^2}{m_T^2} \quad (3.37)$$

Kinematically Forbidden Regions

The region corresponding to $\xi^\pm < m/\sqrt{s}$ is kinematically forbidden for the ξ^\pm spectra integrated over all values of p_T^2 . The region corresponding to $\xi^\pm < m_T/\sqrt{s}$ is forbidden for the ξ^\pm spectra at fixed values of values p_T^2 . The minimum value of ξ^\pm is termed as the threshold value ξ_{th}^\pm

Properties of Light Front distribution

From the older experimetal considerations, ξ^\pm distributions generally have two features, which make them differ from corresponding x_F distributions. They are as follows.

- Existence of the forbidden region near the point $\xi^\pm = 0$ (cross sections vanish in the region).
- Existence of maxima at some $\tilde{\xi}^\pm$ in the region of relatively small $|\xi^\pm|$.

Our scheme of study with Light Front Variables

Following the footsteps of the first experimental studies [47], we make the following pathway towards studying the nature of these maxima. We consider **Cosine**(θ) and p_T^2 distributions in the two regions given by

- **Region 1:** $\xi^\pm < \tilde{\xi}^\pm$ or ($\zeta^\pm > \tilde{\zeta}^\pm$)
- **Region 2:** $\xi^\pm > \tilde{\xi}^\pm$ or ($\zeta^\pm < \tilde{\zeta}^\pm$)

We expect that the angular distributions in these two regions of the phase space differ significantly. We do expect an angular distribution in Region 1 which follows the Boltzmann distribution and a sharply anisotropic distribution in Region 2. We also do expect that the slope of the p_T^2 distribution differ substantially in these two regions and that in Region 1, it obeys the Boltzmann distribution. The surfaces of constant ξ^\pm are the paraboloids [47] in the phase space given by the analytic expression:

$$p_z^c = \frac{p_\perp^c + m^c - (\xi^\pm \sqrt{s})^2}{-2\xi^\pm \sqrt{s}} \quad (3.38)$$

and are shown in the Figure 3.3. We can also see that in the region $\zeta^\pm > \tilde{\zeta}^\pm$, the distributions at two different

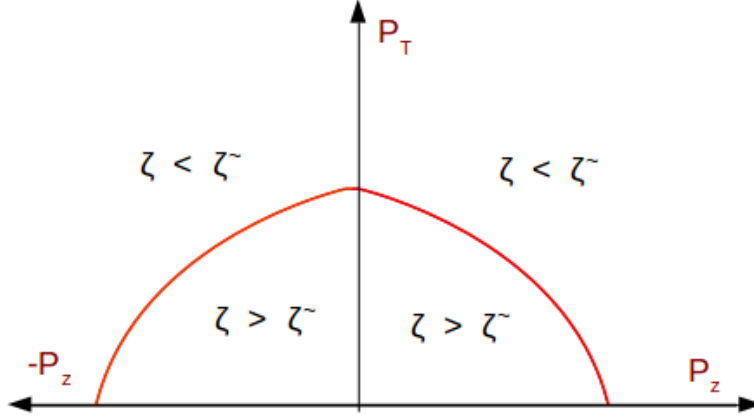


Figure 3.3: The schematic view of the surfaces of constant ζ^\pm

values of Mandelstam variable s_1 and s_2 (square of the total energy in the c. m. s.) are almost parallel curves separated from each other by a distance given by

$$\Delta^\pm = \frac{1}{2} \ln\left(\frac{s_1}{s_2}\right) \quad (3.39)$$

in the ζ scale. So it is clear that the value of $\tilde{\zeta}^\pm$ one chooses plays an important role in how and where the parabola is dividing the phase space. Consequently, the shape of $\mathbf{Cosine}(\theta)$ and p_T^2 distributions also depends on what value of $\tilde{\zeta}^\pm$ we select. So we need to set a method which should give us the value of $\tilde{\zeta}^\pm$. We do follow the hypothesis put forward by prof. Garsevanishvilli in [51], and expect that in region 1, we have particles emerging from a supposedly thermalised medium. So the ζ^\pm distribution in Region 1 is expected to obey Boltzmann distribution as in the following equation

$$\frac{1}{\pi} \frac{dN}{d\zeta} \sim \int_0^{p_T^2(max)} E f(E) dp_T^2 \quad (3.40)$$

where $p_{T,(max)}^2$, is given by

$$p_{T,(max)}^2 = (\xi^+ \sqrt{s})^2 - m^2 \quad (3.41)$$

and the expression for the $f(E)$ for a system following Boltzmann statistics is given by

$$f(E) = \exp(-E/T) \quad (3.42)$$

Corresponding Cosine(θ) distribution in the region 1 is expected to obey the following expression:

$$\frac{dN}{d\cos(\theta)} \sim \int_0^{p_Z(max)} f(E)p^2 dp \quad (3.43)$$

and p_T^2 distribution in region 1 is expected to obey

$$\frac{dN}{dp_T^2} \sim \int_0^{p_Z(max)} f(E)dp_Z \quad (3.44)$$

where,

$$E = \sqrt{p^2 + m_\pi^2} \quad (3.45)$$

and

$$p^2 = \sqrt{p_Z^2 + p_T^2} \quad (3.46)$$

The limits of integration in the expressions above are governed by the boundaries of the paraboloid. So one can find the value for $p_{Z,max}$ and p_{max} from the expression for the parabola defined by the constant value of light front variable ζ . They are given by the following formulae:

$$p_{Z,max} = \frac{(\xi^+ \sqrt{s})^2 + m_\pi^2 + p_T^2}{-2\tilde{\zeta}^+ \sqrt{s}} \quad (3.47)$$

$$p_{max} = \frac{(-\xi^+ \sqrt{s} \cos(\theta)) + \sqrt{(\xi^+ \sqrt{s})^2 - m_\pi^2 \sin^2(\theta)}}{\sin^2(\theta)} \quad (3.48)$$

It is worth to mention that a system of particles with a specific mass, following the Boltzmannian statistics can be described completely by a single parameter, namely the temperature of the system. Now let us see, how are we determining the value of $\tilde{\zeta}$ or $(\tilde{\xi})$ in our analysis.

Scheme of extraction of $\tilde{\zeta}^\pm$

The first step in our scheme is to make the light front variable (ζ) distribution for a specific particle species at a specific centre of mass energy. Then it is fitted with the equation (3.40) and see up to what range of ζ we can do it successfully. We take this boundary value as $\tilde{\zeta}^\pm$. Now based on this $\tilde{\zeta}^\pm$, we divide the phase space of particles into Region 1 and Region 2 as defined in the previous section. Then we make $\cos(\theta)$ and p_T^2 distributions for these two regions and compare the shape qualitatively. Also, to make the quantitative study,

we supply the extracted value of $\tilde{\zeta}^{\pm}$ to equations 3.47 and 3.48 to evaluate equations 3.43 and 3.44. Then the $\cos(\theta)$ and p_T^2 distributions are fitted respectively with these equations to extract the temperature. If the temperatures we get from all the three distributions are the same, within the errors, we can say that the light front scheme works and we could find a part of the phase space of the particle that follows Boltzmann statistics which is possibly thermalised. A numbers of iterations were done to finally reach to such a $\tilde{\zeta}^{\pm}$ which reasonably respects this criterion for the particles under consideration. In the case of event generators, this schme will be followed as such. For the case of ALICE data, there is a slight addition to this story. We are forced to apply kinematic cuts due to the acceptance of the detector. Hence we have to incorporate those cuts into the evaluation of these equations as well. In the expression on the right hand side of equation 3.40, we have to write E as a function of p_T and ζ by rewriting for p_Z for numerical integration and fitting. It is considered for the following two cases in the **positive hemisphere**.

- **Full η Analysis**

We know rom the definition of ξ that,

$$\xi = \frac{E + p_Z}{\sqrt{s}} \Rightarrow E = (\sqrt{s}\xi) - p_Z \quad (3.49)$$

This would give us

$$p_Z = \frac{(\sqrt{s}\xi)^2 - p_T^2 - m^2}{2\sqrt{s}\xi} \quad (3.50)$$

which enables us to write E as

$$E = \sqrt{p_T^2 + m^2 + \left[\frac{(\sqrt{s}\xi)^2 - p_T^2 - m^2}{2\sqrt{s}\xi} \right]^2} \quad (3.51)$$

This form is sufficient to perform numerical integration and fitting for (3.40) for a full pseudorapidity analysis.

- **Analysis with a cut on η**

The cut on η comes into (3.40) through the lower limit of the integral. We know that a constant η would mean a straight line in $p_Z - p_T$ plot (3.2), given by

$$p_Z = \frac{p_T}{\tan(\theta)} \quad (3.52)$$

where

$$\theta = 2\tan^{-1}[\exp(\eta_m)] \quad (3.53)$$

This would enable us to write $p_{T,min}^2$ as the solution to a quadratic equation. The solution is given by

$$p_{T,min}^2 = \frac{-b \pm \sqrt{b^2 - 4ac}}{2a} \quad (3.54)$$

where

$$a = 1 \quad (3.55)$$

$$b = \frac{2\sqrt{s}\zeta}{\tan(\theta)} \quad (3.56)$$

and

$$c = m^2 - (\sqrt{s}\xi)^2 \quad (3.57)$$

When we have a cut on p_T and η together, for each track we can compare the $p_{T,min}^2$ in the above equation with $p_T(\text{cut value})$ and take the strongest one among them in to numerical integration and fitting procedure. The light front analysis of π^\pm in the reaction $p\bar{p} \rightarrow \pi^\pm X$ at a centre of mass energy of around 6 GeV was presented in [47]. The resulting ζ distribution fitted with 3.40, p_T^2 distribution fitted with 3.44 and the $\cos(\theta)$ distribution fitted with 3.43 taking $\tilde{\zeta} = 2.0$ are shown in Figure 3.4. The temperatures obtained from this analysis are 119 ± 3 , 105 ± 1 and 86 ± 3 MeV respectively from the distributions.

Some counter-arguments from the past

The *critical* nature of constant $\tilde{\zeta}^\pm$ surface was confronted in a paper published in 1981, by B.B Levchenko [55]. It was argued that the sharp anisotropy of $\cos(\theta)$ distribution in region 2, in contrast to region 1 and the difference in the slopes of p_T^2 distributions in those two regions, stems from the fact that the inclusive cross-section is a "smoother function of p_Z than p_T ". It was also stated that for heavier particles and collisions at a higher centre of mass energies, the light front scheme does not work at all. In reference [55], the phenomenological parametrisation of Bourguin and Gaillard [56] was used for the description of the spectra of π^- , K^- and \bar{p} in pp interactions. The parametrisation of Borekov and Turbiner [57] was applied for the description of the spectra of J/ψ . For π^+ , ρ^+ and ρ^0 a Monte Carlo model based on the random number generation mechanism explained in [55] was used. The resulting angular distributions for π , ρ^\pm , ρ^0 ,

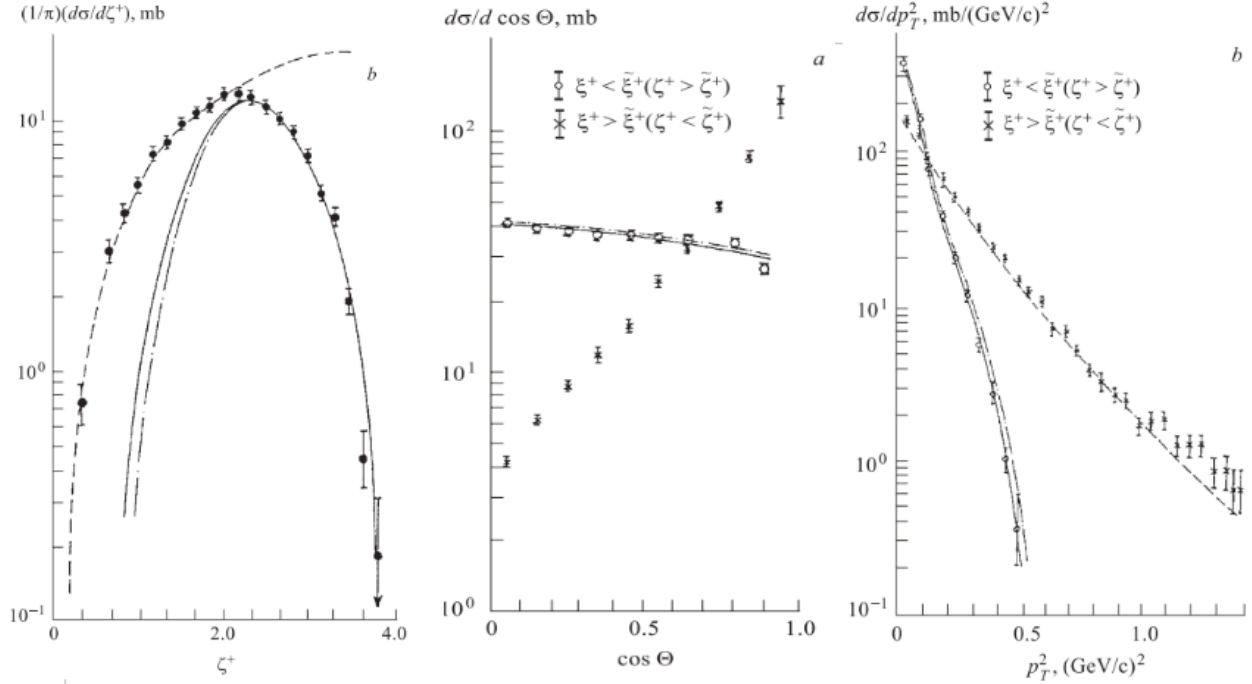


Figure 3.4: ζ , $\cos(\theta)$ and p_T^2 distributions of π^\pm in the reaction $p\bar{p} \rightarrow \pi^\pm X$ at a centre of mass energy of around 6 GeV. The temperatures obtained from this analysis are 119 ± 3 , 86 ± 3 and 105 ± 1 MeV respectively from the distributions with $\tilde{\zeta}$ taken as 2.0. Figures are taken from [47]

K^- , \bar{p} and J/ψ in the region $\zeta > \tilde{\zeta}$ are shown in figure 3.5. Thus, from the observation of the gradual

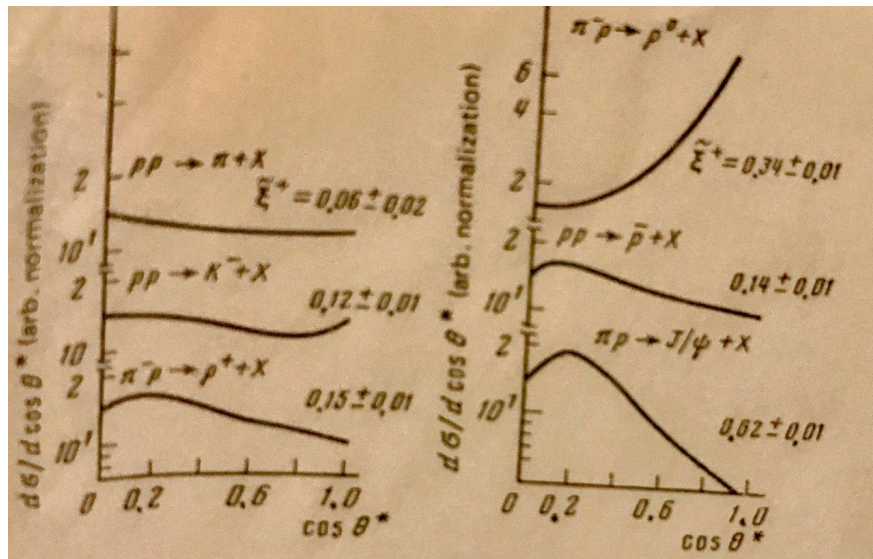


Figure 3.5: The predictions of angular distributions in the c.m.s at 40 GeV/c for $\zeta > \tilde{\zeta}$ from the calculations in [55] (Figure:3 in [55]).

disappearance of the uniformity effect in the angular distribution as the mass of the particle increases, it was

argued that the isotropic behaviour of the polar angle distribution for $\zeta > \tilde{\zeta}$ observed as per the light front scheme is related to the small mass of the pion, small mean transverse momentum of the produced pions and the energy 40 GeV at which it was found for, which is merely a 'fortuitous' coincidence. The conclusion was that there is no connection between the critical surfaces in the phase space and the dynamics of the production process of secondary particles. In the following chapters, using UrQMD and EPOS models of heavy-ion collision at RHIC energy, HIJING model (with and without kinematical cuts) and ALICE data at LHC energy, it will be shown that the particles in that part of the phase space with $\zeta > \tilde{\zeta}^\pm$ do differ from the corresponding distributions in the $\zeta < \tilde{\zeta}^\pm$ region. We will also show that the first region in the phase space will follow Boltzmann distribution for heavier mass particles as well and that the mere shape of the distribution alone does not imply the failure of the light front scheme to separate a thermalised part of the phase space.

Chapter 4

Light Front Analysis with UrQMD, EPOS and HIJING models

There is a wide range of heavy-ion collision models which are having different physical features based on different concepts. A realistic and complete description of the reality of heavy-ion collisions following the experimental data does not seem to be achieved by any of these models. But to have a very basic idea of what to expect from the experiments can be deduced by replicating the intended analysis over these models. Moreover, after having the experimental results, the models can be modified or improved by incorporating any missing physical effects. In this chapter, we see the analysis of the light front variable spectra using the simulated heavy-ion collisions with the Ultra Relativistic Quantum Molecular Dynamics Model (UrQMD) and the EPOS event generator at c.m.s energy of 200 GeV, the HIJING event generator at c.m.s energy of 2.76 TeV. The ROOT v6 [58] software package is used for the calculations presented in this chapter.

Description of the UrQMD Model

The UrQMD models is a microscopic transport model([59],[60],[61]). This means that it deals with the collision at the level of quarks and gluons. The transport model particles have its full phase space information throughout the evolution and subsequent interaction phases. The following Boltzmann equation 4.1

$$\frac{\partial x}{\partial t} \frac{\partial f(x, p)}{\partial x} + \frac{\partial p}{\partial t} \frac{\partial f(x, p)}{\partial p} + \frac{\partial f(x, p)}{\partial t} = I \quad (4.1)$$

has been used to describe the phase space distribution $f(x, p)$ of a particle over time, taking into account the interactions (given by interaction term I). UrQMD simulates the evolution described by 4.1 rather than solving the differential equation itself. The Wood-Saxon distribution describes the initial position of the

| ityp | nucleon | ityp | delta | ityp | lambda | ityp | sigma | ityp | xi | ityp | omega |
|------|------------|------|-----------------|------|------------------|------|-----------------|------|--------------|------|-----------------|
| 1 | N_{938} | 17 | Δ_{1232} | 27 | Λ_{1116} | 40 | Σ_{1192} | 49 | Ξ_{1317} | 55 | Ω_{1672} |
| 2 | N_{1440} | 18 | Δ_{1600} | 28 | Λ_{1405} | 41 | Σ_{1385} | 50 | Ξ_{1530} | | |
| 3 | N_{1520} | 19 | Δ_{1620} | 29 | Λ_{1520} | 42 | Σ_{1660} | 51 | Ξ_{1690} | | |
| 4 | N_{1535} | 20 | Δ_{1700} | 30 | Λ_{1600} | 43 | Σ_{1670} | 52 | Ξ_{1820} | | |
| 5 | N_{1650} | 21 | Δ_{1900} | 31 | Λ_{1670} | 44 | Σ_{1775} | 53 | Ξ_{1950} | | |
| 6 | N_{1675} | 22 | Δ_{1905} | 32 | Λ_{1690} | 45 | Σ_{1790} | 54 | Ξ_{2025} | | |
| 7 | N_{1680} | 23 | Δ_{1910} | 33 | Λ_{1800} | 46 | Σ_{1915} | | | | |
| 8 | N_{1700} | 24 | Δ_{1920} | 34 | Λ_{1810} | 47 | Σ_{1940} | | | | |
| 9 | N_{1710} | 25 | Δ_{1930} | 35 | Λ_{1820} | 48 | Σ_{2030} | | | | |
| 10 | N_{1720} | 26 | Δ_{1950} | 36 | Λ_{1830} | | | | | | |
| 11 | N_{1900} | | | 37 | Λ_{1890} | | | | | | |
| 12 | N_{1990} | | | 38 | Λ_{2100} | | | | | | |
| 13 | N_{2080} | | | 39 | Λ_{2110} | | | | | | |
| 14 | N_{2190} | | | | | | | | | | |
| 15 | N_{2200} | | | | | | | | | | |
| 16 | N_{2250} | | | | | | | | | | |

Figure 4.1: List of Baryons in UrQMD (Taken from [62]).

nucleons in the nuclei and the initial momentum of the nucleon is a function of the beam energy plus the Fermi momentum. However, the later has been incorporated into the calculation only when the interaction cross-sections are calculated to avoid dissolving of the nucleons (this approximation is often referred to as frozen Fermi approximation). The baryons and mesons whose production is included in to the UrQMD model are shown in the tables 4.1 and 4.2. The analysis will be carried out with species of particles having sufficient statistics. The propagating nucleons collide if the geometric criterion given by

$$\pi d^2 \leq \sigma_{tot} C_{\sigma,tot} \quad (4.2)$$

is met. Here d is the distance of closest approach between the two particles, σ_{tot} is the total cross-section for a collision to happen at the given energy between these two particles and $C_{\sigma,tot}$ is the cross-section reduction factor (we will see its definition in the next section). The interaction in UrQMD can be the following

- Elastic scattering
- Resonance Decay
- Soft resonance production
- String Excitation and Fragmentation

The cross-sections are determined using the additive quark model [63] or the detailed balance calculations.

| ityp | 0^{-+} | ityp | 1^{--} | ityp | 0^{++} | ityp | 1^{++} | ityp | charmed |
|-------------|----------|-------------|----------|-------------|-----------------|-------------|-----------------|-------------|----------|
| 101 | π | 104 | ρ | 111 | a_0 | 114 | a_1 | 133 | D |
| 106 | K | 108 | K^* | 110 | K_0^* | 113 | K_1^* | 134 | D^* |
| 102 | η | 103 | ω | 105 | f_0 | 115 | f_1 | 135 | J/Ψ |
| 107 | η' | 109 | ϕ | 112 | f_0^* | 116 | f_1' | 136 | χ_c |
| ityp | 1^{+-} | ityp | 2^{++} | ityp | $(1^{--})^*$ | ityp | $(1^{--})^{**}$ | 137 | Ψ' |
| 122 | b_1 | 118 | a_2 | 126 | ρ_{1450} | 130 | ρ_{1700} | 138 | D_s |
| 121 | K_1 | 117 | K_2^* | 125 | K_{1410}^* | 129 | K_{1680}^* | 139 | D_s^* |
| 123 | h_1 | 119 | f_2 | 127 | ω_{1420} | 131 | ω_{1662} | | |
| 124 | h_1' | 120 | f_2' | 128 | ϕ_{1680} | 132 | ϕ_{1900} | | |

Figure 4.2: List of Mesons in UrQMD (Taken from [62]).

In the additive quark model the hadronic cross-section is the sum of quark cross-sections can written as:

$$\sigma_{tot} = 40 \left(\frac{2}{3}\right)^{n_M} (1 - 0.4n_1^s)(1 - 0.4n_2^s) mb \quad (4.3)$$

where 40 mb is essentially the proton-proton cross-section over a broad range of energies, $\frac{2}{3}$ comes from the ratio of the number of quarks in meson to that in baryon. n_M is the number of mesons in the ingoing channel, n_1^s and n_2^s are the ratio of the number of strange quarks to that of u and d quarks in particle 1 and particle 2 respectively. In order to achieve better results, the equation 4.4 is used to scale known cross-section σ_{CD} to unknown one σ_{AB}

$$\sigma_{AB}(\sqrt{s}) = \sigma_{CD}(\sqrt{s}) \frac{\sigma_{AB}^{aqm}}{\sigma_{CD}^{aqm}} \quad (4.4)$$

where σ_{AB}^{aqm} and σ_{CD}^{aqm} are prediction of cross-sections from additive quark model corresponding to known(σ_{CD}) and unknown(σ_{AB}) cross-sections. The time-reversal invariance is the essence of detailed balance calculations. The square of the matrix elements for $AB \rightarrow CD$ and $CD \rightarrow AB$ are equal in this sense. The transition probability for $AB \rightarrow CD$ given by $P_{AB \rightarrow CD}$ is connected to this matrix element through the Fermi Golden rule. Also $P_{AB \rightarrow CD}$ is connected with the cross-section $\sigma_{AB \rightarrow CD}$ as well. From these considerations, we can see that $\sigma_{AB \rightarrow CD}$ is given by

$$\sigma_{AB \rightarrow CD} = \frac{\langle p_{CD}^2 \rangle g_{CD}}{\langle p_{AB}^2 \rangle g_{AB}} \sigma_{CD \rightarrow AB} \quad (4.5)$$

where g_i are degeneracy factors, $\langle p_{ij}^2 \rangle$ are the mean squared momenta of particles in the centre of mass system. In the famous string fragmentation model, a quark anti-quark pair is formed while pulling a quark from a hadron when the energy required for the new quark-antiquark pair becomes smaller than the energy to pull it further. The flavour conservation makes it sure that the quark-antiquark pairs of the same flavour are produced. Since the flavour composition is following the Schwinger - distribution [64] of the following form

$$P(m_T) \sim \exp\left(-\frac{\pi m_T^2}{k}\right) \quad (4.6)$$

with $k \approx 1\text{GeV}/fm$, there is an inherent strange quark suppression in the interactions of this kind. In the UrQMD model, each hadron formed is assigned with a formation time, which is a sum of the time for fragmentation and the time of formation. During the formation time, the cross-section is reduced by the factor

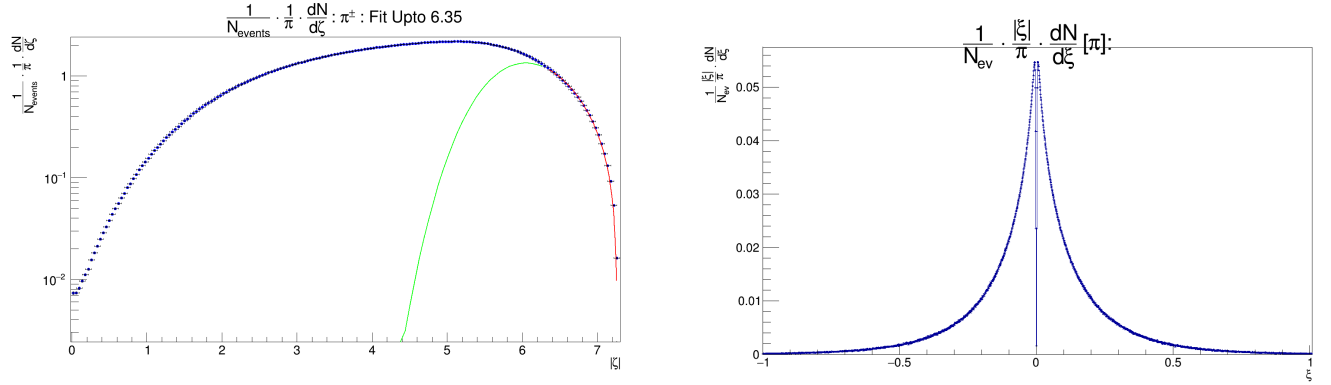
$$C_{\sigma,tot} = C_{\sigma,tot}^{lead} \frac{n_l}{n_q} \quad (4.7)$$

where n_q is the number of quarks in the hadron, n_l is the number of leading quarks that originate from a hadron, not from the string break up. It comes out from the fact that the newly forming partons are not allowed to interact. This can be seen if we put $n_l = 0$. In this case, a new hadron is made up only of new quarks and its cross-section is zero during the formation time implying zero interaction. In the following section, we do the light front analysis as mentioned in the previous chapter over the events generated using UrQMD 3.4 version. It is worth to mention that the PhD thesis of Gunnar Gräf [65] was very helpful in making a basic understanding of the model and getting the right references to the original works. UrQMD also has a hybrid, "Cascade + Hydro", calculation. More about the hybrid model UrQMD, its implementation and testing can be seen in [61]. Explicit permission for simulating and using the analysis plots were obtained from the authors of the model [66].

Light Front Analysis of UrQMD Collisions at $\sqrt{s} = 200 \text{ GeV}$

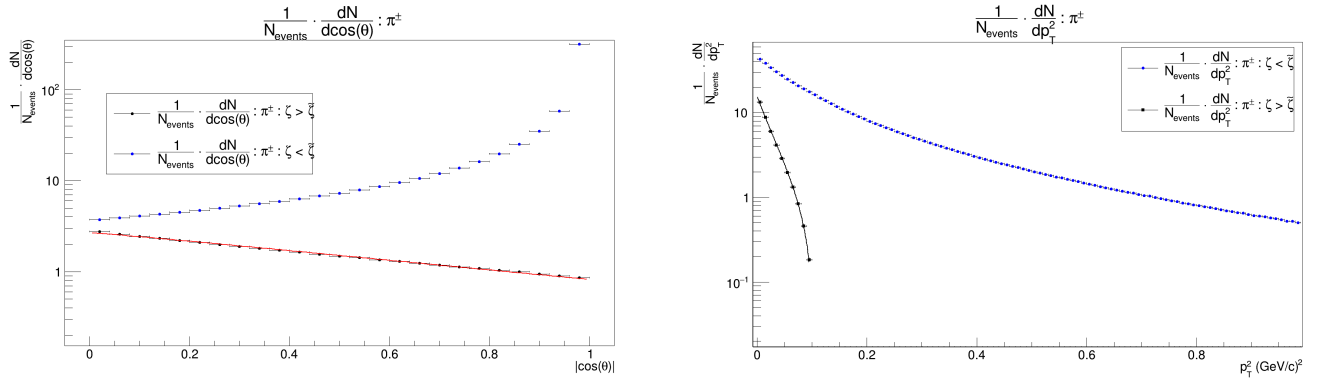
The UrQMD event Generator was downloaded from [62] and was used to generate exactly 55000 Au-Au collisions at a centre of mass energy of 200 GeV. The input file used for the simulation is added in the appendix A. The light front analysis was done on the resulting output file using the scheme mentioned in the previous chapter for various particle species. The distributions are presented in the following sections.

Pions : π^\pm



(a) ζ distribution. Solid red curve is the result of the fit with equation (3.40) up to $\zeta = 6.35$

(b) ξ distribution



(c) $\cos(\theta)$ distribution for $\zeta > 6.35$ (black) and $\zeta < \tilde{\zeta}$ (blue). (d) p_T^2 distribution for $\zeta > 6.35$ (black) and $\zeta < 6.35$ (blue). Solid red curve is the result of the fit with equation (3.43) Solid red curve is the result of the fit with equation (3.44)

Figure 4.3: ζ , p_T^2 and $\cos(\theta)$ distributions fitted with equations 3.40, 3.44 and 3.43 respectively for UrQMD π^\pm . The green curve in the ζ distribution is the extrapolation of the fit.

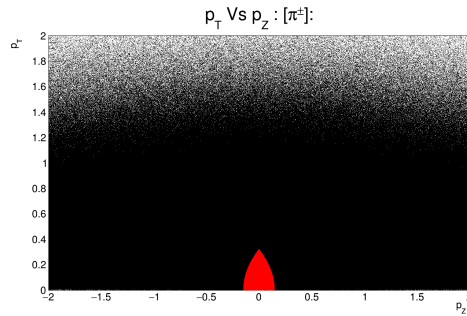
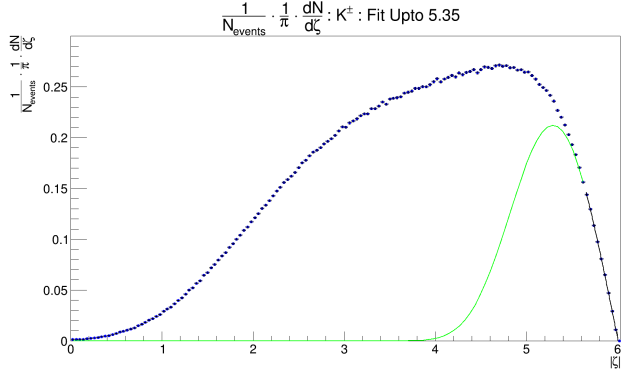
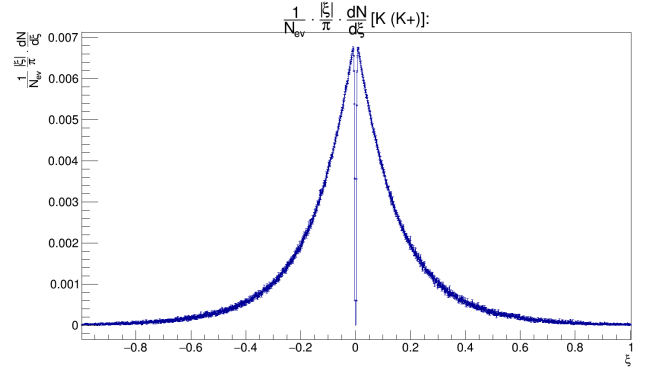


Figure 4.4: Peyrou p_T - p_Z plot of π^\pm . The red region corresponds to $\zeta > 6.35$

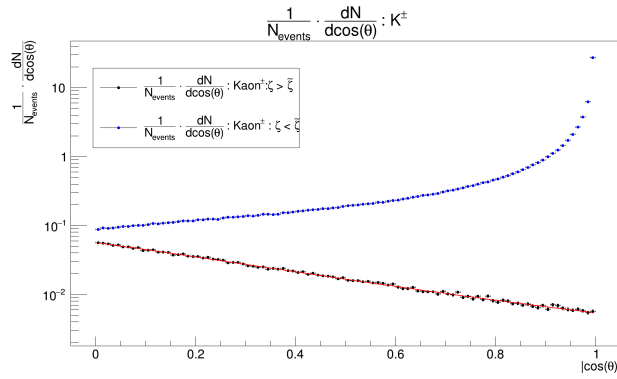
Kaons : K^\pm



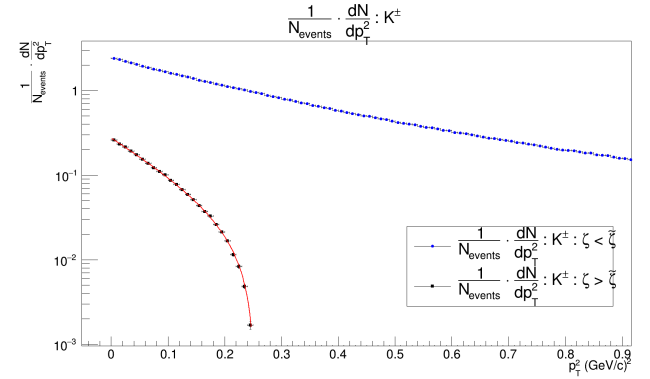
(a) ζ distribution. Solid red curve is the result of the fit with equation (3.40) up to $\zeta = 5.65$



(b) ξ distribution



(c) $\cos(\theta)$ distribution for $\zeta > 5.65$ (black) and $\zeta < 5.65$ (blue). (d) p_T^2 distribution for $\zeta > 5.65$ (black) and $\zeta < 5.65$ (blue). Solid red curve is the result of the fit with equation (3.43)



Solid red curve is the result of the fit with equation (3.44)

Figure 4.5: ζ , p_T^2 and $\cos(\theta)$ distributions fitted with equations 3.40, 3.44 and 3.43 respectively for UrQMD kaons. The green curve in the ζ distribution is the extrapolation of the fit.

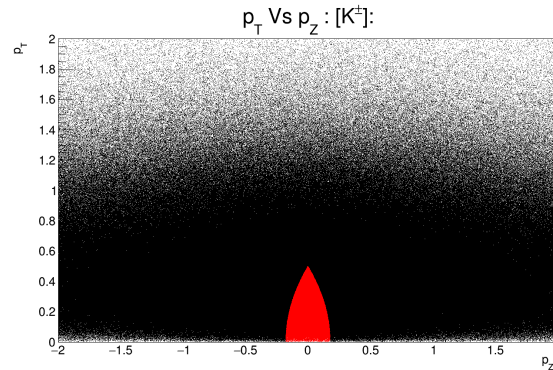
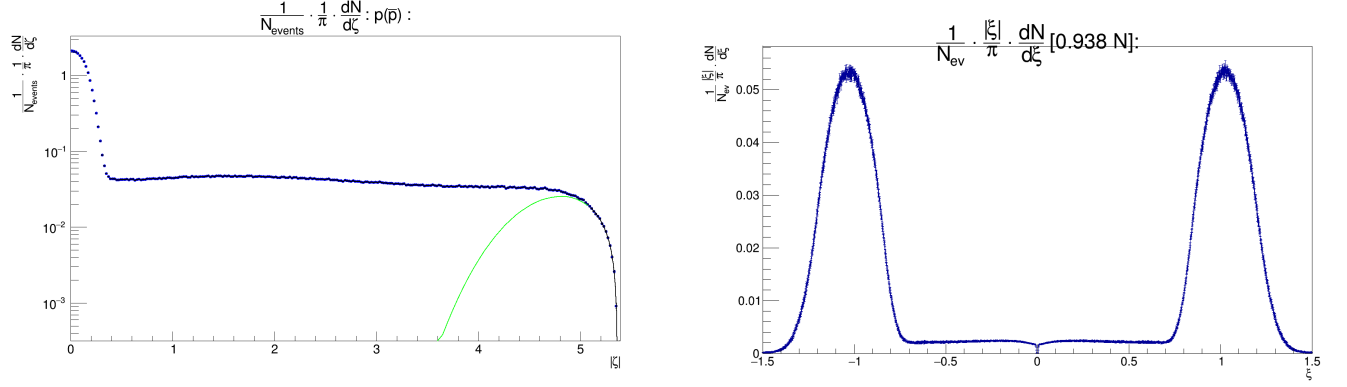


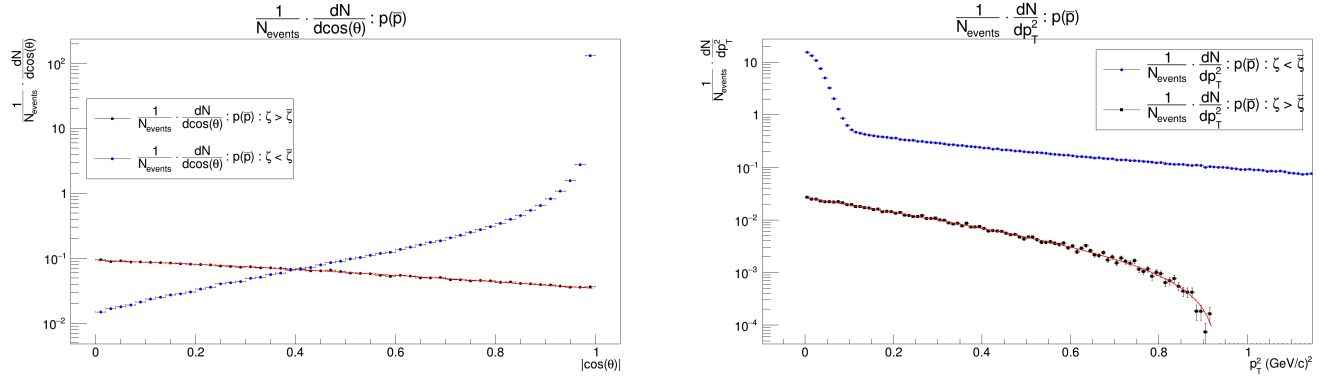
Figure 4.6: Peyrou p_T - p_Z plot of K^\pm . The red region corresponds to $\zeta > 5.65$

Protons: $p(\bar{p})$



(a) ζ distribution. Solid red curve is the result of the fit with equation (3.40) up to $\zeta = 5.0$

(b) ξ distribution



(c) $\cos(\theta)$ distribution for $\zeta > 5.0$ (black) and $\zeta < 5.0$ (blue). (d) p_T^2 distribution for $\zeta > 5.0$ (black) and $\zeta < 5.0$ (blue). Solid red curve is the result of the fit with equation (3.43) Solid red curve is the result of the fit with equation (3.44)

Figure 4.7: ζ , p_T^2 and $\cos(\theta)$ distributions fitted with equations 3.40, 3.44 and 3.43 respectively for UrQMD protons. The green curve in the ζ distribution is the extrapolation of the fit.

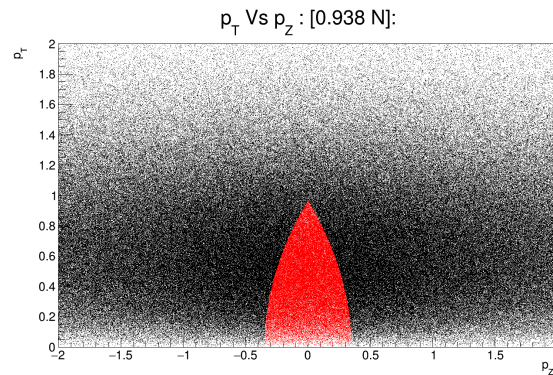


Figure 4.8: Peyrou p_T - p_z plot of UrQMD protons . The red region corresponds to $\zeta > 5.0$

Sigma Hyperons : $\Sigma(1192)$

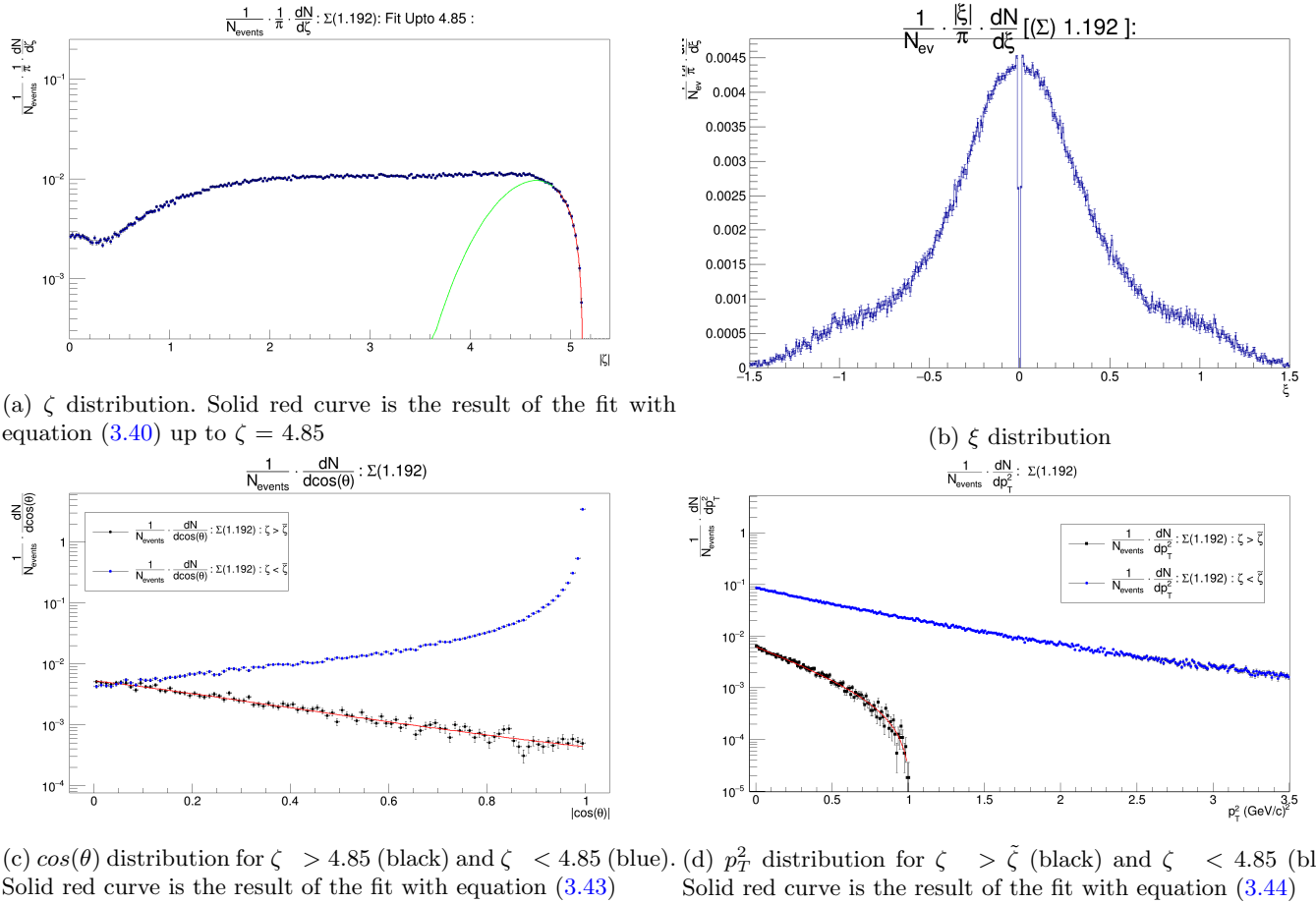


Figure 4.9: ζ , p_T^2 and $\cos(\theta)$ distributions fitted with equations 3.40, 3.44 and 3.43 respectively for UrQMD $\Sigma(1192)$. The green curve in the ζ distribution is the extrapolation of the fit.

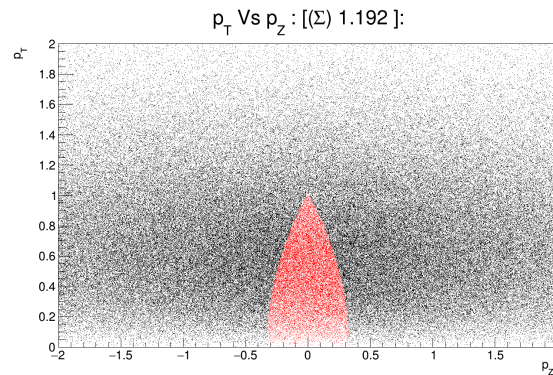


Figure 4.10: Peyrou p_T - p_Z plot of $\Sigma(1192)$. The red region corresponds to $\zeta > 4.85$

Xi Hyperons : $\Xi(1317)$

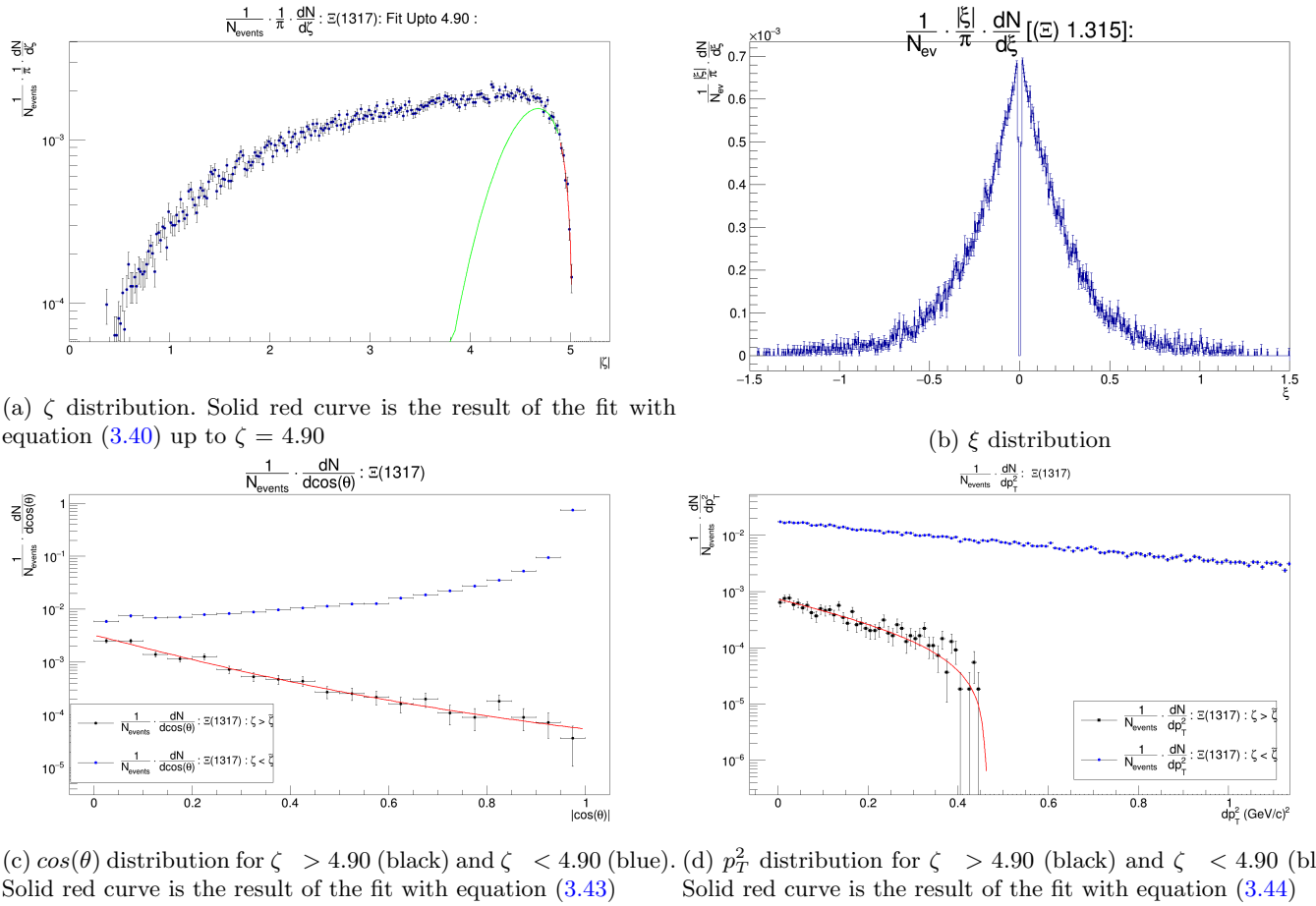


Figure 4.11: ζ , p_T^2 and $\cos(\theta)$ distributions fitted with equations 3.40, 3.44 and 3.43 respectively for UrQMD $\Xi(1317)$. The green curve in the ζ distribution is the extrapolation of the fit.

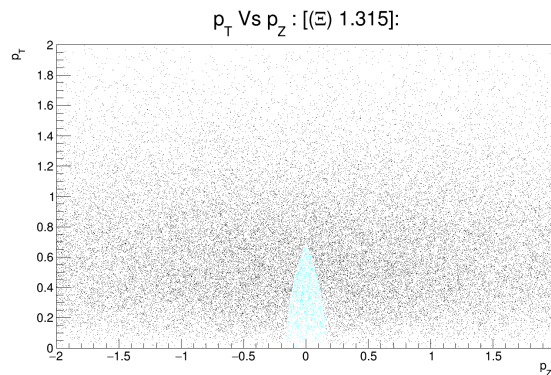
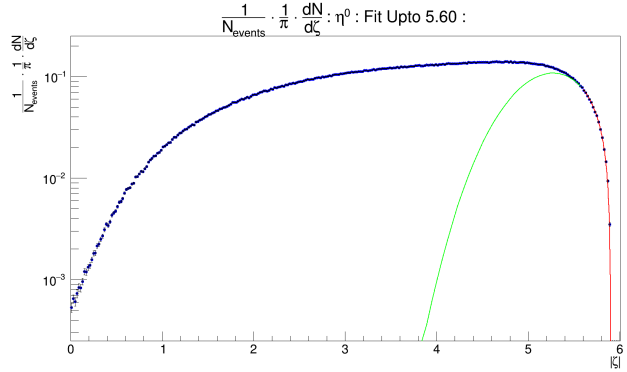
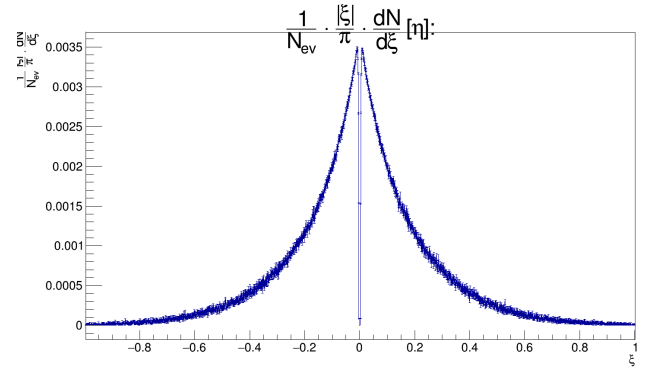


Figure 4.12: Peyrou p_T - p_z plot of $\Xi(1317)$. The cyan region corresponds to $\zeta > 4.90$

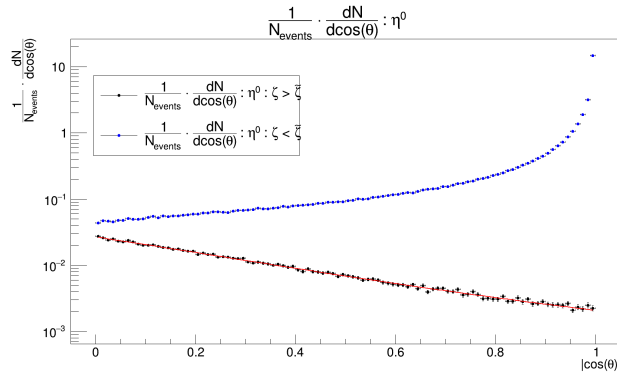
Eta Mesons : η^0



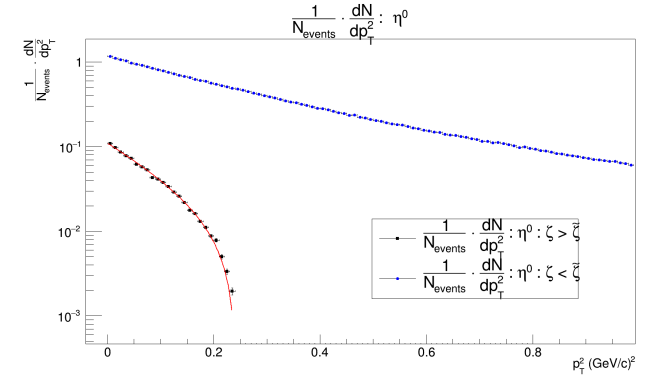
(a) ζ distribution. Solid red curve is the result of the fit with equation (3.40) up to $\zeta = 5.60$



(b) ξ distribution



(c) $\cos(\theta)$ distribution for $\zeta > 5.60$ (black) and $\zeta < 5.60$ (blue). (d) p_T^2 distribution for $\zeta > 5.60$ (black) and $\zeta < 5.60$ (blue). Solid red curve is the result of the fit with equation (3.43)



Solid red curve is the result of the fit with equation (3.44)

Figure 4.13: ζ , p_T^2 and $\cos(\theta)$ distributions fitted with equations 3.40, 3.44 and 3.43 respectively for UrQMD η^0 . The green curve in the ζ distribution is the extrapolation of the fit.

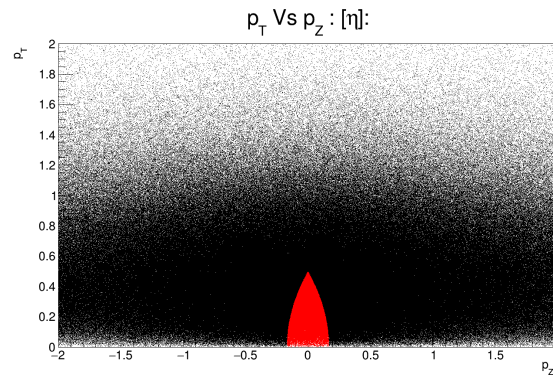


Figure 4.14: Peyrou p_T - p_Z plot of η^0 . The red region corresponds to $\zeta > 5.60$

Lambda Hyperons : Λ^0

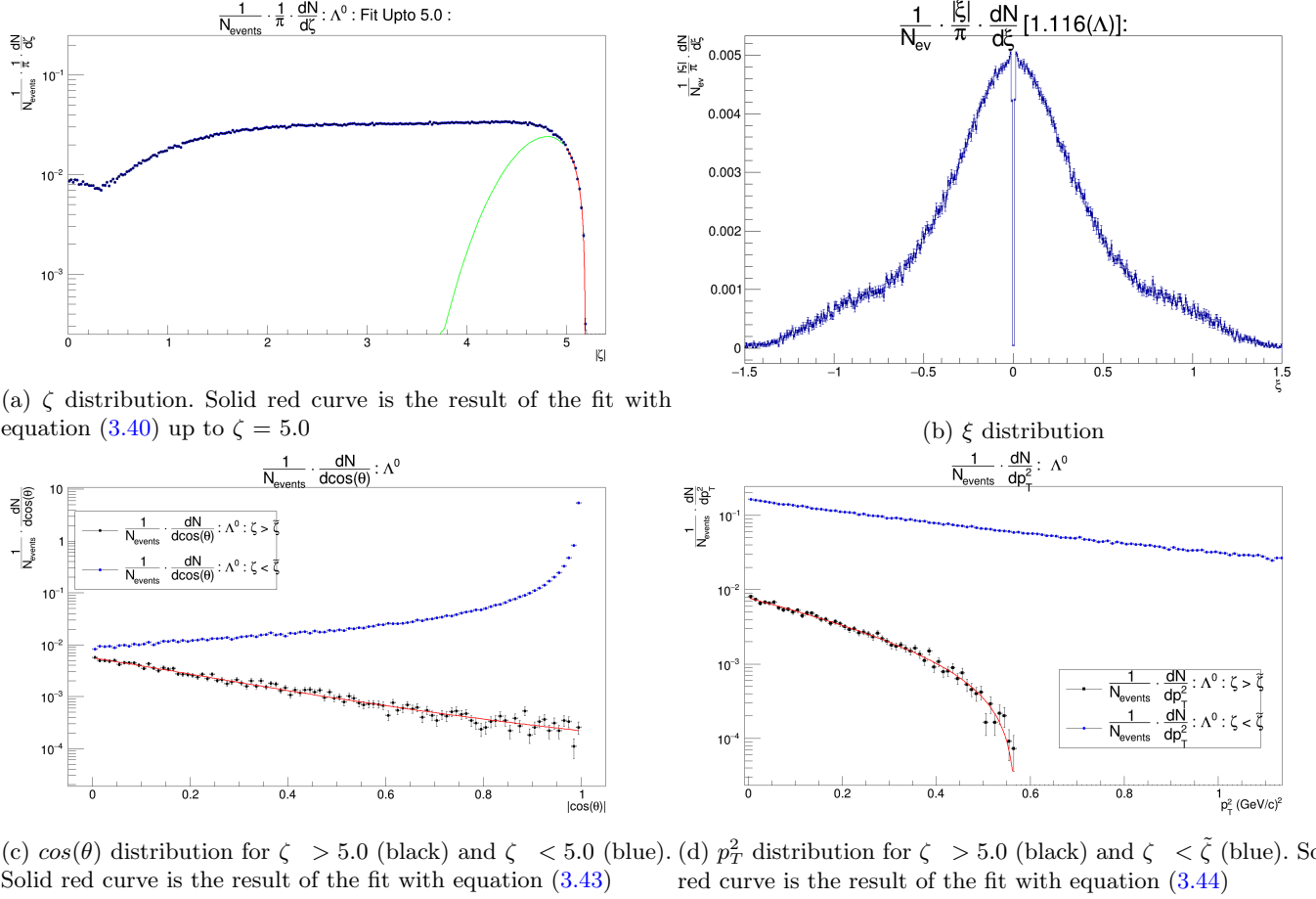


Figure 4.15: ζ , p_T^2 and $\cos(\theta)$ distributions fitted with equations 3.40, 3.44 and 3.43 respectively for UrQMD Λ^0 . The green curve in the ζ distribution is the extrapolation of the fit.

A summary of the extracted temperatures for various species can be seen in Table 4.1.

| Species | $\tilde{\zeta}$ | T(MeV) from ζ | χ^2/ndf | T(MeV) from p_T^2 | χ^2/ndf | T(MeV) from $\cos(\theta)$ | χ^2/ndf |
|----------------|-----------------|---------------------|--------------|---------------------|--------------|----------------------------|--------------|
| π^\pm | 6.35 | 101 ± 5 | 1.0/21 | 89 ± 12 | 0.2/8 | 97 ± 2 | 12/23 |
| K^\pm | 5.65 | 177 ± 38 | 0.2/7 | 146 ± 7 | 0.8/23 | 145 ± 2 | 85/98 |
| p | 5.00 | 267 ± 41 | 1.1/12 | 273 ± 4 | 70/90 | 274 ± 25 | 39/48 |
| η^0 | 5.60 | 171 ± 19 | 1.6/14 | 162 ± 9 | 4.8/21 | 173 ± 1 | 78/98 |
| Λ^0 | 5.00 | 197 ± 42 | 0.5/8 | 199 ± 7 | 35/54 | 210 ± 12 | 101/98 |
| $\Sigma(1192)$ | 4.85 | 266 ± 32 | 1.4/12 | 223 ± 8 | 76/98 | 222 ± 7 | 100/98 |
| $\Xi(1317)$ | 4.90 | 220 ± 15 | 2.2/4 | 189 ± 30 | 44/45 | 210 ± 74 | 12/18 |

Table 4.1: Temperatures obtained using Light Front analysis over UrQMD hadrons

Description of EPOS event Generator

EPOS is the abbreviation for **E**nergy conserving quantum mechanical approach based on **P**artons, parton ladders, strings, **O**ff shell remnants, and **S**plitting of parton ladders. It is a quantum-mechanically consistent, parton and string-based multiple scattering approach where the cross-section is calculated taking into account the energy conservation. Effects such as Cronin p_T broadening, parton saturation and screening have been introduced for having the collective behaviour in heavy-ion collisions. A compact description of the model can be seen in [67]. It uses the parton-based Gribov-Regge theory for its operation. The technical details of it can be seen in [68]. An elementary interaction in EPOS can be considered as a parton ladder which can be imagined as a colour electric field decaying into segments which can be interpreted as hadrons. A simple picture of an EPOS event is depicted in figure 4.16. Lund string model is implemented for particle production. The heavy-ion collision has multi-particle interactions at the initial stage. The modelling in EPOS is done for this particular stage as an exchange of parton ladder which can be soft or hard which allows one to model semi-hard processes as well. All parton ladders exist at the same time conserving total energy which constraint the number of ladders. Each of them has it's own saturation scale depending on the number of connecting participants and the centre of mass energy separating the soft and hard processes. The approach is referred to as the parton based Gribov Regge Theory. After the initial multiple scattering, depending on the energy and density of the strings, a high density "core" area and a low density "corona" area is formed. The core - strings are modelled to reach thermal equilibrium, resulting in hydrodynamical evolution and hadronisation in the final stages. The corona - strings hadronize via Schwinger mechanism and produces the jet part of the system. A selection method for events with hard partons (jet-like) implemented in EPOS can be seen in [70]. Parallel development of EPOS3 also implements a 3+1D viscous hydrodynamical evolution approach based on flux tube initial conditions[71]. The multiplicity of the event is proportional to the number of parton ladders (pomeron). The positions are randomly generated which might cause to create a $\cos(2\delta\phi)$ shaped correlation function. Some LHC energy predictions from the model can be found in [72]. In the following section, we will see the light front analysis of some of the EPOS3 hadrons using the methods that were explained in detail in the earlier chapter. Private communication with the authors of the model was decisively helpful in analyzing the EPOS events [73].

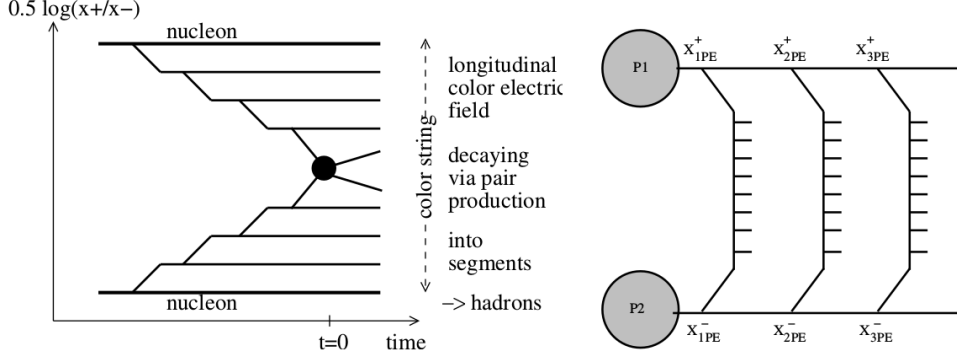


Figure 4.16: Elementary Interaction in EPOS (left) and Multiple Interaction (right) via the exchange of energy-conserving ladders in parallel. Figure is taken from [69]

Light Front Analysis of EPOS Collisions at $\sqrt{s} = 200$ GeV

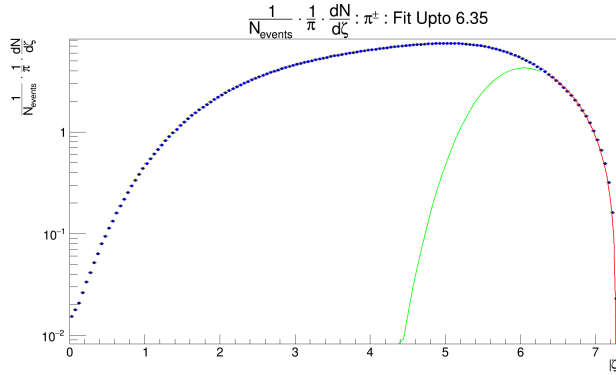
About 38000 central events were generated with EPOS3 version of the model and the resulting data were used for the light front analysis over π^\pm , K^\pm , $p(\bar{p})$ for the full range of pseudorapidity. The $\tilde{\zeta}$ for each species were found by fitting the ζ distribution with 3.40 for each species. The p_T^2 and $\cos(\theta)$ distributions were made for each species and for each region of the phase space separated by the paraboloid described by constant $\tilde{\zeta}$. For ζ grater than $\tilde{\zeta}$, the distributions were fitted with Boltzmann distribution as described earlier and corresponding temperatures were extracted. It is presented in the following sections with a summary of the values in Table 4.2 below.

| Species | $\tilde{\zeta}$ | T(MeV) from ζ | χ^2/ndf | T(MeV) from p_T^2 | χ^2/ndf | T(MeV) from $\cos(\theta)$ | χ^2/ndf |
|-----------|-----------------|---------------------|--------------|---------------------|--------------|----------------------------|--------------|
| π^\pm | 6.35 | 100 ± 4 | 3/17 | 93 ± 4 | 4/18 | 95 ± 2 | 27/23 |
| K^\pm | 5.50 | 217 ± 12 | 0.2/14 | 192 ± 4 | 3/41 | 194 ± 2 | 89/98 |
| p | 5.00 | 408 ± 42 | 0.5/16 | 358 ± 48 | 69/91 | 360 ± 7 | 61/98 |

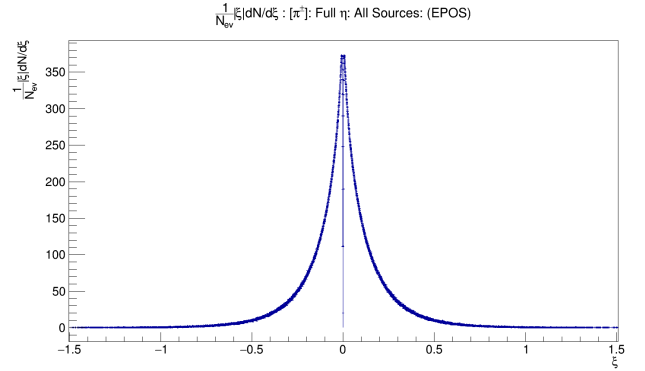
Table 4.2: Temperatures obtained using Light Front analysis over EPOS hadrons

We could in fact fit the lightfront based plots in UrQMD and EPOS at 200 GeV for particles using equations 3.40, 3.44 and 3.43. In both the models, we used both positive and negative particles together to fill the corresponding histograms. Also $|\zeta|$ was used always as the colliding systems were symmetric concerning the positive and negative hemispheres decided by the polar angle. The dynamical ingredients of UrQMD and EPOS do differ a lot as we saw in their descriptions. It is reflected in the temperatures that we extracted as well. But the value of $\tilde{\zeta}$, the factor of centrality etc has to be taken into account in interpreting the temperatures. Let us see the EPOS plots now.

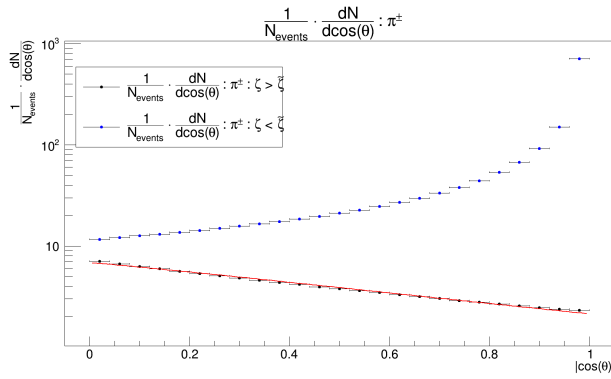
Pions : π^\pm



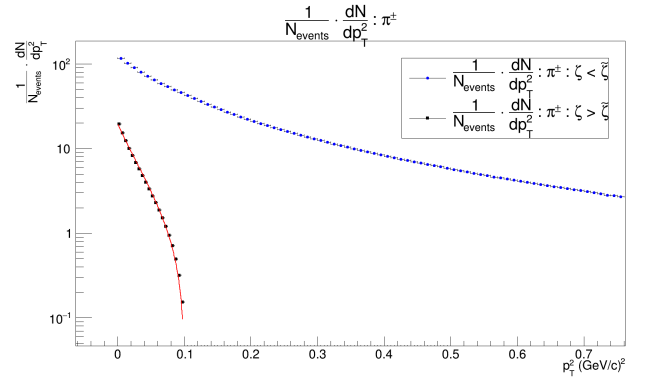
(a) ζ distribution (blue). Solid red curve is the result of the fit with equation (3.40) up to $\zeta = 6.35$



(b) ξ distribution corresponding to 4.17a



(c) $\cos(\theta)$ distribution for $\zeta > 6.35$ (black) and $\zeta < 6.35$ (blue). Solid red curve is the result of the fit with equation (3.43)



(d) p_T^2 distribution for $\zeta > 6.35$ (black) and for $\zeta < 6.35$ (blue). Solid red curve is the result of the fit with equation (3.44)

Figure 4.17: ζ , p_T^2 and $\cos(\theta)$ distributions for EPOS Pions fitted with equations 3.40, 3.44 and 3.43 respectively. The green curve in the ζ distribution is the extrapolation of the fit.

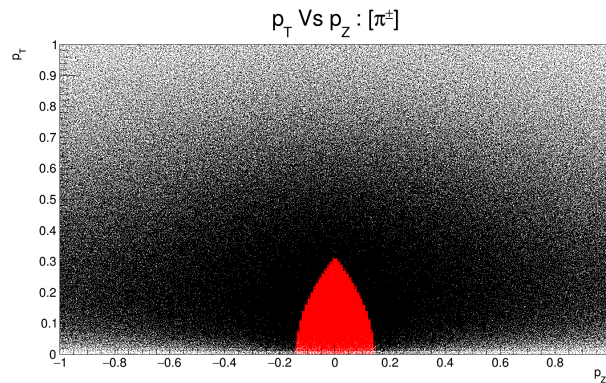
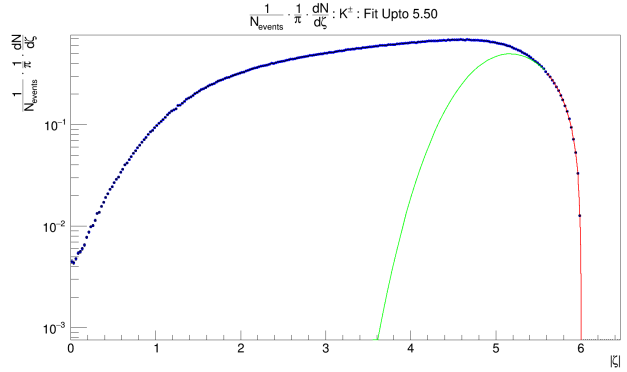
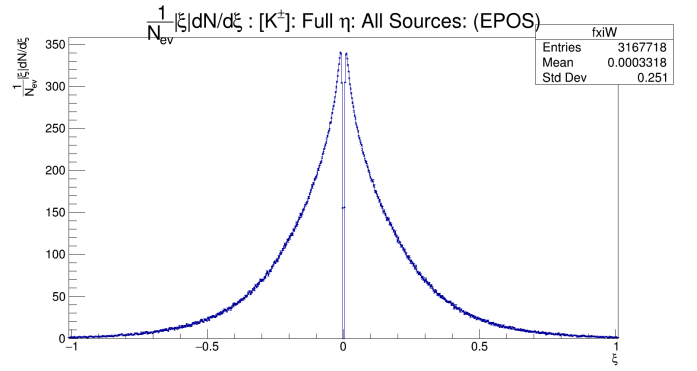


Figure 4.18: Peyrou p_T - p_Z plot of π^\pm . The red region corresponds to $\zeta > 6.35$

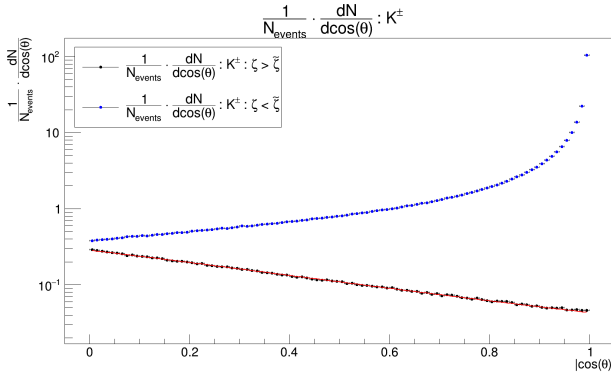
Kaons : K^\pm



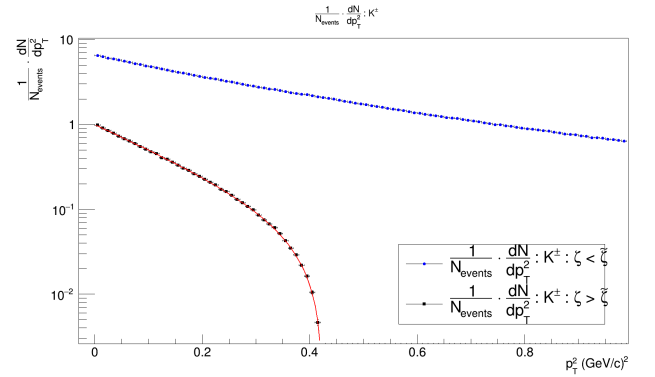
(a) ζ distribution (blue). Solid red curve is the result of the fit with equation (3.40) up to $\zeta = 5.50$



(b) ξ distribution corresponding to 4.19a



(c) $\cos(\theta)$ distribution for $\zeta > 5.50$ (black) and $\zeta < 5.50$ (blue). Solid red curve is the result of the fit with equation (3.43)



(d) p_T^2 distribution for $\zeta > 5.50$ (black) and for $\zeta < 5.50$ (blue). Solid red curve is the result of the fit with equation (3.44)

Figure 4.19: ζ , p_T^2 and $\cos(\theta)$ distributions for EPOS kaons fitted with equations 3.40, 3.44 and 3.43 respectively. The green curve in the ζ distribution is the extrapolation of the fit.

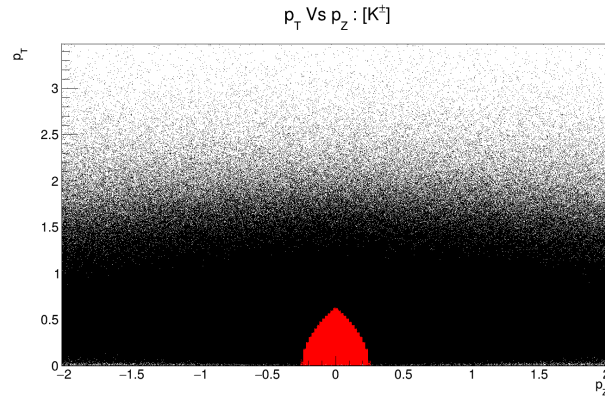
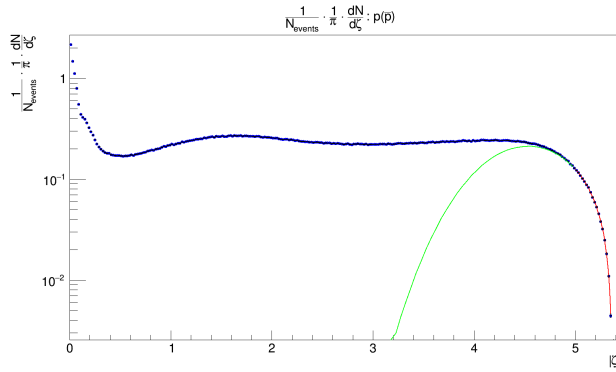
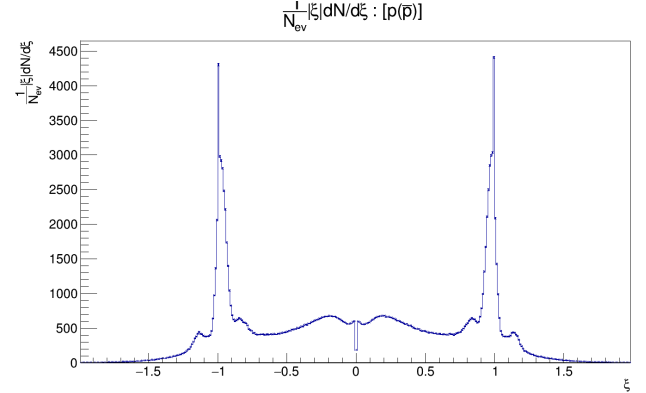


Figure 4.20: Peyrou p_T - p_Z plot of K^\pm . The red region corresponds to $\zeta > 5.50$

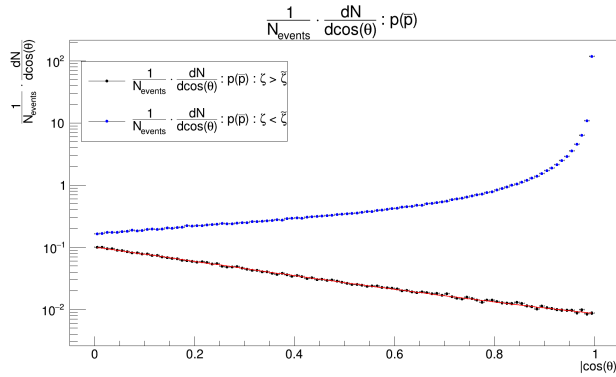
Protons: $p(\bar{p})$



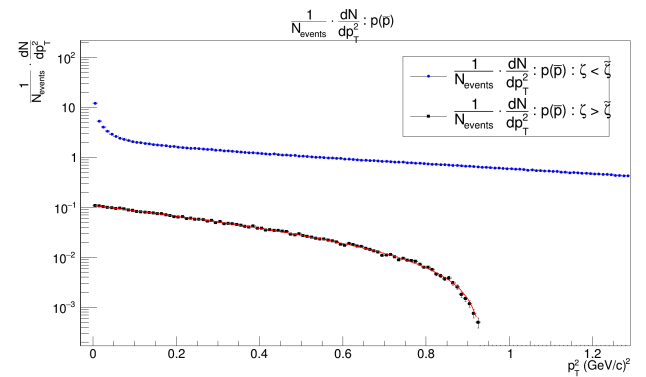
(a) ζ distribution (blue). Solid red curve is the result of the fit with equation (3.40) up to $\zeta = 5.0$



(b) ξ distribution corresponding to 4.21a



(c) $\cos(\theta)$ distribution for $\zeta > 5.0$ (black) and $\zeta < 5.0$ (blue). Solid red curve is the result of the fit with equation (3.43)



(d) p_T^2 distribution for $\zeta > 5.0$ (black) and for $\zeta < 5.0$ (blue). Solid red curve is the result of the fit with equation (3.44)

Figure 4.21: ζ , p_T^2 and $\cos(\theta)$ distributions for EPOS protons fitted with equations 3.40, 3.44 and 3.43 respectively. The green curve in the ζ distribution is the extrapolation of the fit.

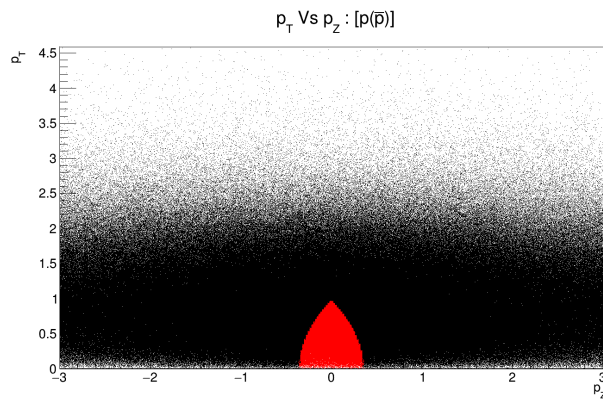


Figure 4.22: Peyrou p_T - p_Z plot of p . The red region corresponds to $\zeta > 5.0$

Description of HIJING event Generator

HIJING stands for **Heavy-Ion Jet Interaction Generator** ([74], [75], [76]). It is a Monte-Carlo program to study jets and particle production in high energy hadron and nucleus-nucleus collisions. Various processes like multiple mini jet productions, multiple scattering in heavy-ion collisions, nuclear shadowing, final state interactions, and jet quenching, hadronization has been included in this model. The) model is based on a *two-component geometrical model of mini-jet production and soft interaction*. It was used to reproduce the bulk hadron spectra and the suppression of high p_T hadrons due to jet quenching in central rapidity region of A + A collisions up to the RHIC centre of mass energies([77], [78], [79]). The two-component model was originally developed to make a phenomenological understanding of the relationship between total cross-section and the available centre of mass-energy ([80], [81], [82] ,[83], [84], [85], [86],[87]) and the production of particles([88], [89], [90] ,[91], [92]). The two-component model was later extended ([93],[94], [95]) and was incorporated into HIJING to provide initial parton production in relativistic heavy-ion collisions. The widely used hadron cascade models such as AMPT model ([96]) uses HIJING to provide its initial conditions. The Duke-Own parameterization ([97]) of PDFs are used to calculate the jet production cross-section. The basic assumption in the two-component model is that the partonic interaction during a nucleon collision can be separated into soft and hard part involving jet production with a cut-off scale p_0 for the transverse momentum of the final jet production. Below p_0 , the interactions are perturbative and above p_0 the cross-sections are governed by the perturbative QCD. A light front analysis of the HIJING Pb-Pb collisions at 2.76 TeV centre of mass-energy has been done **with and without kinematic cuts (on pseudorapidity η , and transverse momentum p_T)** to verify our scheme of integration and minimisation, which was later applied to the ALICE experimental data with same kinematic cuts. The results from HIJING are presented in the next section.

Light Front Analysis of HIJING Collisions at $\sqrt{s} = 2.76$ TeV

The light front variable distribution was made for several hadrons for the minimum bias events generated using HIJING event generator. As in the earlier cases, the phase space was divided into two groups based on the result of Boltzmann fit to the light front distribution ζ and the two groups were studied separately. In this case, we also make distributions for the kinematic cuts as mentioned in Table 4.3 for various species. The aim behind making this additional analysis with the cuts is that we want to know whether the light

front analysis can be done for an experimental case where such cuts are present. Moreover, this is a testing ground to see how consistent are our results in both cases. It is worth to note that the $\tilde{\zeta}$ found from the analysis with no kinematic cuts was used for the analysis with the kinematic cuts as well in contrast to the former case where we rely on the fit results. We can thus test the tools that we are about to use for the

| Particle | p_T Range(GeV) | η Range |
|--------------|------------------|----------------|
| π^\pm | 0.0 to 0.60 | $ \eta < 0.8$ |
| K^\pm | 0.25 to 0.40 | $ \eta < 0.8$ |
| $p(\bar{p})$ | 0.45 to 0.80 | $ \eta < 0.8$ |

Table 4.3: p_T and η ranges for the HIJING analysis with the kinematic cuts

analysis of the ALICE data. So the ζ distribution with the cuts as in 4.3 will be fitted up to the $\tilde{\zeta}$ found from the earlier fit to the ζ distribution where there were no kinematic cuts. A consistent picture from this kind of analysis would mean that the light front scheme works for LHC energies in the context of HIJING model. Also, this would mean that we can proceed to the analysis with ALICE data with the kinematic cuts enforced by the capabilities of the detector. The summary of the temperatures obtained from this analysis are presented in Table 4.4 and Table 4.5

| Species | $\tilde{\zeta}$ | T(MeV) from ζ | χ^2/ndf | T(MeV) from p_T^2 | χ^2/ndf | T(MeV) from $\cos(\theta)$ | χ^2/ndf |
|--------------|-----------------|---------------------|--------------|---------------------|--------------|----------------------------|--------------|
| π^\pm | 9.35 | 94 ± 5 | 0.4/26 | 89 ± 7 | 3/17 | 90 ± 1 | 32/98 |
| K^\pm | 8.32 | 138 ± 14 | 0.2/13 | 121 ± 2 | 60/102 | 123 ± 1 | 57/98 |
| $p(\bar{p})$ | 7.82 | 152 ± 13 | 0.2/15 | 142 ± 2 | 113/85 | 149 ± 2 | 54/98 |

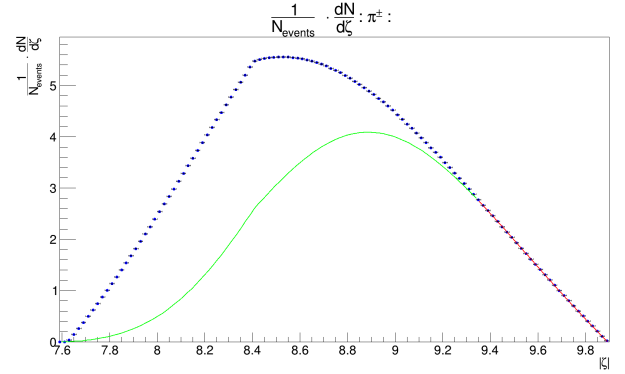
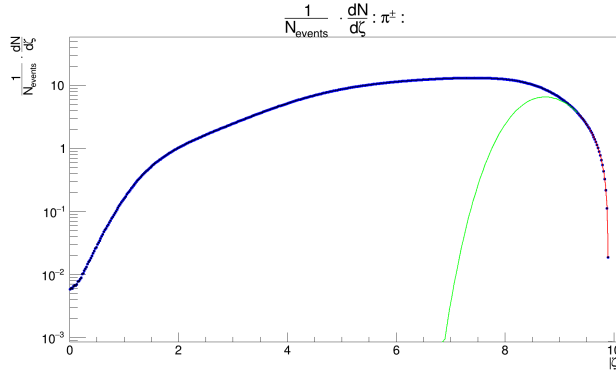
Table 4.4: Temperatures obtained from the full phase space Light Front analysis over HIJING hadrons

| Species | $\tilde{\zeta}$ | T(MeV) from ζ | χ^2/ndf | T(MeV) from p_T^2 | χ^2/ndf | T(MeV) from $\cos(\theta)$ | χ^2/ndf |
|--------------|-----------------|---------------------|--------------|---------------------|--------------|----------------------------|--------------|
| π^\pm | 9.35 | 88 ± 3 | 0.4/25 | 89 ± 3 | 10/37 | 93 ± 1 | 12/64 |
| K^\pm | 8.32 | 139 ± 2 | 161/188 | 136 ± 1 | 100/109 | 139 ± 7 | 7/38 |
| $p(\bar{p})$ | 7.82 | 161 ± 10 | 44/63 | 142 ± 8 | 123/141 | 146 ± 40 | .5/12 |

Table 4.5: Temperatures obtained from the Light Front analysis over HIJING hadrons with kinematic cuts

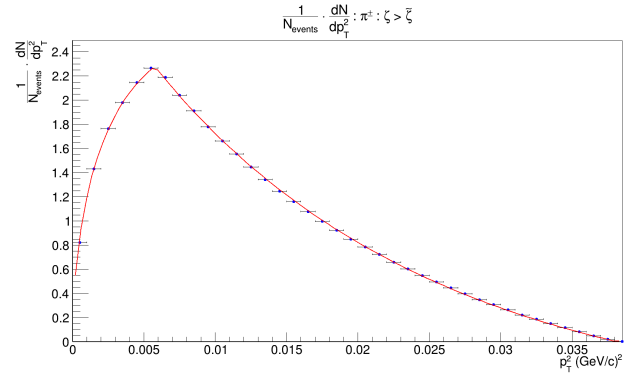
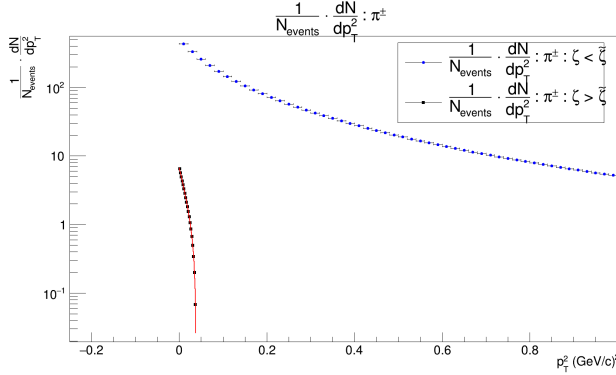
The absolute value of ζ is used to produce the ζ distributions as the system is symmetric around $\zeta = 0$. The value of $\tilde{\zeta}$ thus obtained was used for dividing the particles in both the hemisperes. Let us take a look at the HIJING plots now.

Pions : π^\pm



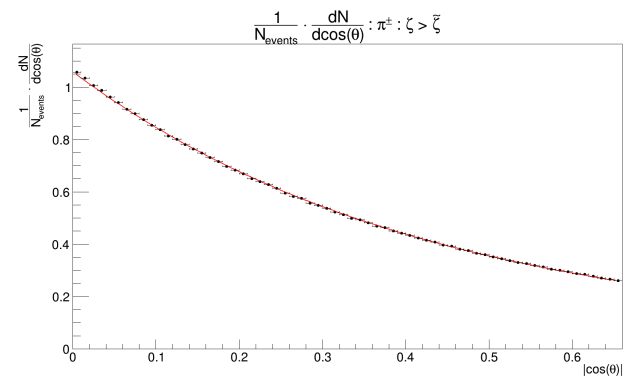
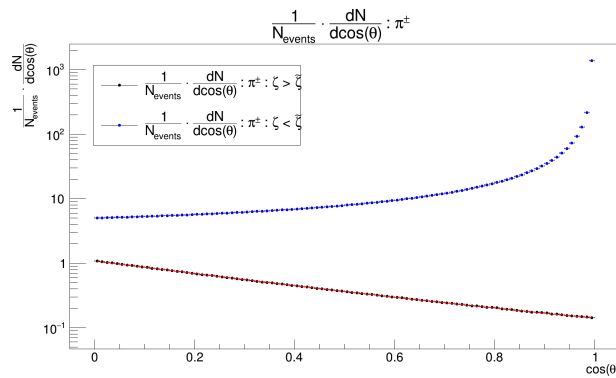
(a) ζ distribution. Solid red curve is the result of the fit with equation (3.40) : $\tilde{\zeta} = 9.35$: Full phase space

(b) ζ distribution. Solid red curve is the result of the fit with equation (3.40) : $\tilde{\zeta} = 9.35$: $|\eta| < 0.8$ & p_T cuts as in 4.3



(c) p_T^2 distribution. Solid red curve is the result of the fit with equation (3.44) : $\tilde{\zeta} = 9.35$: Full phase space

(d) p_T^2 distribution. Solid red curve is the result of the fit with equation (3.44) : $\tilde{\zeta} = 9.35$: $|\eta| < 0.8$ & p_T cuts as in 4.3

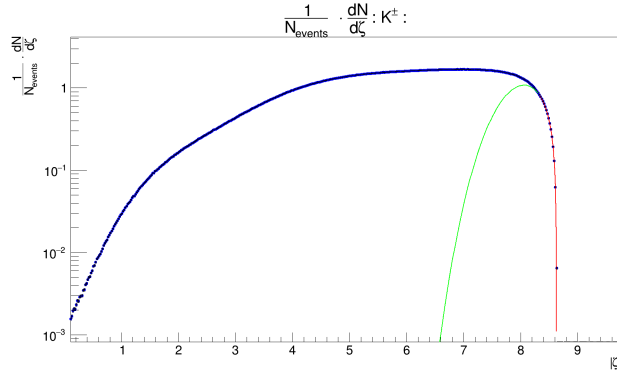


(e) $\cos(\theta)$ distribution. Solid red curve is the result of the fit with equation (3.43) : $\tilde{\zeta} = 9.35$: Full phase space

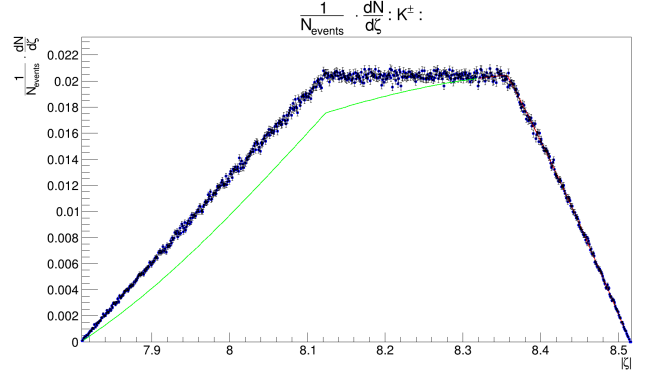
(f) $\cos(\theta)$ distribution. Solid red curve is the result of the fit with equation (3.43) : $\tilde{\zeta} = 9.35$: $|\eta| < 0.8$ & p_T cuts as in 4.3

Figure 4.23: HIJING π^\pm distributions. The green curve in the ζ distribution is the extrapolation of the fit.

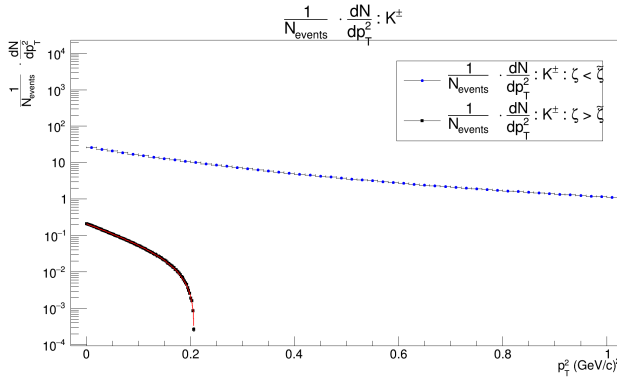
Kaons : K^\pm



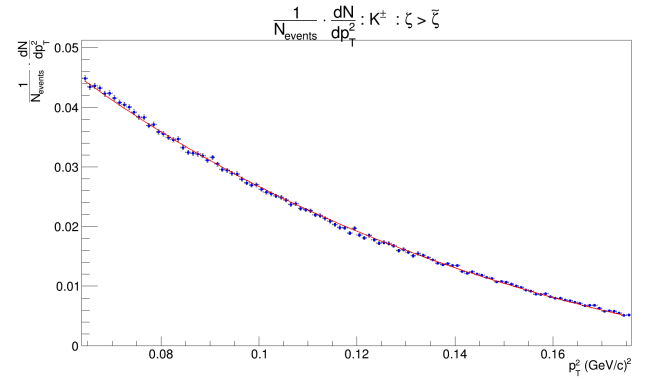
(a) ζ distribution. Solid red curve is the result of the fit with equation (3.40) : $\tilde{\zeta} = 8.32$: Full phase space



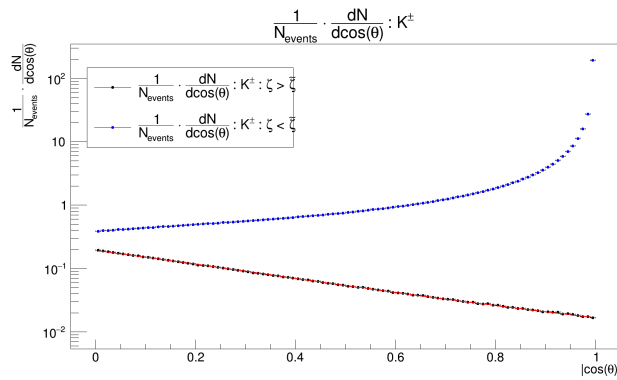
(b) ζ distribution. Solid red curve is the result of the fit with equation (3.40) : $\tilde{\zeta} = 8.32$: $|\eta| < 0.8$ & p_T cuts as in 4.3



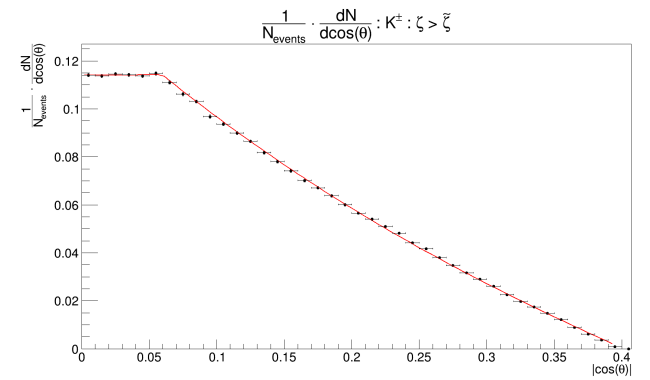
(c) p_T^2 distribution. Solid red curve is the result of the fit with equation (3.44) : $\tilde{\zeta} = 8.32$: Full phase space



(d) p_T^2 distribution. Solid red curve is the result of the fit with equation (3.44) : $\tilde{\zeta} = 8.32$: $|\eta| < 0.8$ & p_T cuts as in 4.3



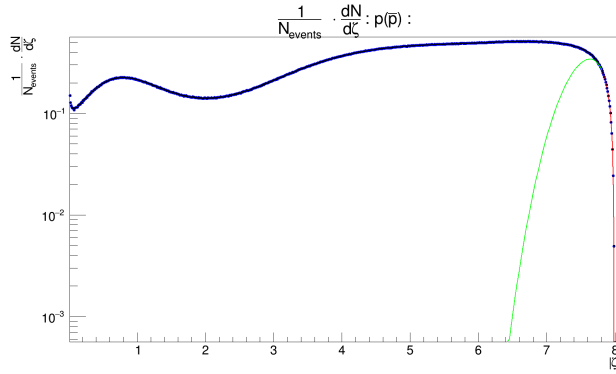
(e) $\cos(\theta)$ distribution. Solid red curve is the result of the fit with equation (3.43) : $\tilde{\zeta} = 8.32$: Full phase space



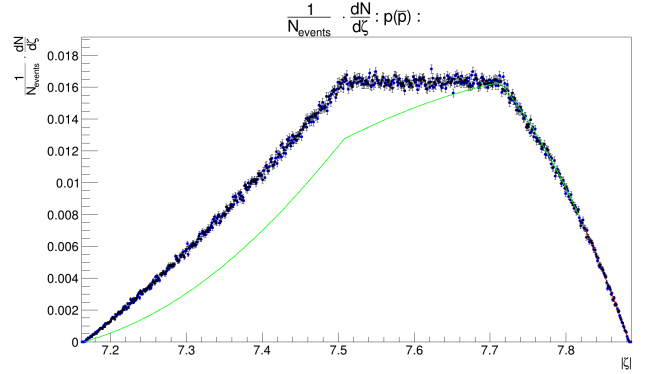
(f) $\cos(\theta)$ distribution. Solid red curve is the result of the fit with equation (3.43) : $\tilde{\zeta} = 8.32$: $|\eta| < 0.8$ & p_T cuts as in 4.3

Figure 4.24: HIJING K^\pm distributions. The green curve in the ζ distribution is the extrapolation of the fit.

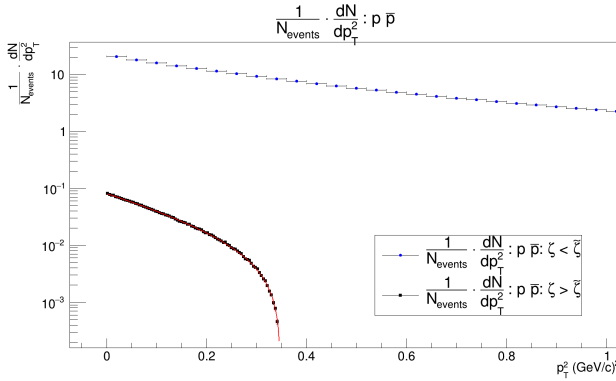
Protons: $p(\bar{p})$



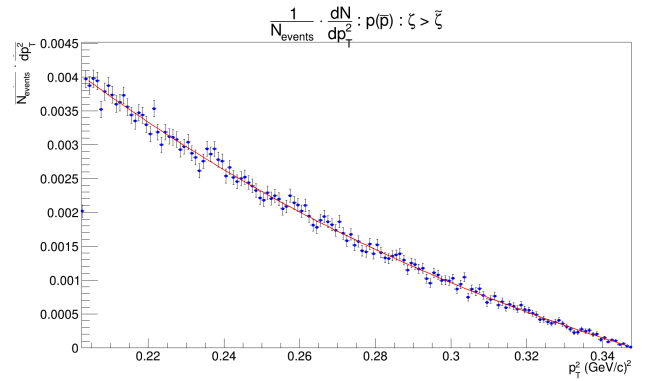
(a) ζ distribution. Solid red curve is the result of the fit with equation (3.40) : $\tilde{\zeta} = 7.82$: Full phase space



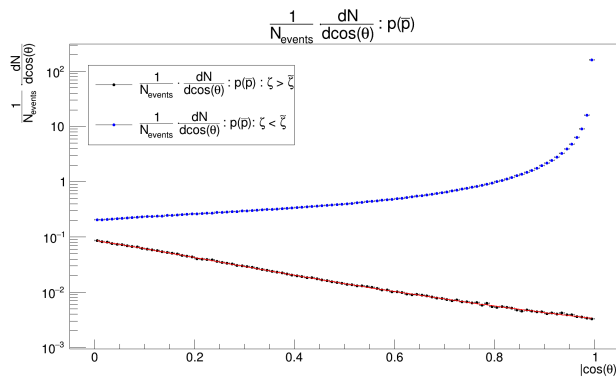
(b) ζ distribution. Solid red curve is the result of the fit with equation (3.40) : $\tilde{\zeta} = 7.82$: $|\eta| < 0.8$



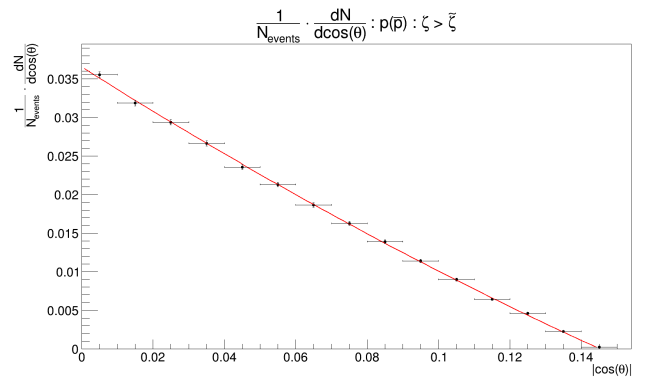
(c) p_T^2 distribution. Solid red curve is the result of the fit with equation (3.44) : $\tilde{\zeta} = 7.82$: Full phase space



(d) p_T^2 distribution. Solid red curve is the result of the fit with equation (3.44) : $\tilde{\zeta} = 7.82$: $|\eta| < 0.8$ & p_T cuts as in 4.3



(e) $\cos(\theta)$ distribution. Solid red curve is the result of the fit with equation (3.43) : $\tilde{\zeta} = 7.82$: Full phase space



(f) $\cos(\theta)$ distribution. Solid red curve is the result of the fit with equation (3.43) : $\tilde{\zeta} = 7.82$: $|\eta| < 0.8$

Figure 4.25: HIJING $p(\bar{p})$ distributions. The green curve in the ζ distribution is the extrapolation of the fit.

Summary of the Monte-Carlo studies and conclusions

In the previous sections, we saw the light front analysis over the hadrons from Monte Carlo models of heavy-ion collisions. The UrQMD and EPOS results show that the light front scheme works at RHIC energies. The constant value of ζ found from the Boltzmann fit of the ζ distribution divides the phase space of particles with p_T^2 and $\cos(\theta)$ distributions of one of the regions (ζ greater than $\tilde{\zeta}$) following the Boltzmann statistics. We have seen that this trend stays so for particles with larger masses as well. Similar analysis over the HIJING data for LHC energies imparts strength to the idea that the light front scheme works irrespective of the large centre of mass energies and the mass of the particle under consideration in contrast to what was argued in [55]. The average temperature was calculated for each species from the three distributions using the formula

$$\langle T \rangle = \frac{\sum_{i=1}^3 T_i W_i}{\sum_{i=1}^3 W_i} \quad (4.8)$$

where

$$W_i = \frac{1}{\sigma_i^2} \quad (4.9)$$

i runs for ζ , p_T^2 and $\cos(\theta)$ distributions for specific species of particles. T_i are the temperatures and σ_i are the respective errors. The expression for the error associated with $\langle T \rangle$ can be written as

$$\sigma(\langle T \rangle) = \frac{1}{\sqrt{2}} \sqrt{\frac{\sum_{i=1}^3 W_i \epsilon_i^2}{\sum_{i=1}^3 W_i}} \quad (4.10)$$

where,

$$\epsilon_i = T_i - \langle T \rangle \quad (4.11)$$

The temperature thus calculated for each species is presented in Figure 4.26 as a function of the mass of the particles. For pions, all the calculations yield nearly the same result. There is a clear mass dependence for the temperatures obtained from all the models. The temperatures obtained from EPOS central collisions for K^\pm and protons are larger than that of UrQMD minimum bias collisions. We can also see that the HIJING analysis with and without kinematic cuts give nearly the same temperatures for all the masses. Comparison between these two sets of results serves as a testing ground for the tools and techniques that

we use in our analysis. A successful convergence in the results of it gives us additional confidence in the implementation of the light front scheme with real data from ALICE. From these considerations, we can say

Temperature Vs Mass

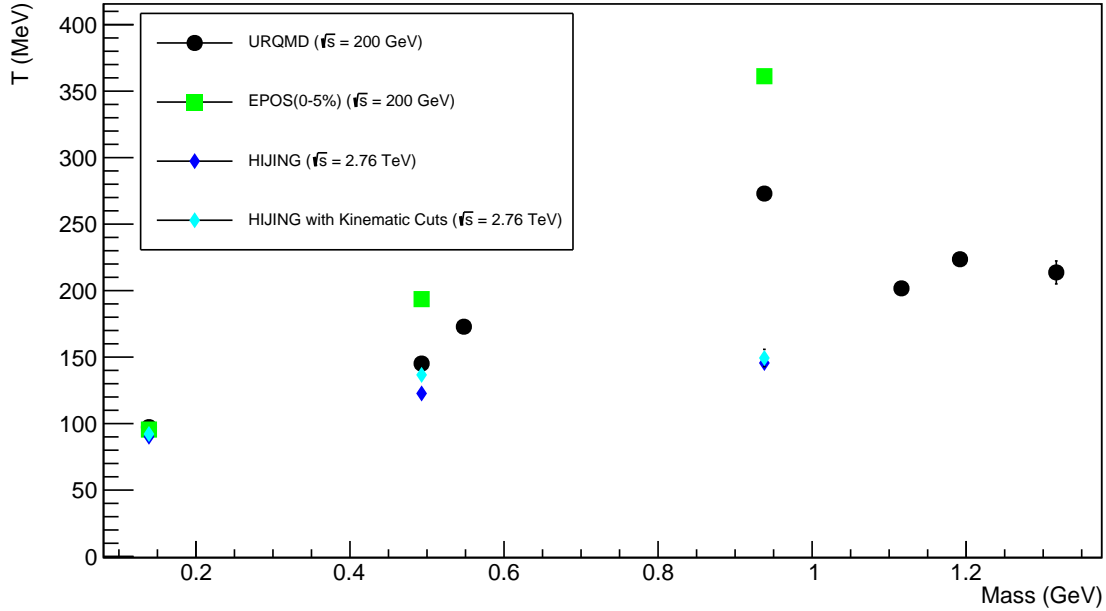


Figure 4.26: Estimated Temperature v/s Mass from the Monte Carlo models using light front analysis.

that there exists a thermalised part of the phase space for different particle species. The smooth continuation of the working trend of the scheme in HIJING with the kinematic cuts gives us confidence that we can test it with the real data from ALICE experiment, constrained by the kinematic cuts enforced by the detector considerations. So we are equipped now to move from the imaginary world of Monte Carlo models to the real world of experimental data with the pieces of information that we gained from this analysis. As a first step in reaching any conclusion regarding the existence of the signals of a thermalised state in ALICE with the light front analysis, let us take a look at the ALICE apparatus in the next chapter.

Chapter 5

ALICE Experiment at The Large Hadron Collider

The Large Hadron Collider (LHC)

The Large Hadron Collider is located at CERN, in Geneva, at the border between France and Switzerland. It is a 26.7 km long underground facility possessing a circular accelerator complex in it. It is the largest laboratory ever built on earth accessing the highest energies we ever had for a particle accelerator. A schematic diagram of the LHC accelerator complex is shown in Figure 5.1. The LHC is primarily constructed for doing various searches in the field of high energy particle and nuclear physics. It searches for beyond standard model(BSM Physics) through many possible ways. It studies symmetries of fundamental forces and also can study the form of matter called quark-gluon plasma through heavy-ion collisions. The four big experimental setups placed on the LHC ring are CMS ([99]), ATLAS([100]), ALICE ([101]) and LHCb([102]). There are several small experimental setups as well placed at specific locations of the entire acceleration complex. The entire process leading to collisions and the collection of data may be briefed as follows ([103], [104]). The acceleration chain begins with the creation of protons (or ions) at the proton (ion) sources. Then the radio frequency Quadrupole (RFQ) will split the proton or ion beams into bunches. Then it enters LINAC2(for proton) or LINAC3 (for heavy -ions) where its energy gets increased to 50 MeV for proton(and 4.2 MeV/u for Lead ions). Then these bunches are accelerated in the Low Energy Ion ring and Proton Synchrotron Booster where its energy gets increased to 94 MeV/u for lead and 1.4 GeV for protons. Then it is injected into Proton synchrotron where its energy gets increased to 25 GeV for proton and 54.9 MeV/u for Lead. In the next step, the bunches are injected to the super proton synchrotron which will accelerate the bunches to 450 GeV(p) and 177 MeV/u (Pb) which is the injection energy of LHC. It is then injected to

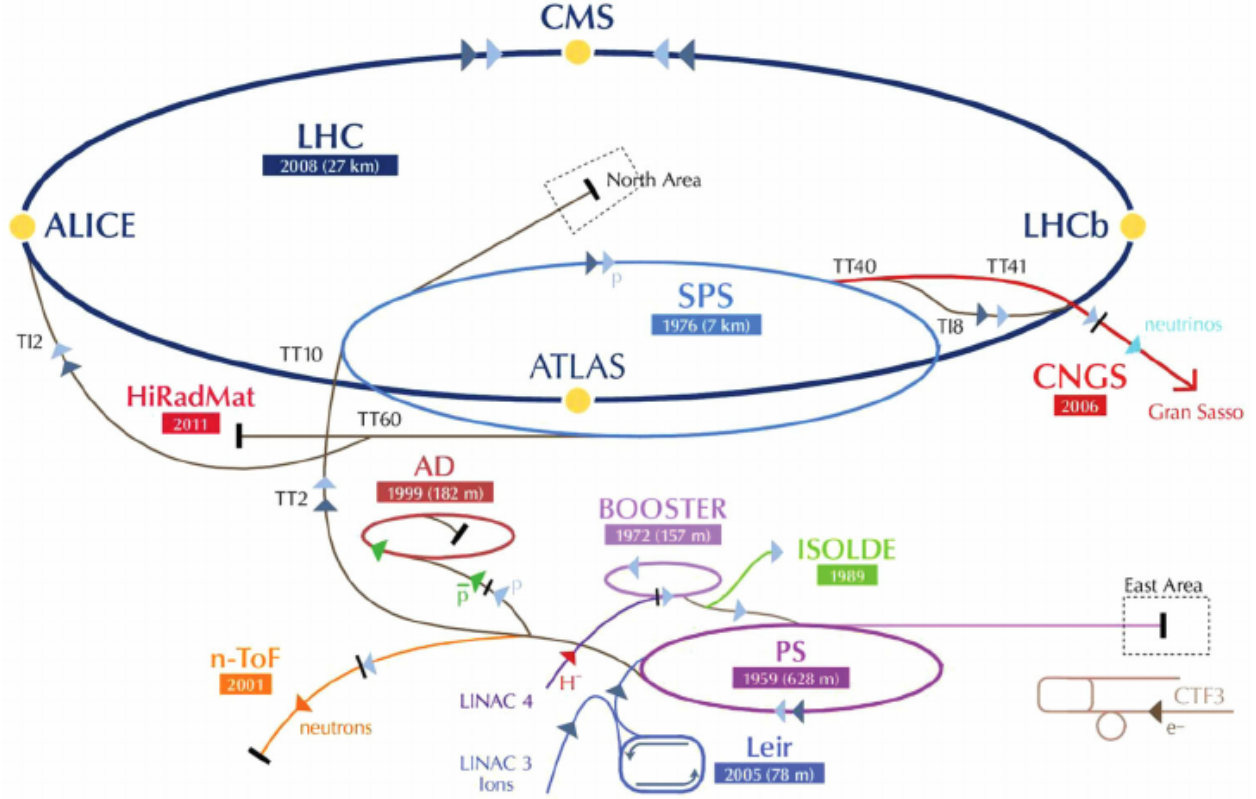


Figure 5.1: Schematics of the CERN accelerator complex. Figure is taken from [98]

the two counter-rotating rings of LHC. So after this, two beams of the proton or Lead ions will accelerate in opposite directions in the LHC. These bunches are then made to collide each other at 4 points where the four large experimental set-ups are placed. The collision will produce a huge number of particles which are detected by the experimental detectors. The data is then processed and analysed to figure out and solve various kinds of problems in particle and nuclear physics. Currently LHC has collisions from proton-proton (design luminosity of $L_{pp} = 10^{34} \text{ cm}^{-2} \text{ s}^{-2}$) with design beam energy of 7 TeV, Lead-Proton and Lead-Lead collisions (design luminosity of $L_{PbPb} = 10^{27} \text{ cm}^{-2} \text{ s}^{-2}$) with designed a collision energy per colliding nucleon pair of $\sqrt{s_{NN}} = 5.52$ TeV. During the phase 2009-2013 (Run -1), the LHC has reached about half of its design energy and luminosity. In this thesis, the processed Pb-Pb collision data from Run-1 period, collected by the ALICE experiment has been used for the light front analysis.

The ALICE Experiment

ALICE experiment is at Point 2 of LHC ring. The data collected at ALICE from Pb-Pb collisions at $\sqrt{s_{NN}} = 2.76$ TeV is used for the analysis in this thesis. The main aim of the ALICE experimental setup includes the investigation of a possible deconfined quark-gluon state with the help of the data from the heavy-ion collisions as discussed in chapter 2. It also aims to study spectra and correlations between various particles and jets in the proton-proton, proton-nucleus, and nucleus-nucleus collisions. It has a very robust tracking and extensive particle Identification(PID) capabilities. There are many sub-detectors in the ALICE setup which are discussed in the following sections of this chapter. A Schematic diagram of the ALICE experiment is shown in figure 5.2.

THE ALICE DETECTOR

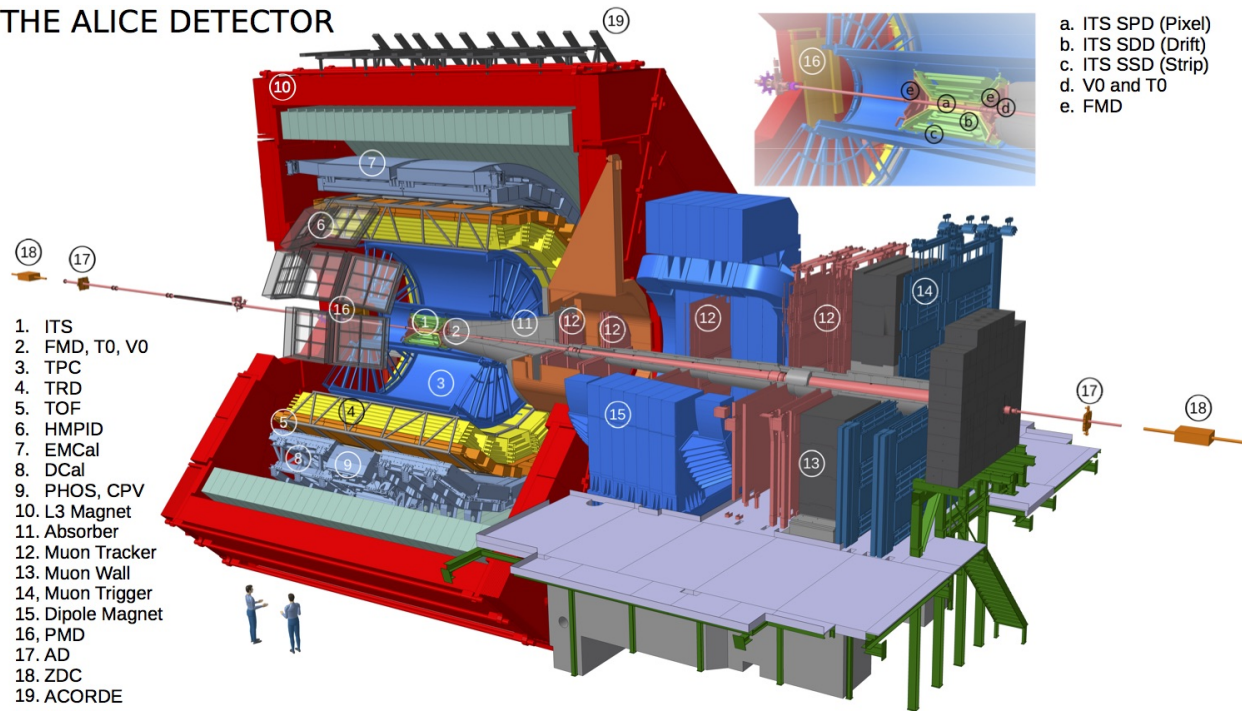


Figure 5.2: ALICE - A Large Ion Collider Experimental setup. The figure is taken from [105]

Detectors in ALICE

The ALICE detectors can be classified into three. Central Barrel Detectors which include ITS, TPC, TOF, TRD, EMCal, PHOS, HMPID, ACORDE. The forward Detectors such as include ZDC, FMD, V0, T0, PMD and the third category consist the Muon Detectors(Muon Spectrometer).

Inner Transition System (ITS)

The inner tracking system ([106], [107]) of the ALICE setup has six layers. It covers a pseudo-rapidity range of $|\eta| < 0.92$. The layout of the ITS assembly is shown in figure(5.3) The main objectives of ITS areas follows

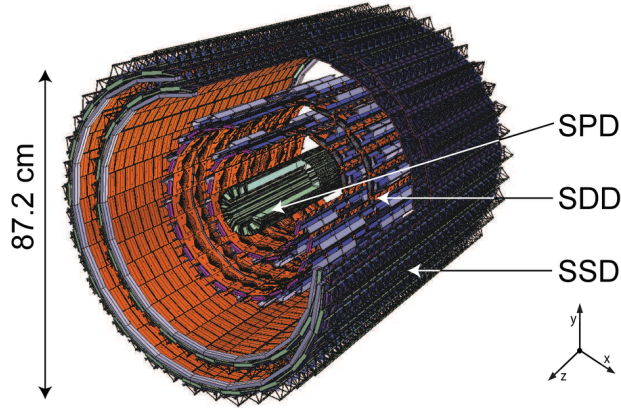


Figure 5.3: Layout of the Inner tracking system. The figure is taken from [107]

- Primary and secondary vertex reconstruction
- Measurement of impact parameter(the distance of closest approach of the track to the primary vertex) of the tracks. the distance of closest approach of the track to the primary vertex.
- Improvement of the momentum resolution for high momentum particles.
- Reconstruction of low momentum tracks which does not reach TPC at all.
- Particle-identification by measuring dE/dx of the tracks

The following three detectors constitute the ITS.

1. Silicon Pixel Detector (SPD)

The SPD forms the two innermost layers of ITS. The main functions for SPD are

- To determine the primary vertex position
- Measurement of impact parameter for secondary particles coming from weak decays.

The two layers of SPD are positioned at 3.9 and 7.6 cm from the interaction point (IP). The track density with which the SPD deals with can be as high as 50 tracks/cm². Hybrid silicon pixels made of reverse-biased silicon detector diodes is the basic element of SPD detector. Each diode detector is connected to a readout chip which forms an input to the SPD electronics readout cell. Depending on the signal from the detector diode in comparison with a pre-set threshold, a binary signal is produced which acts as the readout.

2. Silicon Drift Detector (SDD)

The SDD forms the two intermediate layers of ITS. The main functions for SDD are

- To determine the primary vertex position
- Provide two out of the four dE/dx samples needed for the particle identification with ITS

SDDs are made of very homogeneous high-resistivity Neutron Transmutation Doped (NTD) silicon and they have a sensitive area of $70.17(r\phi \times 75.26(z)) \text{ mm}^2$ and a total area of $72.50 \times 87.59 \text{ mm}^2$. The sensitive area consists of two drift regions, on each of which cathode strips fully deplete the detector volume and generate a drift field parallel to the wafer surface

3. Silicon Strip Detector (SSD)

The SSD forms the two outer layers of ITS. The main functions for SSD are

- To determine the primary vertex position
- Provide two out of the four dE/dx samples needed for the particle identification with ITS
- Provide 2D measurement of the track position and matching of tracks from ITS to TPC

Each detection module of SSD has one sensor each, each of which is connected to two hybrids with six HAL25 chips. Aluminium on polyimide cables are used for all the interconnections between the sensor and the electronics. It has a Sensor area of $75 \times 42 \text{ mm}^2$. Sensors are mounted with the strips which are parallel to the magnetic field of L3 magnet.

Particle Identification with ITS

Particle identification in ITS is done by dE/dx method. When charged particle pass through the ITS, it loses energy in the detector system. The detector response is parametrized for each species based on Bethe Bloch Formula is given below. The dE/dx as a function of momentum for proton-proton collisions at 7 TeV is shown in the following figure(5.4).Based on the value of dE/dx of the track, we can identify the particles using this method with ITS.

Time Projection Chamber (TPC)

The main detector used in the analysis is the Time projection Chamber (TPC) ([108],[109],[110]). TPC is the largest detector in the whole of the ALICE setup and it is the largest TPC ever used till now. It is the main tracking detector in the central barrel of ALICE experimental setup. The main objectives of TPC are

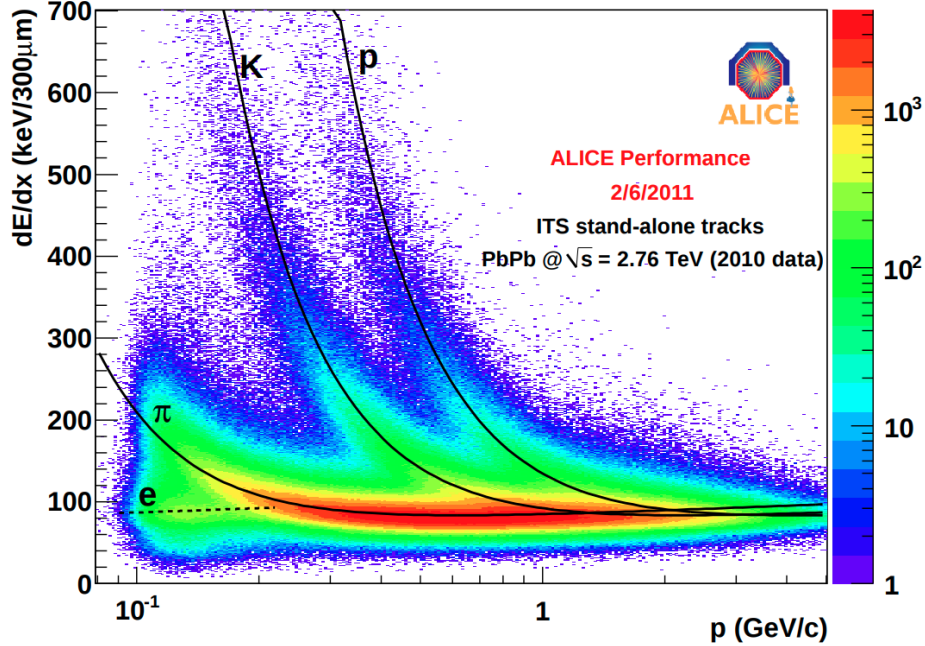


Figure 5.4: Specific energy-loss signal Vs momentum in Pb-Pb collisions for ITS standalone tracks measured with the ITS. The figure is taken from [106]

as follows

- Measurement of charged particle momentum.
- Particle identification using dE/dx method.
- Vertex determination of tracks.
- Provide data to generate a fast online High-Level Trigger (HLT) for the selection of low cross-section signals.

It covers a pseudo-rapidity range of $|\eta| < 0.9$ for full radial track length, and a transverse momentum range of $0.1 \leq p_T \leq 100$ GeV/c. The layout of the TPC detector is shown in figure(5.5) There are mainly two parts for the ALICE TPC. The field cage and the readout chambers. It was cylindrical in shape with an inner radius of 85 cm and out the radius of 247 cm with a length of 510 cm along the beam direction. TPC has an active volume of 88 m^3 and the volume is filled with a gaseous mixture of Neon(90 %) and CO_2 (10 %). The selection of this mixture has the following advantages.

- Provides a large drift velocity to the charges.
- Provides low diffusion coefficient
- Provides low multi scattering which essentially increases the spacial resolution.

The field cage is based on a design with a central high-voltage electrode and two opposite axial potential

Time Projection Chamber: ALICE

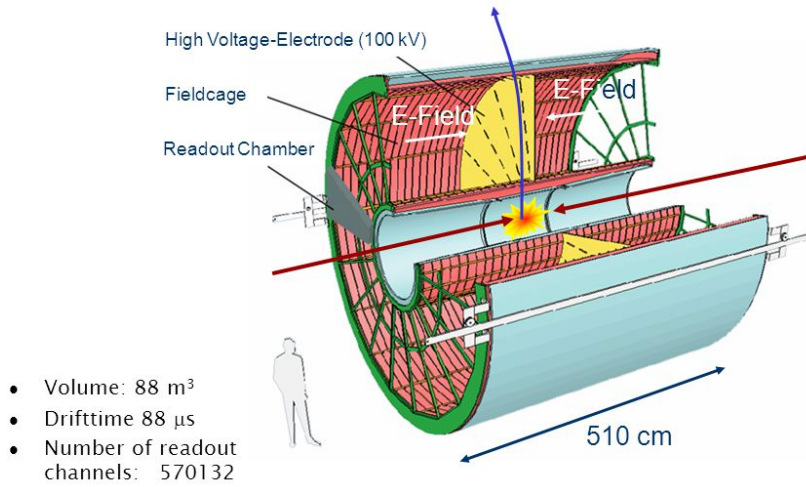


Figure 5.5: Layout of ALICE TPC. The Figure is taken from figure([108])

dividers which create a highly uniform electrostatic field in the common gas volume. Owing to the gas mixture used in the TPC, the field cage is operated at high voltage gradients(about 400 V/cm), with a high voltage of 100 kV at the central electrode, which results in a maximum drift time of about $90\mu s$. The read-out chamber is a multi-wire proportional chamber (MWPC). It has a segmented cathode pad readout which is mounted into 18 trapezoidal sectors of each end-plate. It allows a bi-dimensional measurement of the track. The third coordinate is obtained by measuring the drift time. The anode is supplied with a 1500 V positive voltage which will result in the amplification of the drift of electrons which are created by the ionization process. The readout chamber has an active area of $32.5m^2$ which is greater than the area of the endplates. The readout chambers are closed by a gating grid for electrons from drift region and ions from amplification region. Only a Level-1 trigger can open this gating $6.5\mu s$ after the collision for a period of about $90\mu s$. The laser calibration system in TPC will help in precise position inter-calibration. To have the thermal uniformity of 0.1 K in the TPC drift volume in the presence of thermal gradients, TPC has an extensive cooling system which consists of heat screens and circuits.

Working Principle and Particle Identification with TPC

The figure (5.6) shows a schematic illustration of the working principle of ALICE TPC. When a charged

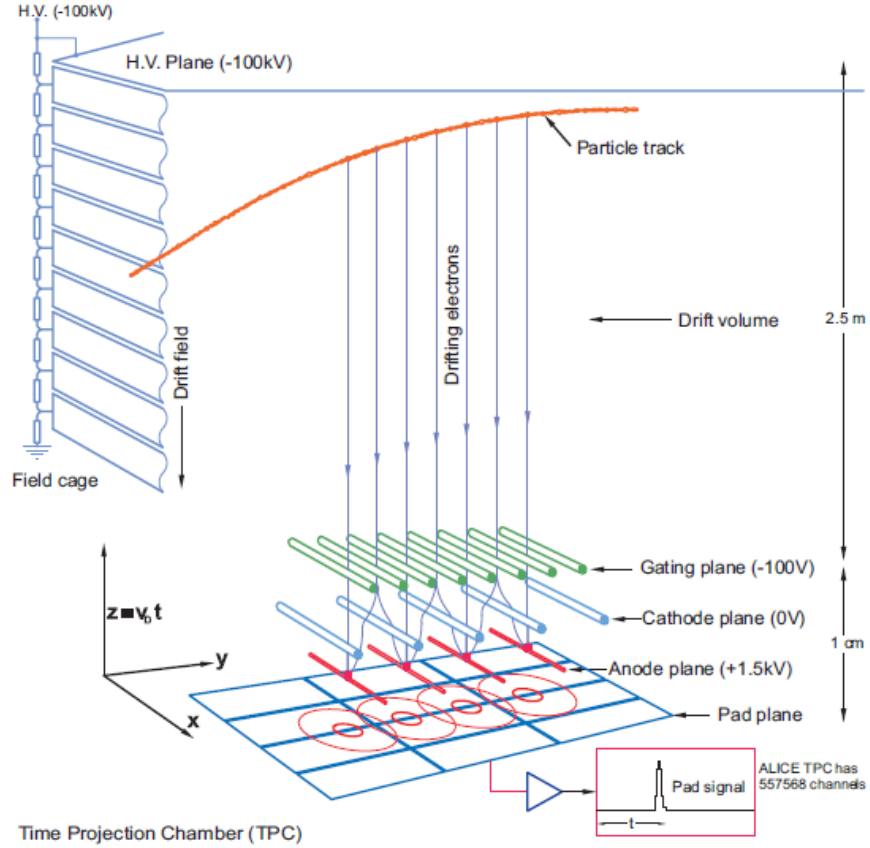


Figure 5.6: Schematic illustration of TPC and readout chambers. The figure is taken from [111]

particle passes through the TPC gas volume, it ionizes the gas molecules, creating electrons along its trajectory. Due to this, the particle will lose some energy while passing through the gas. This energy loss is different for different types of particles. The electrons coming from this ionization process are accelerated due to the magnetic field lines present and it drifts towards the anode. But in the meantime, it has to face several collisions with the molecules of the gas-causing discontinuous motion which microscopically appears as a constant drift. The drift velocity is given by

$$v_D = a\tau = \frac{eE}{m}\tau = \mu E \quad (5.1)$$

where e is the electron charge, m is the electron mass, τ the average time between collisions, E is the electric field, and μ is the mobility. But not all such electrons will reach the readout chamber as it can be attracted to molecules like O_2 . Due to the high positive voltage at the anode, the energy of the drifted electrons gets amplified and it will cause another ionization to happen there in the vicinity of anode wires leading to an

avalanche process. The generated signals at MWPC are proportional to the number of primary electrons and also the energy loss of the projectile. However, due to the avalanche process mentioned above, photons may be produced which might travel further than the longitudinal avalanche size, causing another avalanche. This will affect the above-mentioned proportionality that we want for the operation of the detector. But the quenching process that happens because of the gases present will reduce this effect to a minimum. The ions, on the other hand, drifts much slowly compared to the electrons owing to its heavier mass. The whole setup along with the gating facilitate a three-dimensional tracking of the particle. Whenever a good event is expected, the trigger system will produce triggers which will start the required measurements to begin. The z -component is calculated from the known drift velocity of the electron ($z = v_e \cdot \Delta t$) as mentioned before.

Bethe-Bloch Equation and Particle identification

When the charged particle passes through the gaseous chamber, ionization occurs as mentioned above. This ionization is a function of the particle velocity as well. Hence the particle mass or the type of the particle can be identified by measuring both the energy loss and the energy loss. The energy loss when charged particle travels through a medium is given by the Bethe-Bloch formula given below.

$$\left\langle \frac{dE}{dx} \right\rangle = \frac{4\pi N e^2 z^2}{mc^2 \beta^2} \left(\ln \frac{2mc^2 \beta^2 \gamma^2}{I^2} - \beta^2 - \frac{\delta(\beta)}{2} \right) \quad (5.2)$$

where,

mc^2 = rest energy of the electron

z = charge of the projectile

N = number density of electrons in the matter traversed

e = elementary charge

β = the velocity of the projectile

I = mean excitation energy of the atom.

$\delta(\beta)$ = A material-dependent correction term for "density effect" introduced by Fermi

For a given momentum, $\left\langle \frac{dE}{dx} \right\rangle$ is a function of only charge and mass of the particle . But above certain maximum transferred energy, the electrons δ reaches to an extent which will coast another ionization which does not correspond to the original transfer of the particle. So the above equation has to be modified to the

form given below, which holds good for all the electrons.

$$\left\langle \frac{dE}{dx} \right\rangle = \frac{4\pi N e^2 z^2}{m c^2 \beta^2} \left(\frac{1}{2} \ln \frac{2 m c^2 \beta^2 \gamma^2 E_{max}}{I^2} - \frac{\beta^2}{2} - \frac{\delta(\beta)}{2} \right) \quad (5.3)$$

with an approximate (for the particular case of TPC) statistical fluctuation around the mean given by the Landau distribution given by

$$f(\lambda) = \frac{1}{2\pi} \exp \left(-\frac{1}{2} (\lambda + \exp(-\lambda)) \right) \quad (5.4)$$

where,

$$\lambda = \frac{\Delta E - \Delta E_{MP}}{\langle \Delta E \rangle} \quad (5.5)$$

with E_{MP} being the most probable value.

Measurement of dE/dx signal by ALICE TPC

Figure (5.7) shows dE/dx of charged particles as a function their momentum, both measured by the TPC detector, in Pb–Pb collisions at 2.76 TeV. A very brief explanation of dE/dx measurement from ALICE TPC

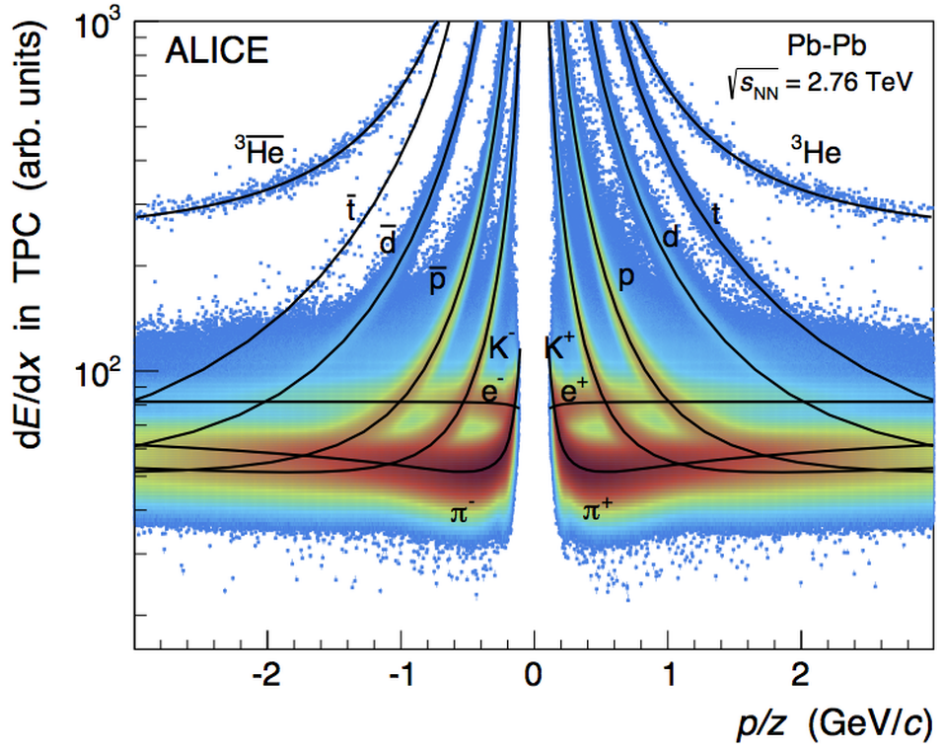


Figure 5.7: Specific energy-loss signal Vs rigidity in Pb-Pb collisions as measured by ALICE TPC. The figure is taken from [112]

on a step by step basis is as follows.

* Clusterization: A charged particle traversing the TPC induces a signal on a given pad-row. If the charge in a search window of 5 pads in wire direction and 5 bins in time direction exceeds a certain threshold and succeeds all quality criteria, it is called a cluster. The raw signals on neighboring pads and time-bins originating from an individual charged particle are combined to find a cluster. Number of clusters may be written as n_{cl} .

* Total cluster charge (Q_{tot}) is the sum of all digits in a cluster. It corresponds to the energy deposit of a track on a given pad-row. (Q_{Max}) represents the maximum value among all digits in a cluster. These are calculated next.

* The clusters thus are connected to build tracks using a Kalman filter approach in the next step. (There are five track parameters considered in this approach). The Kalman filter minimizes the track-to-cluster residuals in a pad and drifts direction. The χ^2/n_{cl} tells us the the quality of the fit. It is defined as,

$$\chi^2/n_{cl} = \frac{1}{n_{cl}} \sum_{i=0}^{n_{cl}} \frac{(y_{i,clus} - y_{i,track})^2}{\sigma_{i,y}^2} + \frac{(z_{i,clus} - z_{i,track})^2}{\sigma_{i,z}^2} \quad (5.6)$$

where σ_y and σ_z are the space point resolution in pad and drift direction * The dE/dx information for a given track is extracted from the clusters for PID. Not all clusters are used for this purpose though. The clusters close to the chamber boundaries are rejected. In Pb-Pb events, the dE/dx calculation is based on the maximum charge Q_{max} . We have a long tail in the distribution of energy loss. This will not allow us to comfortably take the average of the distribution as the mean energy loss. So a truncated mean method is used for TPC.

* The truncated mean is defined as

$$S^\alpha = \frac{1}{m} \sum_{i=0}^m Q_i \quad (5.7)$$

where $i = 0, \dots, n_{pid} + n_{miss}$. α is chosen as 0.6 for ALICE TPC and $S^{\alpha=0.6}$ is known as dE/dx signal for ALICE TPC which is used for particle identification. The variance of the $S^{\alpha=0.6}$ distribution gives the resolution of dE/dx for ALICE TPC.

* Once we have a precise calibration of the dE/dx signal, we need to parametrize dE/dx vs $\beta\gamma$. Then the response of all the particles can be calculated from the scaling given by

$$p/z = \beta\gamma \cdot m/z \quad (5.8)$$

In ALICE, we use the same parametrization from ALEPH experiment which is given as

$$f(\beta\gamma) = \frac{P_1}{\beta^{P_4}} \left(P_2 - \beta^{P_4} - \ln\left(P_3 + \frac{1}{(\beta\gamma)^{P_5}}\right) \right) \quad (5.9)$$

* The quantity $(\frac{dE}{dx})_{measured} - (\frac{dE}{dx})_{fit}$ is calculated and it is used in the relation between the $\sigma_{\frac{dE}{dx}}$ for a given number of clusters used for the PID for the particular track. If a cut like $n\sigma = 3$ is applied, we can identify the particles over a wide range of momentum. But the contamination from the misidentified species will directly affect the results in this approach. A particle identification based on TPC $n\sigma$ method was used in the analysis presented in the next chapter of this thesis.

Time Of Flight (TOF)

The main purposes of the TOF detector [113] are to track and identify particles together with ITS and TPC detectors. It covers the central pseudorapidity region of $|\eta| < 0.9$ and covers a cylindrical surface of polar acceptance $|\phi - 90^\circ| < 45^\circ$. A schematic layout of one of the 18 TOF super modules inside the ALICE space frame is shown in Figure(5.8) It has 18 sectors in ϕ direction and 5 in the z-direction. These modules are kept

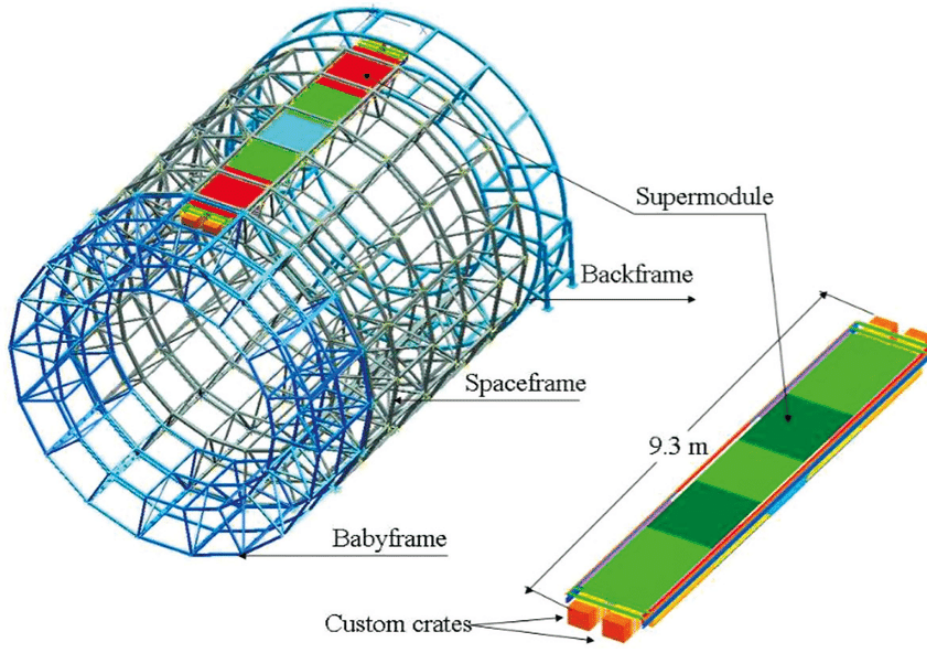


Figure 5.8: Schematic layout of one of the 18 TOF super modules inside the ALICE space frame. The figure is taken from [114]

in a cylindrical shell of inner radius 370 cm and outer radius 399 cm. Each basic unit is a Multi-gap Resistive Plate Chamber (MRPC) with 123 cm length and 13 cm width as shown in the figure. The MRPC strips are placed inside gas-tight modules positioned transversely to the beam direction. The full gaseous chamber of the detector has a uniform magnetic field. So the ionisation produced by the charged particle traversing will immediately produce signals on the pickup electrodes by starting an avalanche. Every module of the TOF detector consists of 15 MRPC strips in the central, 19 in the intermediate and the external modules and the complete TOF system consists of 90 such modules. It provides a good electron-kaon separation up to a track momentum $p_T \approx 2.5$ GeV/c and electron-proton separation up to $p_T \approx 4$ GeV/c. Once we know the flight time and momenta of the particle, we can identify them. The difference in flight time for two particles with the same momenta p and masses m_1 and m_2 is given as

$$\Delta t = \frac{Lc}{2p^2} (m_1^2 - m_2^2) \quad (5.10)$$

Figure(5.9) shows the measurement of the velocity of different particle species as a function of charged particle momentum with the TOF detector for Pb-Pb collisions at ALICE.

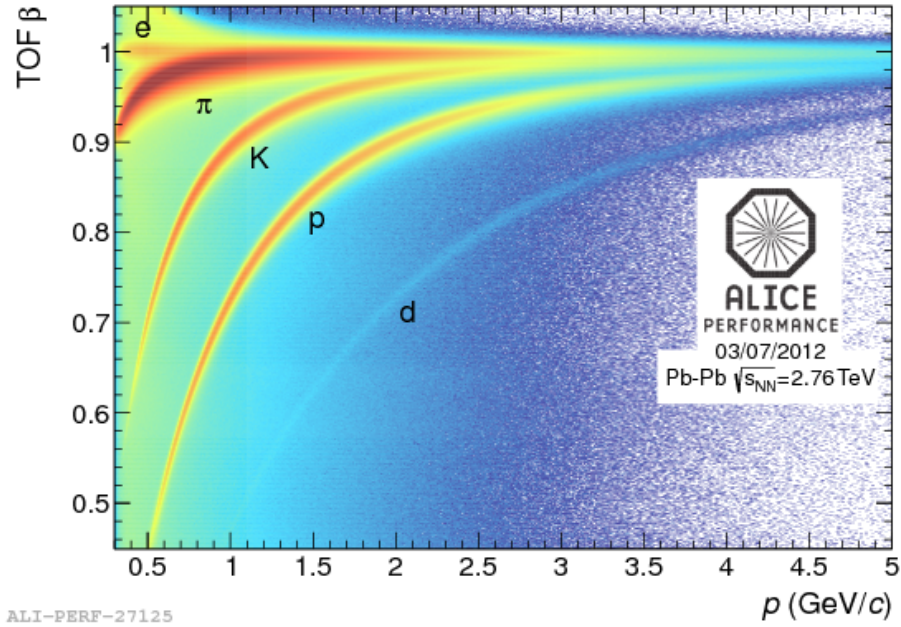


Figure 5.9: β Vs Momentum of particle tracks as measured by TOF. Figure is taken from [115]

Transition Radiation detector (TRD)

The main objective of the TRD detector in ALICE ([116]) is to identify the electrons in the central barrel for momenta greater than 1 GeV/c. The transition radiation emitted when the electrons traverse through radiator can be used together with the specific energy loss in a particular gas mixture for the identification of electron and rejection of pions. TRD has 540 detector readout modules which are arranged into 30 super modules which are arranged in five stacks along the z -axis. Each of the TRD detector element consists of a carbon fibre laminated Rohacell/polypropylene fibre sandwich radiator, a drift section, and a multi-wire proportional chamber section (7 mm) with pad readout. The pad planes are supported by a honeycomb carbon fibre sandwich back panel. The entire readout electronics is directly mounted on the back panel of the detector.

PHOton Spectrometer (PHOS)

The main objectives of the PHOS detector ([117]) include the investigation of thermal and dynamic properties of the initial phase of the collision using low p_T direct photon measurement, a study of jet quenching via the measurement of π^0 at high p_T and *gamma*-jet correlations. The PHOS detector is a single-arm, high granularity, very high resolution, highly segmented electromagnetic calorimeter associate with a Charge Particle Veto(CPV) detector. It is divided into five PHOS + CPV subunits called PHOS modules and it is positioned at the bottom of the ALICE detector at a distance of about 460 cm from the IP. It covers a pseudorapidity of $|\eta| < 0.12$ and an azimuthal acceptance of 100° . Every of the PHOS modules is segmented into 3584 detection cells arranged in 56 rows of 64 cells. The detection cell consists of a $22 \times 22 \times 180 \text{mm}^3$ lead-tungstate crystal, PbWO_4 (PWO), coupled to a $5 \times 5 \text{mm}^2$ Avalanche Photo-Diode (APD) followed by a pre-amplifier. The crystals are arranged in strips having two rows of eight cells and 16 analogue signals from a single strip is fed to the electronics.

Charged Particle Veto detector (CPV): It is a Multi-Wire Proportional Chamber (MWPC) with cathode pad readout([118]). Its efficiency to detect the charged particles is above 99%. It is placed over the PHOS modules at a distance of 5 mm. The active volume of CPV is filled with a gas mixture containing 80% of Ar and 20% of CO_2 at a pressure of about 1 bar. The cathode plane is segmented into 7168 pads and the total area of the CPV module is about 1.88m^2

Electromagnetic Calorimeter (EMCal)

The main aims of EMcal detector [119] at ALICE are to study jet quenching, measuring direct photons, electrons from heavy-flavour decays etc. It is located near to the magnetic coil at a radius of 4.5 m and covers a pseudo-rapidity range of $|\eta| < 0.7$ with an azimuthal acceptance of $\Delta\phi = 107^\circ$. The EMCAL is a Pb-scintillator sampling calorimeter with cylindrical geometry. The cell size of the EMCAL is approximately 0.014×0.014 rad in $\Delta\phi - \Delta\eta$ space. When a particle passes through the detector, it produces electromagnetic showers. These showers are then used to discriminate among electromagnetic and hadronic probes. While electrons and photons deposit their total energy in the detector, hadrons deposit a small fraction of its energy. The EmCal detector is also used as a trigger detector and can be used to provide Level-0 and Level-1 triggers for jets, photons and electrons.

High-Momentum Particle Identification Detector (HMPID)

HMPID is a dedicated detector ([120]) in ALICE. It is meant to identify hadrons with a $p_T > 1$ GeV/c. It is a single-arm array with about 5% of central barrel phase space as its acceptance. It uses proximity-focusing Ring Image Cherenkov (RICH) counters. There are seven modules of such counters mounted on a cradle which is fixed to a space frame. The radiator in the RICH is a 15 mm thick layer of low chromaticity fluoro hexane (C_6F_{14}) liquid with an index of refraction of $n = 1.2989$ at $\lambda = 175$ nm corresponding to $\beta_{min} = 0.77$. When the charge particles transverse through the radiator with a velocity greater than that of light in the medium, it emits Cherenkov photons which are then detected by the photon counter. The photon counter here, consists of a CsI deposited onto the pad cathode of a Multi-Wire Pad Chamber (MWPC). This whole system is one of the largest implemented application of this technique.

ALICE Cosmic Ray Detector (ACORDE)

ACORDE ([121]) is an array of plastic scintillator counters placed on the upper surface of the L3 magnet to provide a Level-0 trigger to the CTP for calibration of ITS, TPC, TOF and HMPID. It also detects atmospheric muons together with TPC, TRD, and TOF detectors. Each of the scintillator counters has an effective area of 190×20 cm² effective area. Each module has two scintillator counters and there are 60 such modules, which is placed over the ALICE magnet.

Muon spectrometer

The prime motive of the muon spectrometer in ALICE ([122]) is to measure the heavy-quark vector-mesons resonances ($J/\psi, \psi', \Upsilon, \Upsilon', \Upsilon''$) and ϕ mesons through $\mu^+\mu^-$ decay channel. This kind of a measurement of all the quarkonia states with a single apparatus will help us in understanding the difference in their production rate as a function of centrality and transverse momentum. It covers a pseudo-rapidity range of $-4.0 \leq \eta \leq -2.5$. It consists of the following parts.

- A passive Front Absorber: It absorbs hadrons and photons from the interaction Point.
- High-granularity tracking system: They are designed to have a spatial resolution of about 100 mm and to operate at the maximum hit density of about 5×10^{-2} as expected in central Pb-Pb collisions, and covers a total area of about 100 m².
- A dipole magnet
- A passive muon filter wall
- Four planes of trigger chambers
- Inner beam shield

It protects the chambers from primary and secondary particles produced at large rapidity ranges.

Photon Multiplicity Detector (PMD)

There is a very large particle multiplicity in the forward region. So the calorimetric methods for measuring the photons are not feasible. The spatial distribution of the photon in the $\eta - \phi$ space and also its multiplicity in the forward pseudorapidity region ($2.3 \leq \eta \leq 3.7$) is measured by the photon multiplicity detector (PMD) using a pre-shower method ([123]). It can be also used to estimate the transverse electromagnetic energy and event plane of the events. The PMD has a three radiation length thick converter made of lead (1.5 cm thick) with a 0.5 cm thick steel backing. This is sandwiched in between highly granular gas proportional counters. The signal from the detector plane placed in front of the converter is then used as a charged particle veto and the signal from the second detector plane is used for the identification of photon. It is worth to mention that PMD was removed from the experimental setup during the upgrade for RUN 3.

Zero Degree Calorimeter (ZDC)

The number of participating nucleons in nucleus-nucleus collisions in ALICE is measured by ZDC detector ([124]). This observable is related to the geometry of the collision and it is estimated by measuring the energy

carried by the non-interacting nucleons in the forward direction. If all the spectators are detected, then the number of participants can be calculated as

$$E_{ZDC}(\text{in TeV}) = 2.76 \times N_{Spectator}$$

$$N_{Participants} = A - N_{Spectator}$$

2.76 TeV is the energy per nucleon of the Pb beam at the LHC for Pb-Pb collisions during Run 1 of LHC (2010) and A is the atomic number of the colliding nuclei. (Although it is not completely valid in a collider as not all the spectator nucleons can be detected). Since ZDC is a position sensitive device, it can as well estimate the reaction plane in nuclear collisions.

Forward Multiplicity Detector (FMD)

The FMD detector ([125]) provides the charged particle multiplicity information for the pseudo-rapidity range of $-3.4 \leq \eta \leq -1.7$ and $1.7 \leq \eta \leq 5.0$. There is an overlap region between ITS inner pixel layer and FMD silicon rings which provides redundancy and ensures continuous coverage of vertex distribution along the beam axis. It also can be used to study multiplicity fluctuations on an event by event basis, owing to its high radial segmentation. It also can be used to determine the reaction plane on an event by event basis due to its high azimuthal angle segmentation. FMD has three separate rings FMD1, FMD2, FMD3 each having 10 or 20 (inner and outer rings) silicon sensors and are located on either side of the ITS detector. FMD2 and FMD3 are positioned to have approximately the same acceptance, while FMD1 is placed away from the IP to extend the multiplicity coverage of charged particles.

VZERO Detector (V0)

The V0 detector ([125]) is a small angle detector consisting of two arrays of scintillator counters, called V0A and V0C, which are installed on either side of the interaction point(IP). Each channel of both arrays is made of a BC404 plastic scintillator from Bicorn with a thickness of 2.5 and 2.0 cm for VZERO-A and VZERO-C respectively. Its functions include providing minimum-bias triggers for the central barrel detectors in proton-proton and nucleus-nucleus collisions. The triggers are produced by the particles from the initial collision and the secondary interactions. The number of particles registered at V0 and the number of primary particles produced is in monotone. This enables one to use V0 used as an estimating machine of the centrality of the collisions through the corresponding multiplicity ([126]). There are three centrality triggers generated by the V0 depending on the number of fired scintillators and total charge. They are the central, semi-central and

multiplicity triggers. In figure 5.10, the summed amplitude of signals from V0 is shown. It is fitted with the Glauber model estimation. The vertical lines separate the centrality classes corresponding from most central to 80% of hadronic collisions. Hence, from the V0 amplitudes for a given event, we get the centrality class in which the event belongs to. V0 detector is also used in the measurement of luminosity in pp collisions.

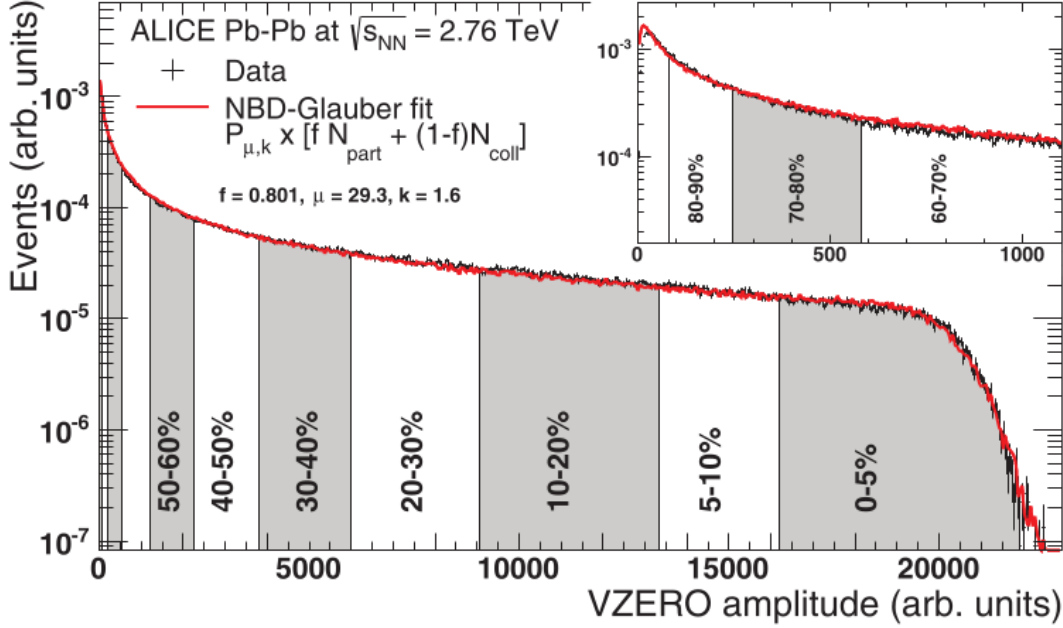


Figure 5.10: Distribution of the summed amplitudes in V0 fitted with Glauber model (red curve).[126]

TZERO Detector (T0)

The T0 detector consists of two Cherenkov counter arrays ([125]). Each array consist of 12 counters and each counter is made with fine-mesh photomultiplier tube PMT-187, 30 mm in diameter, 45 mm long. The two arrays T0-A and T0-C are placed on either side of the interaction point (IP). The T0 detector generates a start time signal for the Time Of Flight(TOF) detector which always corresponds to a real collision with a pre-set time delay. It also has to generate a signal for the Transition Radiation Detector(TRD) and g functions as a minimum bias trigger generator. More about the triggering functions of T0 can be seen in [127]. In the following chapter, we will see the light front analysis of the ALICE data using the frameworks such as ROOT, ALIROOT and its methodologies [128].

Chapter 6

Analysis of the Pb-Pb collisions at $\sqrt{s} = 2.76$ TeV in ALICE

In this chapter, we see the details of the light front analysis performed using the data from the Pb-Pb collisions at $\sqrt{s} = 2.76$ TeV in ALICE at LHC. The raw distributions of charged particles were made for several centrality ranges of the collisions after identifying the particles for the relevant transverse momentum ranges for each species. The Monte Carlo based corrections for the detector acceptance and efficiencies were applied to it and corrected distributions were used for the study of signatures of thermalisation in the data using the light front scheme as discussed in the previous chapters.

Light Front Analysis of the ALICE Data

The entire process of analysis consists of the following steps.

- We select the appropriate data sets (run numbers) from the ALICE experiment.
- Select the appropriate versions of the Analysis Frameworks (see below).
- Select the analysable events from the list of events and classify them into 6 centrality bins.
- Make the appropriate track selection criterion and cuts.
- Identify the particle species of the track which passes the cuts.
- Make kinematic cuts as per the identified particle species.
- Make the light front distributions using the above tracks for each particle species for each centrality region.
- Using the Monte Carlo simulated events, estimate the correction factors for the raw distributions for tracking, acceptance, particle identification etc.
- Perform the lightfront analysis as discussed in the previous chapters over the corrected distributions.
- Find a critical value of the light front variable ($\tilde{\zeta}^{\pm}$) which gives the same temperature within the errors

from the ζ , p_T^2 , and $\cos(\theta)$ distributions.

- Make a study of the centrality and mass dependence of the extracted temperatures to reach the conclusions.

Let us now go through each of these steps in details.

ALICE Data set and Analysis Framework

The data sample consists of the runs of the LHC10h-pass2 period marked as good in the Run Condition Table (RCT) [129]. ESD (Event Summary Data) files contain full information about events, AOD(Analysis Only Data) files contain a subset of information that has been selected for physics analysis. There exist several *passes* for a given data set which means that the data has been reconstructed more than once. The Monte Carlo sample consists of the related anchor runs on LHC11a10a-bis production (B). The anchored MC runs are Monte Carlo events simulated mimicking the actual run conditions of a specific real experimental run. For the Monte Carlo calculation of correction factors, the AOD162 production is used from the LHC11a10a-bis MC data set. The production set AOD160 is used for the real data analysis in this thesis. The ALICE Software consists of ROOT, AliROOT, AliPhysics etc [128]. The version which was used for the plots in this chapter is AliPhysics version: vAN-20191125-1.

Trigger and Event Selections

Approximately 1.45×10^7 minimum-bias Pb-Pb events with a reconstructed primary vertex within 10 cm from the nominal interaction point in the beam direction are used for this analysis. The trigger logic requires a combination of the following conditions:

- At least 2 chips hit in the outer layer of the SPD
- A signal in the VZERO, Aside (V0A)
- A signal in the VZERO, C side (V0C)

According to the period, the trigger implementation requires at least 2 out of 3 of the above conditions.

More information can be seen in [130].

Track Selection and cuts

The following common criterion was considered for the selection of a track. At least one hit in one of the two SPD layers is needed for the track to be selected. At least 70 active TPC clusters and a $\chi^2/\text{number of cluster} < 4$ in the TPC was required. (See Chapter 5 for more details 5.3). In addition to this, a p_T dependent cut on the transverse distance of closest approach (DCA_{xy}), set to be at 7 standard deviations (DCA_{xy}

$< 7 \times (2.6 + 5.0/p_T^{1.01}) \times 10^3$) and a 2 cm cut on the longitudinal distance of closest approach $DCAz < 2\text{cm}$ were applied. The cuts and selections we just discussed are incorporated in the filter number 32 for ALICE which is used as a global track cut measure in this analysis([128], [131]). The kinematic cuts applied for the different particle species are summarized in Table 6.1.

| Particle | p_T Range(GeV) | η Range |
|--------------|------------------|----------------|
| π^\pm | 0.20 to 0.60 | $ \eta < 0.8$ |
| K^\pm | 0.25 to 0.40 | $ \eta < 0.8$ |
| $p(\bar{p})$ | 0.45 to 0.80 | $ \eta < 0.8$ |

Table 6.1: p_T and η ranges for the identified particle species

Particle Identification Scheme using TPC - Raw data distributions

In the analysis discussed in this thesis, ALICE TPC is used for the identification of particles (See section 5.3 for more details). The PID approach in this analysis is called $n\sigma$ method. The number of σ is parametrized as a function of the number of clusters, to reduce the dependence from Monte Carlo. *Number of Sigmas is the deviation of the measured energy loss to the expected energy loss of a certain particle expressed in terms of the detector resolution.* It can be expressed as follows [134]

$$n\sigma(\text{particle}) = \frac{\langle \frac{dE}{dx} \rangle (\text{measured}) - \langle \frac{dE}{dx} \rangle (\text{spline, particle})}{n\sigma(\frac{dE}{dx})(PIDClusters, \frac{dE}{dx}, \eta)} \quad (6.1)$$

The method is used in the p_T region of clear separation between the species for identification. The $n\sigma$ approach is directly identifying the particle in a track by track manner. Each of the tracks stored in the data has the information about the $n\sigma$ value of a track for a given species. For each track which comes from the selected events and those which survives all the track cuts, the $n\sigma_{TPC}(\text{Species})$ is calculated. If the value $|n\sigma(\text{species})_{TPC}|$ less than or equal to 3.0, we take it as that specific species. If the value of $|n\sigma(\text{species})_{TPC}|$ is less than 3.0 for more than one track, the species with the lowest value will be assigned. The energy loss dE/dx vs TPC Momentum, for the selection of particles used in the analysis described in this chapter, are shown in figure 6.1.

Raw data distributions: After the proper identification of the track, corresponding distributions of light front variable ζ is made first. The p_T^2 and $\cos(\theta)$ distributions are made after fitting the corrected ζ distribution with equation 3.40 and making an estimation about the value of $\tilde{\zeta}$ as described in the previous chapters. The process of estimation of the correction factors as used in this thesis is described in the next section.

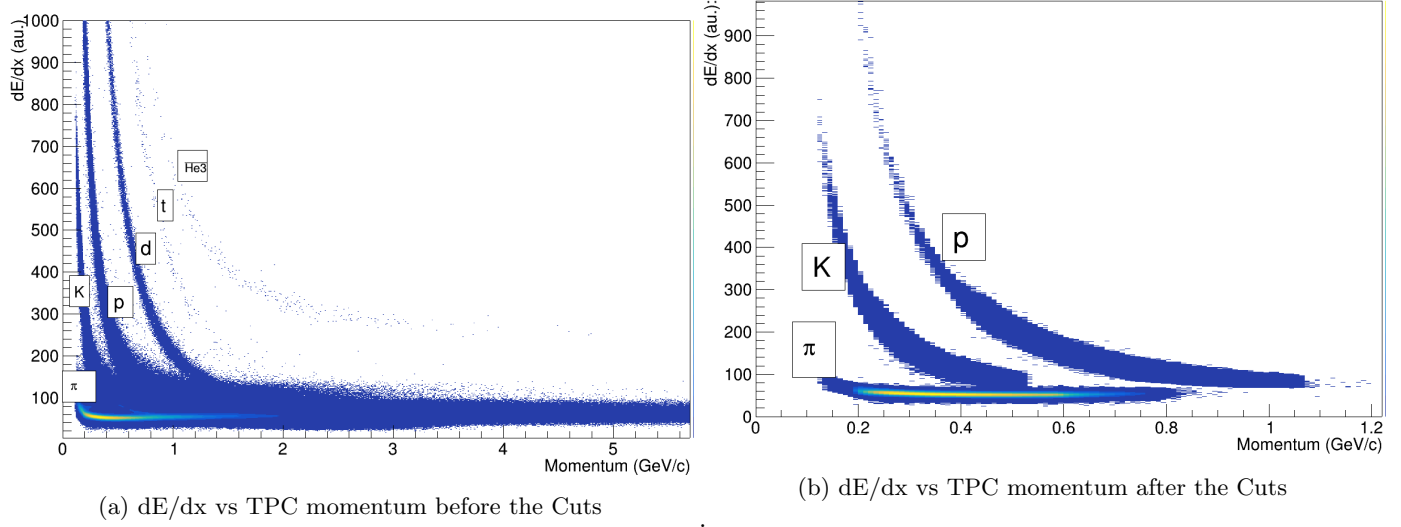


Figure 6.1: dE/dx vs TPC Momentum

Estimation of Correction factor using Monte Carlo

To get any meaningful results from the interpretation of the data, we need to correct the raw data distributions for the effects caused by the detector acceptance and efficiencies of tracking, identification and contamination. The ALICE detector geometry is simulated using Geant ([135], [136]) and the generated Monte Carlo particles are allowed passed through the simulated detector geometry. Then it is made to pass through the exact event and track cuts and identification scheme as in the real data. Such a set of tracks which survives the filter is called "a reconstructed track". Then in terms of these groups of tracks, the efficiency for a species i may be defined as

$$\epsilon_i = \frac{\text{Number of Reconstructed and Correctly identified Primary Particles of Species } i}{\text{Number Of Generated Primary Particles of Species } i} \quad (6.2)$$

Correcting the raw spectrum using this efficiency will take care of the effects in the raw distribution coming from the acceptance of the detector, tracking process, and particle identification. We also need to take into account the contamination of one species by the other. For a given species i , the contamination m_i is defined as,

$$m_i = \frac{\text{Number of Reconstructed and Wrongly identified Primary Particles of Species } i}{\text{Number Of Generated Primary Particles of Species } i} \quad (6.3)$$

Wrong identification here implies the following. A particle species was generated by the MC generator as species i . It was passed through the filter and was identified by the PID scheme as species j ($\neq i$). The Monte Carlo generated tracks has labels associated with it. This means that we have a specific number associated with each generated track, which stays even after the track passes through the detector geometry simulated using Geant 3. If we take a track after it passes through the filter and look at its label, we can trace the originally generated track corresponding to this "survived track". This means that if our PID scheme identifies a generated track of species i as j , we can get to know that our PID scheme did so using the information from the labels. So can have a count of such a wrong identification amounting to contamination in the final distributions. Now the final correction factor C_i can be defined for a species as

$$C_i = \frac{1 - m_i}{\epsilon_i} \quad (6.4)$$

In this way using the MC data mentioned in the previous section, the correction factor for each of the raw distributions were estimated and implemented to make the final corrected distributions presented in the following sections of this chapter. Before going into it, let us see the treatment of the systematic errors in this analysis.

Systematic errors

Systematic errors are reproducible uncertainties consistently appearing mainly in the same direction in measurement due to any imperfections in the instrument used for it, calibration of the device, or due to a particular technique used for the measurement. In our case, these effects can come from the particular selection of event (or track) reconstruction and cuts, the technique used for the estimation of efficiencies etc. we made, taking into account the capabilities of the ALICE apparatus. To evaluate the systematic uncertainties, we identified the sources of such errors in our measurement and estimate them by repeating the entire analysis several times while independently varying the selection criteria. The results given by this variation are then compared to that of the default criteria of our analysis. If the evaluated systematic error does not show any significant functional dependence on the observable under consideration, it would mean that introducing them into the final plots and making a fit with analytic expressions will only change the normalisation constant. In the sources we considered for the estimation of systematic uncertainties in our measurement, we do not see such a significant dependence of the evaluated uncertainty as a function of the variable under consideration. As the shape of the distributions we studied using the light front variable

technique was of prime interest in our analysis, we used the statistical errors in fitting the distributions under consideration with relevant equations. The sources of systematic uncertainties we considered are the following:

- **Centrality Estimator:** The default centrality measurement is based on the average multiplicity at V0A and V0C. To estimate the systematic effects from this selection, we change the estimator to V0A alone, V0C alone and TPC. The maximum observed spread from the default analysis assigned as the systematic error from this source.
- **Magnetic field polarity:** The solenoid magnet of ALICE can operate in positive and negative polarity. The direction of the curvature of the charged particles and the material of the detector itself is subjected to the polarity of the magnetic field. The data set we considered has events from both polarity conditions of the magnet. To evaluate the effect of the magnetic field polarity on the measurements of the light front variable based distributions, the entire analysis has been repeated using only runs with the positive or negative magnetic field. The maximum variation from the positive polarity measurement was assigned as the systematic error in this case.
- **Vertex cut:** The z-component of the primary vertex of an event must be within 10 cm ($10 < |v_Z|$) for it to be an analysable event. To estimate the systematic uncertainty from this selection, the following variations, $10 < |v_Z| < 0 \text{ cm}$ and $0 < |v_Z| < 10 \text{ cm}$ were made on the Z-vertex cut and the entire analysis has been repeated. The maximum spread among the results from the default case ($10 < |v_Z|$) was assigned as the systematic error in the analysis coming from the default cut on v_Z .
- **Track cuts:** The systematic effects related to the track quality cuts were studied by varying the track cuts. The number of clusters required was varied between 70 to 100 and analysis was repeated. Also, the analysis has been repeated using those tracks reconstructed by using the information from TPC alone (ALICE Filterbit 1, 128) [131]. The maximum spread from the default analysis (ALICE Filterbit 32, see the section on track cuts) and was estimated for each species at each centrality and was assigned as the systematic error from the track cuts.
- **PID:** To estimate uncertainty related to the PID procedure, the cut around $|n\sigma_{species}|$ was varied between 1 and 5. This kind of estimation includes effects related to the contamination from other species, uncertainties in the Bethe-Bloch parametrization(See Chapter 5) etc. The maximum variation of the measured values from that of the default case ($|n\sigma_{species}| = 3$) was estimated and assigned as the systematic error the PID procedure for various species at various centralities.

The summary of the systematic errors obtained from various sources for the distributions we study in our

light front analysis from the above-mentioned procedures are summarized in the tables 6.2, 6.3 and 6.4. Now let us see the main analysis strategy implemented in our analysis of the data and see the resulting distributions from it for each particle species at various regions of centrality.

| Source | π^\pm | K^\pm | $p(\bar{p})$ |
|----------------------|-----------|---------|--------------|
| Centrality Estimator | < 1% | < 1% | < 1% |
| v_Z selection | < 1% | < 1% | < 1% |
| Magnetic Field | < 1% | < 1% | < 1% |
| Tracking | 3.8% | 3.5% | 2.5% |
| PID | 2.7% | 3.8% | 1.8% |

Table 6.2: Systematic errors for ζ distribution.

| Source | π^\pm | K^\pm | $p(\bar{p})$ |
|----------------------|-----------|---------|--------------|
| Centrality Estimator | < 1% | < 1% | < 1% |
| v_Z selection | < 1% | < 1% | < 1% |
| Magnetic Field | < 1% | < 1% | < 1% |
| Tracking | 3.5% | 3.0% | 2.7% |
| PID | 3.1% | 3.2% | 1.8% |

Table 6.3: Systematic errors for p_T^2 distribution.

| Source | π^\pm | K^\pm | $p(\bar{p})$ |
|----------------------|-----------|---------|--------------|
| Centrality Estimator | < 1% | < 1% | < 1% |
| v_Z selection | < 1% | < 1% | < 1% |
| Magnetic Field | < 1% | < 1% | < 1% |
| Tracking | 3.0% | 3.2% | 1.5% |
| PID | 2.3% | 2.0% | 1.5% |

Table 6.4: Systematic errors for $\cos(\theta)$ distribution.

Basic Analysis Strategy & Resulting Plots

The basic analysis strategy is the same as in the case of HIJING analysis with the kinematic cuts. However, we need to take into account the correction factors here. The raw ζ distributions for each particle species for each centrality is made first. Then the correction factors corresponding to this variable is applied to the raw distribution and we obtain a corrected plot on which we fit equation 3.40 taking into account the p_T and η cuts. From this we obtain a $\tilde{\zeta}$ for each case and for this value of ζ , we make p_T^2 and $\cos(\theta)$ raw distributions. Then the resulting plots are corrected using the correction factors and are made to fit with 3.44 and 3.43 respectively. In all these calculations, the energy distribution $f(E)$ was assumed to be of the form as in

equation (3.42). The whole procedure is repeated for each particle species for each region of the centrality till we get the same temperatures within errors from all the three distributions (that would mean that we are searching for the existence of a possible $\tilde{\zeta}$ which gives the same temperature within the errors for the three distributions). The resulting plots we obtained from ALICE data are shown in the next section for each particle species. Let us have a close look at them now. **The green curve in the $|\zeta|$ distribution is the extrapolation of the fit curve in the region: $\zeta < \tilde{\zeta}$.** A flow chart of the above mentioned scheme is shown in Figure 6.2.

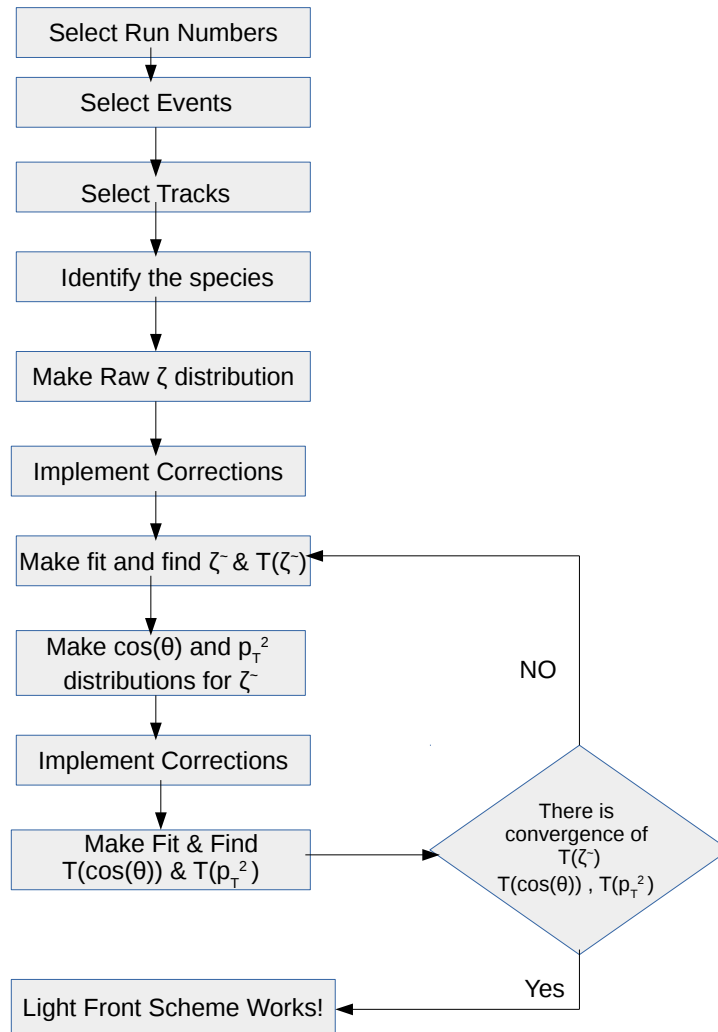
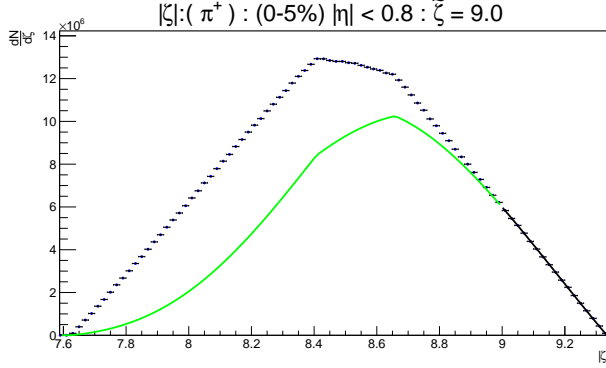
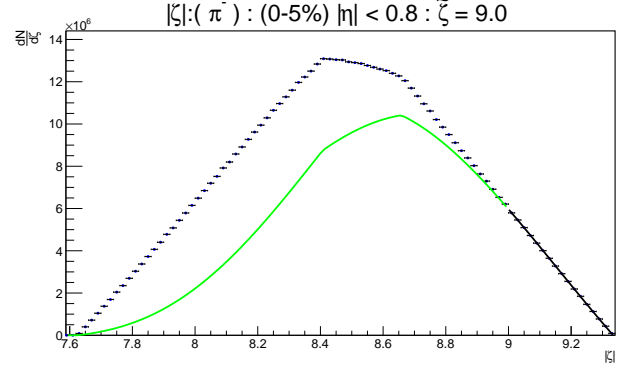


Figure 6.2: Flow chart of the light front analysis Scheme

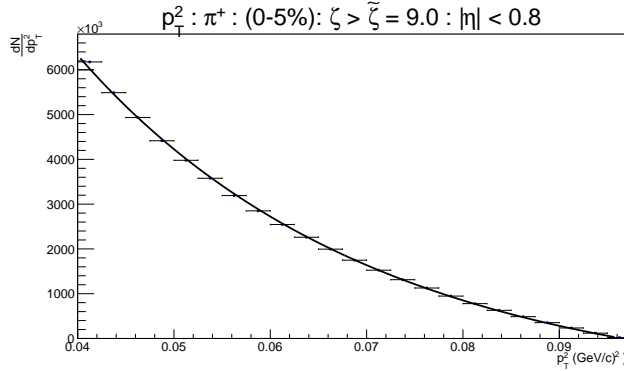
Pions (0-5 %)



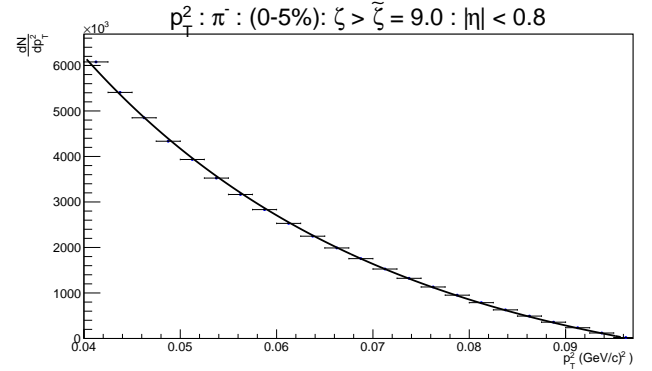
(a) $|\zeta|$ distribution of π^+ . Solid black curve is the result of the fit with equation (3.40): 0 – 5% centrality



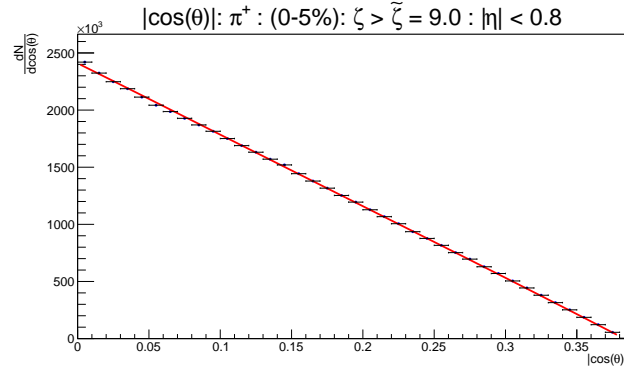
(b) $|\zeta|$ distribution of π^- . Solid black curve is the result of the fit with equation (3.40): 0 – 5% centrality



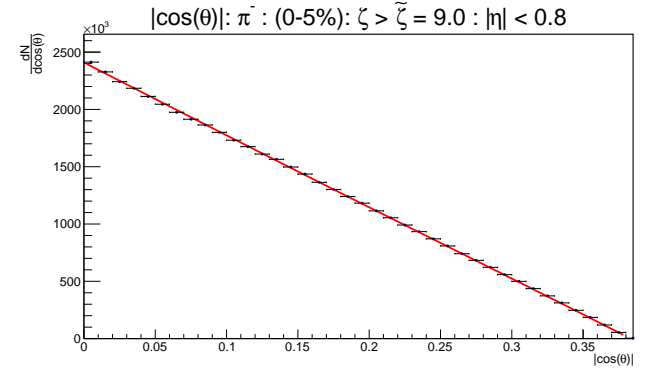
(c) p_T^2 distribution of π^+ . Solid black curve is the result of the fit with equation (3.44): 0 – 5% centrality



(d) p_T^2 distribution of π^- . Solid black curve is the result of the fit with equation (3.44): 0 – 5% centrality



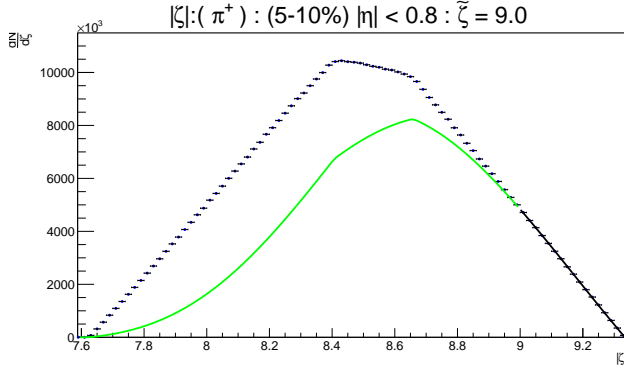
(e) $|\cos(\theta)|$ distribution of π^+ . Solid red curve is the result of the fit with equation (3.43): 0 – 5% centrality



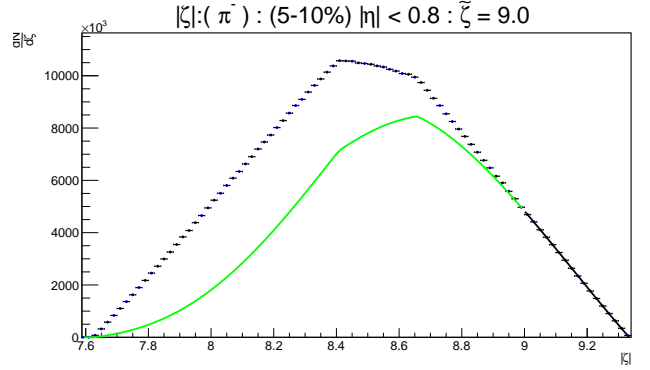
(f) $|\cos(\theta)|$ distribution of π^- . Solid red curve is the result of the fit with equation (3.43): 0 – 5% centrality

Figure 6.3: ALICE $|\zeta|$, p_T^2 and $|\cos(\theta)|$ distributions fitted with (3.40), (3.44), and (3.43) respectively for π^\pm , 0 – 5% centrality. The green curve in the ζ distribution is the extrapolation of the fit.

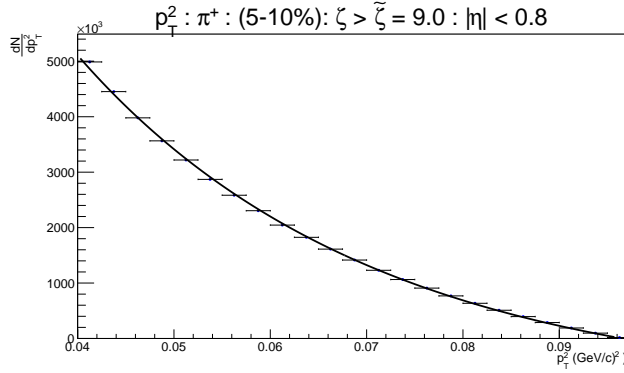
Pions (5-10 %)



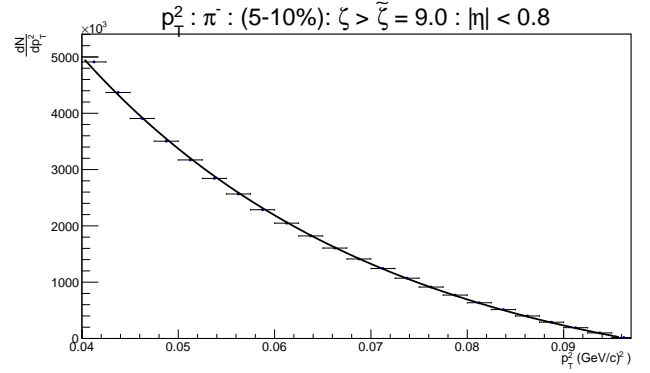
(a) $|\zeta|$ distribution of π^+ . Solid black curve is the result of the fit with equation (3.40): 5 – 10% centrality



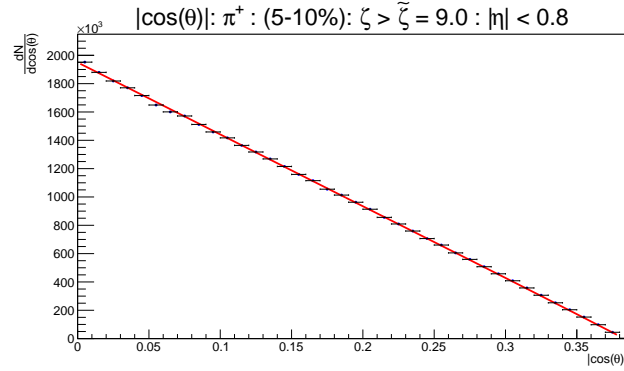
(b) $|\zeta|$ distribution of π^- . Solid black curve is the result of the fit with equation (3.40): 5 – 10% centrality



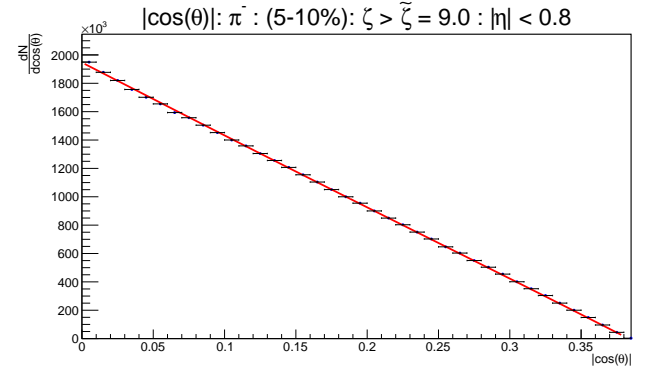
(c) p_T^2 distribution of π^+ . Solid black curve is the result of the fit with equation (3.44): 5 – 10% centrality



(d) p_T^2 distribution of π^- . Solid black curve is the result of the fit with equation (3.44): 5 – 10% centrality



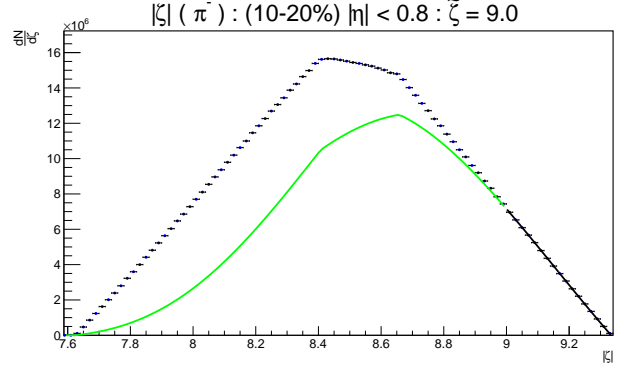
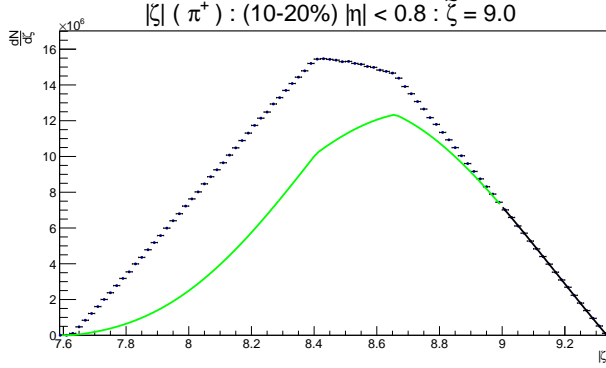
(e) $|\cos(\theta)|$ distribution of π^+ . Solid red curve is the result of the fit with equation (3.43): 5 – 10% centrality



(f) $|\cos(\theta)|$ distribution of π^- . Solid red curve is the result of the fit with equation (3.43): 5 – 10% centrality

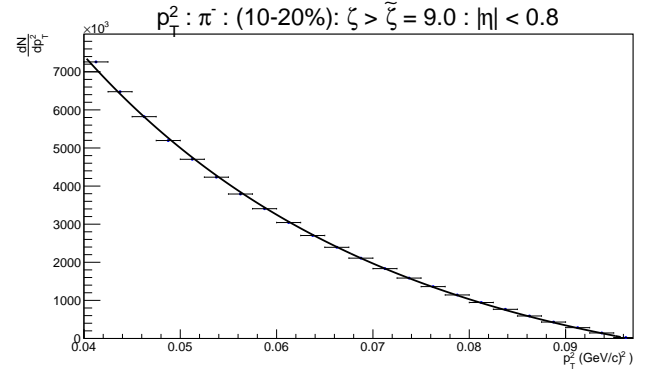
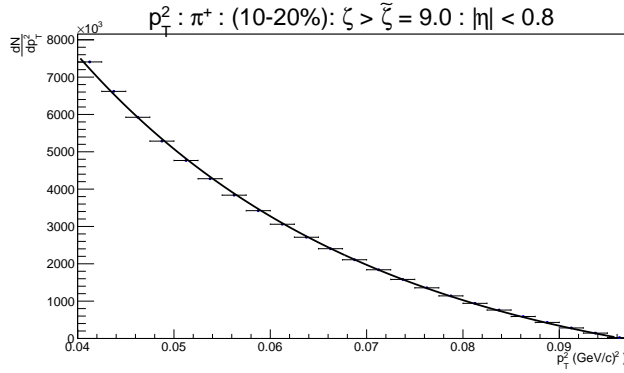
Figure 6.4: ALICE $|\zeta|$, p_T^2 and $|\cos(\theta)|$ distributions fitted with (3.40), (3.44), and (3.43) respectively for π^\pm , 5 – 10% centrality. The green curve in the ζ distribution is the extrapolation of the fit.

Pions (10-20 %)



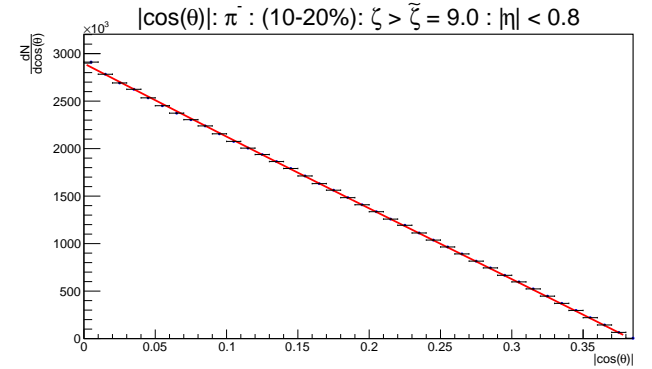
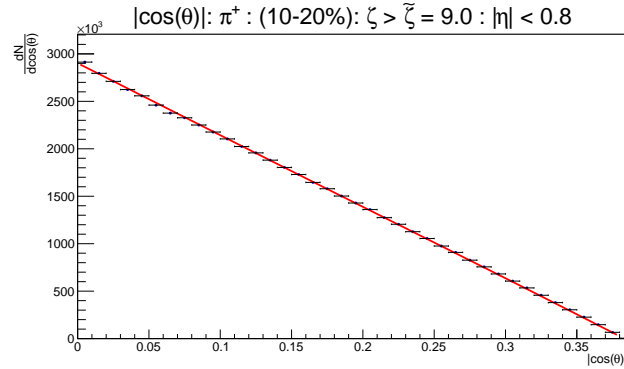
(a) $|\zeta|$ distribution of π^+ . Solid black curve is the result of the fit with equation (3.40): 10 – 20% centrality

(b) $|\zeta|$ distribution of π^- . Solid black curve is the result of the fit with equation (3.40): 10 – 20% centrality



(c) p_T^2 distribution of π^+ . Solid black curve is the result of the fit with equation (3.44): 10 – 20% centrality

(d) p_T^2 distribution of π^- . Solid black curve is the result of the fit with equation (3.44): 10 – 20% centrality

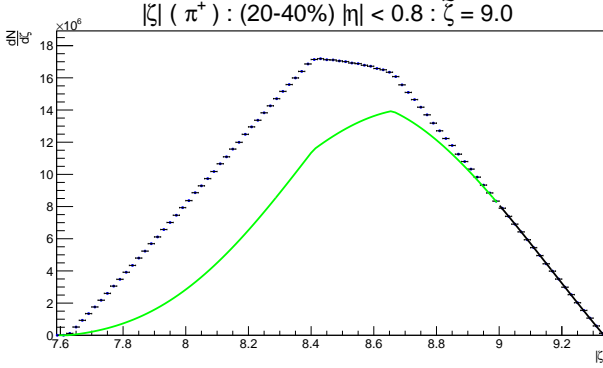


(e) $|\cos(\theta)|$ distribution of π^+ . Solid red curve is the result of the fit with equation (3.43): 10 – 20% centrality

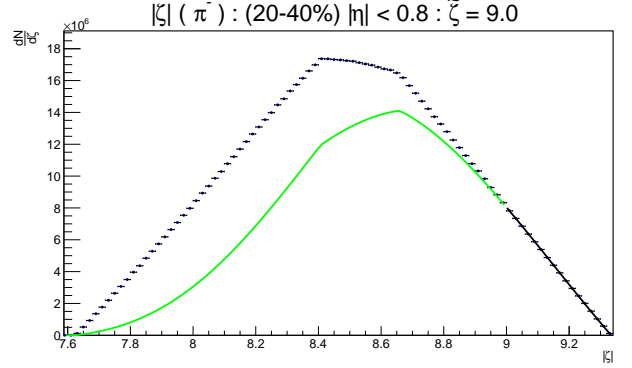
(f) $|\cos(\theta)|$ distribution of π^- . Solid red curve is the result of the fit with equation (3.43): 10 – 20% centrality

Figure 6.5: ALICE $|\zeta|$, p_T^2 and $|\cos(\theta)|$ distributions fitted with (3.40), (3.44), and (3.43) respectively for π^\pm , 10 – 20% centrality. The green curve in the ζ distribution is the extrapolation of the fit.

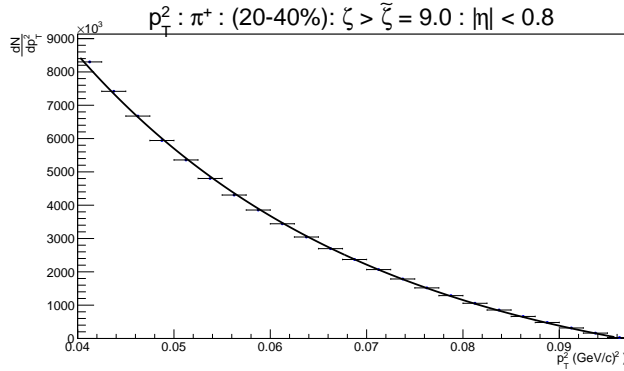
Pions (20-40 %)



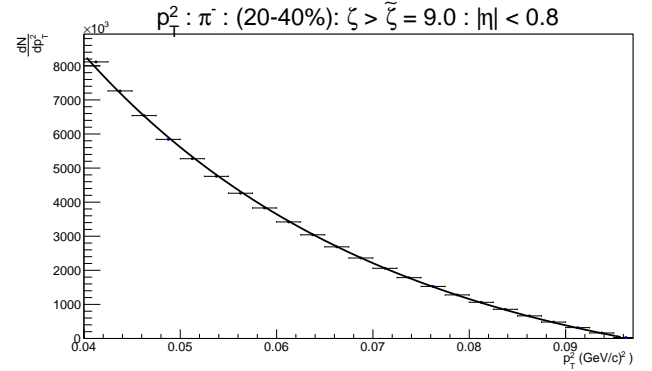
(a) $|\zeta|$ distribution of π^+ . Solid black curve is the result of the fit with equation (3.40): 20 – 40% centrality



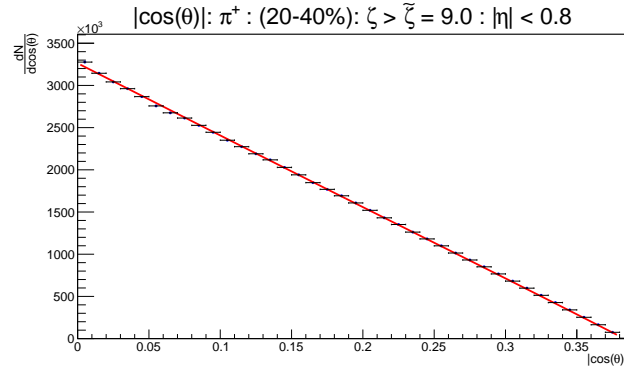
(b) $|\zeta|$ distribution of π^- . Solid black curve is the result of the fit with equation (3.40): 20 – 40% centrality



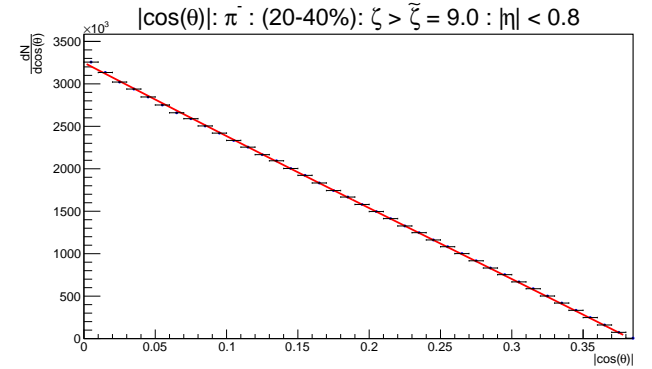
(c) p_T^2 distribution of π^+ . Solid black curve is the result of the fit with equation (3.44): 20 – 40% centrality



(d) p_T^2 distribution of π^- . Solid black curve is the result of the fit with equation (3.44): 20 – 40% centrality



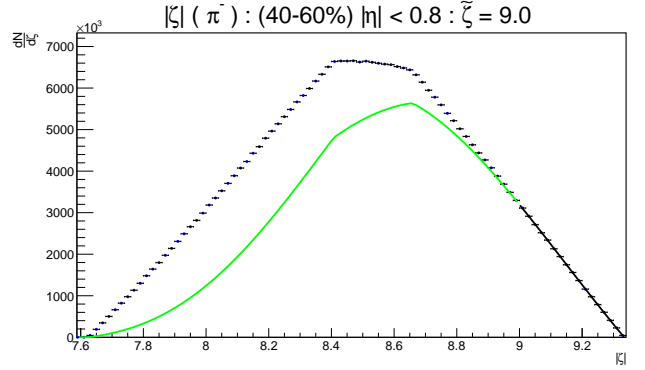
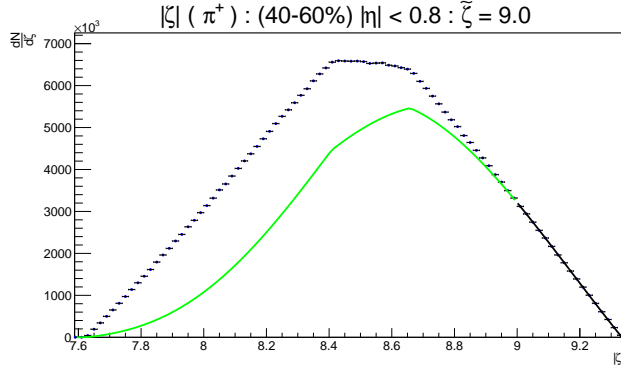
(e) $|\cos(\theta)|$ distribution of π^+ . Solid red curve is the result of the fit with equation (3.43): 20 – 40% centrality



(f) $|\cos(\theta)|$ distribution of π^- . Solid red curve is the result of the fit with equation (3.43): 20 – 40% centrality

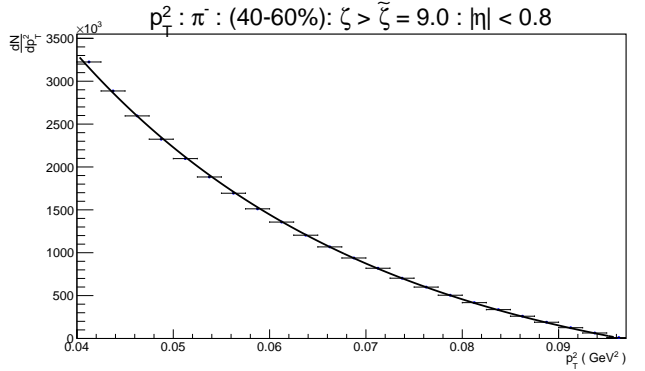
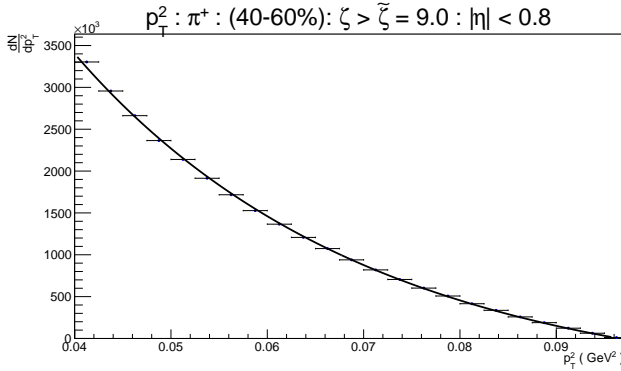
Figure 6.6: ALICE $|\zeta|$, p_T^2 and $|\cos(\theta)|$ distributions fitted with (3.40), (3.44), and (3.43) respectively for π^\pm , 20 – 40% centrality. The green curve in the ζ distribution is the extrapolation of the fit.

Pions (40-60 %)



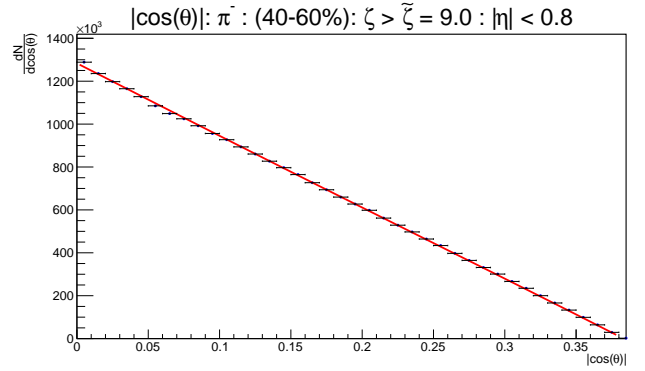
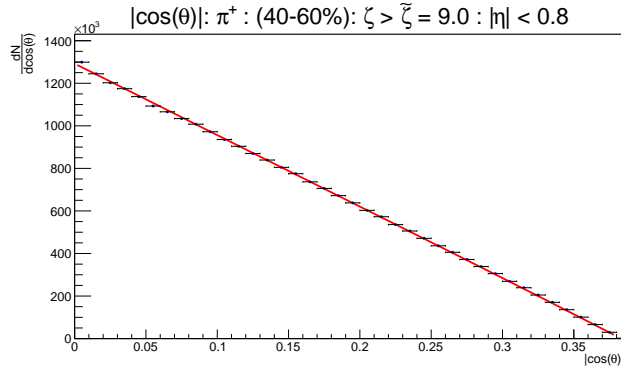
(a) $|\zeta|$ distribution of π^+ . Solid black curve is the result of the fit with equation (3.40): 40 – 60% centrality

(b) $|\zeta|$ distribution of π^- . Solid black curve is the result of the fit with equation (3.40): 40 – 60% centrality



(c) p_T^2 distribution of π^+ . Solid black curve is the result of the fit with equation (3.44): 40 – 60% centrality

(d) p_T^2 distribution of π^- . Solid black curve is the result of the fit with equation (3.44): 40 – 60% centrality

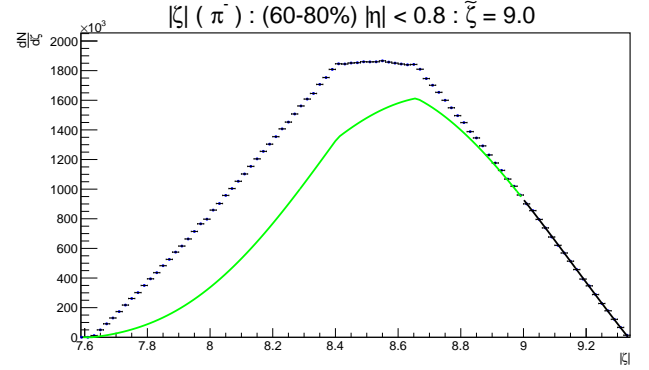
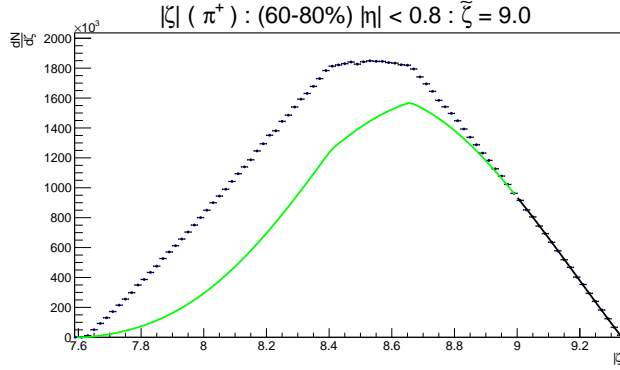


(e) $|\cos(\theta)|$ distribution of π^+ . Solid red curve is the result of the fit with equation (3.43): 40 – 60% centrality

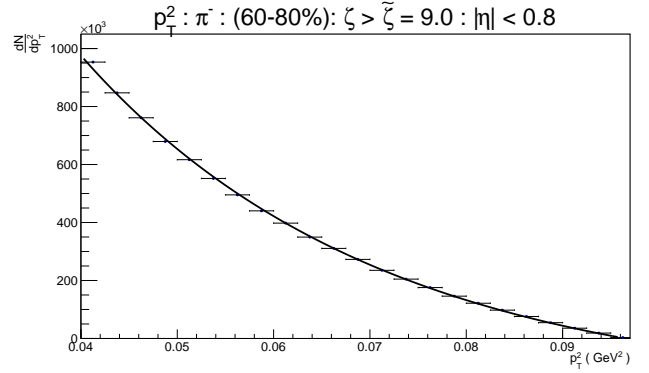
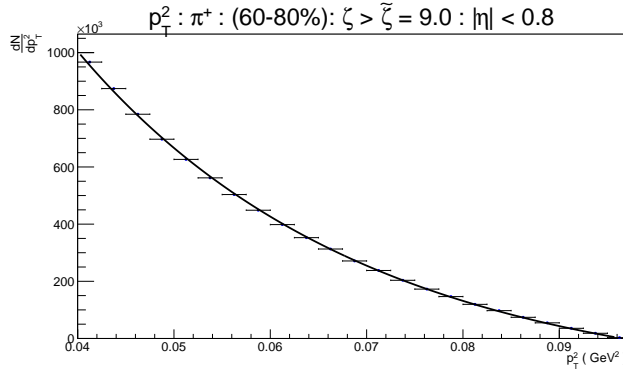
(f) $|\cos(\theta)|$ distribution of π^- . Solid red curve is the result of the fit with equation (3.43): 40 – 60% centrality

Figure 6.7: ALICE $|\zeta|$, p_T^2 and $|\cos(\theta)|$ distributions fitted with (3.40), (3.44), and (3.43) respectively for π^\pm , 40 – 60% centrality. The green curve in the ζ distribution is the extrapolation of the fit.

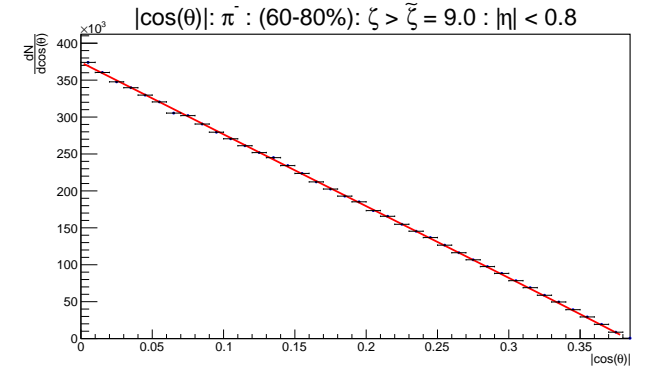
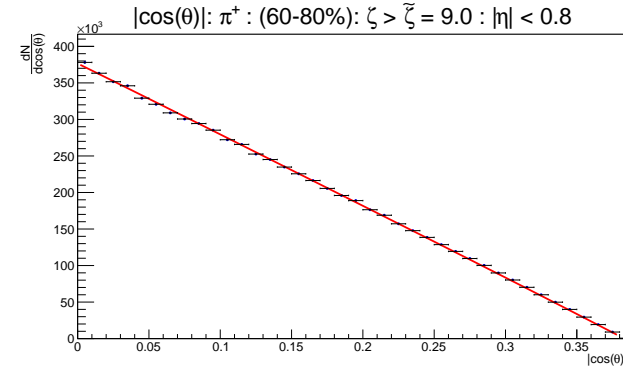
Pions (60 - 80%)



(a) $|\zeta|$ distribution of π^+ . Solid black curve is the result of the fit with equation (3.40): 0 – 5% centrality (b) $|\zeta|$ distribution of π^- . Solid black curve is the result of the fit with equation (3.40): 60 – 80% centrality



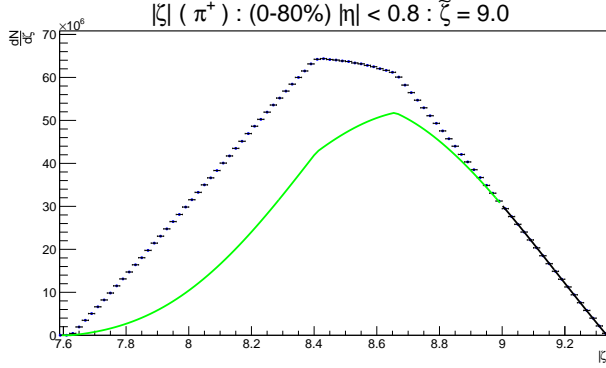
(c) p_T^2 distribution of π^+ . Solid black curve is the result of the fit with equation (3.44): 60 – 80% centrality (d) p_T^2 distribution of π^- . Solid black curve is the result of the fit with equation (3.44): 60 – 80% centrality



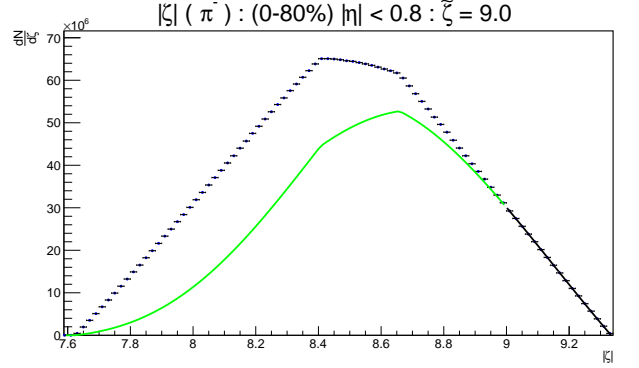
(e) $|\cos(\theta)|$ distribution of π^+ . Solid red curve is the result of the fit with equation (3.43): 60 – 80% centrality (f) $|\cos(\theta)|$ distribution of π^- . Solid red curve is the result of the fit with equation (3.43): 60 – 80% centrality

Figure 6.8: ALICE $|\zeta|$, p_T^2 and $|\cos(\theta)|$ distributions fitted with (3.40), (3.44), and (3.43) respectively for π^\pm , 60 – 80% centrality. The green curve in the ζ distribution is the extrapolation of the fit.

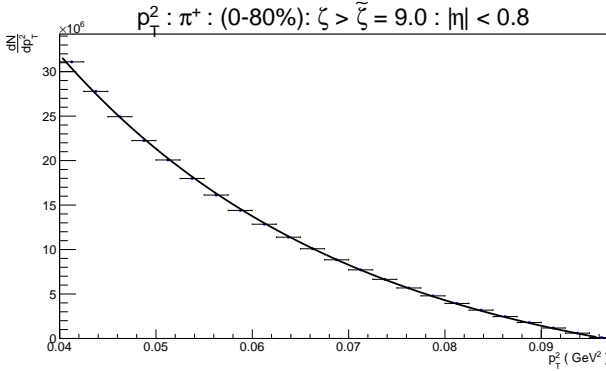
Pions (0 - 80 %)



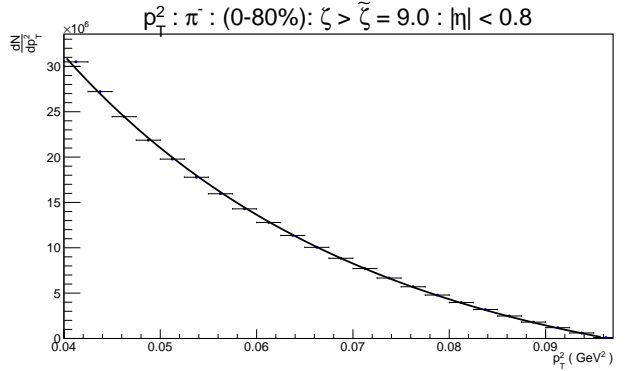
(a) $|\zeta|$ distribution of π^+ . Solid black curve is the result of the fit with equation (3.40): 0 – 80% centrality



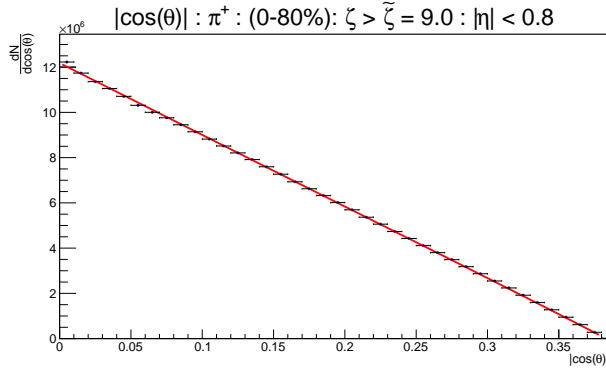
(b) $|\zeta|$ distribution of π^- . Solid black curve is the result of the fit with equation (3.40): 0 – 80% centrality



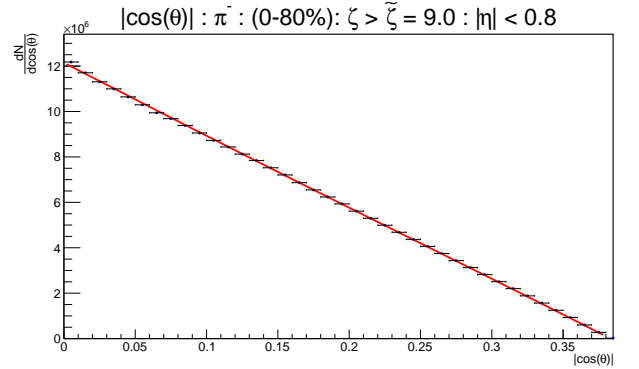
(c) p_T^2 distribution of π^+ . Solid black curve is the result of the fit with equation (3.44): 0 – 80% centrality



(d) p_T^2 distribution of π^- . Solid black curve is the result of the fit with equation (3.44): 0 – 80% centrality



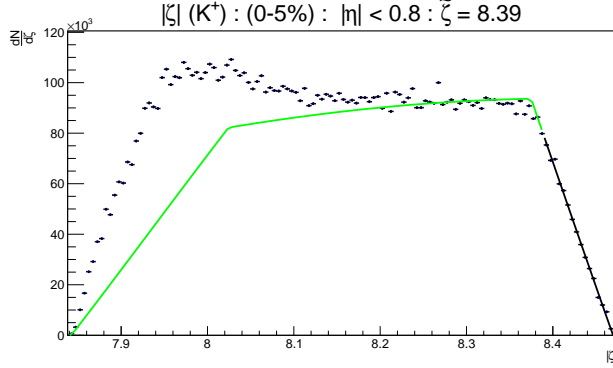
(e) $|\cos(\theta)|$ distribution of π^+ . Solid red curve is the result of the fit with equation (3.43): 0 – 80% centrality



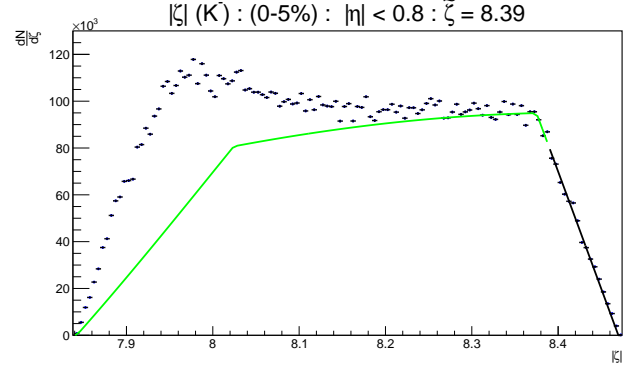
(f) $|\cos(\theta)|$ distribution of π^- . Solid red curve is the result of the fit with equation (3.43): 0 – 80% centrality

Figure 6.9: ALICE $|\zeta|$, p_T^2 and $|\cos(\theta)|$ distributions fitted with (3.40), (3.44), and (3.43) respectively for π^\pm , 0 – 80% centrality. The green curve in the ζ distribution is the extrapolation of the fit.

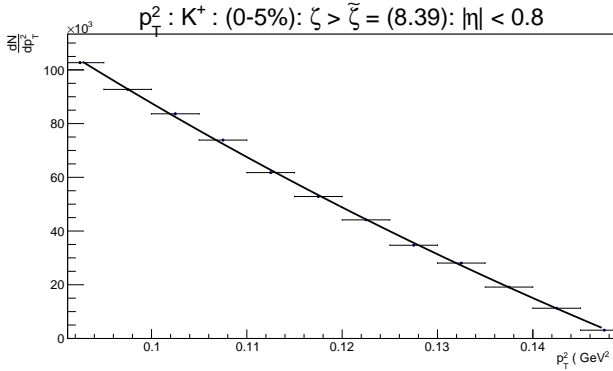
Kaons (0-5 %)



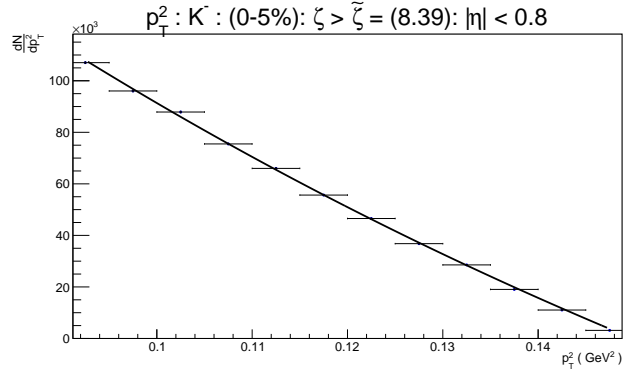
(a) $|\zeta|$ distribution of K^+ . Solid black curve is the result of the fit with equation (3.40): 0 – 5% centrality



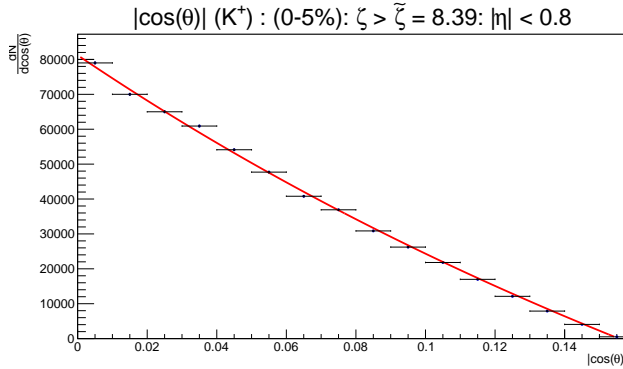
(b) $|\zeta|$ distribution of K^- . Solid black curve is the result of the fit with equation (3.40): 0 – 5% centrality



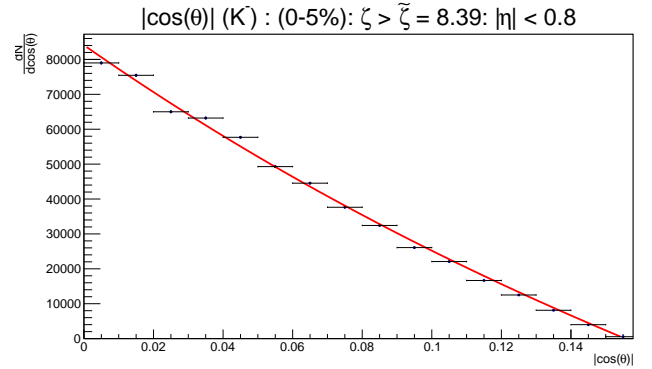
(c) p_T^2 distribution of K^+ . Solid black curve is the result of the fit with equation (3.44): 0 – 5% centrality



(d) p_T^2 distribution of K^- . Solid black curve is the result of the fit with equation (3.44): 0 – 5% centrality



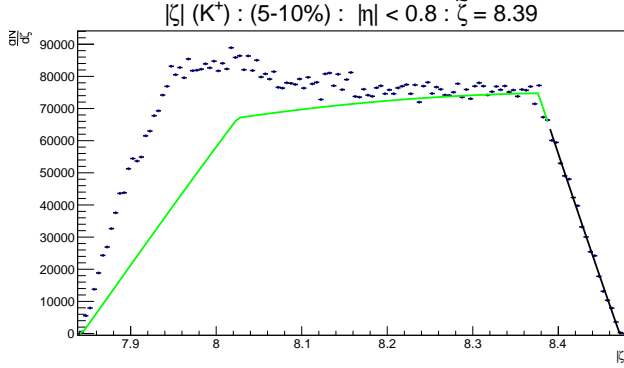
(e) $|\cos(\theta)|$ distribution of K^+ . Solid red curve is the result of the fit with equation (3.43): 0 – 5% centrality



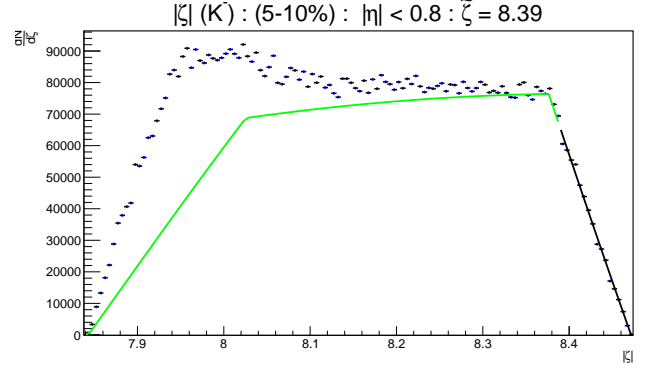
(f) $|\cos(\theta)|$ distribution of K^- . Solid red curve is the result of the fit with equation (3.43): 0 – 5% centrality

Figure 6.10: ALICE $|\zeta|$, p_T^2 and $|\cos(\theta)|$ distributions fitted with (3.40), (3.44), and (3.43) respectively for K^\pm , 0 – 5% centrality. The green curve in the ζ distribution is the extrapolation of the fit.

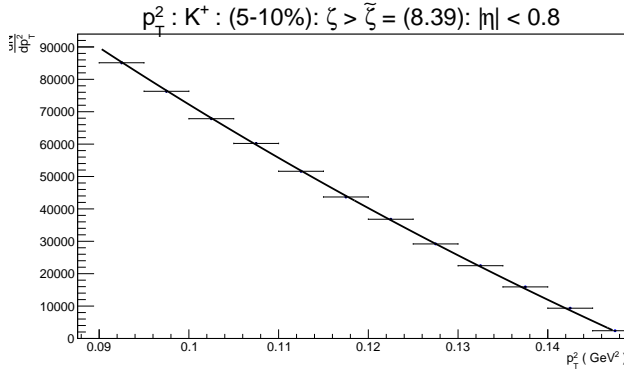
Kaons (5-10 %)



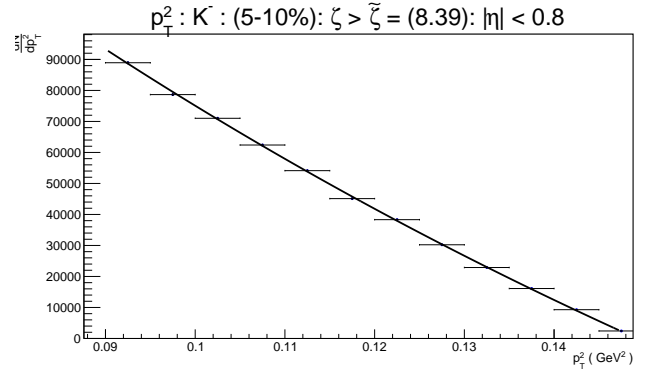
(a) $|\zeta|$ distribution of K^+ . Solid black curve is the result of the fit with equation (3.40): 5 – 10% centrality



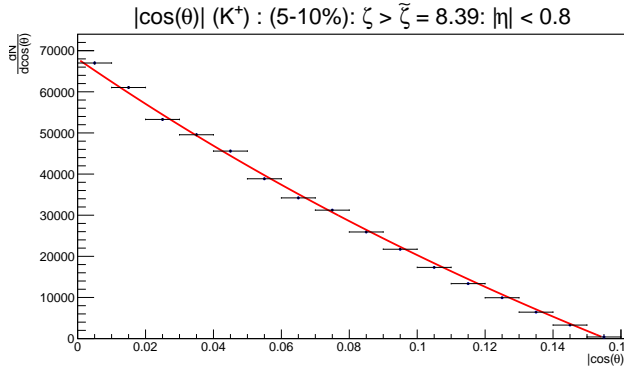
(b) $|\zeta|$ distribution of K^- . Solid black curve is the result of the fit with equation (3.40): 5 – 10% centrality



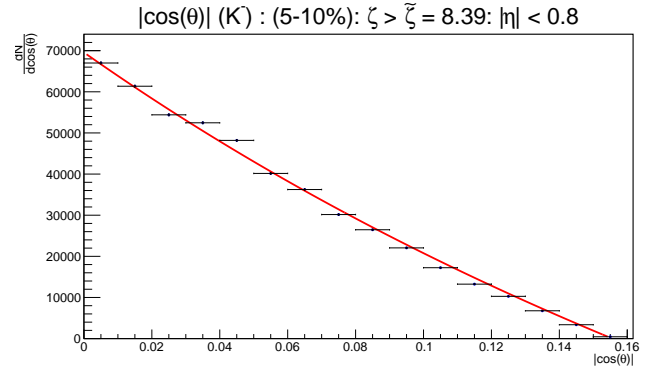
(c) p_T^2 distribution of K^+ . Solid black curve is the result of the fit with equation (3.44): 5 – 10% centrality



(d) p_T^2 distribution of K^- . Solid black curve is the result of the fit with equation (3.44): 5 – 10% centrality



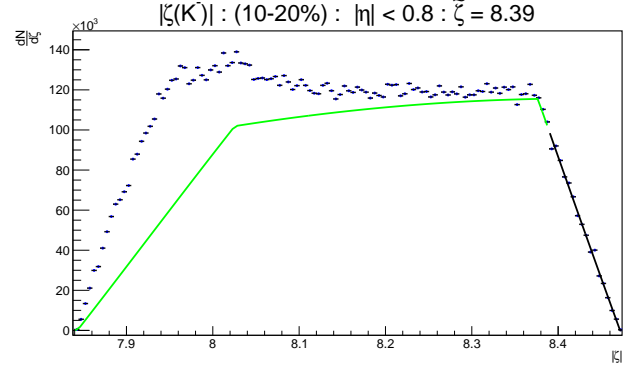
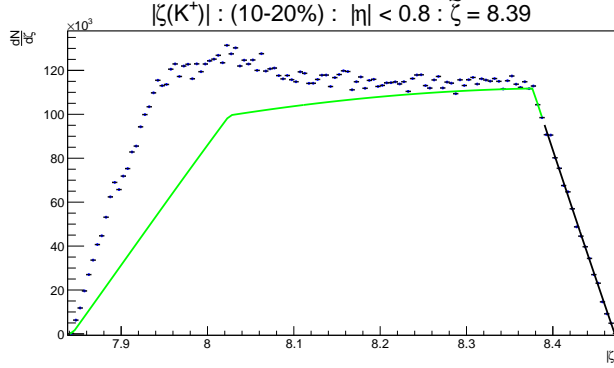
(e) $|\cos(\theta)|$ distribution of K^+ . Solid red curve is the result of the fit with equation (3.43): 5 – 10% centrality



(f) $|\cos(\theta)|$ distribution of K^- . Solid red curve is the result of the fit with equation (3.43): 5 – 10% centrality

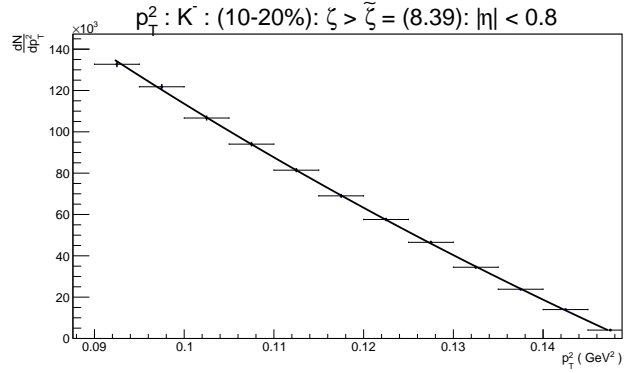
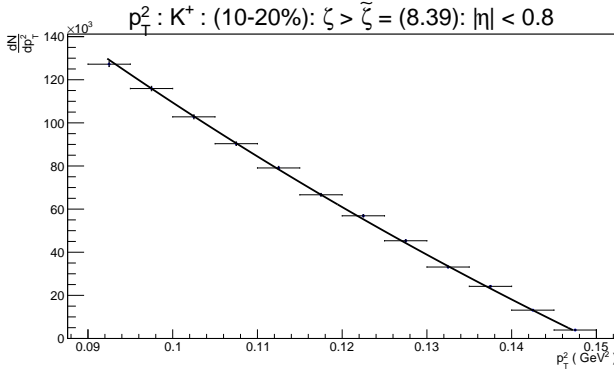
Figure 6.11: ALICE $|\zeta|$, p_T^2 and $|\cos(\theta)|$ distributions fitted with (3.40), (3.44), and (3.43) respectively for K^\pm , 5 – 10% centrality. The green curve in the ζ distribution is the extrapolation of the fit.

Kaons (10-20 %)



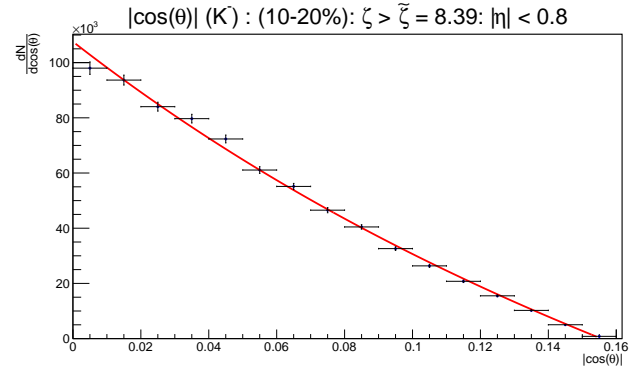
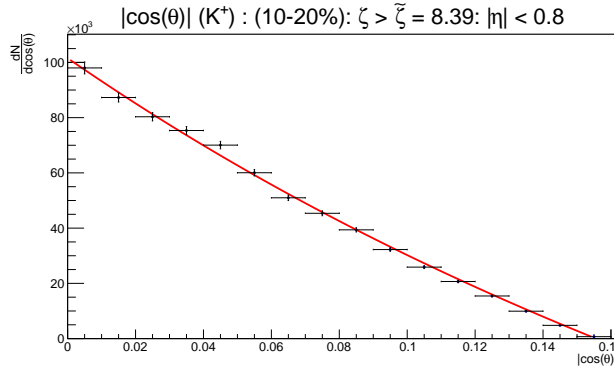
(a) $|\zeta|$ distribution of K^+ . Solid black curve is the result of the fit with equation (3.40): 10 – 20% centrality

(b) $|\zeta|$ distribution of K^- . Solid black curve is the result of the fit with equation (3.40): 10 – 20% centrality



(c) p_T^2 distribution of K^+ . Solid black curve is the result of the fit with equation (3.44): 10 – 20% centrality

(d) p_T^2 distribution of K^- . Solid black curve is the result of the fit with equation (3.44): 10 – 20% centrality

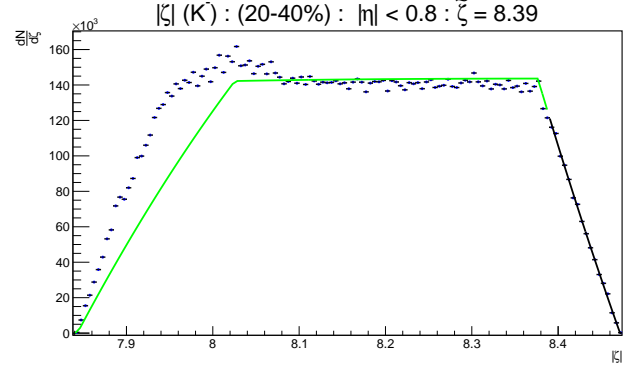
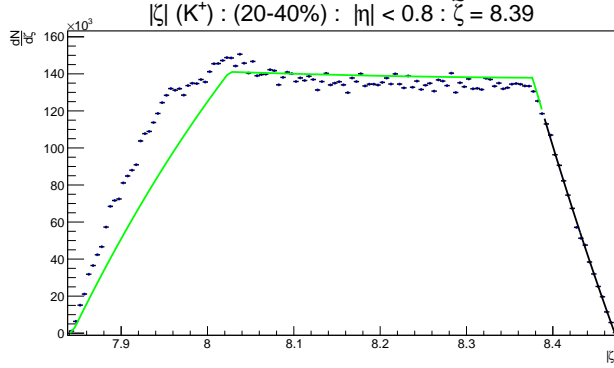


(e) $|\cos(\theta)|$ distribution of K^+ . Solid red curve is the result of the fit with equation (3.43): 10 – 20% centrality

(f) $|\cos(\theta)|$ distribution of K^- . Solid red curve is the result of the fit with equation (3.43): 10 – 20% centrality

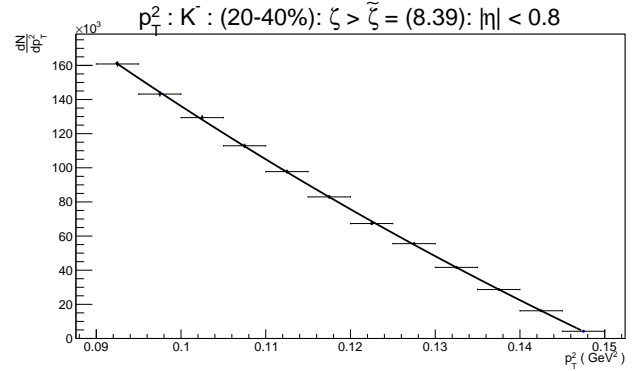
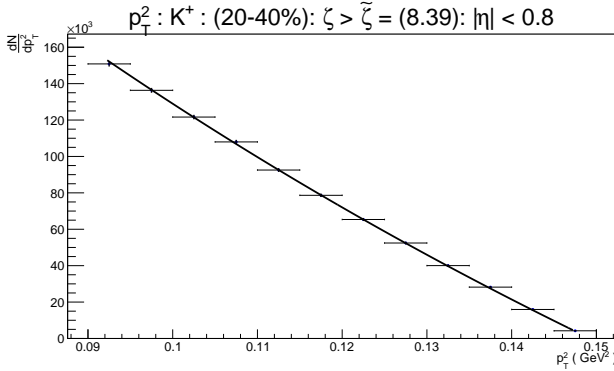
Figure 6.12: ALICE $|\zeta|$, p_T^2 and $|\cos(\theta)|$ distributions fitted with (3.40), (3.44), and (3.43) respectively for K^\pm , 10 – 20% centrality. The green curve in the ζ distribution is the extrapolation of the fit.

Kaons (20-40 %)



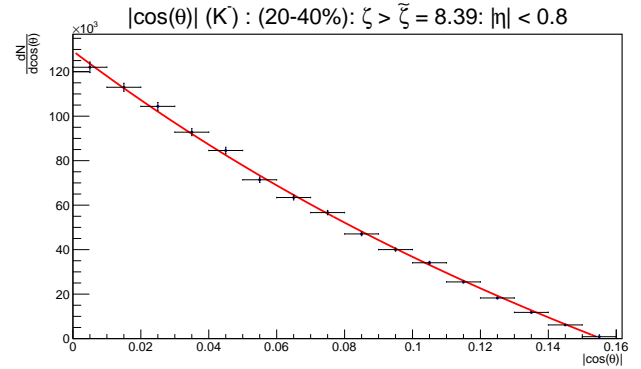
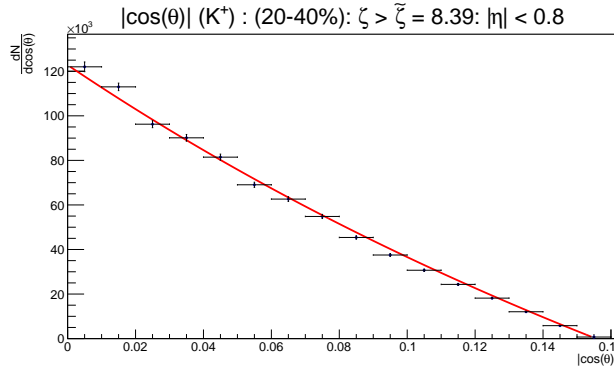
(a) $|\zeta|$ distribution of K^+ . Solid black curve is the result of the fit with equation (3.40): 20 – 40% centrality

(b) $|\zeta|$ distribution of K^- . Solid black curve is the result of the fit with equation (3.40): 20 – 40% centrality



(c) p_T^2 distribution of K^+ . Solid black curve is the result of the fit with equation (3.44): 20 – 40% centrality

(d) p_T^2 distribution of K^- . Solid black curve is the result of the fit with equation (3.44): 20 – 40% centrality

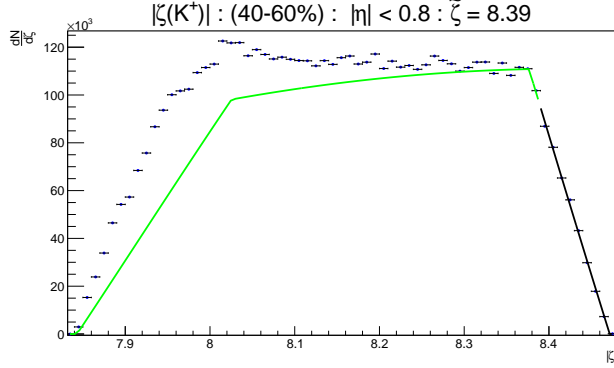


(e) $|\cos(\theta)|$ distribution of K^+ . Solid red curve is the result of the fit with equation (3.43): 20 – 40% centrality

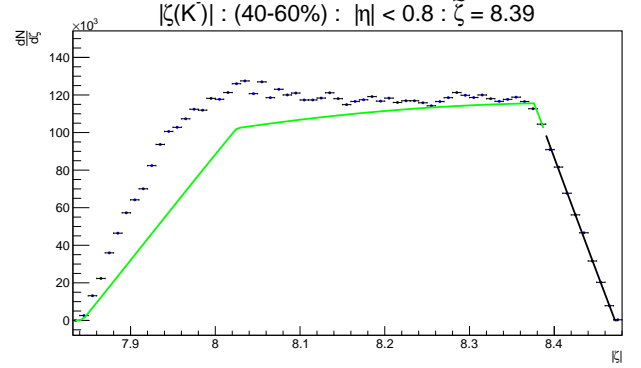
(f) $|\cos(\theta)|$ distribution of K^- . Solid red curve is the result of the fit with equation (3.43): 20 – 40% centrality

Figure 6.13: ALICE $|\zeta|$, p_T^2 and $|\cos(\theta)|$ distributions fitted with (3.40), (3.44), and (3.43) respectively for K^\pm , 20 – 40% centrality. The green curve in the ζ distribution is the extrapolation of the fit.

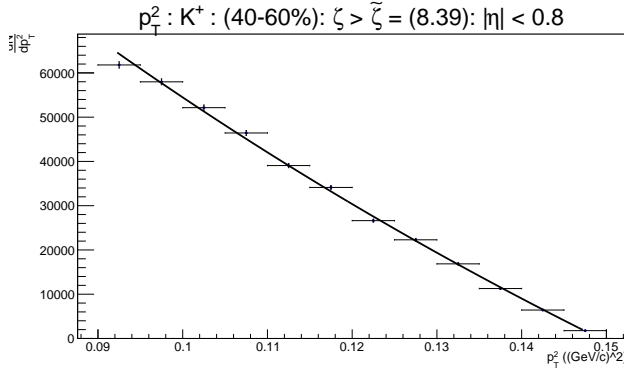
Kaons (40-60%)



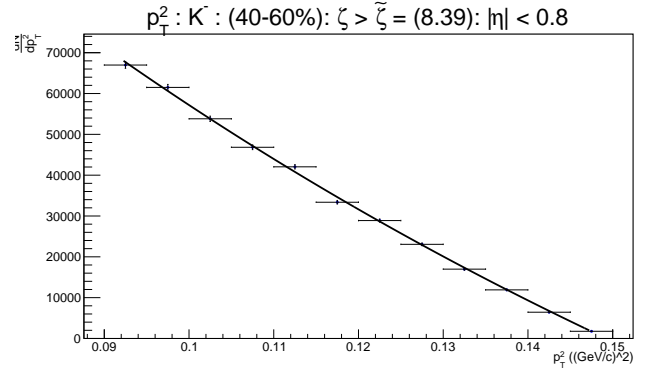
(a) $|\zeta|$ distribution of K^+ . Solid black curve is the result of the fit with equation (3.40): 40 – 60% centrality



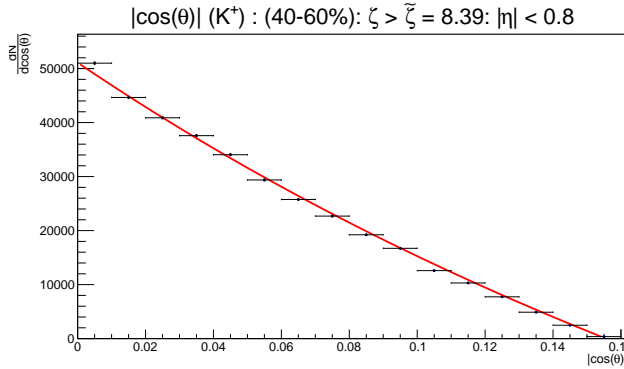
(b) $|\zeta|$ distribution of K^- . Solid black curve is the result of the fit with equation (3.40): 40 – 60% centrality



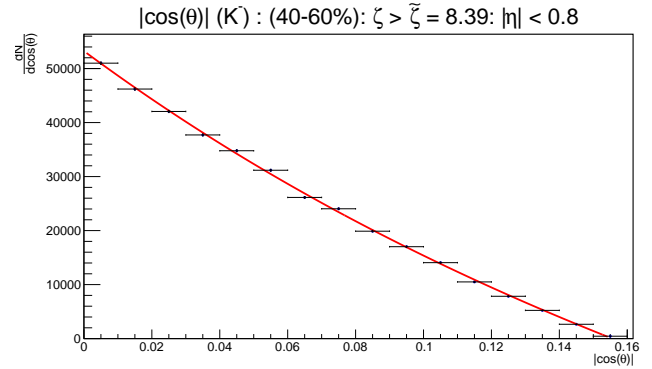
(c) p_T^2 distribution of K^+ . Solid black curve is the result of the fit with equation (3.44): 40 – 60% centrality



(d) p_T^2 distribution of K^- . Solid black curve is the result of the fit with equation (3.44): 40 – 60% centrality



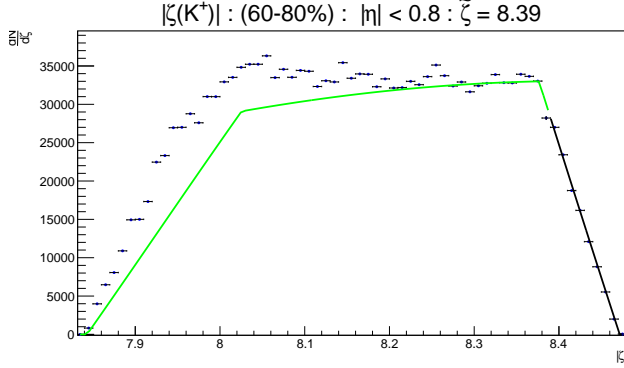
(e) $|\cos(\theta)|$ distribution of K^+ . Solid red curve is the result of the fit with equation (3.43): 40 – 60% centrality



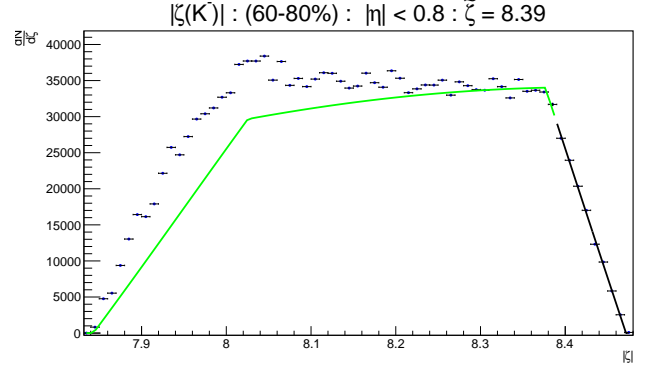
(f) $|\cos(\theta)|$ distribution of K^- . Solid red curve is the result of the fit with equation (3.43): 40 – 60% centrality

Figure 6.14: ALICE $|\zeta|$, p_T^2 and $|\cos(\theta)|$ distributions fitted with (3.40), (3.44), and (3.43) respectively for K^\pm , 40 – 60% centrality. The green curve in the ζ distribution is the extrapolation of the fit.

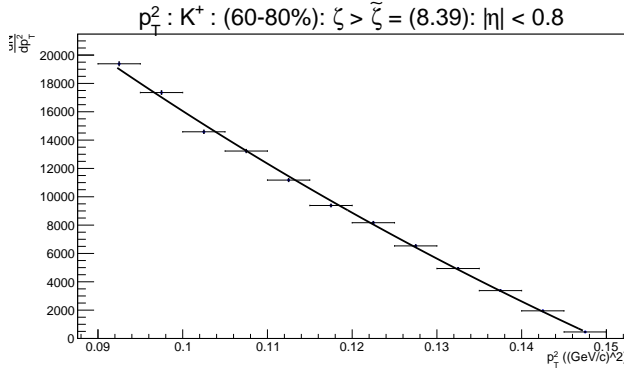
Kaons (60-80 %)



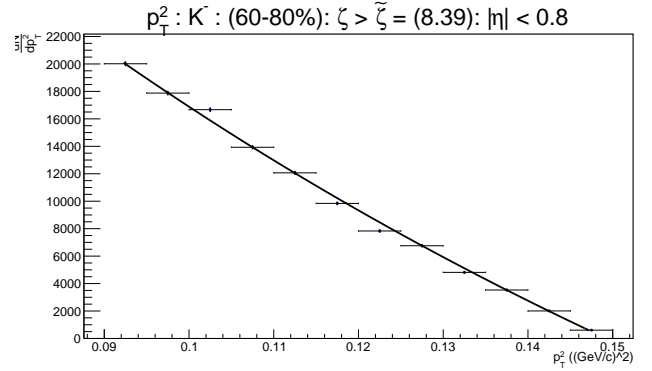
(a) $|\zeta|$ distribution of K^+ . Solid black curve is the result of the fit with equation (3.40): 0 – 5% centrality



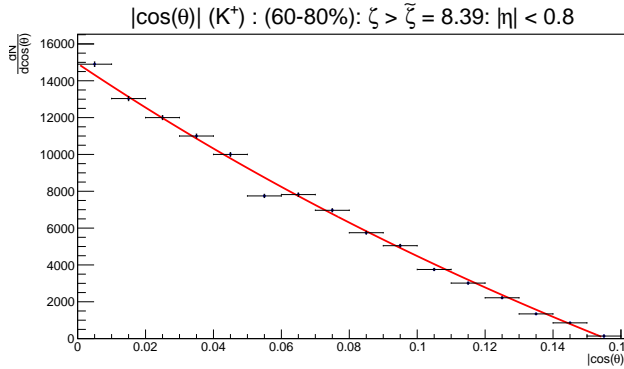
(b) $|\zeta|$ distribution of K^- . Solid black curve is the result of the fit with equation (3.40): 60 – 80% centrality



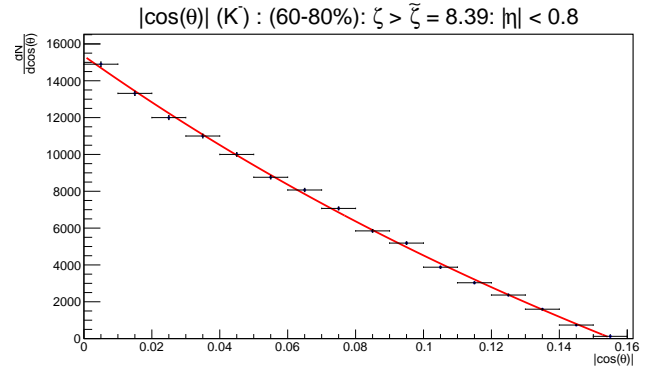
(c) p_T^2 distribution of K^+ . Solid black curve is the result of the fit with equation (3.44): 60 – 80% centrality



(d) p_T^2 distribution of K^- . Solid black curve is the result of the fit with equation (3.44): 60 – 80% centrality



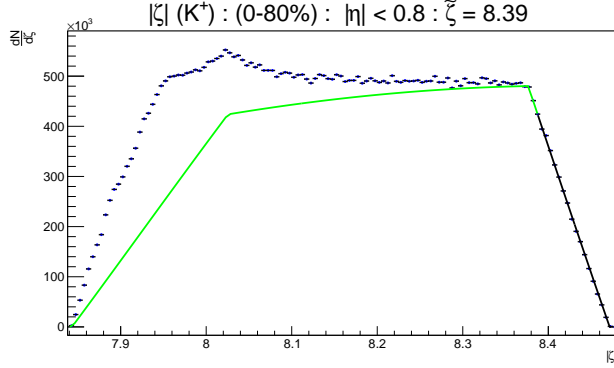
(e) $|\cos(\theta)|$ distribution of K^+ . Solid red curve is the result of the fit with equation (3.43): 60 – 80% centrality



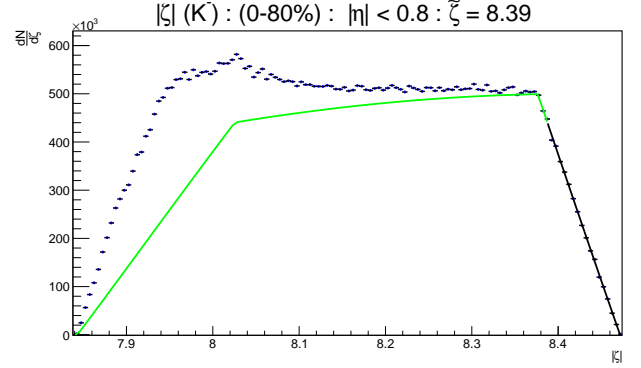
(f) $|\cos(\theta)|$ distribution of K^- . Solid red curve is the result of the fit with equation (3.43): 60 – 80% centrality

Figure 6.15: ALICE $|\zeta|$, p_T^2 and $|\cos(\theta)|$ distributions fitted with (3.40), (3.44), and (3.43) respectively for K^\pm , 60 – 80% centrality. The green curve in the ζ distribution is the extrapolation of the fit.

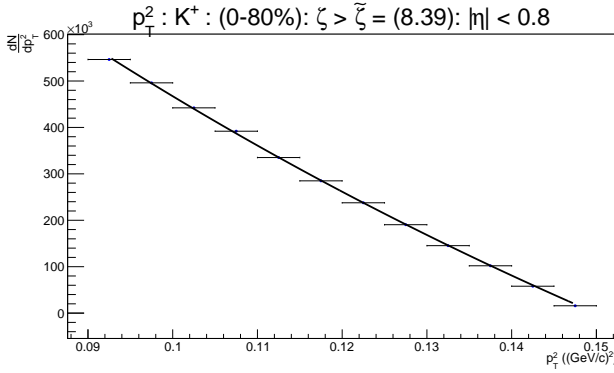
Kaons (0-80 %)



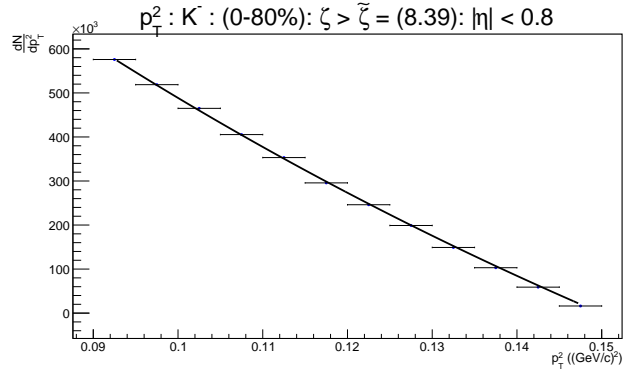
(a) $|\zeta|$ distribution of K^+ . Solid black curve is the result of the fit with equation (3.40): 0 – 80% centrality



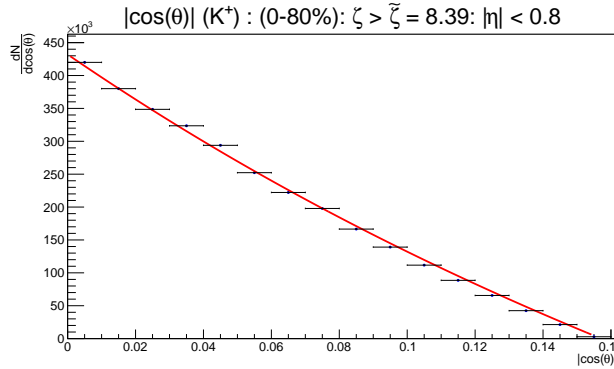
(b) $|\zeta|$ distribution of K^- . Solid black curve is the result of the fit with equation (3.40): 0 – 80% centrality



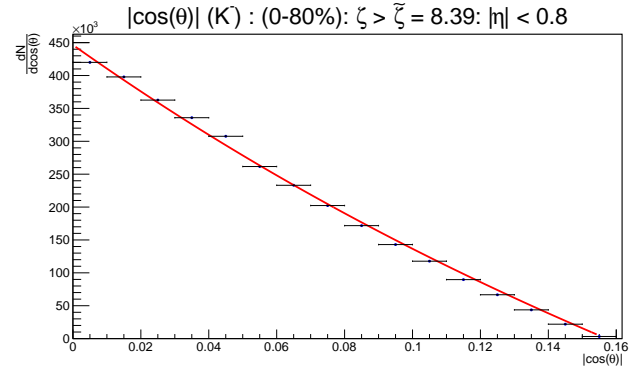
(c) p_T^2 distribution of K^+ . Solid black curve is the result of the fit with equation (3.44): 0 – 80% centrality



(d) p_T^2 distribution of K^- . Solid black curve is the result of the fit with equation (3.44): 0 – 80% centrality



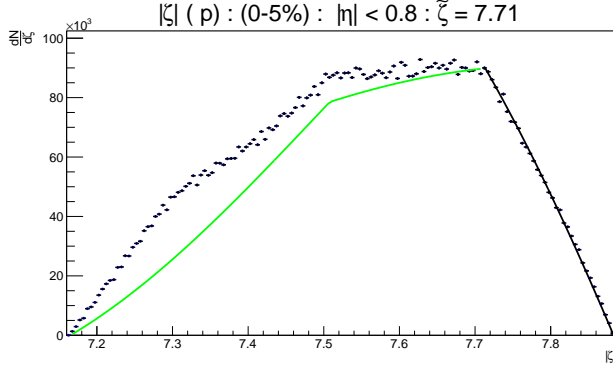
(e) $|\cos(\theta)|$ distribution of K^+ . Solid red curve is the result of the fit with equation (3.43): 0 – 80% centrality



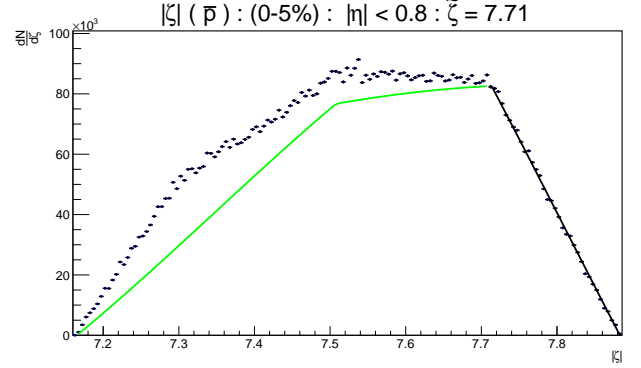
(f) $|\cos(\theta)|$ distribution of K^- . Solid red curve is the result of the fit with equation (3.43): 0 – 80% centrality

Figure 6.16: ALICE $|\zeta|$, p_T^2 and $|\cos(\theta)|$ distributions fitted with (3.40), (3.44), and (3.43) respectively for K^\pm , 0 – 80% centrality. The green curve in the ζ distribution is the extrapolation of the fit.

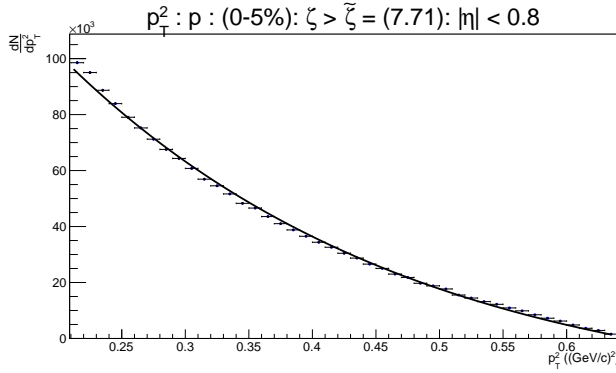
Protons (0-5 %)



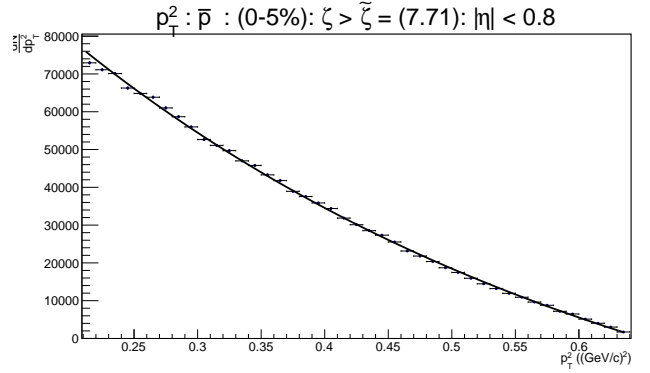
(a) $|\zeta|$ distribution of p . Solid black curve is the result of the fit with equation (3.40): 0 – 5% centrality



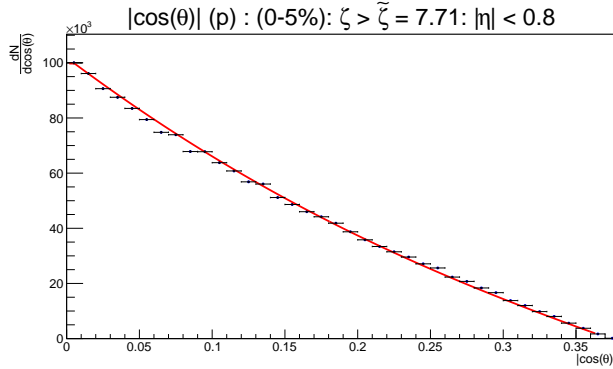
(b) $|\zeta|$ distribution of \bar{p} . Solid black curve is the result of the fit with equation (3.40): 0 – 5% centrality



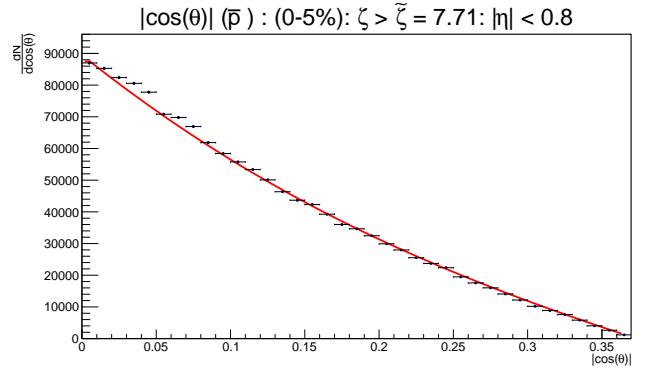
(c) p_T^2 distribution of p . Solid black curve is the result of the fit with equation (3.44): 0 – 5% centrality



(d) p_T^2 distribution of \bar{p} . Solid black curve is the result of the fit with equation (3.44): 0 – 5% centrality



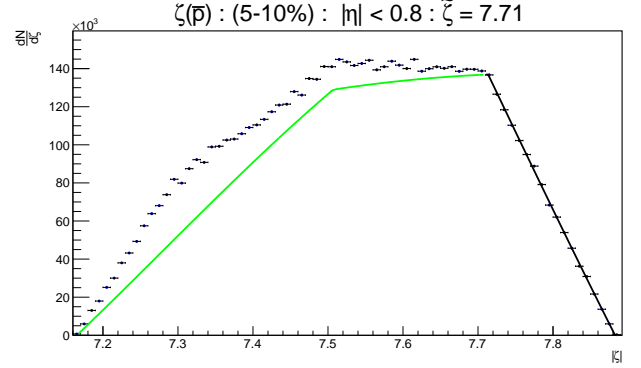
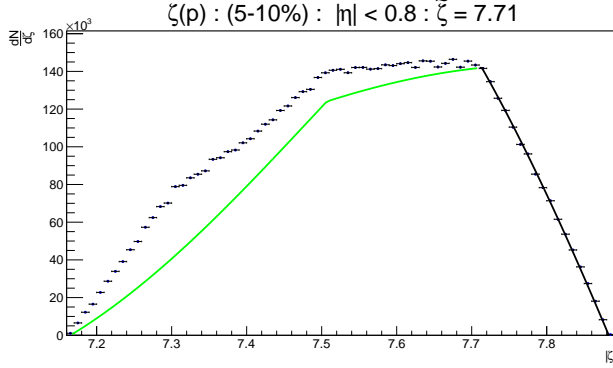
(e) $|\cos(\theta)|$ distribution of p . Solid red curve is the result of the fit with equation (3.43): 0 – 5% centrality



(f) $|\cos(\theta)|$ distribution of \bar{p} . Solid red curve is the result of the fit with equation (3.43): 0 – 5% centrality

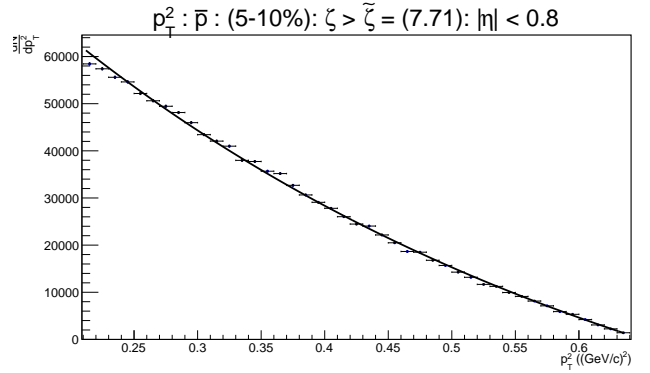
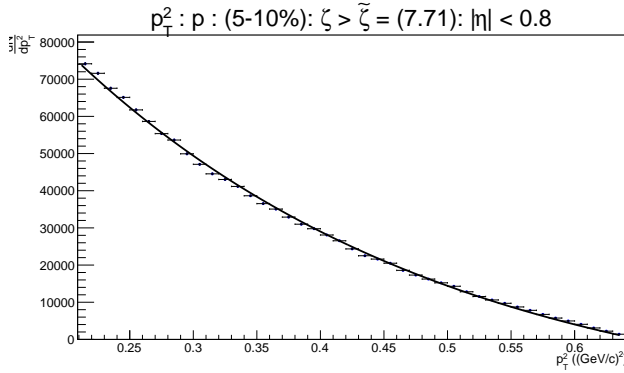
Figure 6.17: ALICE $|\zeta|$, p_T^2 and $|\cos(\theta)|$ distributions fitted with (3.40), (3.44), and (3.43) respectively for $p(\bar{p})$, 0 – 5% centrality. The green curve in the ζ distribution is the extrapolation of the fit.

Protons (5-10 %)



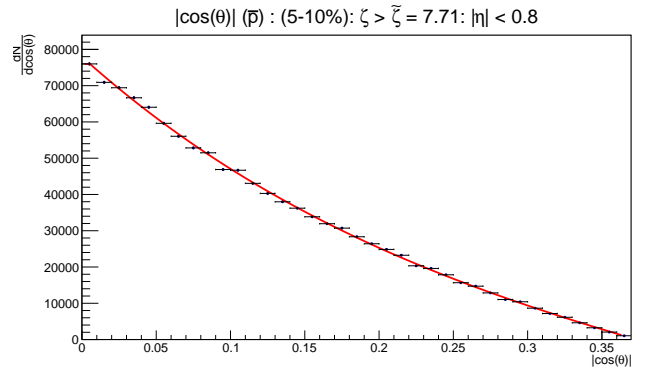
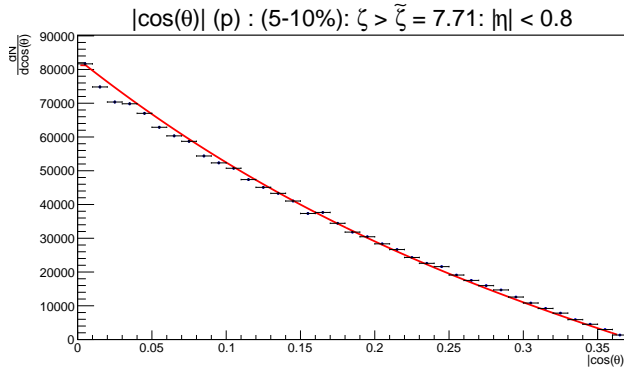
(a) $|\zeta|$ distribution of p . Solid black curve is the result of the fit with equation (3.40): 5 – 10% centrality

(b) $|\zeta|$ distribution of \bar{p} . Solid black curve is the result of the fit with equation (3.40): 5 – 10% centrality



(c) p_T^2 distribution of p . Solid black curve is the result of the fit with equation (3.44): 5 – 10% centrality

(d) p_T^2 distribution of \bar{p} . Solid black curve is the result of the fit with equation (3.44): 5 – 10% centrality

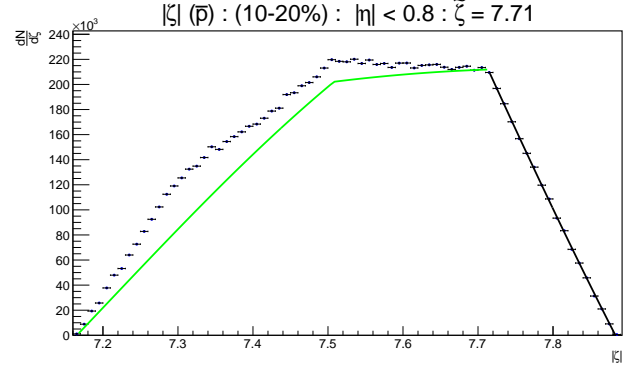
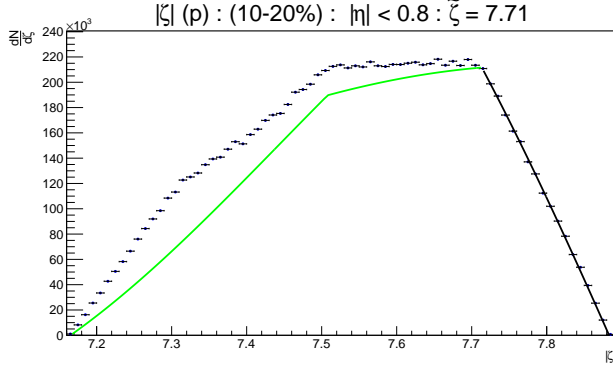


(e) $|\cos(\theta)|$ distribution of p . Solid red curve is the result of the fit with equation (3.43): 5 – 10% centrality

(f) $|\cos(\theta)|$ distribution of \bar{p} . Solid red curve is the result of the fit with equation (3.43): 5 – 10% centrality

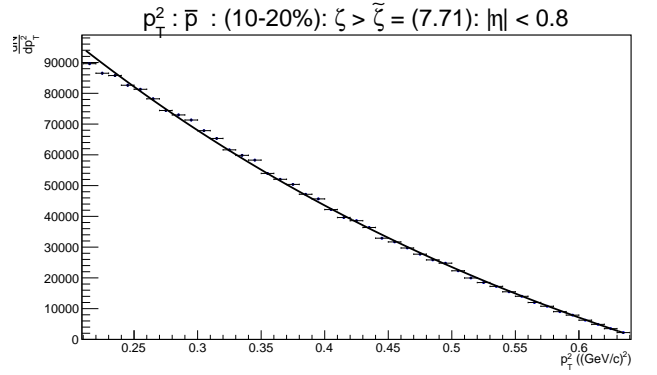
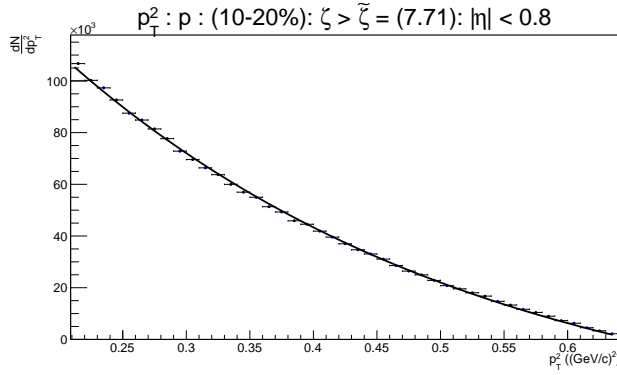
Figure 6.18: ALICE $|\zeta|$, p_T^2 and $|\cos(\theta)|$ distributions fitted with (3.40), (3.44), and (3.43) respectively for $p(\bar{p})$, 5 – 10% centrality. The green curve in the ζ distribution is the extrapolation of the fit.

Protons (10-20 %)



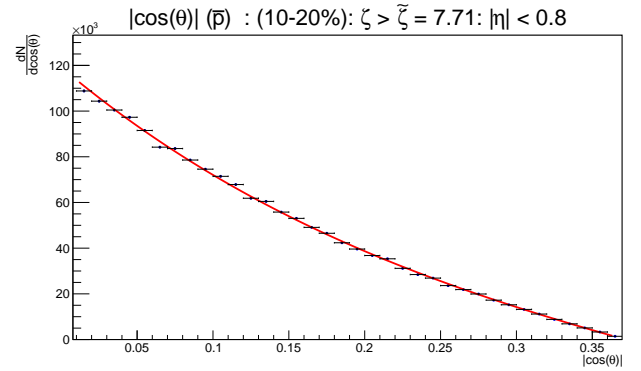
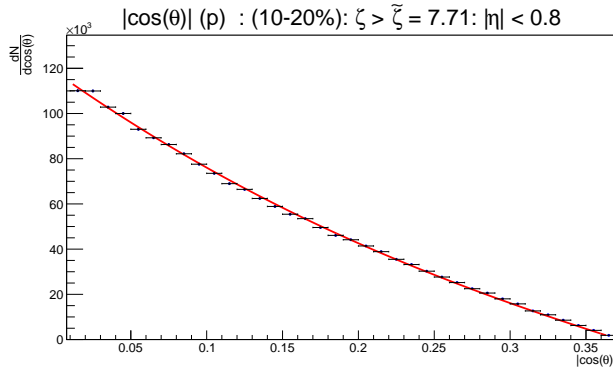
(a) $|\zeta|$ distribution of p . Solid black curve is the result of the fit with equation (3.40): 10 – 20% centrality

(b) $|\zeta|$ distribution of \bar{p} . Solid black curve is the result of the fit with equation (3.40): 10 – 20% centrality



(c) p_T^2 distribution of p . Solid black curve is the result of the fit with equation (3.44): 10 – 20% centrality

(d) p_T^2 distribution of \bar{p} . Solid black curve is the result of the fit with equation (3.44): 10 – 20% centrality

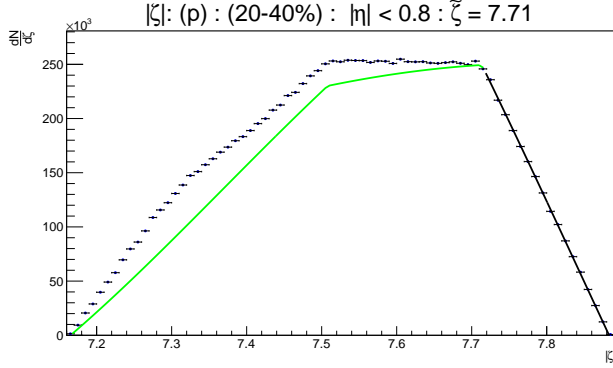


(e) $|\cos(\theta)|$ distribution of p . Solid red curve is the result of the fit with equation (3.43): 10 – 20% centrality

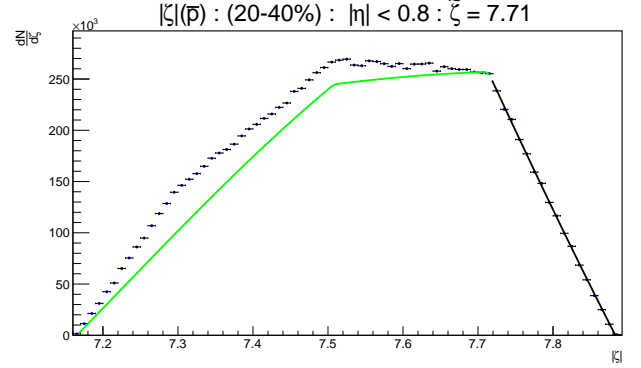
(f) $|\cos(\theta)|$ distribution of \bar{p} . Solid red curve is the result of the fit with equation (3.43): 10 – 20% centrality

Figure 6.19: ALICE $|\zeta|$, p_T^2 and $|\cos(\theta)|$ distributions fitted with (3.40), (3.44), and (3.43) respectively for $p(\bar{p})$, 10 – 20% centrality. The green curve in the ζ distribution is the extrapolation of the fit.

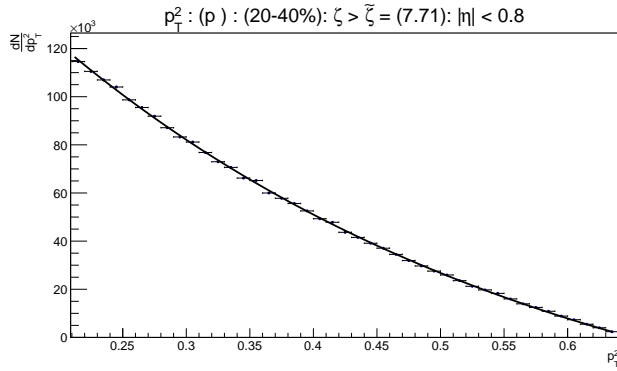
Protons (20-40 %)



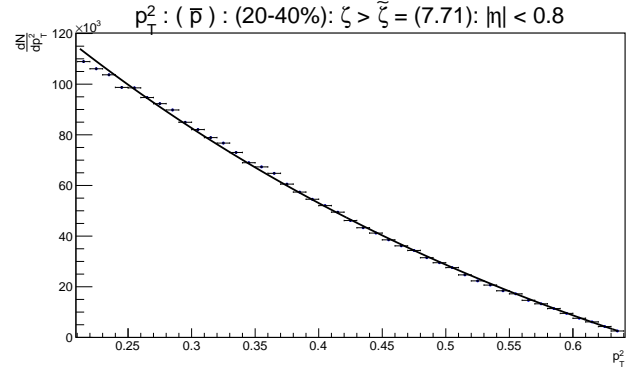
(a) $|\zeta|$ distribution of p . Solid black curve is the result of the fit with equation (3.40): 20 – 40% centrality



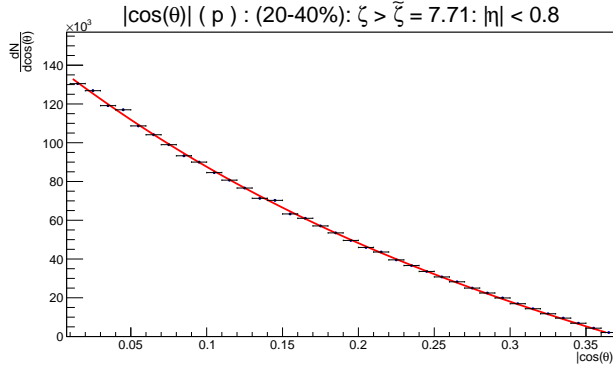
(b) $|\zeta|$ distribution of \bar{p} . Solid black curve is the result of the fit with equation (3.40): 20 – 40% centrality



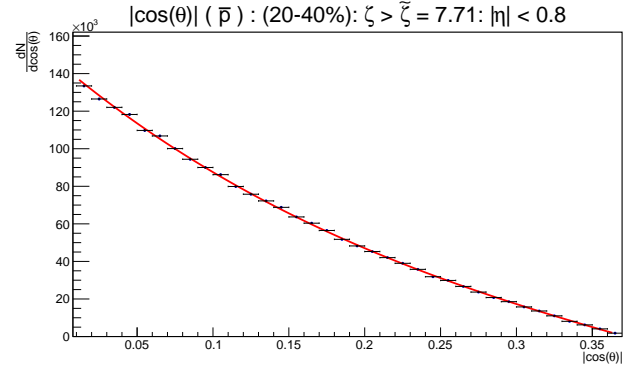
(c) p_T^2 distribution of p . Solid black curve is the result of the fit with equation (3.44): 20 – 40% centrality



(d) p_T^2 distribution of \bar{p} . Solid black curve is the result of the fit with equation (3.44): 20 – 40% centrality



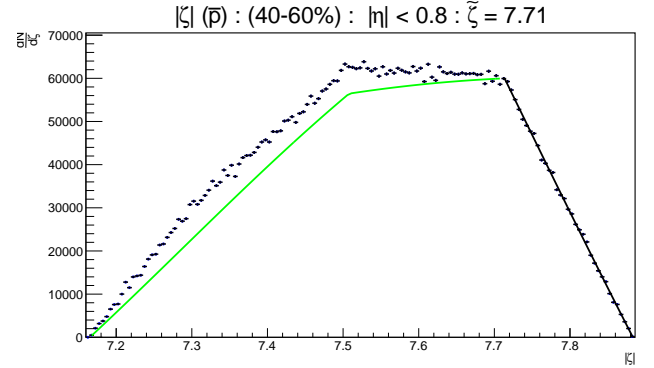
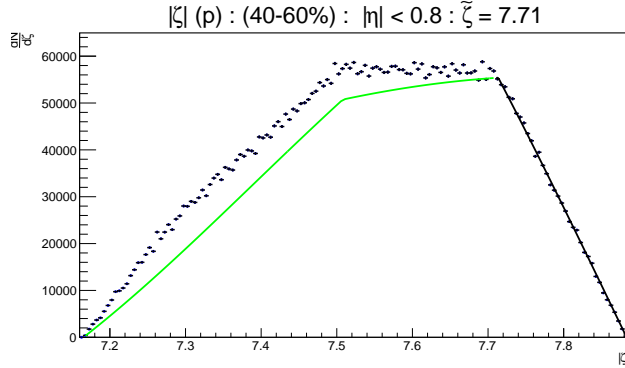
(e) $|\cos(\theta)|$ distribution of p . Solid red curve is the result of the fit with equation (3.43): 20 – 40% centrality



(f) $|\cos(\theta)|$ distribution of \bar{p} . Solid red curve is the result of the fit with equation (3.43): 20 – 40% centrality

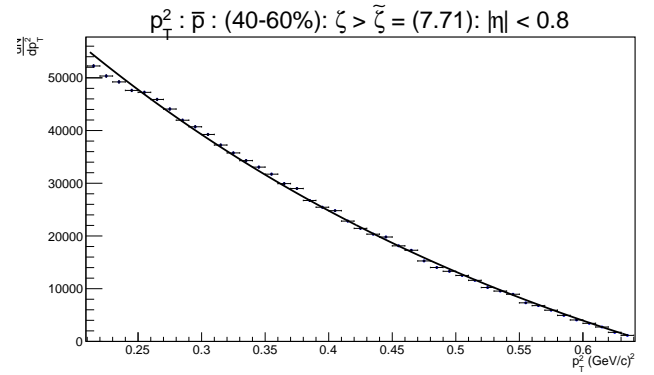
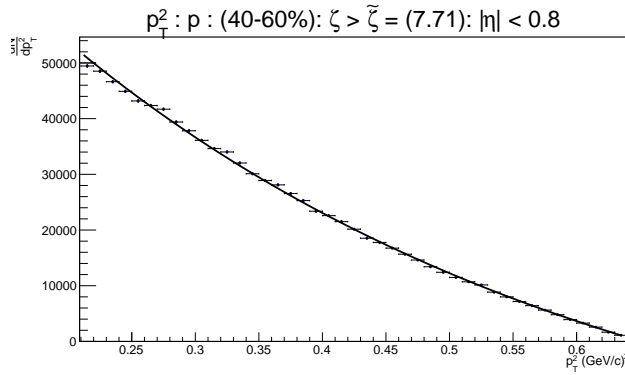
Figure 6.20: ALICE $|\zeta|$, p_T^2 and $|\cos(\theta)|$ distributions fitted with (3.40), (3.44), and (3.43) respectively for $p(\bar{p})$, 20 – 40% centrality. The green curve in the ζ distribution is the extrapolation of the fit.

Protons (40-60 %)



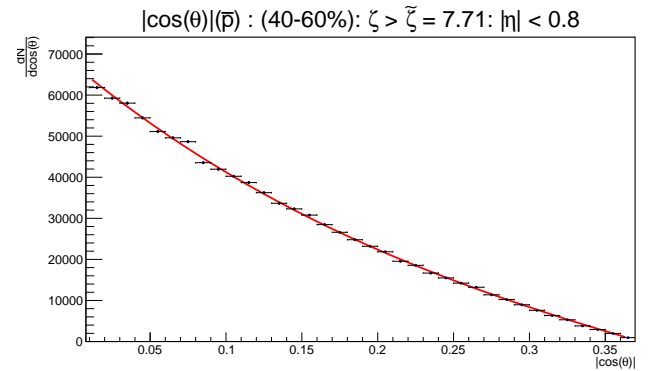
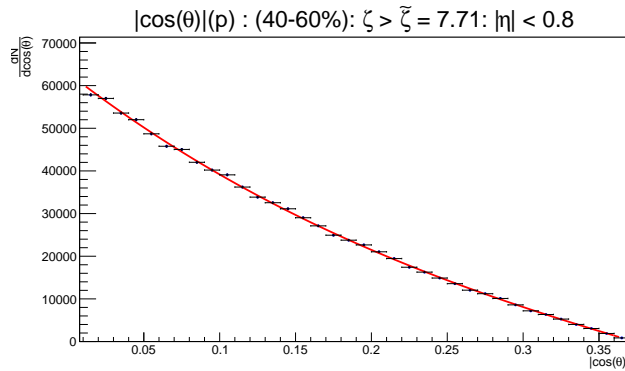
(a) $|\zeta|$ distribution of p . Solid black curve is the result of the fit with equation (3.40): 40 – 60% centrality

(b) $|\zeta|$ distribution of \bar{p} . Solid black curve is the result of the fit with equation (3.40): 40 – 60% centrality



(c) p_T^2 distribution of p . Solid black curve is the result of the fit with equation (3.44): 40 – 60% centrality

(d) p_T^2 distribution of \bar{p} . Solid black curve is the result of the fit with equation (3.44): 40 – 60% centrality

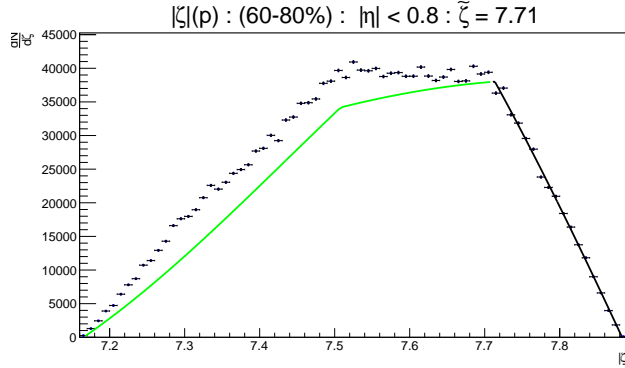


(e) $|\cos(\theta)|$ distribution of p . Solid red curve is the result of the fit with equation (3.43): 40 – 60% centrality

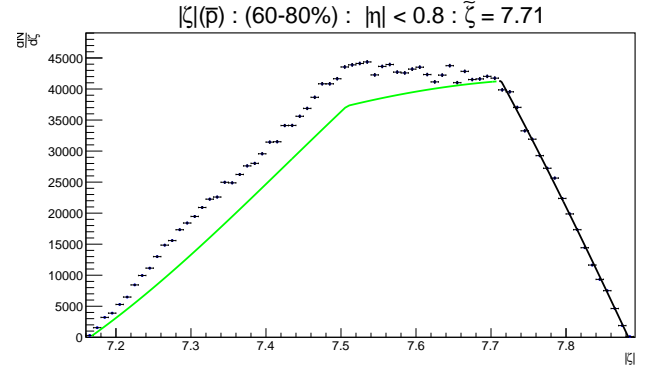
(f) $|\cos(\theta)|$ distribution of \bar{p} . Solid red curve is the result of the fit with equation (3.43): 40 – 60% centrality

Figure 6.21: ALICE $|\zeta|$, p_T^2 and $|\cos(\theta)|$ distributions fitted with (3.40), (3.44), and (3.43) respectively for $p(\bar{p})$, 40 – 60% centrality. The green curve in the ζ distribution is the extrapolation of the fit.

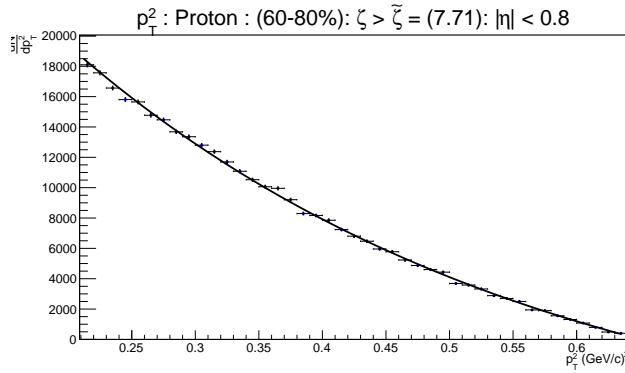
Protons (60-80 %)



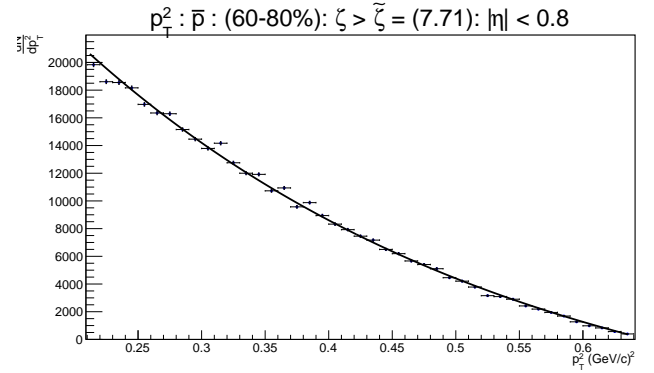
(a) $|\zeta|$ distribution of p . Solid black curve is the result of the fit with equation (3.40): 60 – 80% centrality



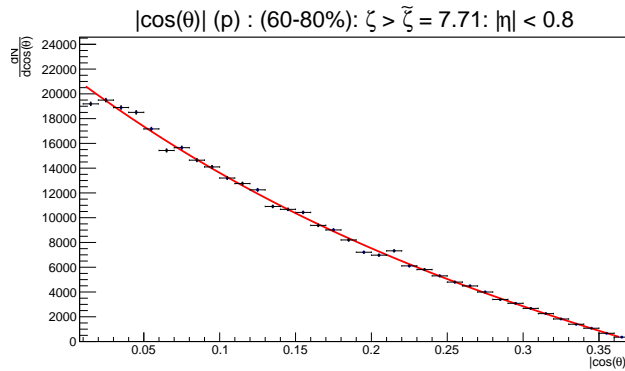
(b) $|\zeta|$ distribution of \bar{p} . Solid black curve is the result of the fit with equation (3.40): 60 – 80% centrality



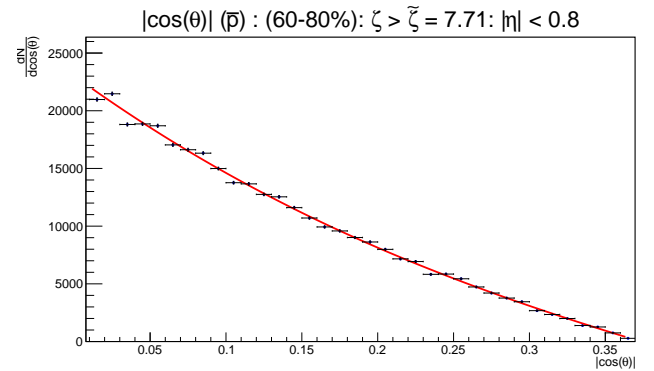
(c) p_T^2 distribution of p . Solid black curve is the result of the fit with equation (3.44): 60 – 80% centrality



(d) p_T^2 distribution of \bar{p} . Solid black curve is the result of the fit with equation (3.44): 60 – 80% centrality



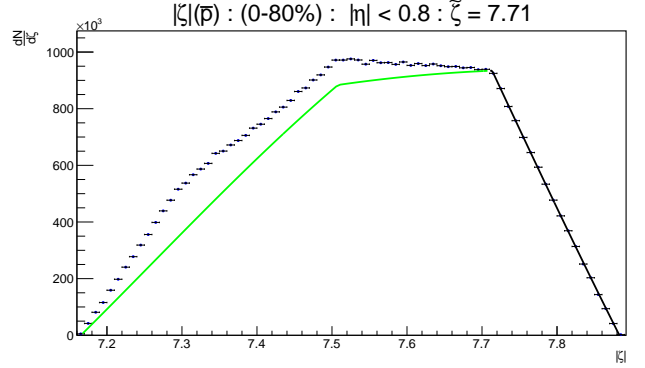
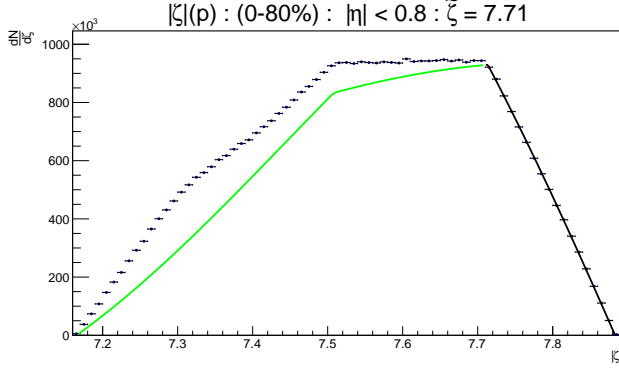
(e) $|\cos(\theta)|$ distribution of p . Solid red curve is the result of the fit with equation (3.43): 60 – 80% centrality



(f) $|\cos(\theta)|$ distribution of \bar{p} . Solid red curve is the result of the fit with equation (3.43): 60 – 80% centrality

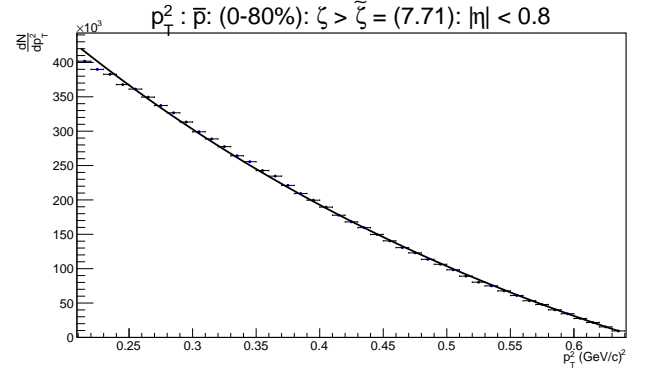
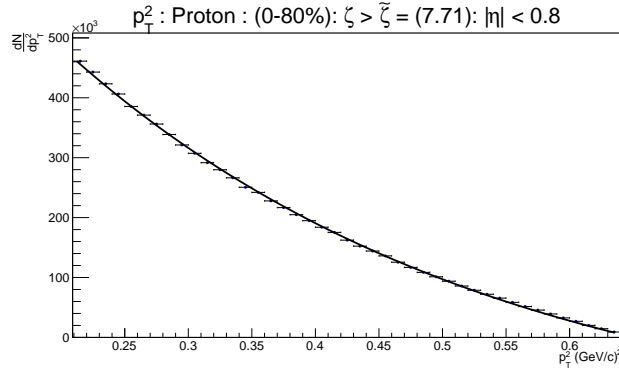
Figure 6.22: ALICE $|\zeta|$, p_T^2 and $|\cos(\theta)|$ distributions fitted with (3.40), (3.44), and (3.43) respectively for $p(\bar{p})$, 60 – 80% centrality. The green curve in the ζ distribution is the extrapolation of the fit.

Protons (0-80 %)



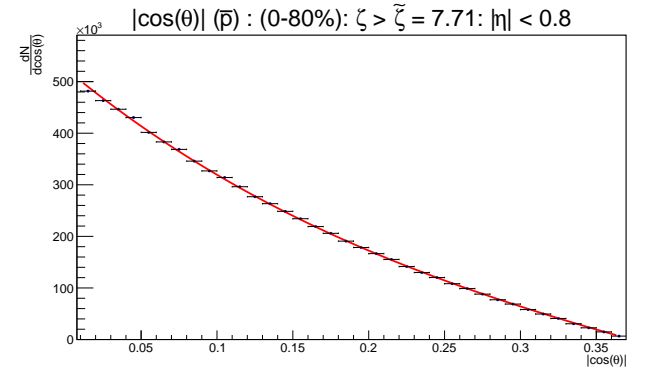
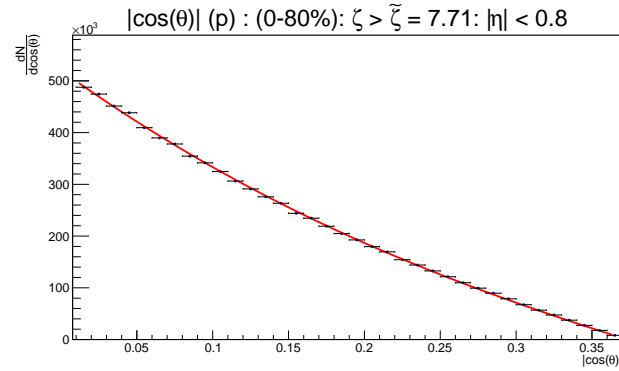
(a) $|\zeta|$ distribution of p . Solid black curve is the result of the fit with equation (3.40): 0 – 80% centrality

(b) $|\zeta|$ distribution of \bar{p} . Solid black curve is the result of the fit with equation (3.40): 0 – 80% centrality



(c) p_T^2 distribution of p . Solid black curve is the result of the fit with equation (3.44): 0 – 80% centrality

(d) p_T^2 distribution of \bar{p} . Solid black curve is the result of the fit with equation (3.44): 0 – 80% centrality



(e) $|\cos(\theta)|$ distribution of p . Solid red curve is the result of the fit with equation (3.43): 0 – 80% centrality

(f) $|\cos(\theta)|$ distribution of \bar{p} . Solid red curve is the result of the fit with equation (3.43): 0 – 80% centrality

Figure 6.23: ALICE $|\zeta|$, p_T^2 and $|\cos(\theta)|$ distributions fitted with (3.40), (3.44), and (3.43) respectively for $p(\bar{p})$, 0 – 80% centrality. The green curve in the ζ distribution is the extrapolation of the fit.

Deuterons

The $n\sigma$ PID scheme also can be used with TPC to identify deuterons. A band of raw deuterons can be seen in the dE/dx versus TPC momentum plot (The topmost band in 6.24a). However, we do not have a reliable Monte Carlo to calculate the correction factors for the raw distributions, unlike the species we discussed so far. But, in the range $0.40 < p_T < 0.90$ GeV/c, we know that the correction factor for protons is nearly flat. It is very much reasonable to assume that the behaviour of the correction factor for deuterons in the same p_T range will be having the same shape [140]. This would mean that the shape of the raw distributions will remain more or less the same even if we apply proper corrections. Making such an assumption, we made a light front analysis on the ALICE deuterons with a $n\sigma = 3.0$ cut. The results of which are presented in Figure 6.24. The temperatures obtained for ζ , p_T^2 and $\cos(\theta)$ distributions are 128 ± 20 , 128 ± 1 and 125 ± 5 MeV

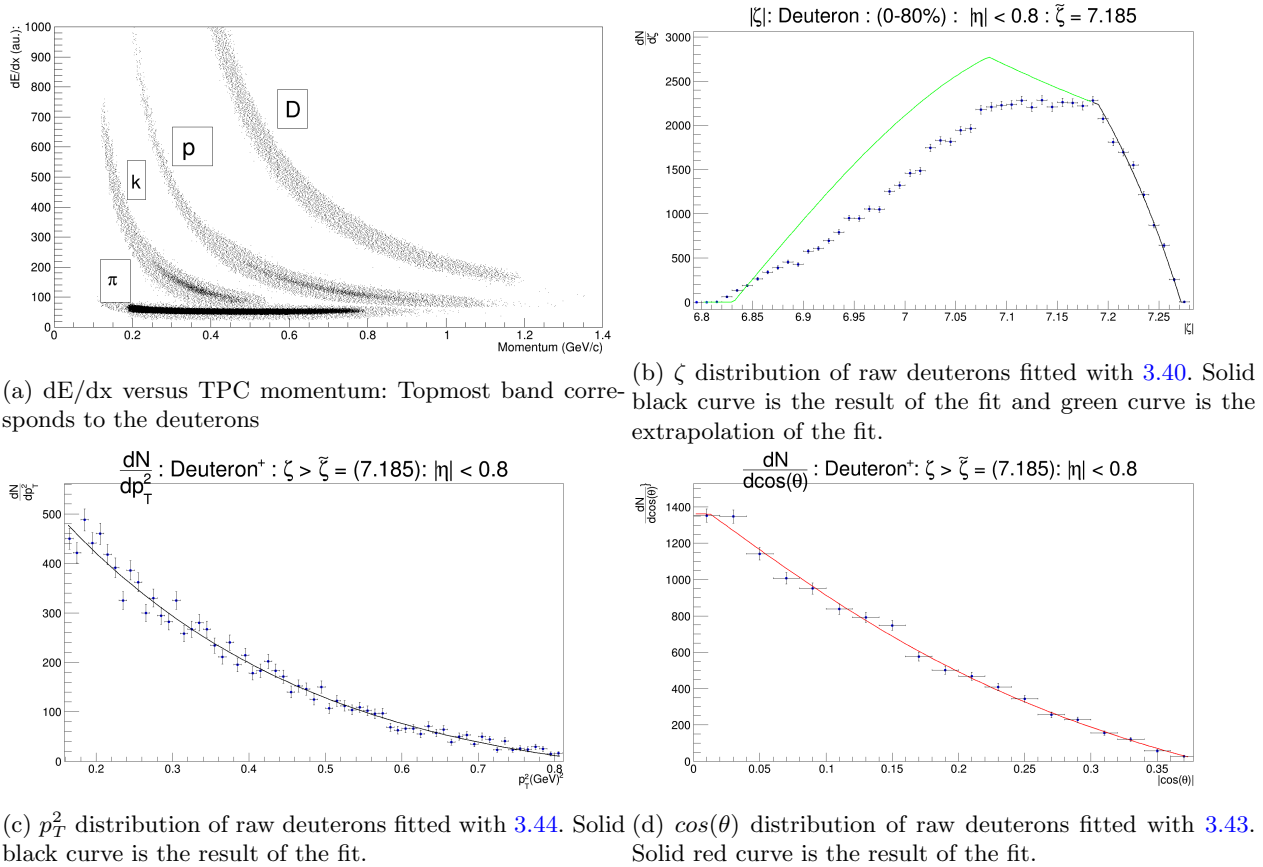


Figure 6.24: Results of the light front analysis over ALICE raw deuterons assuming a flat correction factor in the region $0.40 < p_T < 0.90$ GeV/c and $|\eta| < 0.8$

respectively. We can see that the light front scheme works for the raw deuterons and the equations (3.40),

(3.44) and (3.43) with $f(E)$ having the form as in (3.42) can describe the distributions with a convergence of temperature for the ζ , $\cos(\theta)$ and p_T^2 distributions. The binding energy of deuterons is very small (≈ 2.2 MeV) making it to break up fast. Deuterons produced in the hot and dense medium have no chance to survive. So it is very reasonable to think that the deuterons that we observe are formed in a dilute cold down medium via coalescence of protons and neutrons, not in the initial stages of the collision. For a $\tilde{\zeta} = 7.185$, we get a temperature around 125 MeV from our analysis. **The observed temperature for protons is larger than that of the deuterons. It impels one to think that there are deuterons in the final state, which are indeed produced after the medium getting cooled down and the existing thermalised protons taking part in a coalescence mechanism with the nearby neutrons having small relative momenta in such a dilute medium.** It is worth to note that our result is consistent with that of Han Liu in [141] obtained using techniques of interferometry that the deuterons we observe in nucleus nucleus collisions, which are possibly formed during the freeze-out stage, are emitted from the surface layer of the source. Hence we see that this kind of an analysis using the light front variables may be used to study the production mechanism of the observed deuterons in nucleus-nucleus collisions. Now let us take a quick recap of the light front analysis with ALICE data we have done and the results we obtained from it so far.

A Comprehensive view of the analysis and Conclusions

Our attempts to implement the light front analysis standing within the kinematic restrictions of ALICE experiment at LHC began with a study using the Monte Carlo models. The light front variable ξ originally is defined in the centre of the mass frame as in equation(3.27). It was found in the lower energy experiments that the ξ distribution has very sharp maxima close to the origin [47]. So to study the behaviour about the maxima, a logarithmic version of the same variable namely ζ was introduced as in equation (3.30). The general idea is to make the light front variable ($|\zeta|$) distribution and fit it with the equation 3.40 with energy distribution assuming the form as in equation (3.42). Then find up to what value of ζ , we can do it successfully. The temperature that we get from it is marked as $T(\zeta_0)$. The constant ζ_0 makes a paraboloid in the phase space, which is a realisation of an underlying Lobachevsky geometry. Once we find such a value, say ζ_0 , we divide the phase space of species into two regions. One with particles having $\zeta > \zeta_0$, and another region with $\zeta < \zeta_0$. For each of these regions, we make two distributions. Namely the p_T^2 distribution and the distribution of the cosine of the polar angle ($|\cos(\theta)|$). For each of them, we try to fit the equations 3.44 and 3.43 respectively and obtain temperatures $T(|\cos(\theta)|)$ and $T(p_T^2)$. If these temperatures are consistent with

$T(\zeta_0)$, we take the value $\zeta = \zeta_0 = \tilde{\zeta}$ as our final constant surface of paraboloid. If the temperatures are not consistent, we again search for such a ζ_0 which obeys this criterion. The analysis over HIJING events with the kinematic cuts gave us some confidence that we can incorporate the kinematic cuts in our numerical integration and fitting procedure and still can extract a $\tilde{\zeta}$ which gives us a consistent temperature from all the three distributions. The existence of such a $\tilde{\zeta}$ would mean that there are thermalised particles in the phase space we are looking at, as the equations (3.40), (3.44) and (3.43) with $f(E)$ having the form as in (3.42) used for our calculations assumes a maximum entropy state. Now, knowing that the analysis is feasible with kinematic cuts alone would not solve all the hurdles in our path to reach the goal of implementing it with ALICE data. For this, we have to go through several steps before even starting the actual analysis procedure. We start from the selection of analysable runs. There is a set of runs prescribed by the ALICE collaboration, which are fit for analysis [129]. From this, we took the runs marked as *good* (see Appendix B for the run numbers). After selecting the runs, we implemented the minimum bias trigger and all the events passing the trigger criterion and cut on the Z position of the vertex were selected for further analysis. Using the information about the multiplicity from the V0 detector, we further classify them into seven centrality regions [126]. After this classification, we go into the events and all the tracks which survive our default track quality cuts (6.1.3) are selected for identification. For each species, depending on their separation as discrete bands in dE/dx v/s TPC momentum plot, we make a transverse momentum cut for each species. One of the most difficult points in this entire analysis was the selection of a proper range of p_T for the case of kaons. The kaon band starts to merge with the electron band around 0.42 GeV in TPC momentum. After this point, it is nearly impossible to distinguish between electrons and kaons. If we extend our analysis beyond this point, it will certainly become more dependent on the nature of the Monte Carlo we use to correct the raw distributions. Also, it significantly alters the final results as well. So a narrow transverse momentum range for kaons became an absolute necessity in implementing the analysis over these particles. The p_T ranges considered for the particles are visualised in Figure 6.25. Once we select the tracks, the next step is to implement the $n\sigma(TPC)$ scheme to identify and classify them into different species. After this identification procedure, we have a group of particles belonging to three species for each of the centrality regions under consideration. Now we can come back to our light front analysis. With the tracks thus selected, we make the $|\zeta|$ distribution for each species and each centrality region. These raw $|\zeta|$ distributions have to be corrected for acceptance, tracking, PID and misidentification efficiencies of the detector. For this purpose, there are anchored Monte Carlo data in ALICE for each run. We use it to calculate a final correction factor for the $|\zeta|$ distributions as described in section 6.1.5. The corrected $|\zeta|$ distributions are now used for fitting with

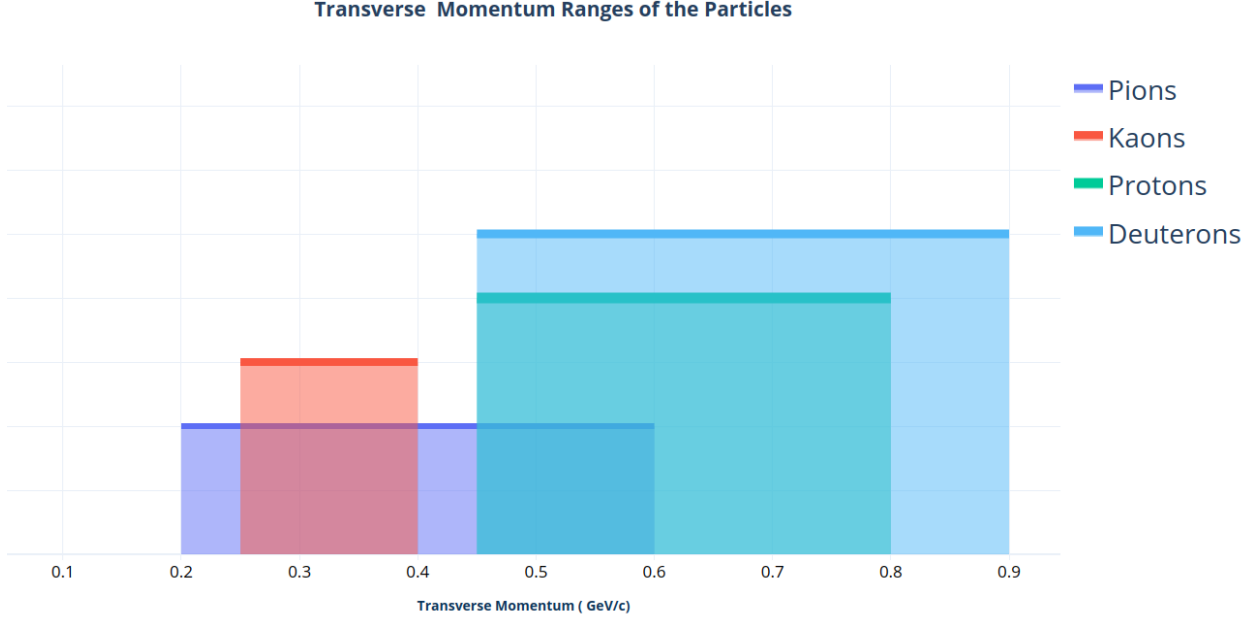


Figure 6.25: p_T Ranges for the identified particle species

the equation (3.40) and we find a ζ_0 up to which we can make a successful fit. For this ζ_0 , we make the raw p_T^2 distribution and raw $|\cos(\theta)|$ distribution. The next step is to apply the correction factor for each of these distributions and make corrected distributions, suitable for fitting. On these corrected p_T^2 and $|\cos(\theta)|$ distributions, we try to fit equations 3.44 and equation 3.43 and see whether the temperatures from the three are consistent or not. If they are consistent, we take our final paraboloidal surface $\tilde{\zeta} = \zeta_0$. If they are not consistent, we repeat the entire analysis until we find such a constant ζ_0 which gives consistent temperatures from all the three distributions. We see that for all our attempts at each of the centrality regions and species, *we were able to find such a critical paraboloid!* The paraboloids we obtained from this analysis for various species are pictured in Figure 6.26. An average temperature (see equation 4.8) obtained from the light front analysis is shown in Figure 6.27 as a function of the mass of the particle. We can see that the obtained temperature varies with the mass of the particle. The HIJING predictions of the temperatures for nearly the same p_T are very close to the measured value for the case of pions. However, it predicts lower values of temperature for higher mass particles compared to the observed temperatures from ALICE. Table 6.5 -6.11 summarises the whole of the Light Front analysis results we have obtained with the ALICE data. A weighted average of the temperatures (see equation 4.8) obtained from various distributions for various species of particles are shown as a function of the collision centrality in Figure 6.28. The first thing that we observe from this analysis is that the temperature we obtained increases as the mass of the particle increases. For the

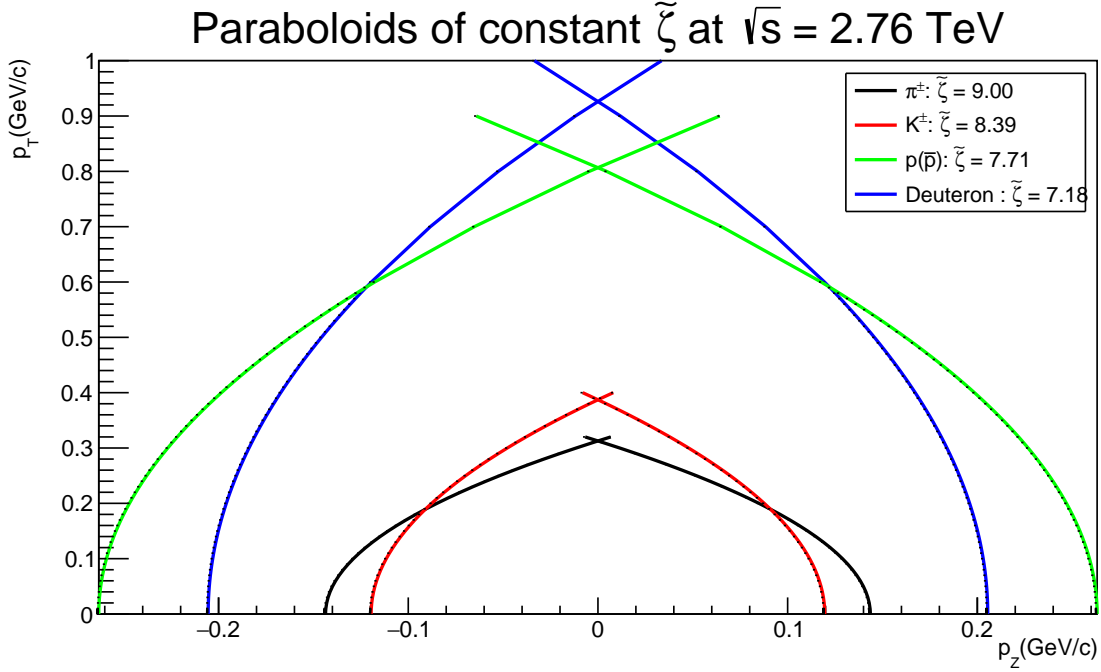


Figure 6.26: Paraboloids corresponding to the $\tilde{\zeta}$ values used in this analysis for various particle species.

case of pions, it is around 85 MeV in the p_T region we considered. The temperature for pions, both positive and negative, does not show any significant change in its value as the centrality of the collision changes. It is very much consistent with the minimum bias temperature (marked as red and black lines in Figure: 6.28). However, for kaons and protons, we can see that the temperatures obtained from the light front scheme slightly vary with the centrality of the collision. For the case of kaons, we see that at centralities 10 – 20% and 60 – 80%, there is a slight difference in the obtained temperatures for positive and negative kaons in addition to the variation concerning the centrality (marked as blue and green rectangular points in Figure 6.28). For the case of protons and antiprotons (marked as salmon and slate-blue diamond-shaped points in Figure 6.28), the difference is even larger. For most of the centrality regions, the antiproton temperature is larger than the proton temperature. Note that both of them were obtained with a $\tilde{\zeta} = 7.71$. We know that the Geant3 (Monte Carlo filter for detector simulations) cross-section for K^- and \bar{p} absorbed in materials are overestimated and K^- generated by weak-decays are underestimated ([142], [143]). This might contribute to the difference in temperatures between the corresponding particles and antiparticles. However, we cannot rule out the possibility of it arising from the difference in their production mechanisms. In short, we need more detailed studies to understand the variation of temperatures obtained from the light front analysis of kaons and protons as a function of the centrality, and the difference in temperatures with protons and

antiprotons. We also performed analysis over the raw deuterons we identified using the same procedures except for the fact that the raw distributions were never corrected in this case using Monte Carlo. The correction factor for the protons in the same p_T range was found to be nearly flat. So we assume that it will stay so for the deuterons as well and that the corrections will not alter the shape of the distributions or the results of the fit. Following this logic, we found out a ζ_0 for deuteron which obeys our criterion and we could obtain a temperature of about 125 MeV from the fit. This would mean that there exist a part of the phase space for deuterons, which can be described by the Boltzmann statistics which assumes a maximum entropy state. So it is compelling to think that there are thermalised deuterons in the phase space. It might also shed some light into the production process of these particles. The binding energy of deuterons is very small (≈ 2.2 MeV). So most probably the deuterons we observe are produced in a dilute medium, not in the initial stages of the collision. One possibility of their formation is that the already thermalised protons take part in coalescence with the neutrons having small relative momenta resulting in the production of deuterons in a medium which is cooled down.

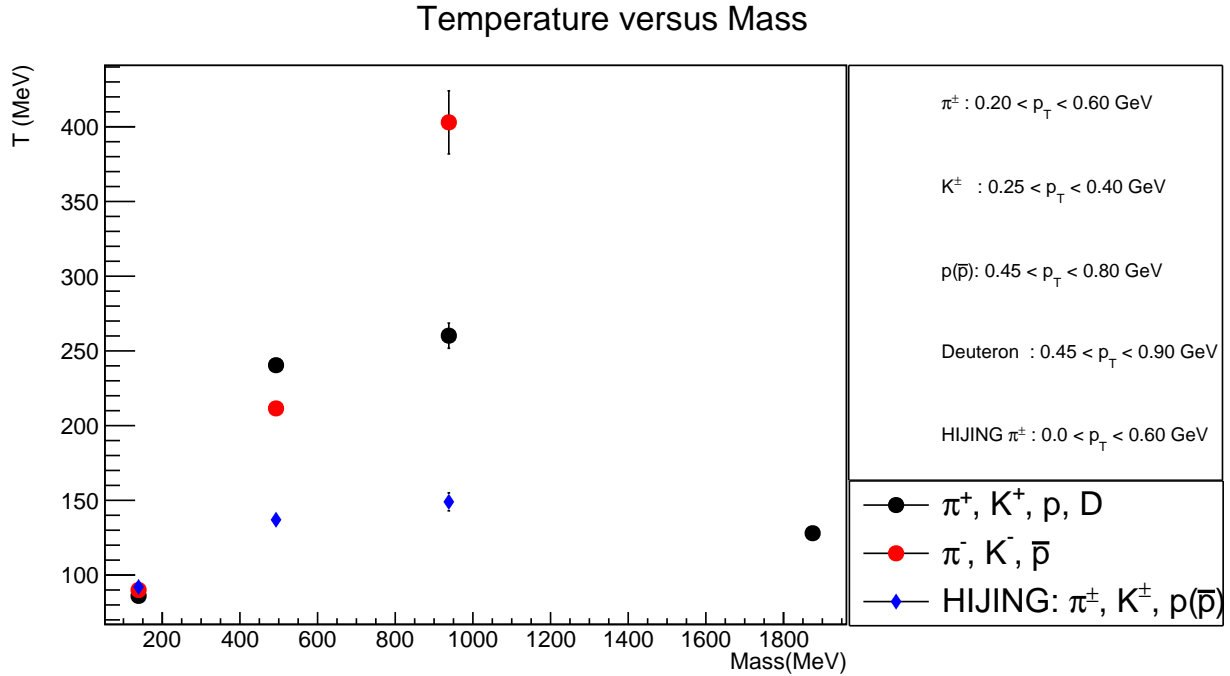


Figure 6.27: Temperature obtained from the light front scheme in the minimum bias trigger as a function of the mass of the particle. (see equation 4.8)

We have seen that the light front scheme we discussed in details, works with ALICE data irrespective of the large centre of mass-energy, the centrality of the collision and the mass of the particles we considered.

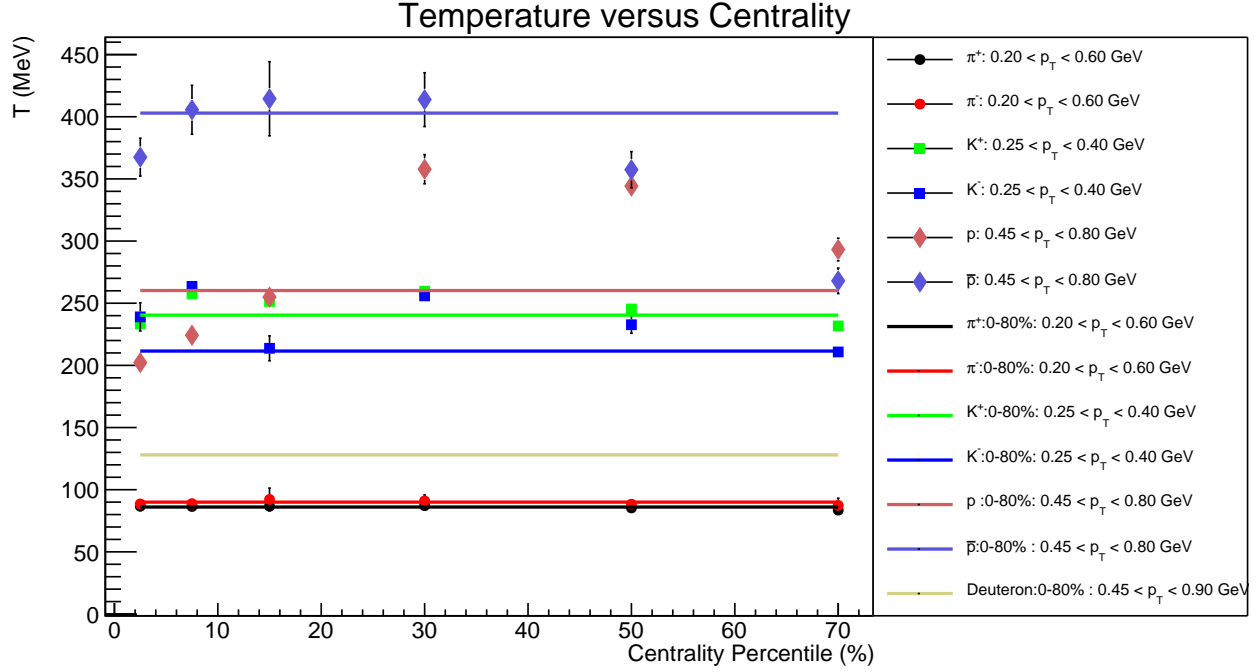


Figure 6.28: Temperature versus centrality percentile. The regions of centrality percentile considered are 0 – 5%, 5 – 10%, 10 – 20%, 20 – 40%, 40 – 60% and 60 – 80%. The mean value is used to mark the points. (see equation 4.8)

| Species | $\tilde{\zeta}$ | T(Mev) from ζ | χ^2/ndf | T(Mev) from p_T^2 | χ^2/ndf | T(Mev) from $\cos(\theta)$ | χ^2/ndf |
|-----------|-----------------|---------------------|--------------|---------------------|--------------|----------------------------|--------------|
| π^+ | 9.00 | 104 ± 13 | 0.1/15 | 86.6 ± 5 | 10./20 | 84.2 ± 5 | 4/36 |
| K^+ | 8.39 | 232 ± 28 | 5/14 | 226.5 ± 27 | 0.3/9 | 237.0 ± 18 | 2/14 |
| p | 7.71 | 243 ± 20 | 2/15 | 200.9 ± 4 | 36/41 | 222.7 ± 12 | 12/34 |
| π^- | 9.00 | 107 ± 13 | 0.1/15 | 89.5 ± 7 | 1/20 | 88.06 ± 2 | 3/36 |
| K^- | 8.39 | 201 ± 26 | 8/14 | 229.6 ± 34 | 0.3/9 | 246.8 ± 11 | 2/14 |
| \bar{p} | 7.71 | 388 ± 17 | 23/33 | 363.0 ± 8 | 14/41 | 344.5 ± 18 | 19/35 |

Table 6.5: Temperatures obtained Light Front analysis over ALICE hadrons: 0 – 5%

| Species | $\tilde{\zeta}$ | T(Mev) from ζ | χ^2/ndf | T(Mev) from p_T^2 | χ^2/ndf | T(Mev) from $\cos(\theta)$ | χ^2/ndf |
|-----------|-----------------|---------------------|--------------|---------------------|--------------|----------------------------|--------------|
| π^+ | 9.0 | 104 ± 13 | 0.12/15 | 87 ± 5 | 1/20 | 85 ± 3 | 3/36 |
| K^+ | 8.39 | 260 ± 22 | 6/15 | 258 ± 15 | 0.1/9 | 251 ± 31 | 3/14 |
| p | 7.71 | 260 ± 13 | 1/15 | 222 ± 3 | 20/41 | 234 ± 13 | 10/34 |
| π^- | 9.0 | 107 ± 13 | 0.1/15 | 90 ± 9 | 1/20 | 88 ± 2 | 3/36 |
| K^- | 8.39 | 264 ± 24 | 6/15 | 262 ± 29 | 0.1/9 | 272 ± 61 | 2/14 |
| \bar{p} | 7.71 | 446 ± 70 | 7/15 | 390 ± 24 | 25/41 | 461 ± 52 | 9/34 |

Table 6.6: Temperatures obtained light front analysis over ALICE hadrons: 5 – 10%

We could always find a constant value in ζ , which gives us a consistent temperature from all the three distributions under consideration. The temperatures extracted from the three distributions for each species

| Species | $\tilde{\zeta}$ | T(Mev) from ζ | χ^2/ndf | T(Mev) from p_T^2 | χ^2/ndf | T(Mev) from $\cos(\theta)$ | χ^2/ndf |
|-----------|-----------------|---------------------|--------------|---------------------|--------------|----------------------------|--------------|
| π^+ | 9.00 | 104 ± 11 | 0.1/15 | 87 ± 5 | 0.8/20 | 86 ± 2 | 4/36 |
| K^+ | 8.39 | 249 ± 6 | 4/15 | 257 ± 10 | 0.3/9 | 261 ± 28 | 2/14 |
| p | 7.71 | 297 ± 14 | 1/15 | 252 ± 4 | 12/41 | 286 ± 21 | 8/34 |
| π^- | 9.00 | 107 ± 13 | 0.1/15 | 90 ± 5 | 0.8/20 | 90 ± 7 | 4/36 |
| K^- | 8.39 | 199 ± 13 | 9/15 | 227 ± 13 | 0.2/9 | 228 ± 37 | 3/14 |
| \bar{p} | 7.71 | 509 ± 103 | 0.5/15 | 396 ± 24 | 24/41 | 516 ± 72 | 8/34 |

Table 6.7: Temperatures obtained light front analysis over ALICE hadrons: 10 – 20%

| Species | $\tilde{\zeta}$ | T(Mev) from ζ | χ^2/ndf | T(Mev) from p_T^2 | χ^2/ndf | T(Mev) from $\cos(\theta)$ | χ^2/ndf |
|-----------|-----------------|---------------------|--------------|---------------------|--------------|----------------------------|--------------|
| π^+ | 9.00 | 105 ± 12 | 0.1/15 | 88 ± 5 | 0.7/20 | 87 ± 2 | 4/39 |
| K^+ | 8.39 | 252 ± 32 | 4/15 | 268 ± 25 | 0.1/9 | 258 ± 17 | 4/14 |
| p | 7.71 | 367 ± 24 | 0.4/14 | 311 ± 53 | 5/41 | 359 ± 28 | 4/34 |
| π^- | 9.00 | 108 ± 13 | 0.1/15 | 90 ± 6 | 0.6/20 | 90 ± 3 | 3/36 |
| K^- | 8.39 | 248 ± 31 | 3/15 | 251 ± 30 | 0.1/9 | 258 ± 40 | 2/14 |
| \bar{p} | 7.71 | 498 ± 48 | 0.7/14 | 403 ± 14 | 23/41 | 505 ± 70 | 3/34 |

Table 6.8: Temperatures obtained light front analysis over ALICE hadrons: 20 – 40%

| Species | $\tilde{\zeta}$ | T(Mev) from ζ | χ^2/ndf | T(Mev) from p_T^2 | χ^2/ndf | T(Mev) from $\cos(\theta)$ | χ^2/ndf |
|-----------|-----------------|---------------------|--------------|---------------------|--------------|----------------------------|--------------|
| π^+ | 9.00 | 103 ± 12 | 0.7/15 | 86 ± 35 | 0.6/20 | 84.7 ± 2 | 4/36 |
| K^+ | 8.39 | 242 ± 6 | 0.4/7 | 261 ± 16 | 1/9 | 248 ± 10 | 3/14 |
| p | 7.71 | 346 ± 19 | 19/33 | 342 ± 15 | 14/41 | 373 ± 63 | 6/34 |
| π^- | 9.00 | 107 ± 12 | 0.1/15 | 90 ± 7 | 0.5/20 | 87.7 ± 2 | 4/36 |
| K^- | 8.39 | 236 ± 39 | .3/7 | 222 ± 22 | 0.5/9 | 242.0 ± 20 | 1/14 |
| \bar{p} | 7.71 | 440 ± 31 | 15/33 | 352 ± 7 | 30/41 | 441 ± 69 | 8/34 |

Table 6.9: Temperatures obtained light front analysis over ALICE hadrons: 40 – 60%

| Species | $\tilde{\zeta}$ | T(Mev) from ζ | χ^2/ndf | T(Mev) from p_T^2 | χ^2/ndf | T(Mev) from $\cos(\theta)$ | χ^2/ndf |
|-----------|-----------------|---------------------|--------------|---------------------|--------------|----------------------------|--------------|
| π^+ | 9.00 | 101 ± 12 | 0.2/15 | 84 ± 5 | 0.4/20 | 83 ± 2 | 7/36 |
| K^+ | 8.39 | 237 ± 8 | 0.5/7 | 230 ± 4 | 0.8/9 | 233 ± 4 | 6/14 |
| p | 7.71 | 303 ± 7 | 4/15 | 286 ± 8 | 18/41 | 336 ± 27 | 28/34 |
| π^- | 9.00 | 106 ± 14 | 0.3/15 | 88 ± 6 | 0.7/20 | 86 ± 4 | 4/36 |
| K^- | 8.39 | 194 ± 27 | 0.3/7 | 211 ± 6 | 1/9 | 223 ± 3 | 2/14 |
| \bar{p} | 7.71 | 311 ± 17 | 6/15 | 264 ± 5 | 39/41 | 306 ± 27 | 24/34 |

Table 6.10: Temperatures obtained light front analysis over ALICE hadrons: 60 – 80%

indicate that a part of the system has got thermalised and follows Boltzmann distributions. However, we cannot discard the possibility of the existence of thermalised particles from the region outside the paraboloid ($\zeta < \tilde{\zeta}$). Apart from the value of temperatures, the shape of the resulting distributions was always fittable with the equations 3.40, 3.43, and 3.44 assuming a Boltzmannian energy distribution (3.42), with cuts on

| Species | ζ | T(Mev) from ζ | χ^2/ndf | T(Mev) from p_T^2 | χ^2/ndf | T(Mev) from $\cos(\theta)$ | χ^2/ndf |
|-----------|---------|---------------------|--------------|---------------------|--------------|----------------------------|--------------|
| π^+ | 9.00 | 104 ± 12 | 0.1/15 | 87 ± 6 | 0.7/20 | 86 ± 2 | 4/36 |
| K^+ | 8.39 | 238 ± 10 | 2/16 | 241 ± 3 | 0.1/9 | 228 ± 18 | 3/14 |
| p | 7.71 | 293 ± 12 | 4/33 | 256 ± 4 | 7/41 | 283 ± 20 | 3/34 |
| π^- | 9.00 | 107 ± 13 | 0.1/15 | 90 ± 6 | 0.7/20 | 89 ± 3 | 3/36 |
| K^- | 8.39 | 228 ± 18 | 1/15 | 212 ± 15 | 0.1/9 | 219 ± 33 | 4/14 |
| \bar{p} | 7.71 | 474 ± 26 | 3/33 | 391 ± 10 | 15/41 | 490 ± 65 | 2/34 |
| d | 7.185 | 128 ± 20 | 7/8 | 128 ± 1 | 109/63 | 125 ± 5 | 7/17 |

Table 6.11: Temperatures obtained light front analysis over ALICE hadrons: 0 – 80%

pseudorapidity and transverse momentum values. So we can conclude that such an analysis is feasible with experiments having the kind of restrictions ALICE has with it on the kinematics of the detected particles. All these forces us to think that the light front scheme indeed is not working just as a sheer coincidence due to the low centre of mass energies of the collision in the old experiments or the low masses of the particle considered in those studies. But something very fundamental to the idea does exist and we see the real-world confirmation of it from these studies. More detailed analysis of this topic now becomes necessary to understand the consequences of the division of the particles into two groups in the phase space at multiparticle levels. The estimation of coefficients of collective flow, fluctuations, two- and multi-particle correlations etc for the two regions separated by the critical value in the light front variable might give us more information about any possible difference in the dynamics of the particles in those two groups.

Levchenko’s paper revisited

Now when the analysis of our data is completed, it is a good moment to confront its results with the opinion made by Levechenko in his paper [55], which we mentioned in the section ”Some counter-arguments from the past” (3.8). We recall that according to Levchenko, the observation at the beginning of the 70s [51] of the critical surface in the phase space at low energy (≈ 6 GeV in c.m.s) allowing to single out the isotropic pions was ’fortuitous’ because:

- (i) The particles studied in the old paper were π^\pm mesons and their low mass caused the observed effect. The isotropisation should disappear for particles with higher masses.
- (ii) The available centre of mass-energy was low: at higher energies, the isotropisation should disappear as well.
- (iii) To justify his statements (i) and (ii), Levchenko made an estimation of the angular distribution for the heavier particles. He admitted in his paper that, ”A direct solution to this problem is impossible: the

experimental information on the spectra of heavy particles is inadequate, and the determination of ξ^\pm requires rather accurate data”. To overcome these problems with the calculation of ξ^\pm and the polar angle distributions for heavier particles, he made a shortcut in his calculations which he claimed will be published, but never were. The distributions he obtained can be seen in Figure 3.5. He did not attempt to analyse them using the equations (3.40), (3.43) and (3.44) with the energy distribution of the Boltzmannian form as in equation(3.42). In the current analysis, all the above points were carefully addressed, checked and studied. In particular:

ad-(i) The analysis was performed for particles with different masses (π^\pm , K^\pm , $p(\bar{p})$, Λ^0 , η^0 , $\Sigma(1192)$ and $\Xi(1317)$), and contrary to the claims of Levchenko in [55], thermalisation of the group of particles with $\zeta > \tilde{\zeta}$ was observed for all species studied.

ad-(ii) The analysis was performed for energies $\sqrt{s} = 200$ GeV and $\sqrt{s} = 2.76$ TeV, i.e. about 2-3 orders of magnitude larger than in the studies performed in [51]. The thermalisation effect was persistently present.

ad-(iii) We did not have problems Levchenko encountered in his calculations mentioned in (iii) as in our search for the critical paraboloid we used, as the inputs to our analysis, the simulated data from three advanced ”full-blooded” event generators and the real data from the LHC ALICE experiment. The paraboloid which allows to select the thermalised group of particles was present in all the cases studied. We conclude therefore that contrary to the opinion made in [55] by Levchenko, the old observation in [51] is confirmed for particles with different masses spanning from pions to deuterons and higher by orders of magnitudes of energies.

Chapter 7

Summary & Conclusions

As we reached the last chapter of this thesis, let us briefly review the ideas we have discussed so far, the calculations made and the conclusions that we have reached. We have seen that the hadronic matter at extreme conditions continues to be a very active field of research from very old times. The pre-QCD studies, the discovery of asymptotic freedom in QCD, proposals of the existence of quark-gluon plasma were all a part of it. As time passes by, more and more tools are getting implemented to know whether we have a thermalised medium in heavy-ion collisions or not. Our approach towards this problem was using the light front variables. A critical value of the light front variable ($\tilde{\zeta}$) defines a paraboloid in the phase space of the particles. We have seen that this paraboloid is a realisation of an underlying Lobachevsky geometry. It was proposed that the particles falling within and outside of this paraboloid have distinct characteristics, with one of them resembling a thermalised system which can be described by a Boltzmannian form of energy distribution. It was shown with the low energy experimental data that one of the groups of particles falling within the parabola obeys Boltzmann distribution. The critical value of the light front variable $\tilde{\zeta}$ we need for the division of the phase space is obtained from the fit over the light front variable distribution with equation (3.40) assuming a Boltzmannian form for the energy distribution as in the equation (3.42). The latter assumes the existence of a thermalised system which corresponds to the maximum entropy state. The existence of a critical value of ζ which divides the particles into two groups and gives the same temperature while fitting, within errors, for the three kinematical distributions (namely ζ , p_T^2 and $\cos(\theta)$) for one of the group of particles we considered would mean that the particle in that group has reached a state of thermalisation. We have tested the idea at RHIC energies using EPOS and UrQMD models we show that the scheme works for various particle species in this case. We also show that it works at LHC energies with HIJING model as well. More importantly, when we apply the kinematic cuts on pseudorapidity and transverse momentum for

various species in HIJING, the results are very much pleasing and promising. This tells us that the analysis is possible with an experiment of the kind of ALICE. With the knowledge gained from the Monte Carlo analysis, we then moved to ALICE experimental data. A set of data produced by one of the largest experiments on the planet. We saw the experimental setup in some details. The data collected during Run 1 of LHC, which was pre-processed for analysis, was used to perform the light front analysis. The "good events" from "good runs" were selected according to the standards of the ALICE collaboration. The events were divided into various centrality regions using the information about multiplicity from the V0 detector so that we can get an idea about how the scheme works or behaves as the impact parameter of the collision changes. Then from each such group of events, pions, kaons, and protons were identified by ALICE TPC. This would mean that we implemented the kinematic cuts and particle identification procedures. The raw distributions were then corrected for detector efficiency, acceptance etc. Finally, a completely corrected light front distribution was obtained. On this corrected light front distributions, we did fitting as mentioned earlier. Then the critical value of the light front variable $\tilde{\zeta}$ which would separate the phase space was extracted. Based on this, the other two distributions, namely the polar angle and square of transverse momentum distributions were made. These were also corrected for the distortions imparted by the detector. The final corrected plots were again used for fitting with the corresponding equations (3.43) and 3.44. We saw from our analysis that the distributions can be described very well with those equations with energy distribution being Boltzmannian. Thus for each of the particle species, temperatures were extracted for various centralities of the collision. We observed that the temperatures obtained do not significantly depend on the centrality of the collision for pions. However, some variations from this behaviour were seen for kaons and protons. A more detailed study is needed for understanding this observation. We also performed analysis over the identified deuterons without the raw distributions getting corrected in this case. The correction factors for protons are nearly flat in the p_T range we considered, which made us extend and assume the same situation for deuterons. The light front scheme works for these deuterons as well which forces us to think that the deuterons we observe are formed in a cooled down medium via coalescence of the existing thermalised protons with neutrons. The main idea of testing the scheme at various energies and masses were successful. We have seen that the UrQMD and EPOS results are indeed promising. It is now very tempting to think that the scheme might work with the RHIC heavy-ion collision data as well. The successful fitting of the scheme with the relativistic and ultrarelativistic heavy-ion collisions for various masses indicate that there is a non-trivial integral relationship between the longitudinal and transverse kinematical variables of the produced particles in the phase space of particles coming from heavy-ion collisions. The various studies we have made and the

conclusions we reached from it are listed as follows:

- The constant value of light front variable ζ forms a paraboloid in the momentum space of the particles coming from nucleus-nucleus collisions. A part of the light front distribution with a boundary defined by a critical value $\tilde{\zeta}$ was shown to obey Boltzmann statistics with old low energy experiments.
- In this thesis, we use UrQMD and EPOS heavy-ion collision models at RHIC energy, HIJING model and ALICE data at LHC energy to show that the light front analysis scheme works at RHIC and LHC energies for particles with significantly different masses.
- Using the HIJING model, we also show that the analysis is feasible with kinematic cuts incorporated into the calculations, which is a vital point in testing the scheme with ALICE experimental data.
- The light front analysis was performed with ALICE experimental data. We could always find a $\tilde{\zeta}$ which gives us the same temperature within errors from the ζ , p_T^2 and $\cos(\theta)$ distributions made from particles in the region $\zeta > \tilde{\zeta}$ for pions, kaons, protons and raw deuterons at various centralities of the collision.
- From such an analysis we reached to a conclusion that there exists a thermalised part in the phase space of the particles we considered, both in Monte Carlo models and in ALICE data.
- The successful description of the deuteron distributions within our light front scheme with a smaller temperature compared to that of protons tells us that the observed deuterons are most probably produced in a cooled down and dilute medium via coalescence mechanism of the already existing thermalised protons with neutrons.

It is very much interesting now to see how do the two groups we selected behave in terms of its multiparticle variables. The azimuthal angle correlation, collective flow coefficients, fluctuations, HBT radii are all on the table to see whether there is any more hint towards understanding the process of thermalisation. A very close and careful study is needed to correctly interpret the temperatures obtained. Moreover, the role of underlying Lobachevsky geometry in the working of this scheme might also contribute to the understanding of thermalisation. With this positive note, let us conclude and wait for more exciting results in the future.

Chapter A

UrQMD input file for minimumm bias data simulation

```
pro 197 79
tar 197 79
nev 1000
imp -14.6
eos 0
ecm 200.
tim 100 100
cto 18 0
f13
# f14
f15
f16
f19
f20
```

Used with explicit consent from authors [66]

Chapter B

Real Data & Monte Carlo Anchored Run Numbers

The Run numbers used are the following.

138872, 138871, 138870,138837, 138732, 138730, 138662, 138653, 138652, 138638, 138624, 138621, 138583,
138582, 138579,138578, 138534, 138469, 138442, 138439, 138438, 138396, 138364, 138275, 138225, 138201,
138197,138192, 138190, 137848, 137844, 137752, 137751, 137724, 137722, 137718, 137704, 137693, 137692,
137691, 137686, 137685, 137639, 137638, 137608, 137595, 137549, 137544, 137541, 137539, 137531, 137530,
137443, 137441, 137440, 137439, 137434, 137432, 137431, 137366, 137243, 137236, 137235,137232, 137231,
137162, 137161.

References

- [1] Taizo Muta. Foundations Of Quantum Chromodynamics: An Introduction To Perturbative Methods In Gauge Theories. World Scientific Lecture Notes in Physics.
- [2] <https://webific.ific.uv.es/web/en/content/lattice-qcd-numerical-approach-strong-force>
- [3] J.C. Collins , M.J. Perry. Superdense Matter: Neutrons or Asymptotically Free Quarks? Physical Review Letters, vol. 34, page 1353, 1975.
- [4] Particle Data Group at Lawrence Berkeley National Lab. <https://particleadventure.org/history-universe.html>
- [5] R. Hagedorn. Statistical thermodynamics of strong interactions at high energies. Nuovo Cimento Supplemento, vol. 3, page 147, 1965.
- [6] R. Hagedorn. Quark matter 84, proceedings helsinki. Springer-Verlag, 1984. Contribution: How we got to QCD matter from the hadron side by trial and error.
- [7] Wojciech Broniowski, Wojciech Florkowski, Leonid Ya.Glozman. Update of the Hagedorn mass spectrum. Physical Review D, vol. 70, page 117503, 2004.
- [8] H.D. Politzer. Reliable Perturbative Results for Strong Interactions? Physical Review Letters, vol. 30, page 1346, 1973.
- [9] D.J. Gross, F. Wilczek. Ultraviolet Behavior of Non-Abelian Gauge Theories. Physical Review Letters, vol. 30, page 1343, 1973.
- [10] N. Cabibbo , G. Parisi. Exponential hadronic spectrum and quark liberation. Physics Letters B, vol. 59, page 67, 1975.
- [11] Edward V. Shuryak. Quark-Gluon Plasma and Hadronic Production of Leptons, Photons and Psions. Physics Letters B, vol. 78, page 150, 1978.

- [12] H. Stocker, F. Jundt, G. Guillaume. *Toute la physique*. DUNOD, 1999.
- [13] F. Halzen, A.D. Martin. *Quarks and leptons: An introductory course in modern particle physics*. John Wiley and Sons, 1984.
- [14] M. Knecht. Une introduction la symétrie chirale. École Joliot-Curie 1998, 1998 <http://www.cenbg.in2p3.fr/heberge/EcoleJoliotCurie/coursJC/JOLIOT-CURIE%201998.pdf>
- [15] Thomas Schaefer. Phases of QCD. 2005. arXiv:hep-ph/0509068, Lectures at the Hampton University Graduate Studies Program (HUGS 2005).
- [16] Opportunities, Challenges, and Fantasies in Lattice QCD Frank Wilczek. [arXiv:hep-lat/0212041](https://arxiv.org/abs/hep-lat/0212041)
- [17] P. Petreczky. Lattice QCD at non-zero temperature. 2012. arXiv:1203.5320v1, Invited review for Journal of Physics G.
- [18] F. Karsch. Lattice QCD at High Temperature and Density. *Lecture Notes of Physics*, vol. 583, 2002. arXiv:hep-lat/0106019.
- [19] D'Enterria, D.; Ballintijn, M.; Bedjidian, M.; Hofman, D.; Kodolova, O.; Loizides, C.; Lokthin, I.P.; Lourenço, C.; Mironov, C.; et al. CMS physics technical design report: Addendum on high density QCD with heavy ions. *J. Phys. G* 2007, 34, 2307.
- [20] Water Structure and Science. http://www1.lsbu.ac.uk/water/water_phase_diagram.html
- [21] http://snelling.web.cern.ch/snelling/img/little_bang.jpg
- [22] Lectures on high-energy heavy-ion collisions at the LHC. Carlos A. Salgado [arXiv:0907.1219\[hep-ph\]](https://arxiv.org/abs/0907.1219)
- [23] Particle production in strong electromagnetic fields in relativistic heavy-ion collisions. Kirill Tuchin. [arXiv:1301.0099\[hep-ph\]](https://arxiv.org/abs/1301.0099)
- [24] J.D. Bjorken. Highly relativistic nucleus-nucleus collisions: The central rapidity region. *Physical Review D*, vol. 27, page 140, 1983.
- [25] Gines Martinez. *Advances in Quark Gluon Plasma*. Subatech CNRS/IN2P3, Ecole des Mines de Nantes, Université de Nantes, France. [arXiv:1304.1452\[nucl-ex\]](https://arxiv.org/abs/1304.1452)
- [26] E. Shuryak, *Phys. Rev. Lett.* 68, 3270 (1992)
- [27] G. R. Shin and B. Müller, *J. Phys. G* 29, 2485 (2003).

- [28] Z. Xu and C. Greiner, Phys. Rev. C 71, 064901 (2005).
- [29] Ulrich W. Heinz, Peter F. Kolb. Early thermalization at RHIC. Nucl.Phys.A702:269-280,2002. [arXiv: hep-ph/0111075](#)
- [30] Ulrich W. Heinz. Thermalization at RHIC. AIP Conf.Proc.739:163-180,2005. [arXiv:nucl-th/0407067](#)
- [31] Michael Strickland. Thermalization and isotropization in heavy-ion collisions. Pramana Vol. 84, No. 5, 671 (2015) [arXiv:1312.2285](#)
- [32] P. Huovinen, P. F. Kolb, Ulrich W. Heinz, P. V. Ruuskanen and S. A. Voloshin, Phys. Lett.B503, 58 (2001). [hep-ph/0101136](#).
- [33] Tetsufumi Hirano and Keiichi Tsuda, Phys. Rev. C66, 054905 (2002). [nucl-th/0205043](#).
- [34] M. J. Tannenbaum, Rept. Prog. Phys. 69, 2005 (2006). [nucl-ex/0603003](#).
- [35] Peter F. Kolb and Ulrich W. Heinz, In Hwa, R.C. (ed.) et al.: Quark gluon plasma pp. 634-714 (2003). [nucl-th/0305084](#).
- [36] F. Noferini, for the ALICE Collaboration, [arXiv:1212.1292](#).
- [37] Peter Arnold. Quark-Gluon Plasmas and Thermalization. Int.J.Mod.Phys.E16:2555-2594,2007. [arXiv: 0708.0812\[hep-ph\]](#)
- [38] E. S. Weibel, Phys. Rev. Lett. 2 (1959) 83.
- [39] S. Mrowczynski, PoS C POD2006 (2006) 042 [arXiv:hep-ph/0611067](#) ;P. Arnold
- [40] J. Lenaghan and G. D. Moore, JHEP 0308 (2003) 002.
- [41] D. Bodeker, JHEP 0510 (2005) 092;
- [42] D.P. Arnold and G. D. Moore, [arXiv:0706.0490\[hep-ph\]](#)
- [43] Statistical Physics of Particles, Mehran Kardar, CAMBRIDGE UNIVERSITY PRESS
- [44] Dirac P. Rev. Mod. Phys. 1949. V. 21. P. 392.
- [45] Bakker, Bernard L.G. Forms of Relativistic Dynamics. https://doi.org/10.1007/3-540-45114-5_1
- [46] Leutwyler H., Stern J., Ann. Phys., 1968, 112, 94–164.

- [47] Light front variables in high energy hadron-hadron and nucleus-nucleus interactions. V. Garsevanishvili et al. Phys. Part. Nucl. 34 (2003) 526
- [48] N. I Lobachevsky. Geometry (printed at the direction of the Council of the Physical and Mathematical Society at the Imperial Kazan University, Kazan, 1909)
- [49] N A Chernikov. Introduction of Lobachevsky Geometry into the theory of gravitation. Fiz. Elem. Chastits At. Yadra 23, 1155-1191 (1992)
- [50] Feynman R. Phys. Rev. Lett. 1969. V. 23. P. 415.
- [51] Garsevanishvili V. R. et al. Sov. J. Theor. Math. Phys. 1971. V. 7. P. 203.
- [52] Garsevanishvili V. R. et al. Sov. J. Theor. Math. Phys. 1975. V. 23. P. 310
- [53] The analysis of π^- meson spectra in semicentral CC and CTA collisions at a momentum of 4.2 GeV/c per nucleon in terms of light-front variables. Chkhaidze, L.V., Djobava, T.D., Garsevanishvili, V.R. et al. Phys. Atom. Nuclei (2004) 67: 1330.
- [54] Vilenkin N., Smorodinsky A. JETP. 1964. V. 46. P. 1793.
- [55] Critical surfaces in the phase space of particles produced inclusively in hadron-hadron collisions. B.B Levchenko, Yad.Fiz. 34,853-856, 1981
- [56] M. Bourquin and J.M Gaillard, Nucl. Phys. B114, 334
- [57] K. G. Boreskov and A.V Turbiner, Yad.Fiz. 29,761, 1979, Sov. J. Nucl. Phys 29,392 (1979)
- [58] ROOT Website: <https://root.cern.ch>
- [59] Bass, S. A. et al.: Microscopic models for ultrarelativistic heavy ion collisions. Prog. Part. Nucl. Phys., 41:255–369, 1998, [arXiv: nucl-th/9803035].
- [60] Bleicher, M. et al.: Relativistic hadron hadron collisions in the ultra-relativistic quantum molecular dynamics model. J. Phys., G25:1859–1896, 1999, [arXiv:9909407](https://arxiv.org/abs/9909407) [hep-ph].
- [61] Petersen, Hannah, Jan Steinheimer, Gerhard Burau, Marcus Bleicher and Horst Stoecker: A Fully Integrated Transport Approach to Heavy Ion Reactions with an Intermediate Hydrodynamic Stage. Phys.Rev., C78:044901, 2008, [arXiv: 0806.1695]
- [62] UrQMD-Collaboration: <http://urqmd.org>. The UrQMD user guide 2014

- [63] Additive quark model of multiparticle production and nucleus-nucleus collisions at high energies A. Bialas, W. Czyz, and L. Lesniak Phys. Rev. D 25, 2328, 1 May 1982
- [64] Schwinger, Julian S.: On gauge invariance and vacuum polarization. Phys.Rev., 82:664–679, 1951.
- [65] Graef, Gunnar (2013). Hanbury-Brown-Twiss interferometry within the UrQMD transport approach. Bibliographic information available from INIS: http://inis.iaea.org/search/search.aspx?orig_q=RN:47087580; Available from: publikationen.uni-frankfurt.de/files/31556/Main.pdf
- [66] Private communications with author of UrQMD Event Generator, Prof. Dr. Dr. h.c. Marcus Bleicher, Professor, Institut fuer Theoretische Physik, Johann Wolfgang Goethe-Universitaet.
- [67] Klaus Werner, Fu-Ming Liu, and Tanguy Pierog. Parton ladder splitting and the rapidity dependence of transverse momentum spectra in deuteron gold collisions at RHIC. Phys. Rev., C74:044902, 2006.
- [68] S.Ostapchenko T.Pierog K.Werner H.J.Drescher, M.Haldik. Parton-based gribov-regge theory. Phys. Rep, 350, 2001.
- [69] S. Porteboeuf, T. Pierog, K. Werner. Producing Hard Processes Regarding the Complete Event: The EPOS Event Generator, Moriond 2010 Porceeding. [arXiv:1006.2967 \[hep-ph\]](https://arxiv.org/abs/1006.2967)
- [70] S. Porteboeuf and K. Werner. Generation of complete events containing very high-p(T) jets. Eur. Phys. J., C62:145–150, 2009
- [71] Klaus Werner. Core-Corona Separation in Ultra-Relativistic Heavy Ion Collisions. Phys.Rev. Lett., 98:152301, 2007.
- [72] (ed.)Armesto, N. et al. Heavy Ion Collisions at the LHC - Last Call for Predictions. J.Phys., G35:054001,2008.
- [73] Private communication with with authors of EPOS. K. Werner and S. Porteboeuf.
- [74] X. N. Wang and M. Gyulassy, Phys. Rev. D 44, 3501 (1991).
- [75] M. Gyulassy and X. N. Wang, Comput. Phys. Commun.83, 307 (1994).
- [76] X. N. Wang, Phys. Rept. 280, 287 (1997).
- [77] S. E. Vance, M. Gyulassy and X. N. Wang, Phys. Lett.B 443, 45 (1998).
- [78] S. E. Vance and M. Gyulassy, Phys. Rev. Lett. 83, 1735(1999).

- [79] V. T. Pop, M. Gyulassy, J. Barrette, C. Gale, X. N. Wang and N. Xu, Phys. Rev. C 70, 064906 (2004).
- [80] T. K. Gaisser and F. Halzen, Phys. Rev. Lett. 54, 1754 (1985).
- [81] P. L’Heureux, B. Margolis and P. Valin, Phys. Rev. D 32, 1681 (1985).
- [82] G. Pancheri and Y. N. Srivastava, Phys. Lett. B 182(1986) 199.
- [83] L. Durand and P. Hong, Phys. Rev. Lett. 58, 303(1987).
- [84] L. Durand and H. Pi, Phys. Rev. D 38, 78 (1988).
- [85] J. Dias de Deus and J. Kwiecinski, Phys. Lett. B 196, 537 (1987).
- [86] R. C. Hwa, Phys. Rev. D 37, 1830 (1988).
- [87] A. Capella, U. Sukhatme and J. Tran Thanh Van, Z. Phys. C 3, 329 (1979).
- [88] T. K. Gaisser, F. Halzen and A. D. Martin, Phys. Lett.B 166, 219 (1986).
- [89] T. Sjostrand and M. van Zijl, Phys. Rev. D 36, 2019(1987).
- [90] T. Sjostrand, Comput. Phys. Commun. 39, 347(1986).
- [91] W. R. Chen and R. C. Hwa, Phys. Rev. D 39, 179 (1989).
- [92] X. N. Wang, Phys. Rev. D 43, 104 (1991).
- [93] J. P. Blaizot and A. H. Mueller, Nucl. Phys. B 289, 847(1987).
- [94] K. Kajantie, P. V. Landshoff and J. Lindfors, Phys. Rev.Lett. 59, 2527 (1987).
- [95] K. J. Eskola, K. Kajantie and J. Lindfors, Nucl. Phys. B 323, 37 (1989).
- [96] B. Zhang, C. M. Ko, B. A. Li and Z. w. Lin, Phys. Rev. 61, 067901 (2000).
- [97] D. W. Duke and J. F. Owens, Phys. Rev. D 30, 49 (1984)
- [98] From CERN Document Server: <https://cds.cern.ch/record/2197559>
- [99] <https://cms.cern>
- [100] <https://atlas.cern>
- [101] <http://alice-collaboration.web.cern.ch>

- [102] <http://lhcb.web.cern.ch/lhcb>
- [103] The operation of the LHC accelerator complex. Lecture by Redaelli, Stefano . From CDS: <http://cds.cern.ch/record/1257972/?ln=en>
- [104] Proceedings of the 2017 Evian Workshop On LHC Beam Operations. Available at: <http://cds.cern.ch/record/2654224/files/CERN-ACC-2019-012.pdf>
- [105] From CERN Document Server: https://cds.cern.ch/record/2657572/files/2017-May-11-ALICE_RUN2_labels_HD.png
- [106] G Contin .Performance of the present ALICE Inner Tracking System and studies for the upgrade Journal of Instrumentation, Volume 7, June 2012.
- [107] ALICE collaboration. Alignment of the ALICE Inner Tracking System with cosmic-ray tracks. Journal of Instrumentation, Volume 5, March 2010
- [108] J. Alme et al. The ALICE TPC, a large 3-dimensional tracking device with fast readout for ultra-high multiplicity events, Nucl. Instrum. Meth. A 622, 316 [arXiv:1001.1950](https://arxiv.org/abs/1001.1950).
- [109] The ALICE Collaboration, Upgrade of the ALICE Time Projection Chamber, CERN-LHCC-2013-020.
- [110] ALICE Collaboration, ALICE TDR 7, CERN/LHCC 2000-001
- [111] Alexander Kalweit. ALICE Collaboration, ALICE TDR 7, CERN/LHCC 2000-001. Production of light flavor hadrons and anti-nuclei at the LHC Doctoral Thesis.
- [112] Properties of hot and dense matter from relativistic heavy ion collisions - Braun-Munzinger, Peter et al. Phys.Rept. 621 (2016) 76-126 [arXiv:1510.00442](https://arxiv.org/abs/1510.00442) [nucl-th] <http://inspirehep.net/record/1395973/files/TPCpidPbPb.png>
- [113] ALICE Collaboration, ALICE Time-Of-Flight system (TOF) : Technical Design Report. <https://cds.cern.ch/record/430132?ln=en>
- [114] ALICE Collaboration , Determination of the event collision time with the ALICE detector at the LHC CERN-EP-2016-253. [arXiv:1610.03055](https://arxiv.org/abs/1610.03055). CERN-EP-2016-253.
- [115] Alici, Andrea. The MRPC-based ALICE Time-Of-Flight detector: status and performance. [arXiv:1203.5976](https://arxiv.org/abs/1203.5976)

- [116] ALICE Collaboration. The ALICE Transition Radiation Detector: construction, operation, and performance. Nucl. Instrum. Meth. A 881 (2018) 88
- [117] ALICE Collaboration. PHOS Technical design report. <https://edms.cern.ch/document/398934/1>
- [118] S Evdokimov, V Izucheev, Yu Kharlov, E Kondratyuk, S Sadovsky, A Shangaraev. The ALICE CPV detector. KnE Energ. Phys. 3 (2018) 260-267
- [119] ALICE Collaboration (A. Fantoni (Frascati) for the collaboration) The ALICE Electromagnetic Calorimeter: EMCAL. J.Phys.Conf.Ser. 293 (2011) 012043
- [120] ALICE Collaboration (Beole, S. et al.) ALICE technical design report: Detector for high momentum PID - CERN-LHCC-98-19
- [121] Arturo Fernandez Tellez. ACORDE, The ALICE Cosmic Ray Detector <http://inspirehep.net/record/1371550>
- [122] Gines Martinez (for the ALICE collaboration). The Muon Spectrometer of the ALICE experiment. Nucl.Phys.A749:313-319,2005
- [123] ALICE Photon Multiplicity Detector (PMD): Technical Design Report. CERN-LHCC-99-032 ; CERN-OPEN-2000-184 ; ALICE-TDR-6. <http://cds.cern.ch/record/451099>
- [124] ALICE Collaboration. ALICE technical design report of the zero degree calorimeter (ZDC) (Dellacasa, G. et al.) CERN-LHCC-99-05. <http://inspirehep.net/record/517333>
- [125] ALICE Collaboration. ALICE Technical Design Report on Forward Detectors: FMD, T0 and V0. CERN-LHCC-2004-025 ; ALICE-TDR-11. <http://cds.cern.ch/record/781854>
- [126] ALICE Collaboration. Centrality determination of Pb-Pb collisions at $\sqrt{s_{NN}} = 2.76$ TeV with ALICE. Phys. Rev. C 88 (2013) 044909
- [127] A.I. Maevskaya (on behalf of the ALICE Collaboration). The Fast Interaction Trigger detector for the upgrade of the ALICE experiment at CERN: design and performance. [arXiv:1812.00594](https://arxiv.org/abs/1812.00594)[physics.ins-det]
- [128] ALICE Analysis Tutorial: <https://alice-doc.github.io/alice-analysis-tutorial>
- [129] ALICE Run Condition Table: <https://alimonitor.cern.ch/configuration>

- [130] Alice Trigger Twiki. <https://twiki.cern.ch/twiki/bin/viewauth/ALICE/TriggerCoordination>.
- [131] ALICE Data Preparation Group : <https://twiki.cern.ch/twiki/bin/viewauth/ALICE/AliceDPG>
- [132] ALICE primary particles: <https://twiki.cern.ch/twiki/bin/viewauth/ALICE/TrackParametersMCTruth>
- [133] Private communication with Alexander Kalweit.
- [134] Jens Wiechula, Universität Tübingen. Everything you wanted to know about the TPC but were afraid to ask. <https://alice-analysis.web.cern.ch/sites/alice-analysis.web.cern.ch/files/documents/Analysis/JensJD.pdf>
- [135] The ALICE Geant4 Simulation. I Hřivnáčov1 et al.for the ALICE Collaboration) Journal of Physics: Conference Series, Volume 331, Part 3: Event Processing.
- [136] I. Hrivnacova and A. Morsch. For the ALICE Off-line Project - ALICE Collaboration. The ALICE Simulation Framework. International Conference on Computing in High Energy and Nuclear Physics, Padua, Italy, 7 - 11 Feb 2000. <http://cds.cern.ch/record/426367>
- [137] Rene A. Mendez, Jorge F. Silva, and Rodrigo Lobos. Analysis and Interpretation of the Cramér-Rao Lower-Bound in Astrometry: One-Dimensional Case. Publications of the Astronomical Society of the Pacific, Volume 125, Number 927
- [138] <https://twiki.cern.ch/twiki/bin/viewauth/ALICE/SystematicErrors>
- [139] T R. Barlow. Systematic errors: facts and fictions. arXiv:hep-ex/0207026v1, 2002.
- [140] TPC detector expert advice: Private conversation with Professor Marek Kowalski, Institute of Nuclear Physics, Krakow, Poland.
- [141] PhD Thesis of Han Liu. Fermi-Dirac and Bose-Einstein interferometry of protons and deuterons from 158 A GeV Pb+Pb collisions. The Andrzej Soltan Institute for Nuclear studeies. Warsaw, Poland.
- [142] R. Brun et al., 1985 GEANT3 User Guide, CERN Data Handling Division DD/EE/841;R. Brun et al. 1994 CERN Program Library Long Write-up, W5013, GEANT Detector Description and Simulation Tool.
- [143] G. Bendiscioli and D. Kharzeev. Anti-nucleon nucleon and anti-nucleon nucleus interaction: A Review of experimental data. Riv.Nuovo Cim. 17N6 (1994) 1-142